

Alma Mater Studiorum – Università di Bologna

DOTTORATO DI RICERCA IN

GEOFISICA

Ciclo XXXII

**Settore Concorsuale:** 02/C1

**Settore Scientifico Disciplinare:** FIS/06

CHARACTERIZATION OF TURBULENT EXCHANGE PROCESSES  
IN REAL URBAN STREET CANYONS WITH AND WITHOUT  
VEGETATION

**Presentata da:** Francesco Barbano

**Coordinatore Dottorato**

Prof.ssa Nadia Pinardi

**Supervisore**

Prof.ssa Silvana Di Sabatino

**Esame finale anno 2020**



# Abstract

Recent studies on turbulent exchange processes between the urban canopy layer and the atmosphere above have focused primarily on mechanical effects and less so on thermal ones, mostly by means of laboratory and numerical investigations and rarely in the real environment. More recently, these studies have been adopted to investigate city breathability, urban comfort and citizen health, with the aim to find new mitigation or adaptation solutions to air pollution and urban heat island, to enhance the citizen wellness. To investigate the small-scale processes characterizing vegetative and non-vegetative urban canopies, two field campaigns have been carried out within the city of Bologna, Italy. New mechanical and thermal time scales, and their ratios (rates), associated with inertial and thermal flow circulations, have been derived to this scope. In the non-vegetated canopy, mechanical time scales are found to describe fast exchanges at the rooftop and slow within the canopy, while thermal ones to describe fast mixing in the whole canopy. Faster processes are found in the vegetative canopy, with rapidly mixed mechanical time scales and varying thermal ones. The exchange rates are found to identify favorable mixing conditions in the 50-75% of the investigated period, but extreme disadvantageous events can totally suppress the exchanges. The exchange rates are also found to drive the pollutant removal from vegetated and non-vegetated canopies, with an efficacy which depends on the incanyon circulation. The impacts of real trees in a real neighborhood of the city is tackled with a simplified fluid-dynamics model, where mean flow and turbulence are studied with different vegetation configurations, topological and morphological characteristics. Vegetation is found to increase both blocking and channeling effects on the mean flow and to modify the production/dissipation rate of turbulence, depending on the wind direction and topology. Nevertheless, buildings maintain a predominant impact on the atmospheric flows.



# Contents

<b>1</b>	<b>Introduction</b>	<b>1</b>
<b>2</b>	<b>The Urban Boundary Layer: an Overview</b>	<b>5</b>
2.1	The Urban Boundary Layer . . . . .	5
2.1.1	The Roughness Sublayer . . . . .	8
2.1.2	The Inertial Sublayer . . . . .	9
2.2	The Urban Canopy Layer . . . . .	10
2.2.1	Inertial and Thermal Circulations . . . . .	11
2.3	Exchange Processes and City Breathability . . . . .	15
2.4	Vegetation in the Urban Environment . . . . .	21
2.5	Summary and Conclusions . . . . .	25
<b>3</b>	<b>The "Bologna Project": the Experimental Field Campaigns</b>	<b>27</b>
3.1	The Experimental Sites . . . . .	27
3.1.1	Non Vegetated Street Canyon - Marconi Street . . . . .	30
3.1.2	Vegetated Street Canyon - Laura Bassi Street . . . . .	35
3.2	Supporting Instrumentation . . . . .	39
3.3	Summary and Conclusions . . . . .	42
<b>4</b>	<b>Data Processing and Methodology</b>	<b>43</b>
4.1	Data processing . . . . .	43
4.1.1	Experimental protocol and despiking procedure . . . . .	43
4.1.2	Coordinate system rotation . . . . .	44
4.2	Data analysis . . . . .	45
4.2.1	The period selection based on the analysis of synoptic conditions . . . . .	45
4.2.2	Exchange processes: time scales and rates . . . . .	49
4.2.3	Pollutant concentration normalization . . . . .	53
4.3	Numerical simulations . . . . .	56
4.3.1	QUIC-URB model description . . . . .	56

## CONTENTS

---

4.3.2	QUIC-PLUME model description . . . . .	63
4.3.3	Vegetation Parametrization . . . . .	65
4.3.4	Model setup . . . . .	67
4.4	Summary and Conclusions . . . . .	70
<b>5</b>	<b>Results and Discussion: Observations and Campaign Comparison</b>	<b>73</b>
5.1	Mean Characteristics of the Summer Campaign . . . . .	73
5.1.1	Pollutant Concentrations . . . . .	73
5.1.2	Background and Mean Flow Fields Characteristics . . . . .	77
5.1.3	Local Flow Field and Turbulence . . . . .	78
5.2	Mean Characteristics of the Winter Campaign . . . . .	85
5.2.1	Pollutant Concentrations . . . . .	85
5.2.2	Background and Mean Flow Fields Characteristics . . . . .	87
5.2.3	Local Flow Field and Turbulence . . . . .	88
5.3	Summary and Conclusions . . . . .	94
<b>6</b>	<b>Results and Discussion: Exchange Processes between the Canopy Layer and the Urban Boundary Layer</b>	<b>97</b>
6.1	Exchange Processes: Time Scales and Rates . . . . .	98
6.1.1	Time Scales Evaluation . . . . .	98
6.1.2	Exchange Rates Evaluation . . . . .	102
6.1.3	Comparison between the Exchange Rates and the Normalized Pollutant Concentrations . . . . .	105
6.1.4	The Circulation Regime Identification: use of New Parametrizations to Compare Different Street Canyon Flow Characteristics . . . . .	110
6.2	The Impact of Trees on Exchange Processes Variables: a Multi-Seasonal Comparative Analysis . . . . .	114
6.3	Summary and Conclusions . . . . .	117
<b>7</b>	<b>Results and Discussion: Modeling the Impacts of Trees on the Exchange Processes</b>	<b>119</b>
7.1	Qualitative Code Verification: $u_*$ associated to the Unperturbed Flow . . . . .	119
7.2	Model Verification among Different Wind Direction Ensembles . . . . .	126
7.2.1	Vegetated Street Canyon - Laura Bassi Street . . . . .	126
7.2.2	Non Vegetated Street Canyon - Marconi Street . . . . .	133
7.3	The Impact of Trees in Laura Bassi Neighborhood under the Input Wind Direction Perpendicular from East to the Street Canyon Orientation . . . . .	139
7.3.1	Vegetation Impact Distributions and Topological Discretization . . . . .	143

---

7.3.2	The Effects of Morphology . . . . .	151
7.4	The Effect of Wind Direction and Surface Roughness on the Vegetation Impact . . . . .	155
7.4.1	Vegetation Impact Distributions and Topological Discretization . . . . .	156
7.4.2	The Effects of Morphology . . . . .	170
7.5	Summary and Conclusions . . . . .	177
<b>8</b>	<b>Conclusions and Further Remarks</b>	<b>181</b>
8.1	Future Perspectives . . . . .	185
<b>Appendices</b>		
<b>A</b>	<b>Technical Specifications for the Instrumentation</b>	<b>189</b>
<b>B</b>	<b>Application of Buckingham Theorem</b>	<b>199</b>
<b>C</b>	<b>Generalized Extreme Value Distribution Theory</b>	<b>201</b>
	<b>Bibliography</b>	<b>203</b>



# List of Figures

2.1	Schematic structure of the UBL (Source: Piringner et al. (2002)). . . . .	6
2.2	Time and space scales of the characteristic atmospheric processes within the UBL (Source: Oke et al. (2017)) . . . . .	7
2.3	Idealized 2D sketches of the in-canyon flow regimes from Oke (1987) classification. $H$ and $W$ are the building height and width. (Source: Oke et al. (2017)) . . . . .	11
2.4	Idealized 2D sketches of the in-canyon flow regimes in irregular street canyons originally from Xiaomin et al. (2006). $h_1$ and $h_2$ are the leeward and windward building height respectively, and $g$ is the canyon width. (Source: Zajic et al. (2011))	12
2.5	Sketches of the (a) IC and (b) TC inside an idealized SC. $H$ and $W$ are the mean building height and width of the canyon, $T_1$ and $T_2$ the building facade temperatures, $U_b$ and $\theta_b$ the background wind speed and air potential temperature, $\overline{w'u'}$ and $\overline{w'\theta'}$ the TKMF and the TKSHF evaluated inside the canyon (subscript S) and at the rooftop level (subscript H). . . . .	13
2.6	Simplified velocity profiles within and above the urban canopy. $H$ is the mean building height, $U_C$ the canopy layer velocity, $U_{ref}$ the velocity above the canopy layer and $U_E$ the exchange velocity between at the rooftop interface. (Source: Bentham and Britter (2003)) . . . . .	17
3.1	Satellite view of the Po Valley and Bologna historical center. (Source: Google Earth). . . . .	28
3.2	Top view of Bologna city center (a, ©Comune di Bologna) and the surrounding area (b). . . . .	29
3.3	Map of Bologna with localization of the campaign sampling sites. In order: (a) SI, (b) PSF, (c) MA, (d) GM, (e) LB, (f) AT and (g) IR. (Source: Google Earth).	30
3.4	Top (a) and frontal (b) views of MA. . . . .	31
3.5	Measurement sites locations at the three levels inside and above MA canyon. Colors link the location (dots) to the corresponding measurement site (boxes). Instrumentation at each level is reported on table 3.1. (Source: Google Earth). . . . .	32
3.6	Top (a) and frontal (b) views of LB. . . . .	35

## LIST OF FIGURES

---

3.7	Measurement sites locations at the three levels inside and above LB canyon. Colors link the location (dots) to the corresponding measurement site (boxes). Instrumentation at each level is reported on table 3.2. (Source: <a href="https://earth.google.com/web/">https://earth.google.com/web/</a> ).	36
3.8	PSF (a) and GM (b) air quality monitoring sites. . . . .	39
3.9	The Vaisala Ceilometer CL31 located on the rooftop of the Physics and Astronomy department in IS. . . . .	40
4.1	Three dimensional coordinate rotations for alignment of coordinate axes to the flow field over sloping terrain. Modified from figure 6.20 of Kaimal and Finnigan (1994). . . . .	44
4.2	GFS analysis of the surface isobars (white lines) superimposed on the geopotential at 500 hPa (colormap). Each panel shows the midnight UTC of a single day within the summer period. Bologna is identified by the black dot. . . . .	46
4.3	Wind velocity, air temperature and dew point temperature profiles retrieved from sounding data measured during (a) 20, (b) 21, (c) 22 and (d) 23 September from San Pietro in Capofiume, a small village 30 km to the north-east of Bologna (Data source: University of Wyoming, <a href="http://weather.uwyo.edu/upperair/sounding.html">http://weather.uwyo.edu/upperair/sounding.html</a> ).	47
4.4	GFS analysis of the surface isobars (white lines) superimposed on the geopotential at 500 hPa (colormap). Each panel shows the midnight UTC of a single day within the winter period. Bologna is identified by the black dot. . . . .	48
4.5	Wind velocity, air temperature and dew point temperature profiles retrieved from sounding data measured during (a) 08 and (b) 09 February from San Pietro in Capofiume, a small village 30 km to the north-east of Bologna (Data source: University of Wyoming, <a href="http://weather.uwyo.edu/upperair/sounding.html">http://weather.uwyo.edu/upperair/sounding.html</a> ). . . . .	48
4.6	Wind velocity streamlines retrieved from CFD simulations of MA, in condition of background wind direction perpendicular (a) and parallel (b) to the canyon orientation. $H$ and $W$ are the mean building height and width of the canyon, $T_1$ and $T_2$ the building facade temperatures, $U_b$ and $\theta_b$ the background wind speed and air potential temperature, $\overline{w'u'}$ and $\overline{w'\theta'}$ the TKMF and TKS HF respectively evaluated inside the canyon (GL and ML, subscript S) and at the RL (subscript H). . . . .	50
4.7	Comparison between $CO$ concentrations (red line) measured in (a) MA and (b) LB and the respective traffic rates (blue line) expressed as the number of cars passing through the street during the summer period. Data are averaged over a 30 minutes window. The shadowed areas highlight nighttime periods. On average sun rises at 6:00 AM and sets at 18:00 PM (GMT+1). . . . .	54

4.8	Comparison between $CO$ concentrations (red line) measured in (a) MA and (b) LB and the respective traffic rates (blue line) expressed as the number of cars passing through the street during the winter period. Data are averaged over a 30 minutes window. The shadowed areas highlight nighttime periods. On average sun rises at 7:30 AM and sets at 17:30 PM (GMT+1). . . . .	55
4.9	2D simplified schematic of the interaction of an incident boundary layer flow with the front face of a rectangular obstacle and the initial wind field for the rooftop recirculation scheme. In the upwind region, the boundary layer first adjusts to the adverse pressure gradient associated with the obstacle in the displacement zone where wind speeds are retarded. This zone is followed by flow separation and the formation of a frontal eddy. In the rooftop region, the model produces a monotonically decreasing profile with high velocities (opposite in direction to the incident boundary layer) near the roof and zero velocity at the core of the recirculation region. Above the vortex core, the velocities are specified to be the same as the upstream incident boundary layer. (Source: Gowardhan et al. (2010))	58
4.10	Schematic illustrating the flow regions and initial velocity fields associated with the street canyon parametrization in the vertical plane. (Source: Gowardhan et al. (2010)) . . . . .	61
4.11	Schematic illustrating the flow regions and initial velocity fields associated with the street canyon parametrization in the horizontal plane. (Source: Gowardhan et al. (2010)) . . . . .	62
4.12	(a) MA and (b) LB domains. . . . .	67
5.1	Boxplot of the summer campaign (a) $NO_2$ , (b) $CO$ , (c) $PM_{10}$ , (d) $PM_{2.5}$ , (e) $O_3$ concentrations and (f) air temperature $T$ within the reference canyons and the supporting sites. . . . .	75
5.2	Typical day for $NO$ and $NO_2$ concentrations in MA, LB and PSF during the summer campaign. . . . .	75
5.3	Typical relative concentrations of $NO$ , $NO_2$ and $O_3$ in (a) MA and (b) LB during the summer campaign. . . . .	76
5.4	Wind roses of the summer campaign within (a) MA, (b) LB and (c) on the supporting site of SI. . . . .	77
5.5	1 hour average wind speed (a), wind direction (b) and temperature (c) measured above the UCL. Colors indicate the following sites: (●) AT at 100 m agl, (●) SI at 35 m agl, (●) RL at 33 m agl in MA and (●) RL at 20 m agl in LB. The shadowed areas highlight nighttime periods. On average sun rises at 06:00 AM and sets at 18:00 PM (GMT+1). . . . .	78

## LIST OF FIGURES

---

5.6	Daytime (a) and nighttime (b) typical wind speed profiles in MA and LB relative to the period 20-23 September. Measurements are taken from the respective GLs, MLs and RLs and coupled with SI. Profiles are the hourly average over the investigated period taken at the 12:00, 14:00 and 16:00 GMT+1 during the day and the 00:00, 02:00 and 04:00 GMT+1 during the night. . . . .	79
5.7	Time evolution of the wind speed in (a) MA and (b) LB during the period 20-23 September. Measurements are taken from the respective GLs (blue), MLs (red) and RLs (green) of the canyons. The shadowed areas highlight nighttime periods. On average sun rises at 06:00 AM and sets at 18:00 PM (GMT+1). . . . .	80
5.8	Time evolution of the air temperature (a) in MA and LB, and their in-canyon comparison (b) during the period 20-23 September. Measurements are taken from the respective GLs (blue), MLs (red) and RLs (green) of the canyons. In (b) red asterisks correspond to MA, the blue ones to LB. The shadowed areas highlight nighttime periods. On average sun rises at 06:00 AM and sets at 18:00 PM (GMT+1). . . . .	80
5.9	Time evolution of the TKMF measured in (a) MA and (b) LB during the period 20-23 September. Measurements are taken from the respective GLs (blue), MLs (red) and RLs (green) of the canyons. The shadowed areas highlight nighttime periods. On average sun rises at 06:00 AM and sets at 18:00 PM (GMT+1). . . . .	81
5.10	Time evolution of the TKSHF measured in (a) MA and (b) LB during the period 20-23 September. Measurements are taken from the respective GLs (blue), MLs (red) and RLs (green) of the canyons. The shadowed areas highlight nighttime periods. On average sun rises at 06:00 AM and sets at 18:00 PM (GMT+1). . . . .	82
5.11	Time evolution of the $Tke$ measured in (a) MA and (b) LB during the period 20-23 September. Measurements are taken from the respective GLs (blue), MLs (red) and RLs (green) of the canyons. The shadowed areas highlight nighttime periods. On average sun rises at 06:00 AM and sets at 18:00 PM (GMT+1). . . . .	82
5.12	Time evolution of the stability parameter $H - d/L_O$ measured in (a) MA and (b) LB at the RLs of the canyons during the period 20-23 September. The shadowed areas highlight nighttime periods. On average sun rises at 06:00 AM and sets at 18:00 PM (GMT+1). . . . .	83
5.13	Time evolution of the 5-minute average normalized carbon monoxide concentrations $CO^+$ in MA (red) and LB (blue) during the analyzed period (20-23 September). The shadowed areas highlight nighttime periods. On average sun rises at 6:00 AM and sets at 18:00 PM (GMT+1). . . . .	84
5.14	Normalized $CO^+$ concentration as function of the emission source $Q_e$ in (a) MA and (c) LB, and the rooftop wind speed $U_H$ in (b) and (d) respectively. . . . .	85

5.15	Typical day for $NO$ and $NO_2$ concentrations in MA, LB and PSF during the winter campaign. . . . .	85
5.16	Boxplot of the winter campaign (a) $NO_2$ , (b) $CO$ , (c) $PM_{10}$ , (d) $PM_{2.5}$ , (e) $O_3$ concentrations and (f) air temperature $T$ within the reference canyons and the supporting sites. . . . .	87
5.17	Wind roses of the winter campaign within (a) MA, (b) LB and (c) on the supporting site of SI. . . . .	88
5.18	1 hour average wind speed (a), wind direction (b) and temperature (c) measured above the canopy layer. Colors indicate the following sites: (●) AT at 100 m agl, (●) SI at 35 m agl, (●) RL at 33 m agl in MA and (●) RL at 18 m agl in LB. The shadowed areas highlight nighttime periods. On average sun rises at 07:30 AM and sets at 17:30 PM (GMT+1). . . . .	88
5.19	Daytime (a) and nighttime (b) typical wind speed profiles in MA and LB relative to the period 08-09 February. Measurements are taken from the respective GLs (blue), MLs (red) and RLs (green) of the canyons. Profiles are the hourly average over the investigated period taken at the 12:00, 14:00 and 16:00 GMT+1 during the day and the 00:00, 02:00 and 04:00 GMT+1 during the night. . . . .	89
5.20	Time evolution of the wind speed in (a) MA and (b) LB during the period 08-09 February. Measurements are taken from the respective GLs (blue), MLs (red), RLs (green) and extrapolated rooftop levels (cyan, specific for LB) of the canyons. The shadowed areas highlight nighttime periods. On average sun rises at 07:30 AM and sets at 17:30 PM (GMT+1). . . . .	89
5.21	Time evolution of the air temperature (a) in MA and LB, and their in-canyon comparison (b) during the period 08-09 February. Measurements are taken from the respective GLs (blue), MLs (red) and RLs (green) of the canyons. In (b) red asterisks correspond to MA, the blue ones to LB. The shadowed areas highlight nighttime periods. On average sun rises at 07:30 AM and sets at 17:30 PM (GMT+1). . . . .	90
5.22	Time evolution of the TKMF measured in (a) MA and (b) LB during the period 08-09 February. Measurements are taken from the respective GLs (blue), MLs (red), RLs (green) and extrapolated rooftop levels (cyan, specific for LB) of the canyons. The shadowed areas highlight nighttime periods. On average sun rises at 07:30 AM and sets at 17:30 PM (GMT+1). . . . .	91

## LIST OF FIGURES

---

5.23	Time evolution of the TKSHF measured in (a) MA and (b) LB during the period 08-09 February. Measurements are taken from the respective GLs (blue), MLs (red), RLs (green) and extrapolated rooftop levels (cyan, specific for LB) of the canyons. The shadowed areas highlight nighttime periods. On average sun rises at 07:30 AM and sets at 17:30 PM (GMT+1).	91
5.24	Time evolution of the $Tke$ measured in (a) MA and (b) LB during the period 08-09 February. Measurements are taken from the respective GLs (blue), MLs (red), RLs (green) and extrapolated rooftop level (cyan, specific for LB) of the canyons. The shadowed areas highlight nighttime periods. On average sun rises at 07:30 AM and sets at 17:30 PM (GMT+1).	92
5.25	Time evolution of the stability parameter $H - d/L_O$ measured in (a) MA and (b) LB during the period 08-09 February. Measurements are taken from the respective RLs (green) of the canyons. The shadowed areas highlight nighttime periods. On average sun rises at 07:30 AM and sets at 17:30 PM (GMT+1).	92
5.26	Time evolution of the 5-minute average normalized carbon monoxide concentrations $CO^+$ in MA (red) and LB (blue) during the analyzed period (08-09 February). The shadowed areas highlight nighttime periods. On average sun rises at 7:30 AM and sets at 17:30 PM (GMT+1).	93
5.27	Normalized $CO^+$ concentration as function of the emission source $Q_e$ in (a) Marconi Street and (c) LB, and the rooftop wind speed $U_H$ in (b) and (d) respectively.	94
6.1	Normalized density distributions of the 5 minutes average $\tau_d$ (a) and $\tau_h$ (b) data inside and above MA during the analyzed period (20-23 September 2017). All the wind direction cases are considered together at each level.	98
6.2	Normalized density distributions of the 5 minutes average $\tau_d$ (a) and $\tau_h$ (b) data inside and above LB during the analyzed period (20-23 September 2017). All the wind direction cases are considered together at each level.	99
6.3	Generalized extreme value density functions of $\tau_d$ (a) and $\tau_h$ (b) distributions in Fig. 6.1 inside and above MA during the analyzed period (20-23 September 2017). All the wind direction cases are considered together at each level.	99
6.4	Generalized extreme value density functions of $\tau_d$ (a) and $\tau_h$ (b) distributions in Fig. 6.2 inside and above LB during the analyzed period (20-23 September 2017). All the wind direction cases are considered together at each level.	100
6.5	Normalized density distributions of $\eta_d$ (a) and $\eta_h$ (b) data inside and above MA during the analyzed period (20-23 September 2017). All the wind direction cases are considered together at each level.	103

6.6	Normalized density distributions of $\eta_d$ (a) and $\eta_h$ (b) data inside and above LB during the analyzed period (20-23 September 2017). All the wind direction cases are considered together at each level. . . . .	104
6.7	Data distributions and relative fits for the normalized $CO^+$ concentrations in (a) MA and (b) LB. . . . .	106
6.8	Wind speed ratios $U_C/U_b$ as a function of $B$ in (a) MA and (b) LB. Wind speed ratios are averaged over $B$ bins and the errorbars represent the standard deviation computed in each bin. Dashed lines are the trends from which Eq. (6.2) are extrapolated, black the one associated with the IC and red the one associated with the TC. . . . .	107
6.9	Time evolution of the buoyancy parameter $B$ defined by Eq. (6.1) in (a) MA and (b) LB. The dashed lines highlight the critical values $B_c$ . The shadowed areas highlight nighttime periods. On average sun rises at 6:00 AM and sets at 18:00 PM (GMT+1) . . . . .	109
6.10	Evolution comparison between $CO^+$ (blue) and $\eta_t$ (red) for (a) the GL to RL and (b) the ML to RL exchange rates in MA. . . . .	109
6.11	Evolution comparison between $CO^+$ (blue) and $\eta_t$ (red) for (a) the GL to RL and (b) the ML to RL exchange rates in LB. . . . .	110
6.12	Experiment setup, with aspect ratio shown. The view is looking towards north (Source: Dallman et al. (2014)). . . . .	111
6.13	Wind speed ratios $U_C/U_b$ as a function of $B$ in (a) MA and (b) LB modified according to Eq. (6.5a) and (6.5b) to compare with Dallman et al. (2014). Wind speed ratios are averaged over $B$ bins and the errorbars represent the standard deviation computed in each bin. . . . .	113
6.14	Wind speed ratios $U_C/U_b$ as a function of $B$ in LB modified according to Eq. (6.5a) and (6.5b) to account for the effective aspect ratio defined considering trees instead of buildings to compare with Dallman et al. (2014). Wind speed ratios are averaged over $B$ bins and the errorbars represent the standard deviation computed in each bin. . . . .	113
7.1	Simulated $u_*$ in (a) MA and (b) LB at the three monitoring levels as it was computed by the original version of the model. . . . .	120
7.2	Simulated $Tke$ in (a) MA and (b) LB at the three monitoring levels as it was computed by the original version of the model. . . . .	120

## LIST OF FIGURES

---

7.3	Simple domain for testing the newly computed $u_*$ . $x_i$ identify the locations where the simulated $u_*$ profiles are taken, and represent specific morphological structures depending on the input wind direction. Domain size ( $X \times Y \times Z$ ): 20x20x100 m; Domain resolution: 1x1x0.5 m. Dark blue building size: 10x2x20 m; light blue building size: 8x2x25 m; red tower size (diameter $d$ and height $h$ ): $d=3$ m, $h=50$ m; trees sizes: $d=2$ m, $h=15$ m, attenuation coefficient $a=1.7$ . . . . .	121
7.4	Simulated $u_*$ profiles with the original QUIC (blue line) and the new computation (red line) for the Case 2 (Tab. 7.1). Each panel shows one location from the list (Fig. 7.3). . . . .	123
7.5	Simulated $u_*$ in (a) MA and (b) LB at the three monitoring levels using the new computation for $u_*$ . . . . .	125
7.6	Simulated $Tke$ in (a) MA and (b) LB at the three monitoring levels using the new computation for $u_*$ . . . . .	125
7.7	Simulated $U$ , $Tke$ and $ \overline{w'u'} $ at (a) GL, (b) ML, (c) RL and (d) canyon center locations for the EP wind direction ensemble in LB. The blue profile represents the $90^\circ$ wind direction to the canyon orientation, while the shadowed area is the wind direction ensemble. The black dots and error bars refer to the averaged measured value and standard deviation within the selected period. . . . .	127
7.8	Simulated $U$ , $Tke$ and $ \overline{w'u'} $ at (a) GL, (b) ML, (c) RL and (d) canyon center locations for the WP wind direction ensemble in LB. The blue profile represents the $270^\circ$ wind direction to the canyon orientation, while the shadowed area is the wind direction ensemble. The black dots and error bars refer to the averaged measured value and standard deviation within the selected period. . . . .	129
7.9	Simulated $U$ , $Tke$ and $ \overline{w'u'} $ at (a) GL, (b) ML, (c) RL and (d) canyon center locations for the NP wind direction ensemble in LB. The blue profile represents the $0^\circ$ wind direction to the canyon orientation, while the shadowed area is the wind direction ensemble. The black dots and error bars refer to the averaged measured value and standard deviation within the selected period. . . . .	130
7.10	Simulated $U$ , $Tke$ and $ \overline{w'u'} $ at (a) GL, (b) ML, (c) RL and (d) canyon center locations for the SP wind direction ensemble in LB. The blue profile represents the $180^\circ$ wind direction to the canyon orientation, while the shadowed area is the wind direction ensemble. The black dots and error bars refer to the averaged measured value and standard deviation within the selected period. . . . .	132

7.11	Simulated $U$ , $Tke$ and $ \overline{w'u'} $ at (a) GL, (b) ML, (c) RL and (d) canyon center locations for the EP wind direction ensemble in MA. The blue profile represents the $90^\circ$ wind direction to the canyon orientation, while the shadowed area is the wind direction ensemble. The black dots and error bars refer to the averaged measured value and standard deviation within the selected period. . . . .	134
7.12	Simulated $U$ , $Tke$ and $ \overline{w'u'} $ at (a) GL, (b) ML, (c) RL and (d) canyon center locations for the WP wind direction ensemble in MA. The blue profile represents the $270^\circ$ wind direction to the canyon orientation, while the shadowed area is the wind direction ensemble. The black dots and error bar refer to the averaged measured value and standard deviation within the selected period. . . . .	135
7.13	Simulated $U$ , $Tke$ and $ \overline{w'u'} $ at (a) GL, (b) ML, (c) RL and (d) canyon center locations for the NP wind direction ensemble in MA. The blue profile represents the $0^\circ$ wind direction to the canyon orientation, while the shadowed area is the wind direction ensemble. The black dots and error bars refer to the averaged measured value and standard deviation within the selected period. . . . .	137
7.14	Simulated $U$ , $Tke$ and $ \overline{w'u'} $ at (a) GL, (b) ML, (c) RL and (d) canyon center locations for the SP wind direction ensemble in MA. The blue profile represents the $180^\circ$ wind direction to the canyon orientation, while the shadowed area is the wind direction ensemble. The black dots and error bars refer to the averaged measured value and standard deviation within the selected period. . . . .	138
7.15	Cross sections of the wind speed simulated at the GL (a-b) and ML (c-d) monitoring sites of LB. (a-c) simulate the real environment of the street while (b-d) represent the scenario where vegetation has been removed. Solid boundaries are displayed in white, trees are represented as white towers of dashed lines. . . . .	140
7.16	Cross sections of the $Tke$ simulated at the GL (a-b) and the ML (c-d) monitoring sites of LB. (a-c) simulate the real environment of the street while (b-d) represent the scenario where vegetation has been removed. Solid boundaries are displayed in white, trees are represented as white towers of dashed lines. . . . .	141
7.17	Cross sections of the TKMF $ \overline{w'u'} $ simulated at the GL (a-b) and the ML (c-d) monitoring sites of LB. (a-c) simulate the real environment of the street while (b-d) represent the scenario where vegetation has been removed. Solid boundaries are displayed in white, trees are represented as white towers of dashed lines. . . . .	142
7.18	Wind speed $U$ distributions evaluated in the (a) UCL and (b) UBL above for the REF-scen (in blue), the NOVEG-scen (in green) and the VEG50-scen (in cyan). . . . .	144
7.19	$Tke$ distributions, normalized on the squared wind speed $U$ , evaluated in the (a) UCL and (b) UBL above for the REF-scen (in blue), the NOVEG-scen (in green) and the VEG50-scen (in cyan). . . . .	145

## LIST OF FIGURES

---

7.20	TKMF $ \overline{w'u'} $ distributions, normalized on the squared wind speed $U$ , evaluated in the (a) UCL and (b) UBL above for the REF-scen (in blue), the NOVEG-scen (in green) and the VEG50-scen (in cyan). Ground layer in (a) has a different ordinate tick to make the distribution differences appreciable. . . . .	146
7.21	Wind speed $U$ variation factor distributions evaluated in the (a) UCL and (b) UBL above for the difference between REF-scen VEG-scen for the EWcanopy (blue), NScanopy (green) and Intersect (red) topological categories. . . . .	147
7.22	$Tke$ variation factor distributions, normalized on the squared wind speed $U$ ( $< Tke >$ ), evaluated in the (a) UCL and (b) UBL above for the difference between REF-scen and NOVEG-scen for the EWcanopy (blue), NScanopy (green) and Intersect (red) topological categories. . . . .	148
7.23	TKMF $ \overline{w'u'} $ variation factor distributions, normalized on the squared wind speed $U$ ( $< \overline{w'u'} >$ ), evaluated in the (a) UCL and (b) UBL above for the difference between REF-scen and NOVEG-scen for the EWcanopy (blue), NScanopy (green) and Intersect (red) topological categories. . . . .	149
7.24	Wind speed $U$ variation factor distributions evaluated in the (a) UCL and (b) UBL above for the difference between REF-scen and VEG50-scen for the EWcanopy (blue), NScanopy (green) and Intersect (red) topological categories. . . . .	150
7.25	$Tke$ variation factor distributions, normalized on the squared wind speed $U$ ( $< Tke >$ ), evaluated in the (a) UCL and (b) UBL above for the difference between REF-scen and VEG50-scen for the EWcanopy (blue), NScanopy (green) and Intersect (red) topological categories. . . . .	150
7.26	TKMF $ \overline{w'u'} $ variation factor distributions, normalized on the squared wind speed $U$ ( $< \overline{w'u'} >$ ), evaluated in the (a) UCL and (b) UBL above for the difference between REF-scen and VEG50-scen for the EWcanopy (blue), NScanopy (green) and Intersect (red) topological categories. . . . .	151
7.27	Wind speed as a function of the planar ( $\lambda_p$ ) and frontal ( $\lambda_f$ ) area fraction coefficients retrieved at (a) ground, (b) mid-canyon, (c) rooftop and (d) roughness layers respectively. Wind speeds are normalized over their maximum values in each layer to enhance the comparability. Blue circles identify to the REF-scen, the green ones the NOVEG-scen and the black ones the VEG50-scen. Each dot is the wind speed averaged over each $\lambda_p$ or $\lambda_f$ bin 0.01 large, and the error bars are the standard deviation in each bin. . . . .	152

7.28	$Tke$ , normalized on the squared wind speed $U$ , as a function of the planar ( $\lambda_p$ ) and frontal ( $\lambda_f$ ) area coefficients retrieved at (a) ground, (b) mid-canyon, (c) rooftop and (d) roughness layers respectively. $Tke/U^2$ s are normalized over their maximum values in each layer to enhance the comparability. Blue circles identify to the REF-scen, the green ones the NOVEG-scen and the black ones the VEG50-scen. Each dot is the $Tke/U^2$ averaged over each $\lambda_p$ or $\lambda_f$ bin 0.01 large and the error bars are the standard deviation in each bin. . . . .	153
7.29	TKMF, normalized on the squared wind speed $U$ , as a function of the planar ( $\lambda_p$ ) and frontal ( $\lambda_f$ ) area coefficients retrieved at (a) ground, (b) mid-canyon, (c) rooftop and (d) roughness layers respectively. $ \overline{w'u'} $ s are normalized over their maximum values in each layer to enhance the comparability. Blue circles identify to the REF-scen, the green ones the NOVEG-scen and the black ones the VEG50-scen. Each dot is the $ \overline{w'u'} $ averaged over each $\lambda_p$ or $\lambda_f$ bin 0.01 large and the error bars are the standard deviation in each bin. . . . .	154
7.30	Wind speed $U$ distributions evaluated in the (a) UCL and (b) UBL above for REF-scen (in blue), NOVEG-scen (in green) and VEG50-scen (in cyan). Ground layer in (a) has a different ordinate tick to make the distribution differences appreciable. . . . .	156
7.31	$Tke$ distributions, normalized on the squared wind speed $U$ , evaluated in the (a) UCL and (b) UBL above for REF-scen (in blue), NOVEG-scen (in green) and VEG50-scen (in cyan). Ground layer in (a) has a different ordinate tick to make the distribution differences appreciable. . . . .	157
7.32	TKMF $ \overline{w'u'} $ distributions, normalized on the squared wind speed $U$ , evaluated in the (a) UCL and (b) UBL above for REF-scen (in blue), NOVEG-scen (in green) and VEG50-scen (in cyan). Ground layer in (a) has a different ordinate tick to make the distribution differences appreciable. . . . .	158
7.33	Wind speed $U$ variation factor distributions evaluated in the (a) UCL and (b) UBL above for the difference between REF-scen and NOVEG-scen for the EW-canopy (blue), NScanopy (green) and Intersect (red) topological categories. . . . .	159
7.34	$Tke$ variation factor distributions, normalized on the squared wind speed $U$ ( $<Tke>$ ), evaluated in the (a) UCL and (b) UBL above for the difference between REF-scen and NOVEG-scen for the EWcanopy (blue), NScanopy (green) and Intersect (red) topological categories. . . . .	159
7.35	TKMF $ \overline{w'u'} $ variation factor distributions, normalized on the squared wind speed $U$ ( $< \overline{w'u'} >$ ), evaluated in the (a) UCL and (b) UBL above for the difference between REF-scen and NOVEG-scen for the EWcanopy (blue), NScanopy (green) and Intersect (red) topological categories. . . . .	160

## LIST OF FIGURES

---

7.36	Wind speed $U$ variation factor distributions evaluated in the (a) UCL and (b) UBL above for the difference between REF-scen and VEG50-scen for the EW-canopy (blue), NScanopy (green) and Intersect (red) topological categories. . . . .	161
7.37	$Tke$ variation factor distributions, normalized on the squared wind speed $U$ ( $\langle Tke \rangle$ ), evaluated in the (a) UCL and (b) UBL above for the difference between REF-scen and VEG50-scen for the EWcanopy (blue), NScanopy (green) and Intersect (red) topological categories. . . . .	162
7.38	TKMF $ \overline{w'u'} $ variation factor distributions, normalized on the squared wind speed $U$ ( $\langle  \overline{w'u'}  \rangle$ ), evaluated in the (a) UCL and (b) UBL above for the difference between REF-scen and VEG50-scen for the EWcanopy (blue), NScanopy (green) and Intersect (red) topological categories. . . . .	163
7.39	Wind speed $U$ distributions evaluated in the (a) UCL and (b) UBL above for REF-scen (in blue), NOVEG-scen (in green) and VEG50-scen (in cyan). Ground layer in (a) has a different ordinate tick to make the distribution differences appreciable. . . . .	164
7.40	$Tke$ distributions, normalized on the squared wind speed $U$ , evaluated in the (a) UCL and (b) UBL above for REF-scen (in blue), NOVEG-scen (in green) and VEG50-scen (in cyan). Ground layer in (a) has a different ordinate tick to make the distribution differences appreciable. . . . .	165
7.41	TKMF $ \overline{w'u'} $ distributions, normalized on the squared wind speed $U$ , evaluated in the (a) UCL and (b) UBL above for REF-scen (in blue), NOVEG-scen (in green) and VEG50-scen (in cyan). Ground layer in (a) has a different ordinate tick to make the distribution differences appreciable. . . . .	166
7.42	Wind speed $U$ variation factor distributions evaluated in the (a) UCL and (b) UBL above for the difference between REF-scen and NOVEG-scen for the EW-canopy (blue), NScanopy (green) and Intersect (red) topological categories. . . . .	166
7.43	$Tke$ variation factor distributions, normalized on the squared wind speed $U$ ( $\langle Tke \rangle$ ), evaluated in the (a) UCL and (b) UBL above for the difference between REF-scen and NOVEG-scen for the EWcanopy (blue), NScanopy (green) and Intersect (red) topological categories. . . . .	167
7.44	TKMF $ \overline{w'u'} $ variation factor distributions, normalized on the squared wind speed $U$ ( $\langle  \overline{w'u'}  \rangle$ ), evaluated in the (a) UCL and (b) UBL above for the difference between REF-scen and NOVEG-scen for the EWcanopy (blue), NScanopy (green) and Intersect (red) topological categories. . . . .	168
7.45	Wind speed $U$ variation factor distributions evaluated in the (a) UCL and (b) UBL above for the difference between REF-scen and VEG50-scen for the EW-canopy (blue), NScanopy (green) and Intersect (red) topological categories. . . . .	169

7.46 *Tke* variation factor distributions, normalized on the squared wind speed  $U$  ( $\langle Tke \rangle$ ), evaluated in the (a) UCL and (b) UBL above for the difference between REF-scen and VEG50-scen for the EWcanopy (blue), NScanopy (green) and Intersect (red) topological categories. . . . . 169

7.47 TKMF  $|\overline{w'u'}|$  variation factor distributions, normalized on the squared wind speed  $U$  ( $\langle |\overline{w'u'}| \rangle$ ), evaluated in the (a) UCL and (b) UBL above for the difference between REF-scen and VEG50-scen for the EWcanopy (blue), NScanopy (green) and Intersect (red) topological categories. . . . . 170

7.48 Wind speed as a function of the planar ( $\lambda_p$ ) and frontal ( $\lambda_f$ ) area coefficients retrieved at (a) ground, (b) mid-canyon, (c) rooftop and (d) roughness layers respectively. Wind speeds are normalized over their maximum values to enhance the comparability. Blue circles identify to the REF-scen, the green ones the NOVEG-scen and the black ones the VEG50-scen. Each dot is the wind speed averaged over each  $\lambda_p$  or  $\lambda_f$  bin 0.01 large and the error bars are the standard deviation in each bin. . . . . 171

7.49 *Tke*, normalized on the squared wind speed  $U$ , as a function of the planar ( $\lambda_p$ ) and frontal ( $\lambda_f$ ) area coefficients retrieved at (a) ground, (b) mid-canyon, (c) rooftop and (d) roughness layers respectively. *Tkes* are normalized over their maximum values to enhance the comparability. Blue circles identify to the REF-scen, the green ones the NOVEG-scen and the black ones the VEG50-scen. Each dot is the *Tke* averaged over each  $\lambda_p$  or  $\lambda_f$  bin 0.01 large and the error bars are the standard deviation in each bin. . . . . 172

7.50 TKMF, normalized on the squared wind speed  $U$ , as a function of the planar ( $\lambda_p$ ) and frontal ( $\lambda_f$ ) area coefficients retrieved at (a) ground, (b) mid-canyon, (c) rooftop and (d) roughness layers respectively.  $|\overline{w'u'}|$ s are normalized over their maximum values to enhance the comparability. Blue circles identify to the REF-scen, the green ones the NOVEG-scen and the black ones the VEG50-scen. Each dot is the  $|\overline{w'u'}|$  averaged over each  $\lambda_p$  or  $\lambda_f$  bin 0.01 large and the error bars are the standard deviation in each bin. . . . . 173

7.51 Wind speed as a function of the planar ( $\lambda_p$ ) and frontal ( $\lambda_f$ ) area coefficients retrieved at (a) ground, (b) mid-canyon, (c) rooftop and (d) roughness layers respectively. Wind speeds are normalized over their maximum values to enhance the comparability. Blue circles identify to the REF-scen, the green ones the NOVEG-scen and the black ones the VEG50-scen. Each dot is the wind speed averaged over each  $\lambda_p$  or  $\lambda_f$  bin 0.01 large and the error bars are the standard deviation in each bin. . . . . 175

## LIST OF FIGURES

---

- 7.52  $Tke$ , normalized on the squared wind speed  $U$ , as a function of the planar ( $\lambda_p$ ) and frontal ( $\lambda_f$ ) area coefficients retrieved at (a) ground, (b) mid-canyon, (c) rooftop and (d) roughness layers respectively.  $Tkes$  are normalized over their maximum values to enhance the comparability. Blue circles identify to the REF-scen, the green ones the NOVEG-scen and the black ones the VEG50-scen. Each dot is the  $Tke$  averaged over each  $\lambda_p$  or  $\lambda_f$  bin 0.01 large and the error bars are the standard deviation in each bin. . . . . 176
- 7.53 TKMF, normalized on the squared wind speed  $U$ , as a function of the planar ( $\lambda_p$ ) and frontal ( $\lambda_f$ ) area coefficients retrieved at (a) ground, (b) mid-canyon, (c) rooftop and (d) roughness layers respectively.  $|\overline{w'u'}|$ s are normalized over their maximum values to enhance the comparability. Blue circles identify to the REF-scen, the green ones the NOVEG-scen and the black ones the VEG50-scen. Each dot is the  $|\overline{w'u'}|$  averaged over each  $\lambda_p$  or  $\lambda_f$  bin 0.01 large and the error bars are the standard deviation in each bin. . . . . 177

# List of Tables

3.1	Table summarizing the instrumentation setup deployed in MA. . . . .	34
3.2	Table summarizing the instrumentation setup deployed in LB. . . . .	38
3.3	Table summarizing the instrumentation setup deployed at the supporting sites. . . . .	41
4.1	Setup configuration for the QUIC simulations. . . . .	68
4.2	Setup quantities for Marconi and Laura Bassi domains. Between brackets is reported the inlet wind direction considered (when important). . . . .	69
5.1	Significant statistics for the air quality and air temperature within the reference SCs and the supporting monitoring sites during the summer campaign. Left to right: mean, standard deviation, 25 <sup>th</sup> percentile, 50 <sup>th</sup> percentile, 75 <sup>th</sup> percentile . . . . .	74
5.2	Significant statistics for the air quality and air temperature within the reference SCs and the supporting monitoring sites during the winter campaign. Left to right: mean, standard deviation, 25 <sup>th</sup> percentile, 50 <sup>th</sup> percentile, 75 <sup>th</sup> percentile. . . . .	86
6.1	Table summarizing the characteristic time scales $\tau$ in MA derived from the modes of the probability density functions computed for the whole period overall flow, NP, SP and EWP background wind direction cases. . . . .	101
6.2	Table summarizing the characteristic time scales $\tau$ in LB derived from the modes of the probability density functions computed for the whole period overall flow, NP, SP and EWP background wind direction cases. . . . .	102
6.3	Table summarizing the characteristic exchange rates $\eta$ in MA derived from the modes of the probability density functions computed for the whole period overall flow, NP, SP and EWP background wind direction cases. . . . .	104
6.4	Table summarizing the characteristic exchange rates $\eta$ in LB derived from the modes of the probability density functions computed for the whole period overall flow, NP, SP and EWP background wind direction cases. . . . .	105

## LIST OF TABLES

---

6.5	Ratios between the summer (subscript $s$ ) and the winter (subscript $w$ ) mean wind speed, TKMF, TKSHF and $Tke$ for different background wind direction classes under near-neutral atmospheric stability condition at the three levels of LB. . . .	115
6.6	Ratios between the summer (subscript $s$ ) and the winter (subscript $w$ ) mean wind speed, TKMF, TKSHF and $Tke$ for different background wind direction classes under strongly unstable atmospheric stability condition at the three levels of LB.	116
7.1	Input variables for the seven test cases used to assess the reliability of the new $u_*$ computation. . . . .	122
7.2	Retrieved wrong $u_*$ values, together with the newly computed ones with the updated method and the corresponding wind speeds for each grid point. . . . .	124
7.3	Retrieved wrong $u_*$ values, together with the newly computed ones with the updated method in MA and LB neighborhoods. . . . .	124
A.1	Technical specifications of sonic anemometers. . . . .	189
A.2	Technical specifications of sonic anemometers. . . . .	190
A.3	Technical specifications of the open path gas analyzer. . . . .	191
A.4	Technical specifications of HCS2S3 thermohygrometer, CNR4 net radiometer and PTB110 barometer. . . . .	192
A.5	Technical specifications of $CO$ , $NO_x$ and $SO_2$ gas analyzers. . . . .	193
A.6	Technical specifications of $O_3$ and $BTX$ gas analyzers. . . . .	194
A.7	Technical specifications of $PM_{10}$ and $PM_{2.5}$ particulate samplers. . . . .	195
A.8	Technical specifications of thermohygrometers inside the mobile laboratories. . .	195
A.9	Technical specifications of the cup and vane anemometers inside the mobile laboratories. . . . .	196
A.10	Technical specifications of the ceilometer CL31. . . . .	196
A.11	Technical specifications of thermohygrometers in Silvani Street and Asinelli Tower.	197
A.12	Technical specifications of the cup and vane anemometers in Silvani Street and Asinelli Tower. . . . .	198

# Acronyms

**ACI** Italian Car Club. [56](#)

**ARPAE** Environmental and Energy Regional Protection Agency. [28](#), [31](#), [34](#), [37–42](#)

**AT** Asinelli Tower. [29](#), [40](#), [78](#), [128–131](#), [137](#)

**BT** Buckingham Theorem. [51](#), [52](#)

**CB** City Breathability. [16–19](#), [21](#), [23](#), [25](#)

**CFD** Computational Fluid Dynamics. [18](#), [25](#), [50](#), [56](#), [70](#), [102](#), [139](#), [177](#)

**CNR** National Council of Researches. [28](#), [34](#), [38](#)

**DIFA-UNIBO** Department of Physics and Astronomy of the University of Bologna. [27](#), [28](#), [34](#), [38](#), [40–42](#)

**EMEP/EEA** European Monitoring and Evaluation Program of the European Environment Agency. [56](#)

**EP** East Perpendicular. [114](#), [116](#), [121](#), [126](#), [128](#), [133–135](#), [139](#), [143](#), [155–157](#), [174](#), [177–179](#)

**EWcanopy** East-West Oriented Street Canyons. [146–150](#), [158–163](#), [165](#), [167](#), [179](#)

**EWP** East-West Perpendicular. [97](#), [101](#), [102](#), [104](#), [114](#), [117](#), [134](#), [137](#)

**GEV** Generalize Extreme Value. [100](#), [101](#), [103](#), [106](#), [117](#)

**GL** Ground Level. [vi](#), [viii–xi](#), [xiii](#), [31](#), [37](#), [50](#), [52](#), [79–82](#), [89–92](#), [98](#), [100–103](#), [107–110](#), [112](#), [117](#), [128](#), [129](#), [131](#), [134](#), [135](#), [137–139](#), [141](#)

**GM** Giardini Margherita. [29](#), [39](#), [40](#), [76](#), [86](#)

**IC** Inertial Circulation. [11](#), [14](#), [15](#), [21](#), [79](#), [81](#), [82](#), [92](#), [105–110](#), [114](#), [157](#)

## Acronyms

---

- Intersect** Major Intersections. [xvii](#), [146](#), [147](#), [150](#), [158–163](#), [165–167](#), [169](#), [179](#)
- IS** Irnerio Street. [29](#), [40](#), [70](#)
- iSCAPE** Improving the Smart Control of Air Pollution in Europe. [2](#), [42](#)
- ISL** Inertial SubLayer. [7–10](#), [16](#), [139](#)
- ISTAT** National Institute of Statistics. [28](#)
- LB** Laura Bassi Street. [27](#), [35](#), [36](#), [39](#), [42](#), [54](#), [55](#), [66](#), [67](#), [71](#), [75–84](#), [86–88](#), [90–92](#), [94](#), [95](#), [98–109](#), [111](#), [112](#), [115](#), [117–121](#), [125](#), [126](#), [128](#), [130](#), [131](#), [137–139](#), [143](#), [149](#), [155](#), [156](#), [163](#), [177](#), [178](#)
- MA** Marconi Street. [vi](#), [ix](#), [27](#), [30](#), [31](#), [35–37](#), [42](#), [50](#), [54](#), [55](#), [67](#), [71](#), [74–77](#), [79–81](#), [83](#), [84](#), [86–88](#), [90–92](#), [94](#), [95](#), [98–101](#), [103–112](#), [114](#), [117–121](#), [125](#), [126](#), [133](#), [134](#), [136–138](#), [177](#)
- ML** Mid-canyon Level. [vi](#), [viii–xi](#), [xiii](#), [31](#), [33](#), [37](#), [50](#), [52](#), [79–82](#), [89–92](#), [98](#), [100–105](#), [107–110](#), [112](#), [117](#), [128](#), [129](#), [131](#), [137](#), [139](#), [141](#)
- NOVEG-scen** No Vegetation Scenario. [143](#), [144](#), [146](#), [151](#), [153–158](#), [163–165](#), [168](#), [170](#), [171](#), [173](#), [175](#), [176](#), [178](#), [179](#)
- NP** Northerly Parallel. [97](#), [101](#), [102](#), [104](#), [116–118](#), [130](#), [136](#), [155](#), [158](#), [170](#), [177–179](#)
- NScanopy** North-South Oriented Street Canyons. [146](#), [147](#), [150](#), [158–163](#), [165](#), [167–169](#), [179](#)
- PBL** Planetary Boundary Layer. [5](#)
- PSF** Porta San Felice. [29](#), [39](#), [40](#), [74–76](#), [85](#), [87](#)
- QUIC** Quick Urban & Industrial Complex. [56](#), [67](#), [70](#), [71](#), [119](#), [126](#), [134](#), [138](#), [177](#), [178](#), [183](#)
- QUIC-PLUME** Quick Urban & Industrial Complex Lagrangian random-walk dispersion model. [56](#), [63](#), [67](#), [70](#), [71](#)
- QUIC-URB** Quick Urban & Industrial Complex mass-conserved wind solver. [56](#), [58](#), [64](#), [67](#), [71](#)
- REF-scen** Reference Scenario. [143–146](#), [148](#), [151](#), [153–158](#), [160](#), [163–168](#), [170](#), [171](#), [173](#), [175–178](#)
- RL** Rooftop Level. [vi–xi](#), [25](#), [31](#), [33](#), [37](#), [50–53](#), [66](#), [78–84](#), [88–94](#), [98](#), [100–105](#), [109](#), [110](#), [117](#), [126–129](#), [131](#), [134](#), [135](#), [138](#)

- RSL** Roughness SubLayer. 7–9, 15, 17
- ShL** Shear Layer. 9, 13, 16, 25, 50, 52, 61, 121, 126, 134
- SI** Silvani Street. 29, 40, 67, 70, 77, 78, 87, 107, 112, 121, 127–130, 133, 134, 136, 137
- SL** Surface Layer. 6–9, 25, 49, 70
- SP** Southerly Parallel. 97, 101, 102, 104, 116, 117, 131, 137, 155, 177
- SW** 45° Oblique from SouthWest. 155, 163, 167, 173, 178
- TC** Thermal Circulation. 14, 15, 21, 81, 105–110, 114
- TKE** Turbulence Kinetic Energy. 177–179, 184
- TKMF** Turbulent Kinematic Momentum Flux. vi, xiii, xvi, 8, 11, 13, 16, 17, 25, 50, 51, 79, 81, 82, 92, 100, 101, 105, 108, 115, 126, 128, 131, 134, 139, 141–143, 145, 146, 148, 150, 151, 154, 155, 157, 159, 160, 162–170, 172, 173, 176–179, 184
- TKSHF** Turbulent Kinematic Sensible Heat Flux. vi, 8, 25, 50, 51, 81, 82, 92, 100, 101, 105, 109, 115, 118
- UBL** Urban Boundary Layer. 5, 6, 8–12, 15, 24, 25, 40, 70, 79, 120, 123–125, 127, 128, 131, 134, 137–139, 143, 150, 177, 178, 183
- UCL** Urban Canopy Layer. vii, 7–10, 12, 15, 18, 24, 25, 49, 70, 78, 79, 120, 123–125, 127, 129, 131, 134, 137, 143, 149, 150, 166, 177, 178, 183
- VEG50-scen** 50% Vegetation Increase Scenario. 143, 144, 146, 149, 151, 153–157, 160, 161, 163–165, 167, 168, 171, 173, 175, 176, 178, 179
- WP** West Perpendicular. 114, 116, 118, 128, 134, 177
- WRF** Weather Research and Forecasting. 58

# Chapter 1

## Introduction

The basic physical processes underlying the small scale atmospheric circulations in urban environment have been widely explored for few decades now. A rising number of investigations concerning the urban environment have been tackled in view in the recent years. Micrometeorology, fluid dynamics, air quality, thermal comfort are some of the studied topic of the urban atmosphere. Local flow circulations, coherent and transient turbulent structures, interaction processes and local thermal budget are the key investigated aspects that drive or have an implication on the majority of the local atmospheric issues. Of particular interest in recent years are the application of these fundamental aspects of the local processes to investigate city breathability and thermal comfort in the urban canopy, with the aim to mitigate air pollution and urban heat island effects and rise the livability of the urban environment. In this contest, it is fundamental to fully understand the processes at the basis or that drive the local atmospheric flow and turbulent phenomena responsible for the city livability enhancement. A large effort has been spent in the recent past on city breathability investigations, focusing on the ventilation processes and their implication on the pollutant removal and thermal comfort of the urban canopy. Key aspects of the exchange processes have been investigated as fundamental phenomena regulating the exchanges of momentum and heat between the canopy and the atmosphere above through the rooftop interface. Of large interest is also the evaluation of the impacts the presence of vegetation causes to different aspects of the urban atmosphere, from the aerodynamics effects to the implication on pollutant deposition and resuspension and thermal comfort. In this context, the present work aims to suggest new simple diagnostic quantities to be representative of fundamental aspects of the flow circulations within the urban canopies, such as the exchange processes developing within real street canyons and at the interface between the canopy and the outer layers. The scope of these new quantities is twofold: to quantify duration and efficacy of mechanical and thermal exchange processes associated respectively with the inertial and thermal circulations, and to identify the key mechanisms of pollutant removal from the canopy. When dealing with real urban environments, complexity can be added by the

## CHAPTER 1. INTRODUCTION

---

different type and location of obstacles within the urban network. The purpose of this work is also to quantify the impact of vegetation within urban canopies on the mean flow and turbulent fields at the basis of the evaluation of the diagnostic quantities. The investigations proposed in this thesis are conducted on data collected from field measurements and numerical simulations performed in a real urban environment by means of two experimental field campaigns core of this work. The campaigns were designed and developed within and thanks to the H2020 European founded project Improving the Smart Control of Air Pollution in Europe (iSCAPE), a multidisciplinary project with the aim to integrate and advance the control of air quality and carbon emissions in European cities in the context of climate change through the development of sustainable and passive air pollution remediation strategies, policy interventions and behavioral change initiatives. Within the project, the field investigation conducted in Bologna were aimed to reveal the local circulations, ventilation, air quality and thermal aspects in a typical European city, and assess the impact of vegetation on these processes through the present and future climatic challenges. To this aim, a great instrumental effort has been arranged to satisfy the research aims, providing good datasets to be used for data analysis or to validate numerical simulation both in the present and in other topic-related works.

The present thesis develops as follow: after this brief introduction, Chapter 2 will give the reader an insight on the literature review that inspires the current analysis, by adding to the most fundamental milestones the recent updates from field, laboratory and numerical investigations. A brief description of the urban boundary layers directly involved or influenced by the urban canopy is followed by more fundamental insights on the exchange processes and their application to city breathability and the most recent technique to reveal the vegetation role in urban environment. Chapter 3 will be dedicated to the description of the experimental field campaigns, revealing the experimental design and focusing on the main or reference sites, i.e. the two street canyons, within the city of Bologna. Chapter 4 will be used to illustrate the basic data processing technique commonly used for high temporal resolution data, like gap filling, despiking and wind speed coordinate rotation, followed by a description of the methodology and the model used for the analysis. Methodology will account for the period identification based on the adopted criterion, and the presentation of the investigation method, including the evaluation of the new diagnostic quantities and the application of the normalization technique to the real environment. Chapter 5, 6 and 7 are dedicated to the results and discussion. Chapter 5 details the results concerning the main observations from the two experimental campaigns, allowing to compare the representative quantities. Particular effort has been given to the identification of the city and local scales circulations, the characterization of the thermal properties of the canopy and the air quality issues given by the traffic related pollution. Chapter 6 focuses on the core of the exchange processes investigation through the characterization of the new diagnostic quantities and their use as key factor to reveal in-canyon pollutant concentration and its re-

---

moval properties. A bulk comparison between the key variables defining the exchange processes retrieved during the two campaigns is used to broadly address the impact of tree crowns from the measured data. Chapter 7 details the modeling results concerning the impact of trees on the exchange processes. After a brief insight on the code modification, the model is verified among the summer experimental campaign data for the four cardinal wind directions. Detail on the tree impact is performed for different scenarios in terms of wind direction and vegetation amount, analyzing topological and morphological parameters dependency of the different simulated scenarios. Finally, Chapter 8 provides the final conclusive remarks to the thesis.



## Chapter 2

# The Urban Boundary Layer: an Overview

The majority of the world population lives in urban areas, a proportion that is expected to increase to 68% by the 2050 (UN DESA, 2018). Long term projections indicate that urbanization, along with the overall growth of the world's population, could add further 2.5 billion people to urban areas by 2050, with percentages reaching 90% in Asia and Africa (UN DESA, 2018). Increasing urbanization can deeply affect regional and local scale meteorology and air quality, modifying the mass, momentum and energy exchange processes at the interfaces (Li et al., 2019). It is therefore fundamental to characterize the urban atmosphere to fully understand the processes developing within it. A brief literature review on the urban atmosphere and its characteristic processes is presented in the following sections. First, some milestones as well as recent developments in the field of urban environment involving exchange processes, pollutant removal and evaluation of the vegetation role are reported. The key characteristics of the atmospheric boundary layer in urban environment will guide the reader to the identification of the relevant boundary layer depths for the current investigation, and their properties. Then the focus will shift toward an insight on the key aspects of the exchange processes as fundamental phenomena regulating the exchanges of momentum and heat between the canopy and the atmosphere above through the rooftop interface, and their implication on pollutant removal from the canopy. Finally, a brief review will highlight the major impacts the presence of vegetation causes to different aspects of the urban atmosphere, from the aerodynamics effects to the implication on pollutant deposition and resuspension and thermal comfort.

### 2.1 The Urban Boundary Layer

The Urban Boundary Layer (UBL) is the portion of the Planetary Boundary Layer (PBL) whose characteristics are affected by the presence of an urban area at its lower boundary (Oke, 1976). It

## CHAPTER 2. THE URBAN BOUNDARY LAYER: AN OVERVIEW

is characterized by a heterogeneous environment where different spatial scales can be defined to identify different homogeneous morphology (Bitter and Hanna, 2003). The street scale extends for a horizontal scale in the range 10-100 m describing small and single environments, as a single building or a street. The neighborhood scale ranges from 100 to 1000 m and it is used to describe a collection of similar obstacles (buildings or vegetation) in the same area. The city scale (10-20 km) embeds the whole urban environment, to be considered as a complex structure in opposition to the surrounding rural areas. The vertical characterization of the UBL is of fundamental importance to characterize the atmospheric dynamics developing within it. Following the classification proposed by Roth (2000), the UBL extends from the ground to the top of the boundary layer, it is vertically structured in different layers and it involves different scale phenomena, ranging from the local scale to the mesoscale. Fig. 2.1 sketches the vertical

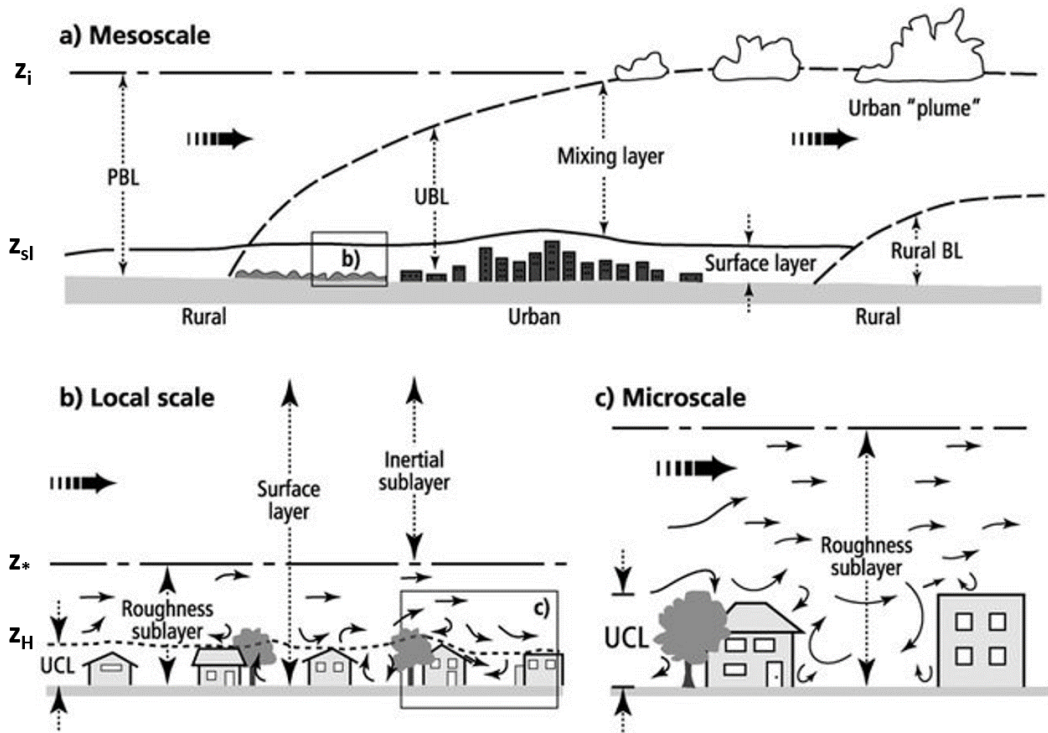


**Figure 2.1:** Schematic structure of the UBL (Source: Piringer et al. (2002)).

structure of the UBL. From the ground a Surface Layer (SL) extends vertically up to the height  $z_{sl}$  (Fig. 2.1a) where the flow has readjusted from the perturbation produced by the embedded urban environment (Roth, 2000). Mean flow and turbulent structures are strongly influenced by the urban environment. As a consequence, the SL identifies the local UBL affected by the presence of the urban environment. From  $z_{sl}$  to the UBL top  $z_i$  (Fig. 2.1a), the flow can be considered unperturbed and it follows the unperturbed (rural) boundary layer dynamics, which could be a mixed layer or a nocturnal residual layer dynamics depending on the day time.

The typical of  $z_{sl}$  is approximately  $0.1 z_i$ . The SL is characterized by spacial heterogeneity and strong vertical discontinuities which subdivide the SL in three sublayers, namely Urban Canopy Layer (UCL), Roughness SubLayer (RSL) and Inertial SubLayer (ISL) from the ground to  $z_{sl}$  (Roth, 2000). Extending from the ground to the obstacle (buildings and vegetation) top  $z_H$  (Fig. 2.1b), the UCL (Sect. 2.2) is an atmospheric portion directly affected by the microscale site characteristics (Roth, 2000). Despite being a sublayer, the UCL is traditionally considered as a layer since it is the atmospheric depth where the flow has a direct interaction with the obstacles of the urban environment. The UCL develops within the RSL (Sect. 2.1.1), a layer extending

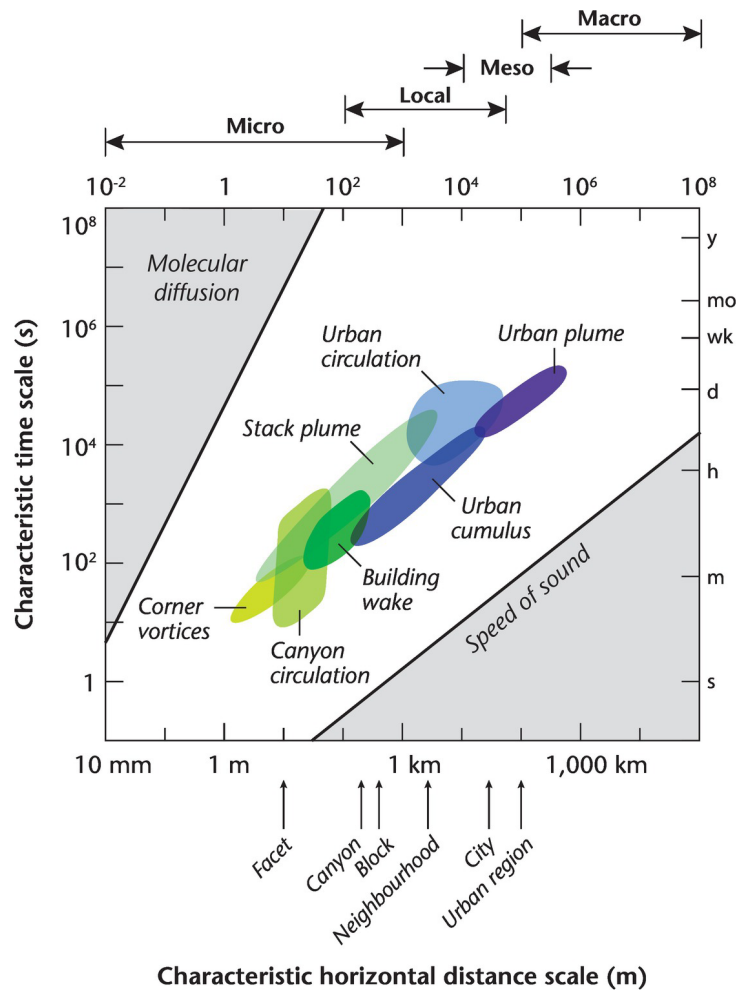


**Figure 2.2:** Time and space scales of the characteristic atmospheric processes within the UBL (Source: Oke et al. (2017))

from the ground to a  $z_*$  (Fig. 2.1b) ranging between 2 and 5 times the mean building height (Raupach et al., 1991b), and affected by mechanical and thermal processes associated with the roughness length scale. Above the RSL, the atmosphere restores its unperturbed behavior. There the ISL (Sect. 2.1.2) develops, extending from  $z_*$  to  $z_{sl}$ . In the following sections, a brief

focus on the SL will be given to better detail the urban environment key characteristics for the current investigations.

Depending on the spatial and temporal scales characterizing their evolution, a large and various quantities of atmospheric phenomena can develop in the UBL. Fig. 2.2 summarizes the most important atmospheric processes developing in the UBL as function of time and space scales. The genesis and evolution of these processes must be searched in the interaction between the atmospheric flow with the urban obstacles, the restoring forces that drive the perturbed flows to the unperturbed conditions and the further complexity introduced by an environment that modifies the surface energy budget. The flow dynamics, and the consequent development of turbulent structures, change with the atmospheric height, and it will be better assess in the specific layer section. Also the modified surface energy budget changes the flow characteristics through the Turbulent Kinematic Momentum Flux (TKMF) and the Turbulent Kinematic Sensible Heat Flux (TKSHF) from the heterogeneous surface (Arnfield, 2003). The TKSHFs are enhanced by the storage-emission capacity of the different obstacles in the urban environment (Grimmond and Oke, 2002) which are mostly made of non reflective materials, like concrete and tarmac, with large thermal inertia. The latent heat fluxes are lowered due to the small fraction of vegetation (Barlow, 2014), except for parks and largely vegetated neighborhoods, which however have an impact only at small scales. The human activities also provide a source of heat for the urban energy budget. Finally, the radiation budget is perturbed by the shadowing effect of buildings and vegetative elements, resulting in the formation of local radiative fluxes and temperature gradients which can drive local flow circulations. In the following subsections, a brief focus on the sublayers of the UBL is presented pointing out the main features of the RSL and the ISL in terms of vertical extension and characteristic flows dynamics. A stand alone section will be dedicated to the UCL which is of fundamental importance for the current study, despite being a sublayer of the RSL.

### 2.1.1 The Roughness Sublayer

The atmospheric layer influenced by the mechanical and thermal length scales associated with the roughness is the RSL (Roth, 2000). It is a transition layer between the ground and the ISL (Ground- $z_*$ , Fig. 2.1b), characterized by three dimensional turbulent flow fields (Roth and Oke, 1995), driven by the momentum and heat transport source and sink and the wake diffusion (Schmid et al., 1991), as schematically represented by the chaotic behavior of the wind vectors in Fig. 2.1c. The vertical depth of the RSL can vary according to the different local geometrical and atmospheric conditions, since  $z_*$  is not a fixed depth but is defined as the height where the horizontal homogeneity of the flow is achieved (Kastner-Klein and Rotach, 2004), i.e. where the ISL begins. Geometrically,  $z_*$  is found to depend on the roughness length of the obstacles and their horizontal spacing (Roth, 2000). Atmospheric stability is also found to modify the

RSL depth, with an increase of  $z_*$  with an increasing unstable stratification (Garratt, 1980). Raupach et al. (1991a) found the RSL depth oscillates between 2 and 5 times the mean building height, but it can also extend for the whole SL superimposing the ISL in presence of particular morphological conditions such as a tall building (Rotach, 1999) or sparse canopies (Cheng et al., 2007). The height  $z_*$  is usually estimated from the turbulent fluxes or the wind speed profiles. In the first case,  $z_*$  is identified as the base of the ISL, i.e. where the fluxes become constant with the height (Grimmond et al., 2004). In the second case,  $z_*$  is the lowest height where wind speed profiles measured simultaneously at different domain locations are equal above the canopy (Kastner-Klein and Rotach, 2004). To enhance the degree of complexity, a Shear Layer (ShL) can overlap the RSL at the building rooftops, modifying the interface turbulence kinetic energy and the outward inward turbulent transport. Due to the roughness dependency of the atmospheric flows in the layer, the wind velocity profile does not satisfy neither the logarithmic wall law in the RSL nor the exponential law (Cionco, 1965) typical of the UCL contained within it, at least not above the canopy displacement height. Kastner-Klein and Rotach (2004) suggested an empirical wind speed profile valid for the portion of the RSL bounded by the canopy and the ISL as

$$U_{RSL}(z) = \frac{u_*}{0.6k} \left[ 1 - 0.6 \ln 0.12 - \exp 0.6 - 0.072 \frac{z-d}{z_0} \right],$$

where  $u_*$  ( $\text{ms}^{-1}$ ) is the friction velocity,  $k$  is the Von Karman constant equal to 0.4,  $d$  (m) is the displacement height and  $z_0$  (m) the roughness length. The RSL profile was obtained from laboratory investigations, but found to apply to the real environment, despite it is not so commonly used.

### 2.1.2 The Inertial Sublayer

The atmospheric depth between the RSL and the remnant of the UBL (mixed or residual layer) is called the ISL and it is characterized by the atmospheric flow that has restored the perturbation given by the roughness elements of the canopy and turbulent eddies influenced by the urban reduced atmospheric volume (Barlow, 2014). It is also defined as the region where turbulent fluxes are constant with the height, which is also a main feature that enables the identification of this sublayer (Grimmond et al., 2004). The vertical depth of the ISL is determined by the development of the whole surface layer which responds to the larger scale dynamics (Roth, 2000). As already depicted in Sect. 2.1.1, the existence and depth of the ISL is also tied to the extension of the RSL, and in turn to the geometrical roughness and stability conditions of the RSL itself. When the RSL does not involve the whole SL, the mean flow in the ISL has restored to the unperturbed boundary layer values at least in the near-neutral stability condition. In this condition, the wind speed profile follows the wall law (Barlow, 2014) as in a rural boundary

layer over flat terrain but displaced to account for the presence of the canopy:

$$U_{ISL}(z) = \frac{u_*}{k} \ln \frac{z-d}{z_0},$$

where  $u_*$  ( $\text{ms}^{-1}$ ) is the friction velocity,  $k$  is the Von Karman constant equal to 0.4,  $d$  (m) is the displacement height and  $z_0$  (m) the roughness length. Turbulence intensity in near-neutral conditions is instead larger in the ISL than at similar layers in the rural boundary layer (Barlow, 2014), caused by the presence of the canopy.

## 2.2 The Urban Canopy Layer

The UCL is the atmospheric depth extending from the ground to the building and tree heights. In real environments, its depth is not constant since its upper limit follows the shape of the city rooftops. A representative constant height to identify the canopy layer is given by the mean rooftop height  $H$ , defined as the level beneath which the local scale dynamics and turbulence are largely perturbed by the canopy morphology, obstacles porosity and structural material composition and human activities (Oke, 1976). The drag force generated by large and irregular obstacles, the heat and moisture injections from human activities and the heat storage capacity of non reflective materials, like concrete or tarmac, modify the wind circulation (Bitter and Hanna, 2003) and the thermal budget (Grimmond and Oke, 2002) of this layer. The ensemble of obstacles displaced in an urban environment constitutes the morphology of the city, which contributes to identify the roughness properties of the canopy. Morphology is mainly quantified throughout two coefficients evaluating the normalized cross section of the obstacles the incoming wind impacts against. The planar area coefficient  $\lambda_p = A_p/A_t$  is the plan area of the obstacles normalized on the total domain area. The frontal area coefficient  $\lambda_f = A_f/A_t$  is the frontal area of the obstacles normalized on the total domain area. The most high-impact morphology on the atmospheric flows is the street canyon. The street canyon constrains the atmospheric flows within an air volume defined by the canyon length, height and width. In fact, the most important geometrical parameter that influences the flow regime within a street canyon is the canyon aspect ratio  $AR = H/W$ , i.e. the ratio between the mean obstacle height  $H$  and the mean canyon width  $W$ . Despite the complexity associated with the morphology and the necessity to approximate its representation, the mean wind speed has a simple and verified equation given by Cionco (1965) as

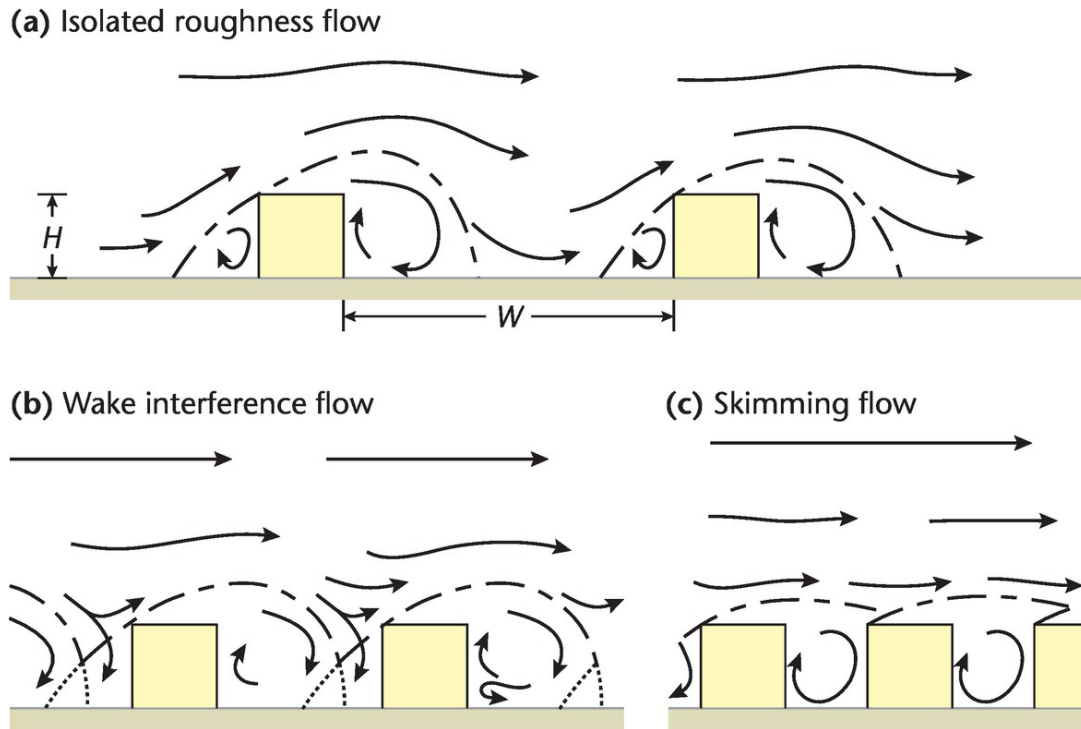
$$\bar{U}_{UCL}(z) = \bar{U}_H \exp \left[ a \left( \frac{z}{H} - 1 \right) \right],$$

where  $U_H$  ( $\text{ms}^{-1}$ ) is the mean wind speed at the mean rooftop height  $H$  and  $a$  is the attenuation coefficient. As the mean flow behavior is described by the Cionco (1965) equation, the flow circulation regime is driven by the momentum transport from the UBL eddies. Moreover, the

horizontal temperature differences within the canopy can modify the circulation forcing the local flow regimes.

### 2.2.1 Inertial and Thermal Circulations

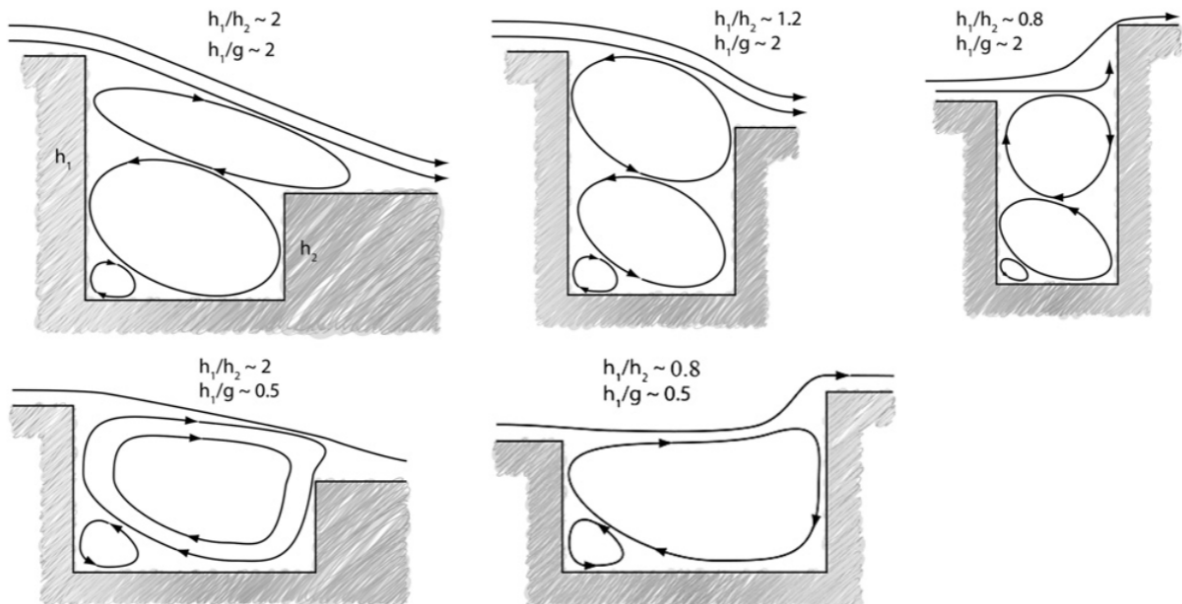
During periods of weak synoptic forcing, i.e. when the geostrophic winds are smaller than  $5 \text{ ms}^{-1}$ , the local scale turbulence and gradients become the main driver of the atmospheric circulation and recirculation flows inside the canopy (Britter and Hanna, 2003). Depending on the intensity of the city scale flows, background flows from now on, characteristics of the UBL, the circulation within the canopy can be inertially driven by the mean flow and the TKMF from the background flow or thermally driven by the horizontal temperature gradient within opposite facades of the in-canyon buildings. The Inertial Circulation (IC) is driven by the mean flow and/or the TKMF entrainment in the canopy from the background flow, as shown in the sketch of Fig. 2.3. Momentum is transferred from the mean flow over-passing the buildings to



**Figure 2.3:** Idealized 2D sketches of the in-canyon flow regimes from Oke (1987) classification.  $H$  and  $W$  are the building height and width. (Source: Oke et al. (2017))

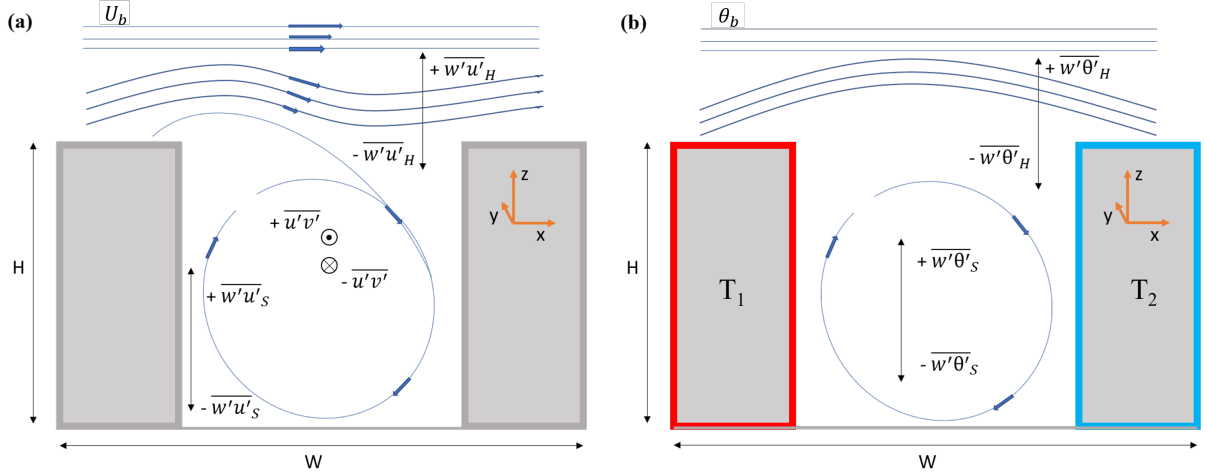
the in-canyon flow and generate one or more structures whose shapes and numbers depend on the canyon aspect ratio  $H/W$  (Britter and Hanna, 2003). Depending on the in-canyon structure, and therefore on the aspect ratio of the canopy, the flow can follow a different circulation regime as classified by Oke (1987). Sketches of the flow regimes in 2D idealized canopies are shown in

Fig. 2.3. As mentioned, the identification of the flow regime is aspect ratio dependent. When the buildings are well apart ( $0.05 < H/W < 0.4$ ) their impact on the flow field is equal to that imposed by an isolated building. The flow creates two recirculation zones at the windward and leeward walls of each building (Fig. 2.3a). This flow regime is identified as *isolated roughness flow* (Oke, 1988). A more complete definition of the isolated roughness regime was also given by Hosker (1987) and adopted by Fernando et al. (2010) and Zajic et al. (2011) among others, identifying this regime anytime the sum of the horizontal length of the flow recirculation volumes in front and rear of the impacted building is smaller than the mean width  $W$  of the canopy. When  $W$  becomes smaller than the sum of the horizontal length of the flow recirculation volumes in front and rear of the impacted building, the wake of the first building interferes with that of the second (Zajic et al., 2011), and the flow regimes take the name of *wake interference flow* (Fig. 2.3b). This regime is characterized by secondary flows in the canopy space where the downward flow of the eddy within the cavity is reinforced by the downward deflection at the windward side of the canopy (Oke, 1988). Commonly, the wake interference flow regime involves a small range of aspect ratios ( $0.4 < H/W < 0.7$ ), upper-bounded by an UBL-to-UCL mean flow decoupled regime. In fact, at smaller building separation ( $H/W > 0.7$ ), the flow skims over the canopy and generates stable vortices within it, which number depends on the aspect ratio (Fernando et al., 2010). This flow regime is named *skimming flow* (Fig. 2.3c) and it is typical of dense canopies, where the bulk of the flow does not penetrate within them (Oke, 1988). The idealized



**Figure 2.4:** Idealized 2D sketches of the in-canyon flow regimes in irregular street canyons originally from Xiaomin et al. (2006).  $h_1$  and  $h_2$  are the leeward and windward building height respectively, and  $g$  is the canyon width. (Source: Zajic et al. (2011))

2D canopy inertial flow investigations have been extended to irregular 2D canopies where the opposite building heights are unequal and a different number and shape of vortices develop within the canyon according to different geometrical configurations (Chan et al. 2003; Xiaomin et al. 2006), resulting in a more realistic evaluation of the in-canyon circulations. An idealized summary of these investigations is reported in Fig. 2.4. In condition of narrow street canyons and skimming flow regime, with the taller building height at least twice as large as the canyon width, two main vortices develop in the canyon, trapping the lower circulation at the ground. For street canyons in the wake interference regime ( $h_1/g \approx 0.5$ ), a single main vortex is formed, connecting the free atmosphere to the canopy. Single small recirculation zones appears at the leeward wall independently on the geometrical configuration. Since the reference street canyons, whose flows and turbulence are investigated in this thesis, develop in the skimming flow regime, a larger effort will be spent for its characterization. As sketched in Fig. 2.5a, the background flow passing above the city is characterized by a wind speed  $U_b$ . The vertical TKMFes are the key



**Figure 2.5:** Sketches of the (a) IC and (b) TC inside an idealized SC.  $H$  and  $W$  are the mean building height and width of the canyon,  $T_1$  and  $T_2$  the building facade temperatures,  $U_b$  and  $\theta_b$  the background wind speed and air potential temperature,  $\overline{w'u'}$  and  $\overline{w'\theta'}$  the TKMF and the TKSHF evaluated inside the canyon (subscript S) and at the rooftop level (subscript H).

parameters regulating the local turbulent exchanges between the mean flow and the in-canyon structures (Klein and Galvez, 2015). The vertical TKMF at the rooftop ( $\overline{w'u'}|_H$ ) drives fresh air in the canyon through the ShL while the inside canyon one ( $\overline{w'u'}|_S$ ) creates mixing and swirling motions. Theoretically, horizontal TKMFes have also to be considered as a mean for vector or scalar transport within the canyon (Klein and Galvez, 2015), but they are not addressed in this introduction since the focus of this study is only directed to the vertical removal capacity. In the skimming flow regime, the ShL at the building tops can cause vortex shedding and flow oscillations, which results in a periodical impinging on the flow at the downward building and

in a turbulent enhancement (Fernando et al., 2010).

When the background wind speed is small, the thermal effects associated with the horizontal temperature difference between opposite building facades become important. This horizontal temperature difference is the driver of the Thermal Circulation (TC). Building facades are warmer than the surrounding air and, depending on the heating and background wind intensities, TC can dominate the IC (Kim and Baik 1999, 2001; Fernando et al. 2010; Dallman et al. 2014). In this case, the differential heating of the opposite building facades ( $T_1 \neq T_2$ ) induces a swirly circulation within the canopy (Dallman et al., 2014). The differential heating also affects the turbulent heat transport, mixing and thermal stratification within and above the canopy (Nazarian et al., 2017), leading to a modification of the exchanges efficacy on pollutant removal (Nazarian et al., 2018). An additional input is provided by the ground heat release which strengthens the upwind branch of the vortex (Li et al., 2012) modifying the thermal and flow fields (Nazarian et al., 2017). Inertial and thermal aspects contribute to the development of the actual circulation in a real street canyon. It is therefore fundamental to consider both these effects not to misjudge flow and turbulence behaviours and effectiveness for exchanges (Cheng et al., 2009b).

Following Dallman et al. (2014), the identification of IC among TC can be done through a simple buoyancy parameter valid in the skimming flow regime. Within this regime the horizontal and vertical inertially driven wind components within the canopy, named  $u_m$  and  $w_m$  respectively, are related through the continuity equation as

$$\frac{w_m}{H} \approx \frac{u_m}{W} \sim \frac{u_b}{W},$$

where  $u_b$  ( $\text{ms}^{-1}$ ) is the horizontal component of the background wind supposed to be equal to  $u_m$  because the IC is directly driven by the background flow. Assuming the TC to be driven by the horizontal temperature difference between opposite building facades, when  $u_b$  is weak the TC velocity  $\mathbf{u}_t = (u_t, w_t)$  can be estimated from the vorticity ( $\boldsymbol{\omega}$ ) evolution

$$\frac{D\boldsymbol{\omega}}{Dt} = \boldsymbol{\omega} \cdot \nabla \mathbf{u}_t + \nabla \times \beta \hat{k} + \nu \nabla^2 \boldsymbol{\omega}, \quad (2.1)$$

where  $\beta = g\alpha T$  is the buoyancy acting in the vertical direction ( $\hat{k}$ ) with  $\alpha = 1/\bar{T}$  the thermal expansion coefficient with  $\bar{T}$  (K) the average air temperature within the canyon,  $T$  (K) the air temperature,  $g$  ( $\text{ms}^{-2}$ ) the gravitational acceleration,  $\mathbf{u}_t$  ( $\text{ms}^{-1}$ ) the wind velocity and  $\nu$  ( $\text{m}^2\text{s}^{-1}$ ) the kinematic viscosity. Considering that  $x$  (cross-canyon) and  $z$  (vertical) are the main directions within the canopy, the vortex stretching ( $\boldsymbol{\omega} \cdot \nabla \mathbf{u}_t$ ) and viscous diffusion  $\nu \nabla^2 \boldsymbol{\omega}$  are negligible. The only non negligible vorticity component is the along canyon one  $\omega_y$ . Under steady state condition, and applying the previously discussed simplifications, Eq. (2.1)

becomes

$$\mathbf{u}_t \cdot \nabla \omega_y \sim -g\alpha \frac{\partial T}{\partial x}. \quad (2.2)$$

Using once again the dimensional analysis on the vorticity component on the left hand side of Eq. (2.2) the following approximation is retrieved

$$\omega_y = \frac{\partial u}{\partial z} - \frac{\partial w}{\partial x} \sim \left[ \frac{u_t}{H} + \frac{w_t}{W} \right] \sim \left[ \frac{u_t}{H} + \frac{u_t}{H(H/W)^2} \right] \sim \left( \frac{u_t}{H} \right) \left[ 1 + \left( \frac{H}{W} \right)^2 \right], \quad (2.3)$$

where  $u_t/W \approx w_t/H$  as for the IC case. Substituting Eq. (2.3) into (2.2), the vorticity equation becomes

$$\frac{u_t}{W} \frac{u_t}{H} \left[ 1 + \left( \frac{H}{W} \right)^2 \right] \sim \frac{g\alpha\Delta T}{W}, \quad (2.4)$$

where  $\Delta T = T_1 - T_2$  is the horizontal temperature difference between opposite building facades. From Eq. (2.4), the velocity scale for the TC becomes

$$u_t \sim \left( \frac{g\alpha\Delta TH}{\left[ 1 + \left( \frac{H}{W} \right)^2 \right]} \right)^{1/2}. \quad (2.5)$$

When both IC and TC divers are present, the first dominates the second if  $u_b \gg u_t$ . To evaluate this condition, the buoyancy parameter  $B$  is defined from Eq. (2.5) as

$$B = \left( \frac{g\alpha\Delta TH}{u_b^2 \left[ 1 + \left( \frac{H}{W} \right)^2 \right]} \right)^{1/2} \gg B_c, \quad (2.6)$$

where  $B_c$  is the critical value of the buoyancy parameter discerning the inertial ( $B < B_c$ ) from the thermal ( $B > B_c$ ) circulations. From this parameter the identification of the canopy circulation is performed to characterize the flow and assess the dominant processes correlated to them. In the next section, the characteristics of the exchange processes developing in conditions of IC and TC are introduced.

## 2.3 Exchange Processes and City Breathability

The term *exchange processis* used in boundary-layer meteorology to identify all the atmospheric phenomena involving the outward and inward exchange of both vector and scalar quantities between the UCL and the UBL above through the rooftop interface. The understanding and good representation of these processes is fundamental to correctly predict flow and turbulent fields within the RSL. Milestones in the understanding of the exchange processes have been

given by [Barlow and Belcher \(2002\)](#), [Bentham and Britter \(2003\)](#) and [Harman et al. \(2004\)](#)) at the beginning of the 21<sup>st</sup> century, revealing the intricacy of momentum and heat exchanges through the canopy interface. In the same period, several studies have focused on the nature of the exchange processes, by means of field, laboratory and numerical investigations. Key findings concluded that exchange processes are driven and scale with the vertical TKMF at the canopy interface ([Louka et al. 1998](#); [Barlow et al. 2004](#); [Solazzo and Britter 2007](#)), especially in presence of a ShL dynamics. The efficacy of the exchange processes increases with the intensity of the background wind in the ISL ([Barlow and Belcher 2002](#); [Harman et al. 2004](#)), the turbulent momentum ([Kim and Baik, 2003](#)) and turbulent kinetic heat ([Salizzoni et al., 2011](#)) transports from the ShL to the street canyon. The efficacy also varies according to local morphology characteristics such as the street canyon aspect ratio ([Barlow and Belcher, 2002](#)) and the roof geometry ([Kastner-Klein et al., 2004](#)).

In more recent years, the exchange processes focus has shifted from the fundamental nature investigation to their implication on more practical problems such as air quality and pollutant dispersion or removal from the urban canopy. The application of the exchange processes to the pollutant removal from an urban canopy takes the terminology of City Breathability (CB), as adopted by several authors ([Buccolieri et al. 2010](#); [Panagiotou et al. 2013](#); [Chen et al. 2017](#)), which incorporates any scalar (e.g. heat, moisture, pollutant concentration) ejection from ground level, transport throughout a canopy interface or turnover time scales. The CB concept has been applied to different spatial scales of the urban environment, ranging from street canyon ([Cheng et al. 2009a](#); [Liu and Wong 2014](#); [Di Bernardino et al. 2018](#)) to neighbourhood ([Soulhac and Salizzoni 2010](#); [Buccolieri et al. 2015](#)) and city ([Hang et al. 2012](#)) scales, corroborated by laboratory and numerical investigations. Despite several field experimental campaigns have been realized in the last two decades ([Louka et al. 2000](#); [Rotach et al. 2005](#); [Eliasson et al. 2006](#); [Kanda and Moriwaki 2006](#); [Nelson et al. 2011](#); [Zajic et al. 2011](#); [Dallman et al. 2013](#)), CB has been poorly investigated in real environments due to the complex interactions between different atmospheric phenomena and the irregular morphology of the real cities.

Following [Lo and Ngan \(2017\)](#), CB is assessed by two categories of diagnostic parameters. The first category is based on the evaluation of turbulent mass exchange between the canopy and the overlying atmosphere, typically quantified by exchange velocities or exchange rates. The second category is based on the evaluation of diagnostic time scales associated with pollutant removal or in-canyon circulations. Diagnostic time scales enable the characterization of CB for different background conditions (e.g. change in mean wind direction), aspect ratios, canyon orientation and exposure to solar radiation, domain size and morphology, pollutant emissions and turbulence regimes. The investigations conducted in the current study focus on the second category, but it is worth mentioning at least two examples of exchange velocity and rate to better qualify the research effort in the field of the CB. The first is the exchange velocity that

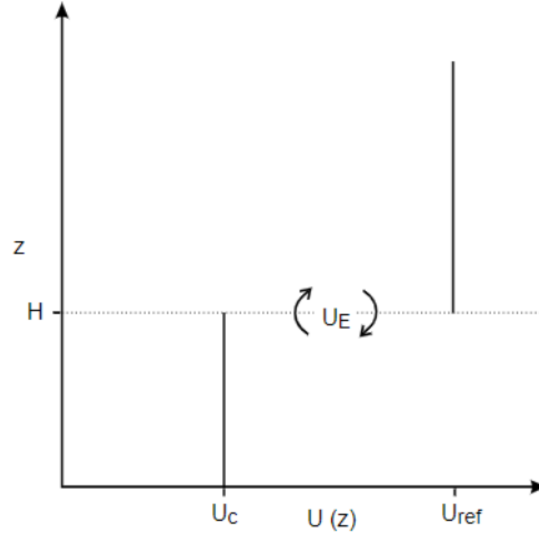


**Figure 2.6:** Simplified velocity profiles within and above the urban canopy.  $H$  is the mean building height,  $U_C$  the canopy layer velocity,  $U_{ref}$  the velocity above the canopy layer and  $U_E$  the exchange velocity between at the rooftop interface. (Source: [Bentham and Britter \(2003\)](#))

was defined by [Bentham and Britter \(2003\)](#). Through their investigation, [Bentham and Britter \(2003\)](#) define the exchange velocity as the average rate at which the pollutant is exchanged from the top of the canopy. The definition is very bulk since it involves two constant velocities characterizing the canopy  $U_C$  ( $\text{ms}^{-1}$ ) air volume and the RSL air volume above it  $U_{ref}$  ( $\text{ms}^{-1}$ ) respectively, displaying a very simple but efficient model reported in Fig. 2.6. On average, the drag force exerted by the surface is balanced by the TKMF across the rooftop interface

$$\tau_w A_p = \rho A_p U_E (U_{ref} - U_C), \quad (2.7)$$

where  $\tau_w$  ( $\text{kgm}^{-1}\text{s}^{-1}$ ) is the surface shear stress acting over the volume planar cross section  $A_p$  ( $\text{m}^2$ ),  $\rho$  ( $\text{kgm}^{-3}$ ) is the air density and  $U_E$  ( $\text{ms}^{-1}$ ) is the exchange velocity. Substituting  $\tau_w = \rho u_*^2$  to the shear stress term, the exchange velocity exploited from Eq. (2.7) becomes

$$\frac{U_E}{u_*} = \left( \frac{U_{ref} - U_C}{u_*} \right)^{-1}. \quad (2.8)$$

The potential of this simple formulation is in the possibility to shift from momentum exchange velocity (Eq. 2.8) to heat or pollutant exchanges simply using heat ( $Q_w$ ) or pollutant ( $P_w$ ) stress tensor approximations in place of the shear stress  $\tau_w$  and constant temperatures ( $T_{ref}$  and  $T_C$ ) or pollutant concentrations ( $C_{ref}$  and  $C_C$ ) for the canopy and above canopy volumes instead of the velocities  $U_{ref}$  and  $U_C$ . An example of application to CB problems of the pollutant exchange velocity has been successfully given by [Di Sabatino et al. \(2007\)](#).

A comprehensive definition for the exchange rate is given by (Liu et al., 2005). Exchange rate was classified in air and pollutant exchange rates to respectively account for the vertical velocity and pollutant concentration transport fluctuations through the rooftop level interface of the UCL. Again, the formulations are simple but they enclose the essence of the canopy to free atmosphere interaction. The air exchange rate ( $ACH$ ) is defined as the integral over planar cross section of the canopy volume  $A_p$  ( $\text{m}^2$ ) of the vertical wind velocity fluctuations at the rooftop interface  $w'(t) |_{interface}$  ( $\text{ms}^{-1}$ ):

$$ACH(t) = \int_{A_p} w'(t) |_{interface} dA_p.$$

The sign of the air exchange rate is directly given by the vertical velocity fluctuations, so that a positive  $ACH$  value describes air removal from the canopy while a negative one identifies an entrainment.

Similarly, the pollutant exchange rate  $PCH$  describes the pollutant concentration transport  $w'(t) |_{interface} \bar{C}(t) |_{interface}$  ( $\mu\text{gm}^{-3} \text{ms}^{-1}$ ) through the rooftop interface

$$PCH(t) = \int_{A_p} w'(t) |_{interface} \bar{C}(t) |_{interface} dA_p.$$

The sign of the pollutant exchange rate follows the behavior of the air exchange rate with positive  $PCH$  values describing pollutant removal from the canopy while negative ones identifying an entrainment. Simple as they are, they can easily be used to describe a time dependent refreshment or stagnation of the air in the UCL.

The second category of Lo and Ngan (2017) describes the diagnostic parameters by which the exchange processes can be characterized. Particularly used from this ensemble, the diagnostic time scales enable the characterization of CB for different background conditions (e.g. change in mean wind direction), aspect ratios, canyon orientation and exposure to solar radiation, domain size and morphology, pollutant emissions and turbulence regimes. In the recent past, different time scales have been derived using Computational Fluid Dynamics (CFD) models and wind tunnel experiments. Below, a brief summary of the most used and work-inspiring time scales is presented. A retention time  $\bar{\tau}_a |_V$  is defined by Liu et al. (2005) as the average pollutant concentration  $\bar{C} |_V$  ( $\mu\text{gm}^{-3}$ ) within the canyon mean volume  $V = W \cdot H \cdot L$  ( $\text{m}^3$ ) and the pollutant emission rate  $Q_e |_V$  ( $\mu\text{gm}^{-3}\text{s}^{-1}$ ) of the source

$$\bar{\tau}_a |_V = \frac{\bar{C} |_V}{Q_e |_V}.$$

The pollutant retention time expresses the time a certain pollutant remains in the canopy before from its emission. The retention time is found to be dependent on the aspect ratio  $H/W$ , with a time scale increase as the aspect ratio increases. As the aspect ratio increases, the pollutant transport from the ground sources to the canopy top becomes more and more

inefficient, since multiple independent vortices can form within the canopy. In this last scenario, the retention time scale is enhanced by this transport inefficiency. Similar to the retention time is the mean age of the air defined by [Hang et al. \(2009\)](#). The definition follows exactly the retention time of [Liu et al. \(2005\)](#), expressing the ratio between the pollutant concentration and the emission rate of its source. Again the lower the local mean age of air is, the more efficiently the local exchange processes remove the pollutant concentrations from the canopy. Being of simple practical use especially in laboratory and numerical investigations, the mean age of air (or retention time, since they are equally defined) has been used for several analysis to characterize different aspects of the removal processes in different conditions. In fact, the city shape, the configuration of streets and the approaching wind conditions are all aspects that influence the age of air and the air exchange efficiency of the urban canopies. [Hang et al. \(2012\)](#) first confirms the direct proportionality between the time scale and the single street canyon aspect ratio found by [Liu et al. \(2005\)](#), extending the analysis to the neighborhood and city scales with contrasting results. At the city scale, the dependency of the age of the air on the street canyon aspect ratio is again found to be directly proportional, while at the neighborhood scale the proportionality was inverse. This inverse behavior of the time scale at the neighborhood scale is confirmed by [Hang et al. \(2013\)](#) who suggested the dependency on the planar area fraction coefficient (not retrieved at the city scale) to be the cause. [Hang et al. \(2013\)](#) also investigates the variation of the age of the air with the background wind direction, founding an improvement of the CB with an increasing background wind direction in the range  $0^\circ$ - $45^\circ$  to the canyon orientation.

The average residence time  $\bar{\tau}_r$  was introduced by [Bady et al. \(2008\)](#) and used by [Kato and Huang \(2009\)](#) to assess the ventilation performance of the street canyon exchange processes by representing the time of permanence of pollutants in the canopy volume. It is defined as the ratio between the canopy volume  $V$  ( $\text{m}^3$ ) and the product between the purging flow rate  $P_r$  ( $\text{m}^3\text{s}^{-1}$ ) and the adimensional visitation frequency  $f_V$

$$\bar{\tau}_r = \frac{V}{P_r f_V}$$

The purging flow rate represents the effective airflow rate required to remove or purge the air pollutants from the volume and it is computed as  $P_r = Q_e / (1000 \bar{C}_q \rho)$ , where  $Q_e$  ( $\text{gs}^{-1}$ ) is the pollutant source rate,  $\bar{C}_q$  ( $\text{kgkg}^{-1}$ ) is the volume averaged canopy concentration and  $\rho$  ( $\text{kgm}^{-3}$ ) is the air density. The visitation frequency describes the history of a pollutant particle in the canopy volume by establishing the number of times the particle enters and exits the canopy volume. It is defined as  $f_V = 1 + \Delta Q_e / Q_e$ , where  $\Delta Q_e$  ( $\text{kgs}^{-1}$ ) is the inflow flux of pollutants into the canopy volume. Therefore, the average residence time describes the time a pollutant particle takes between its entrance in and exit from the canopy volume, and therefore it is an indication of the pollutant dilution capability of the volume itself operated by the atmospheric

exchange processes. The average residence time was found by both [Bady et al. \(2008\)](#) and [Kato and Huang \(2009\)](#) to increase as the street canyon aspect ratio increases, as it was for the retention time and age of the air.

[Salizzoni et al. \(2009\)](#) define an exchange time scale  $\tau_e$  to account for the pollutant mass transport through the rooftop interface in dependency on the mean building height  $H$  (m) of the canopy. It is defined as the ratio between the square value of the mean building height, the averaged pollutant concentration within the canopy  $\bar{C}$  ( $\mu\text{gm}^{-3}$ ) and the inflow mass rate from the canopy rooftop  $\dot{M}_q$  ( $\mu\text{gm}^{-1}\text{s}^{-1}$ )

$$\tau_e = \frac{H^2 \bar{C}}{\dot{M}_q}.$$

The exchange time scale describes the wash-out of pollutants from the canopy. From [Salizzoni et al. \(2009\)](#) investigations, it is found to increase as the aspect ratio of the single street canyon increases, confirming the previously introduced time scales.

More recently, time scales related to the exchange processes have been addressed by Lagrangian models, directly describing the trajectories of single fluid particles from the source to the sink or removal. An example of time scales derived from Lagrangian model investigations is presented by [Lo and Ngan \(2017\)](#). Two Lagrangian time scales, namely the residence  $\tau_r^L$  and exposure  $\tau_e^L$  times, have been evaluated to establish the time required for a pollutant particle to exit the canopy and the time spent by a pollutant particle in a region of interest respectively. Within the canopy cavity volume  $V$  ( $\text{m}^3$ ), the residence time is defined as

$$\frac{D\tau_r^L}{Dt} \Big|_V = 1,$$

with  $\tau_r^L(0) = 0$  at the open frontier  $\partial V$  of the volume, i.e. the rooftop interface in the case of a single street canyon. The exposure time scale is defined in a volume of interest  $V_e \in V$  ( $\text{m}^3$ ) as

$$\frac{D\tau_e^L}{Dt} \Big|_{V_e} = \begin{cases} 1 & \text{if } \mathbf{x} \notin V_e \\ 0 & \text{if } \mathbf{x} \in V_e, \end{cases}$$

with  $\tau_e^L(0) = 0$  at the open frontier  $\partial V_e$  of the volume, and where  $\mathbf{x}$  is the position vector. It accounts for the overall time a particle stays within the volume  $V_e$ , summing all multiple enter/exit situations. Both the Lagrangian time scales have been found to be in agreement with the in-canyon recirculation time in the case of pure diffusion.

All the previously mentioned time scales relate directly to pollutant concentrations, emissions and mass transport through the canyon interface, giving the purpose of this work to find new diagnostic quantities to characterize the fundamental nature of the momentum and heat exchange

processes associated with the in-canyon IC and TC.

## 2.4 Vegetation in the Urban Environment

Investigations on CB of urban environment have rapidly developed an interest in the impact of vegetation on the flow and turbulent fields. Within the last two decades, different approaches have been tried to tackle the problem, mostly involving laboratory and (especially) numerical investigations. Common results have led to the conclusion that the vegetation in urban environment exerts a drag force that reduces the flow field intensity by causing a net loss of momentum, with a consequent modification of both production (transfer from the mean flow) and destruction (the eddy fragmentation can enhance the dissipation) of the turbulent field. As a consequence of the flow and turbulent field modifications, scalar transport and removal are affected, with primary implications on the air quality and thermal comfort of the urban environment. Other impacts generated by vegetation concern the enhancement of the particle deposition on the vegetation leaves, the transpiration and evaporation processes, and the shadowing effect. In this section, a brief description of the role of vegetation on the fluid dynamics, thermodynamics and air quality investigations is given, focusing only on the most widely used vegetation type in urban environment, the tree. Only the vegetation embedded in street canyon environments will be considered, excluding designated green areas such as parks.

A vastly used way to consider trees in fluid dynamics investigations establishes to decompose the tree in two parts. A solid trunk, defined as a long and thin cylinder of non reflective material, on top of which the tree crown is simulated as a solid geometry (generally a cube or a sphere) of porous medium (Gromke and Ruck 2008; Gromke and Ruck 2009). This configuration allows to capture both the flow channeling beneath the crown and the flow intensity reduction caused by the crown porosity, resulting in an overall wind speed modification due to the exerted drag force the tree. The drag force  $F_{drag}$  (N) employed by the tree crown is simply evaluated as the friction force exerted by a medium against the motion of the fluid:

$$F_{drag} = \frac{1}{2} C_v \rho u_x^2 A_f^v,$$

where  $\rho$  ( $\text{kgm}^{-3}$ ) is the air density,  $u_x$  ( $\text{ms}^{-1}$ ) is the flow velocity component directed toward the tree,  $C_v$  is the vegetation drag coefficient and  $A_f^v$  ( $\text{m}^2$ ) is the vegetated frontal area. The vegetation drag coefficient is an indication of the aerodynamic drag exerted by the crown on the flow. Commonly it is considered as a property of the tree species and the season, and it is given as an averaged value representative of the full crown (Di Sabatino et al. 2015; Jeanjean et al. 2017). A more sophisticated and computational costly evaluation of the vegetation drag coefficient has been proposed by Chester et al. (2007), which trees are represented as a fractal geometry of increasing order with the increasing branching. A drag coefficient is evaluated for

each ramification order  $m$  with branching resolving simulations as

$$C_v^n(m) = -\frac{2 \sum_{r=1}^m \left( \mathbf{F}_{drag}^{n,r} (C_v^{n-1} \cdot \mathbf{V}^{n,r} \mid \mathbf{V}^{n,r} \mid A_f^v) \right)}{\sum_{r=1}^m \rho \mid \mathbf{V}^{n,r} \mid^4 \left( A_f^v \right)^2}$$

where  $\mathbf{V}$  ( $\text{ms}^{-1}$ ) is the spatially averaged wind velocity vector,  $r$  is the ramification level and  $n$  is the iteration index. The first iteration of  $C_v$  is an a priori guess. Despite the mathematical accuracy and detailed precision in the evaluation of this drag coefficient, its value seems to be similar to those reported in look-up tables relative to the single tree species. Therefore, it is barely used due to the large computational costs and the very detailed simulation grid required. As a consequence of the drag force application, the tree exerts a pressure modification on the environment consisting in a reduction of the pressure itself when the air flow passes through the porous crown. This pressure drop is generally computed as a coefficient  $\lambda$  ( $\text{m}^{-1}$ ), normalizing the static pressure difference  $\Delta p_{stat}$  (hPa) between the static pressure retrieved at the windward  $p_{wind}$  and leeward  $p_{lee}$  sides of the crown with the drag pressure  $p_{drag} = F_{drag}/A_f^v$  (hPa) of the porous medium of extent  $X$  (m) (Buccolieri et al., 2011):

$$\lambda = \frac{\Delta p_{stat}}{p_{drag} X} = \frac{p_{wind} - p_{lee}}{0.5 \rho u_x^2 X} \quad (2.9)$$

This pressure loss coefficient is a useful piece of information that gives the aerodynamic characteristics of the tree crown, but it is not always simple to compute since it involves measurements of pressure all around the tree to account for all the possible wind directions. An alternative and commonly adopted way (by Van Renterghem and Botteldooren 2008 for instance) is to compute the pressure drop in dependency of a pressure resistance coefficient  $k_r$  as

$$\Delta p_{stat} = \frac{1}{2} k_r \rho u_x^2. \quad (2.10)$$

The pressure resistance coefficient is simply the aerodynamic drag of the tree crown weighted on the leaf area density  $LAD$  ( $\text{m}^2\text{m}^{-3}$ ), the total area of the leaves per unit volume of the canopy, and it can be evaluated following Wilson (1985) as

$$k_r = \int_0^X C_v LAD dx, \quad (2.11)$$

Substituting Eq. (2.11) into (2.10) and back into Eq. (2.9), the pressure loss coefficient simply becomes

$$\lambda = C_v LAD. \quad (2.12)$$

This method of estimating the impact of the trees on the mean flow was largely used in recent numerical and laboratory investigations (Gromke et al. 2008; Van Renterghem and Botteldooren

2008; Buccolieri et al. 2011; Jeanjean et al. 2017). Due to its simplicity, Eq. (2.12) can be adopted also as a bulk estimation of the tree effect in field experiment. As largely discussed in the review of Buccolieri et al. (2019), the other very common parametrization of the tree largely used in numerical simulation employs the evaluation of a mean momentum sink  $S_{u_i}$  ( $\text{hPam}^{-1}$ ) to be added for each velocity component of the momentum equation as

$$S_{u_i} = -\rho LADC_v | \mathbf{u} | u_i, \quad (2.13)$$

where the subscript  $i$  identifies the three Cartesian directions and  $u_i$  is the  $i$ -th wind velocity component. The negative sign enables  $S_{u_i}$  to be interpreted as a momentum sink in the Navier-Stokes equations, where the larger the foliage density and wind speed are, the larger the momentum sink will be. This approach based on the momentum sink in Eq. 2.13 is equivalent to the pressure loss coefficient method in Eq. (2.12), but it is preferred by several authors (Katul et al. 2004; Gromke et al. 2008, 2015; Buccolieri et al. 2009, 2018; Rafael et al. 2018; Li and Wang 2018 among others) because it is generally followed by a computation of the turbulent field modification. In fact, the vegetation subtracts momentum and energy from the mean flow into wake turbulence. At the same time, the smaller length scales of turbulence generated by the shear induced by the vegetation are rapidly dissipation (Buccolieri et al., 2019). These processes are usually parameterized as source and sink terms of Turbulence Kinetic Energy (TKE), as its value  $Tke$  gives the source-sink term  $S_{Tke}$  ( $\text{kgm}^{-1}\text{s}^{-3}$ ), and turbulent dissipation rate  $\epsilon$  ( $S_\epsilon$ ,  $\text{kgm}^{-1}\text{s}^{-4}$ ) as

$$\begin{aligned} S_{tke} &= \rho LADC_v \left( \beta_p | \mathbf{u} |^3 - \beta_d | \mathbf{u} | Tke \right) \\ S_\epsilon &= \rho LADC_v \left( C_{\epsilon,4} \beta_p \frac{\epsilon}{Tke} | \mathbf{u} |^3 - C_{\epsilon,5} \beta_d | \mathbf{u} | \epsilon \right), \end{aligned}$$

where  $\beta_p$  is the fraction of mean kinetic energy converted into  $Tke$  by means of the drag force and has a value in the range 0-1,  $\beta_d$  is the short-circuiting coefficient of the turbulent cascade and  $C_{\epsilon,i}$  are model constants, with the second controlling the destruction of dissipation induced by the foliage (Buccolieri et al., 2019). Although it is certain that the mean flow momentum is consumed by the vegetation, the impact of turbulence is more uncertain due to the source/sink balance operated by the  $Tke$  production and dissipation. This ambivalent behavior of the turbulent field is also at the basis of the recent investigation on the advantage/disadvantage balance the tree can induce on the CB.

Despite the aerodynamic effects of vegetation on the mean flow and turbulent fields correspond to the major impact generated by trees in urban canopies (Buccolieri et al., 2019), particle deposition and resuspension, thermal and shadowing effects must be taken into account too. The deposition and resuspension effects are important, since they are the second factor of pollutant removal after the aerodynamic effects related to the exchange processes. Deposition

is active as a sink  $S_d$  ( $\text{kgm}^{-3}\text{s}^{-1}$ ) of atmospheric pollutant concentrations  $C(x, y, z)$  ( $\text{kgm}^{-3}$ ) caused by the particle capture of the tree leaves (Vos et al. 2013; Jeanjean et al. 2017; Buccolieri et al. 2018):

$$S_d = -LADu_d C(x, y, z),$$

where  $u_d$  ( $\text{ms}^{-1}$ ) is the deposition velocity associated with the investigated pollutant type. Resuspension is instead a source of pollution, especially for the particulate matters (Nowak et al., 2013) and provides an increase of the pollutant concentrations in the urban environment by detaching particles from the tree leaves. The most recent parametrization for the resuspension effect is given by Hong et al. (2018), and it provides a source of particulate concentrations as

$$S_r = LADu_r C_{sinked}(x, y, z),$$

where  $u_r$  ( $\text{ms}^{-1}$ ) is the resuspension velocity from the tree foliage associated with the investigated pollutant particulate type and  $C_{sinked}(x, y, z)$  ( $\text{kgm}^{-3}$ ) is the particulate matter concentration deposited on the plant foliage, i.e. the available particle concentration for resuspension. Thermal and shadowing effects are also important for the regulation of the air temperature and the thermal comfort of the UCL but they have been poorly investigated so far. This category accounts for two factors: the shadowing effect of the tree crown, that reduces the amount of solar radiation reaching the buildings and the street surfaces, and the thermal cooling provided by tree foliage evapotranspiration. The overall effect is a temperature variation  $\delta T$  (K) caused by the sensible heat variation rate  $\dot{H}$  (W) induced by a mass flow rate  $\dot{m}$  ( $\text{kgs}^{-1}$ ) passing through the vegetated crown (Gromke et al. 2015; Moradpour et al. 2017) as

$$\delta T = \frac{\dot{H}}{\dot{m}c_p},$$

where  $c_p$  ( $\text{JK}^{-1}\text{kg}^{-1}$ ) is the specific heat capacity at constant pressure. Notably on the shadowing effects of the trees, infrared imaging is a useful measurement technique to evaluate the emission temperature reduction of solid obstacles covered by trees as it allows to retrieve the obstacles infrared brightness temperatures. This technique is used during field campaigns (for example Di Sabatino et al. 2015) where a spatial computation of the thermal cooling is difficult to obtain.

All these effects define vegetation from its interaction with the urban canopy atmosphere, accounting for the different modification vegetation can introduce in the environment.

## 2.5 Summary and Conclusions

A brief literature review has been given to contextualize the argument of this thesis. First, a classical description of the UBL is presented, focusing on the lower atmospheric layers directly involved in the investigation, which are the UCL and the ShL. The focus then shifted on presenting the most meaningful and recent works characterizing the exchange processes within the UCL and with the atmosphere above. The fundamental aspects describing the role of the exchange processes in regulating momentum and energy transport in street canyons have provided a baseline for the current work computations. In particular the importance of TKMF and TKSHF as driver and regulative factors of the transport through the RL interface becomes a key factor in the current investigation, where these behaviors will be extended to assess the in-canyon mixing efficacy. The geometrical and background flow constraints have also been considered to be of fundamental importance for the current work, as mitigating factors of the exchange processes intensity

Following investigations in the field of CB, the different time scales reported in literature has provided useful information on the pollutant removal time from the UCL. A considerable number of different time scales have been presented to show the spectra of possible investigation approaches to the same problem. All the reported time scales have in common their use of pollutant emission source rates, removal or entrainment velocities. On the contrary, this thesis will focus on computing the time scales for the momentum and heat exchanges between different atmospheric layers, using only the fundamental aspects of the exchange processes to describe the transport and mixing characteristics of the SL, in dependency on the observed in-canyon circulation. Subsequently, the time scales will be used to evaluate the impact of the exchange processes on pollutant removal.

Finally, this literature review described the most recent update concerning vegetation simulation using CFD models, introducing the second part of the current work tackling the impact of trees on the mean flow and turbulence in UCL. Evaluation of the vegetation impact is found to assess different aspects of the atmospheric flow in the UBL. Most of the CFD simulations focused on the attenuation of the mean flow velocity exerted by the vegetation, but several other impacts have been tackled. In particular, vegetation is founded to play the dual role of source and sink for turbulence, as the mechanical  $Tke$  production is balanced by turbulent dissipation. A dual role is also associated with deposition and resuspension of the particulate matter. At last, the shadowing effect of the tree crowns is associated with a strong modification of the heat capacity of the ground, causing a modification in the circulation intensity.

Given this overview of the fundamental studies and recent improvements, the aim of this work is to present new and alternative formulations or investigations of both exchange processes and vegetation impact in a real urban environment by means of simple quantities and operative model.



## Chapter 3

# The "Bologna Project": the Experimental Field Campaigns

The data analysis from two experimental field campaigns is at the basis of this thesis work. In this chapter, the experimental measurements will be introduced. First, a brief overview of the city hosting the campaigns will be provided to describe its geographical location and which are the related implications in terms of expected large scale circulations and air pollution. Second, the morphology of the city will be described to introduce the reader to the field campaigns sites. Then, the main measurement sites of the campaigns will be introduced, focusing on the description of their location in the urban network, their morphology characteristics and instrumental equipment deployed within them. Finally, the supporting monitoring sites and the instrumentation deployed were described.

### 3.1 The Experimental Sites

At the core of my research there are two experimental field campaigns performed in the city center of Bologna (latitude  $44^{\circ} 29'$  N, longitude  $11^{\circ} 20'$  E, altitude 56 m above means sea level), a mid-size city in Emilia-Romagna region in the north of Italy, during summer 2017 (07/08/2017-26/09/2017) and winter 2018 (16/01/2018-14/02/2018) respectively. The campaigns were designed to explore the complex behavior of the mean flow and turbulent structures in two real urban street canyons, Marconi Street (MA) and Laura Bassi Street (LB) respectively, i.e. the main sites, representative morphology of their respective neighborhoods. The campaigns also aimed at monitoring the air quality within the main sites, enabling to investigate the pollutant removal caused by the atmospheric flows. Having two main sites enabled the inter-comparison between two different areas of the same city subject to the same background conditions, while the different seasons investigation allowed to self compare each site as well as to reveal flow and air pollutant seasonality. A great effort was made by the Department of Physics and Astron-

### CHAPTER 3. THE "BOLOGNA PROJECT": THE EXPERIMENTAL FIELD CAMPAIGNS

omy of the University of Bologna (DIFA-UNIBO), the National Council of Researches (CNR) and the Environmental and Energy Regional Protection Agency (ARPAE) to provide all the instrumentation needed for the campaigns. The full description of the street canyons and the instrumentation deployed in them will be given in Sect. 3.1.1 and 3.1.2.

Bologna is a mid-size city located in the south of the Po Valley, southerly bounded by the Apennines chain (Fig. 3.1). The Po Valley is the basin crossed by the Po river which has origin from Monviso in the western mountains and run-off in Venice gulf in the east. The flat basin is surrounded by the Alps and Appennins chains, except for a small opening to the Adriatic see in the east. Large metropolitan areas lay in the basin, like Turin, Milan, and Bologna, as well as industrial areas for agricultural and vehicular productions, food packaging and distribution, weaving among others. The remaining territory is densely cultivated. The metropolitan area of



**Figure 3.1:** Satellite view of the Po Valley and Bologna historical center. (Source: Google Earth).

Bologna (Fig. 3.1) extends for  $3703 \text{ km}^2$  and accounts for an overall population of 1'014'619 inhabitants<sup>1</sup>. The city center is a small hexagonal area of  $140.86 \text{ km}^2$  bounded by the remnant of the historical walls that enclosed the once-it-was city. From the morphological perspective, the city center can be described as a dense network of narrow streets bounded by tall historical buildings (Fig. 3.2a). The majority of the streets are pedestrian or subjected to traffic warrant but still covered by bus tracks. The dense array of street canyons is sometimes interrupted by squares, rounds or small parks. Very few vegetative elements are present within the historical walls. The characteristic feature of Bologna historical center is the presence of galleries (named *portici*) that flank the streets replacing ground and first floors of the buildings, and where people

<sup>1</sup>Value retrieved from the demographic report of the National Institute of Statistics (ISTAT), 31/12/2018.

can walk shadowed by the tall arcs on top of the vault. Outside the city center, the building density decreases as the neighborhoods become more residential until the suburbs as well as the industrial area are reached (Fig. 3.2b). Roads become accessible to all private vehicles as the bus tracks reduce their number. Residential buildings are typical of those areas of the city, surrounded by small gardens. The regular urban texture leaves designed spaces to parks and



**Figure 3.2:** Top view of Bologna city center (a, ©Comune di Bologna) and the surrounding area (b).

open areas like shopping centers, while vegetative elements spread through the various neighborhoods. The industrial area is confined in the suburbs as well as the airport. Most of the citizens lived and worked in the city center and the close surroundings, but as the population increases also suburbs inhabitants are growing fast. Summarizing, the morphology of Bologna can be considered as typical for European cities (Ratti et al. 2002; Di Sabatino et al. 2010) characterized by a historical densely build-up center surrounded by residential and industrial areas, generally less populated.

Due to its geographical location and the slow wind regimes that characterize a plain surrounded by high mountain chains (Mazzola et al., 2010), Bologna and the whole Po Valley are well-recognized hot-spots of air pollution in Europe (Finardi et al., 2014). A network of monitoring stations were deployed to fulfill the aims of the campaigns. An overlook of the monitoring network is presented on the map in Fig. 3.3. The map collects the main sites locations (Fig. 3.3, panels (c) and (e)) and the supporting monitoring stations of both air quality and meteorological variables. Silvani Street (SI), Innerio Street (IS) and Asinelli Tower (AT) (Fig. 3.3, panels (a), (f) and (g)) are meteorological stations for the background flow and atmospheric boundary layer characterization. Porta San Felice (PSF) and Giardini Margherita (GM) (Fig. 3.3, panels



**Figure 3.3:** Map of Bologna with localization of the campaign sampling sites. In order: (a) SI, (b) PSF, (c) MA, (d) GM, (e) LB, (f) AT and (g) IR. (Source: Google Earth).

(b) and (d)) are air quality monitoring stations. A full description of the supporting monitoring sites and instrumentation will be given in Sect. 3.2.

### 3.1.1 Non Vegetated Street Canyon - Marconi Street

MA is a 700 m long main bus artery located in the core of the business area of the city center (Fig. 3.3c). This is a busy road embedded in the urban network as a sequence of equally spaced blocks, with inter-distance smaller than the street width. MA is embedded in a traffic-restricted neighborhood. Its street is composed of four lanes (with mean street width  $W_{MA} \simeq 20$  m) and only usable by buses (more than 50% of the city bus lines pass through this street) and residents or citizens with special passes. MA is characterized by tall and densely packaged buildings, with mean height  $H_{MA} \simeq 33$  m above ground level (AGL), interrupted only by few small junctions and one major intersection. The average aspect ratio  $AR_{MA} = H_{MA}/W_{MA}=1.65$  is used as representative parameter of the street geometry. The street is oriented north-south at a displaced angle of  $17^\circ$  to east from north. Fig. 3.4 gives an insight of the street from top and frontal perspectives. Top view in Fig. 3.4a also shows an overlook of the surrounding neighborhood. MA neighborhood resembles the typical characteristics of the city center, with 5-6 stores historical buildings towering on narrow single lane streets. Small areas with single store buildings, e.g. kiosks, are also present, lowering the building height of the neighborhood  $H_{MA}^n$  to an average value of 15 m. Two small city parks provide a small contribution to the almost null amount of

vegetation in the neighborhood. A large set of instrumentation was installed in MA to quantify the pollutant concentrations at the ground and to reveal the flow and turbulence behaviors inside and above the canyon. Instrumentation were subdivided in three different locations and heights above the ground. Fig. 3.5 displays the locations (dots) of the instrumentation in the street. The dots color highlights a different level where the measurement stations are deployed: green refers to the rooftop, red to the mid-canyon and blue to the ground levels respectively. Ground Level (GL) is located on the west side of the road, in a parking spot close to the building gallery at 4 m (AGL). Mid-canyon Level (ML) protrudes from a balcony of an east side building toward the road at 7 m (AGL), in the northern part of the street. Rooftop Level (RL) is located on the same building of the ML on rooftop balcony at 33 m (AGL). Each site is equipped to measure high frequency wind velocity components and sonic virtual temperature, along with low frequency air temperature and relative humidity. This set enables the computation of mean flow and turbulence characteristics at different levels of the canyon, structuring the flow behavior and gradients. Single displayed instrumentation completes the street canyon equipment. The

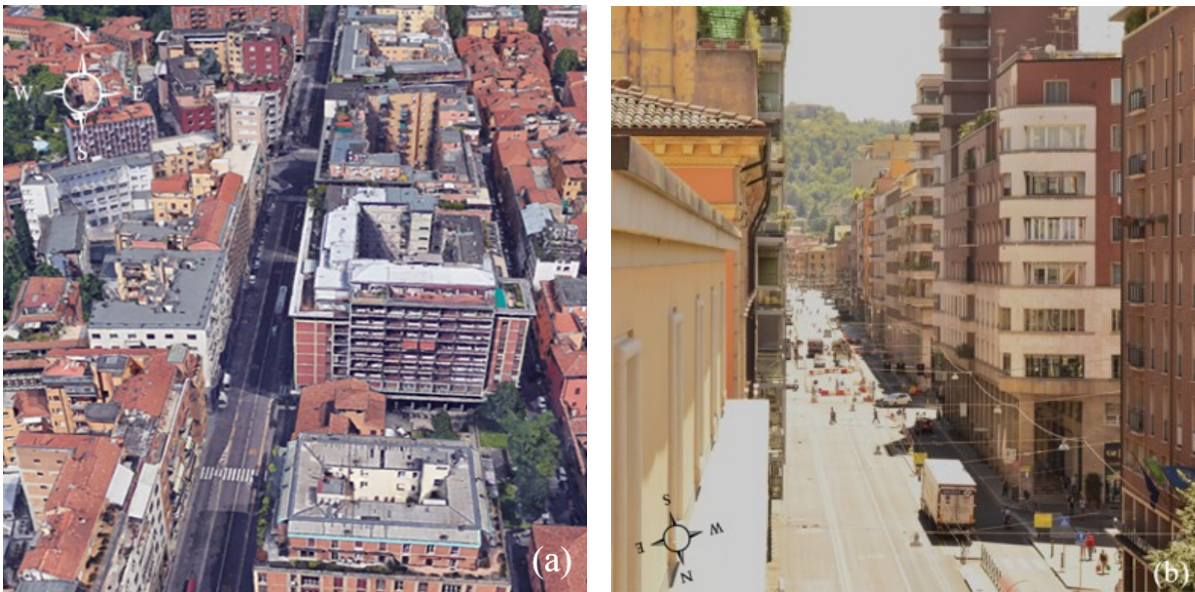


**Figure 3.4:** Top (a) and frontal (b) views of MA.

GL station is equipped to assess both air quality and meteorological aspects. The basement of the station is represented by an ARPAE mobile laboratory, a van equipped for the measure of different air pollutants and basic meteorological variables (Fig. 3.5, Ground level). Both gas analyzers and particulate samplers suck air toward the detector from a chimney located on top of the van at 4 m AGL. Gas analyzers use a detection method varying according to the pollutant type coupled with state-of-the-art microprocessor technology to provide the sensitivity, stability and ease of use needed for ambient or dilution monitoring requirements of gaseous

### CHAPTER 3. THE "BOLOGNA PROJECT": THE EXPERIMENTAL FIELD CAMPAIGNS

pollutant concentrations. Particulate samplers retrieve the mass of particles trapped on a filter the air is forced to go through. Gas analyzer and particulate samplers perform continuous measurements of pollutant concentrations such as nitrogen dioxides ( $NO$  and  $NO_2$ ), carbon monoxide ( $CO$ ), ozone ( $O_3$ ), sulfur dioxide ( $SO_2$ ), particulate matter ( $PM_{10}$  and  $PM_{2.5}$ ) and aromatic compounds  $BTX$ , i.e. benzene, toluene, ethylbenzene and xylene. Since the main source of air pollution in a street canyon is given by vehicle emissions, traffic related pollutants like  $NO$ ,  $NO_2$  and  $CO$ , together with  $O_3$ , are sampled at a rate of 0.2 Hz (12 measurements per minute) and automatically averaged over one minute intervals. The interval is discarded if less than 6 measurements are collected within the averaging window. This short averaging rate enables to assess the fluctuations in traffic related emissions and to evaluate the effect of robust turbulent structures on the concentrations. Averaged measurements of secondary pollutants for a street canyon environment, like  $SO_2$  and  $BTX$ , are evaluated hourly. Finally, the daily

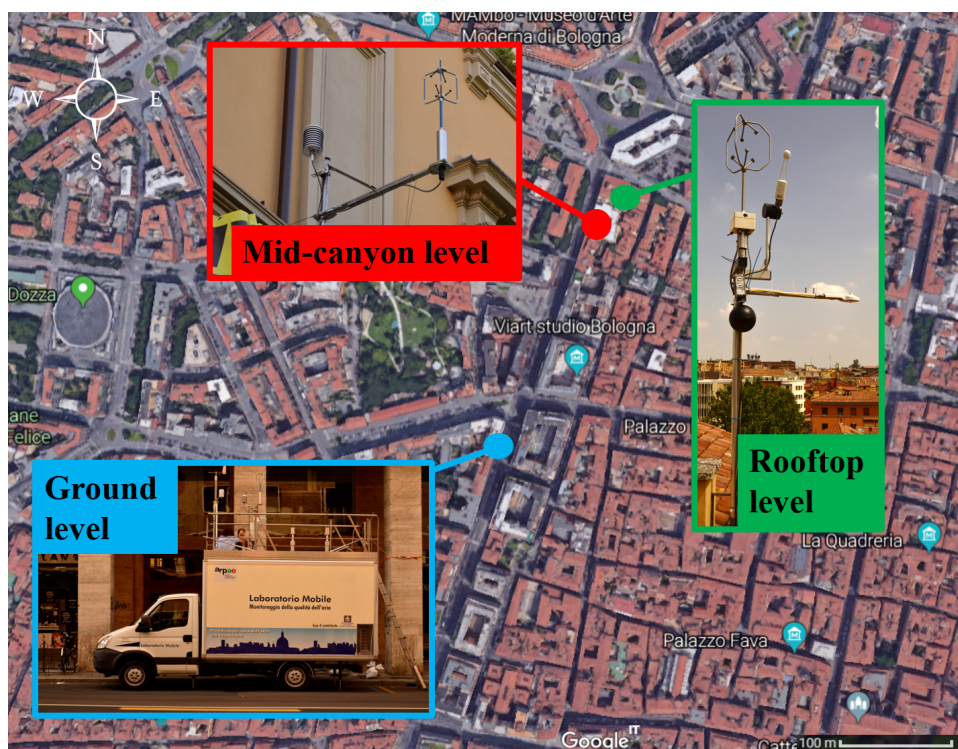


**Figure 3.5:** Measurement sites locations at the three levels inside and above MA canyon. Colors link the location (dots) to the corresponding measurement site (boxes). Instrumentation at each level is reported on table 3.1. (Source: Google Earth).

amount is collected for particulate matters. Every 23 hours, gas analyzers and particle samplers automatically perform a calibration test. Supporting instrumentation also allows to measure the basic meteorological variables at 0.2 Hz, storing the 1 minute average. A thermohygrometer probe is located on the van top to measure air temperature and relative humidity. A cup

and vane anemometer is also collocated on the van top collecting the 2D wind velocity and direction. Wind velocity is retrieved from a measurement of cup spins per second, given by the mechanical torque generated by the flow on the cups. This characteristic of the instrumentation involves an activation threshold of approximately  $0.5 \text{ ms}^{-1}$  to overpower the static friction of the rotation mechanisms. Moreover, cups have a slow response to flow variations due to the inertia of the rotation. Therefore cup and vane anemometer is not suitable for turbulence estimation. To cover this gap, supplementary instrumentation was installed on the van top. A sonic anemometer was set to collect high frequency measurements of the three wind velocity components, together with the sonic temperature (a quantity close to the virtual temperature). The operative method, based on the retrieval of a sonic wave perturbation generated by the velocity of the medium the waves goes through, allows to collect data at a sampling rate of 20 Hz, corresponding to 20 measurements per second. This fast sampling rate is sufficient for the evaluation of turbulent quantities, necessary to fulfill the aims of the whole investigation. Sonic anemometers are also coupled with a thermohygrometer and a barometer sampling at 1 Hz, to access the fast variation of air temperature, relative humidity and pressure. The ML was equipped with the essential core of each site, i.e. the sonic anemometer for the measurements of mean flow velocity and direction and turbulence, and the thermohygrometer for air temperature and relative humidity. As for the ground level, the sonic anemometer sampled at 20 Hz while the thermohygrometer samples at 1 Hz. The instrumentation was mounted on an ad-hoc metal structure at the edge of a balcony facing the street from the eastern side (Fig. 3.5, Mid-canyon level). To minimize the building facade and balcony perturbation effect on the atmospheric flow, the sonic anemometer was mounted on a branch of the metal structure 0.5 m above the balcony rail protruding approximately 2 m from the balcony edge toward the street center. The RL was located on the rooftop balcony of the same building hosting the ML (Fig. 3.5, Rooftop level). The site was equipped by a sonic anemometer coupled with an open path gas analyzer and a net radiometer. The sonic anemometer differs from the in-canyon ones since it ensures measurement stability over a wider temperature range, but reduces the sampling rate to 10 Hz. The open path gas analyzer is an optical instrument which enables the retrieval of water vapor  $H_2O$  and carbon dioxide  $CO_2$  concentrations at a sampling rate of 10 Hz from the backscatter of a laser beam. When coupled with a sonic anemometer,  $CO_2$  and  $H_2O$  fluxes can be determined combining the gas concentrations to the wind velocity components by means of the eddy covariance technique. The net radiometer is an optical instrumentation formed by 2 couples of sensors for the evaluation of the radiative energy balance. Each sensors couple is formed by a pyranometer to measure the shortwave ( $0.3\text{-}2.8 \mu\text{m}$ ) radiation and a pyrgeometer to measure the longwave ( $4.5\text{-}42 \mu\text{m}$ ) radiation. A couple is set on top of the instrumentation facing the sky to retrieve the incoming solar radiation; the other couple is set on the bottom facing the ground to retrieve the surface longwave emission and shortwave scatter.

CHAPTER 3. THE "BOLOGNA PROJECT": THE EXPERIMENTAL FIELD CAMPAIGNS

Experimental setup and measurements				
Site	Instrumentation	Association	Sample	Measurements
Rooftop level (33m AGL)	Sonic anemometer uSonic-3, Metek, Elmshorn, Germany	CNR	10 Hz	wind velocity components, sonic temperature
	Gas analyzer LI-7500A, LI-COR, Lincoln, Nebraska, USA	CNR	10 Hz	$CO_2$ and $H_2O$ concentrations
	Net radiometer CNR4, Kipp and Zonen, Delft, Netherlands	DIFA-UNIBO	1 min	Solar radiation components, radiative temperature
Mid-canyon level (7m AGL)	Sonic anemometer Windmaster 3D, Gill, Lymington, Hampshire, UK	DIFA-UNIBO	20 Hz	wind velocity components, sonic temperature
	Thermohygrometer HCS2S3-L, Campbell Scientific, Logan, Utah, USA	DIFA-UNIBO	1 Hz	air temperature relative humidity
	Sonic anemometer Windmaster 3D, Gill, Lymington, Hampshire, UK	DIFA-UNIBO	20 Hz	wind velocity components, sonic temperature
Ground level (4m AGL)	Thermohygrometer HCS2S3-L Campbell Scientific, Logan, Utah, USA	DIFA-UNIBO	1 Hz	air temperature, relative humidity
	Barometer PTB110, Vaisala, Helsinki, Finland	DIFA-UNIBO	1 Hz	air pressure
	Gas analyzer T300, T200, T100 Teledyne API, San Diego, California, USA	ARPAE	1 min	carbon monoxide, nitrogen oxides and sulfur dioxide concentrations
	Gas analyzer 49i, Thermo Fischer Scientific, Rodano, Italy	ARPAE	1 min	ozone concentration
	Gas analyzer air ToXIC, Chromatotech, Val de Virvee, France	ARPAE	1 min	BTX concentration
	Particle sampler Swam 5a, Fai Instruments, Fonte Nuova, Italy	ARPAE	1 day	particulates concentration
	Cup and vane anemometer, DNA301.1 and DNA310.1, LSI-Lastem, Milano, Italy	ARPAE	1 min	wind velocity and direction
	Thermohygrometer HMP230, EXP815, LSI-Lastem, Milano, Italy	ARPAE	1 min	air temperature, relative humidity

Table 3.1: Table summarizing the instrumentation setup deployed in MA.

From the solar radiation measurements, the radiative temperature is also retrieved. Data collected from the net radiometer were automatically averaged over a 1 minute interval. The sonic anemometer and gas analyzer couple were mounted on a two branches support at the top of a metal pole, about 2 m above the balcony rail (3 m from the balcony floor). The support enables the correct disposition of the couple. The gas analyzer head must be located at the same height of the air volume analyzed by the anemometer, inclined by 10-15° with respect to the sonic anemometer head. The net radiometer was mounted on a branch toward the south. A summary of the instrumentation deployed at each site of MA, together with location, model specification, affiliation, sampling rate and measured variables is reported in Tab. 3.1. A more exhaustive description of the instrumentation technical specifications is given in Appendix A.

### 3.1.2 Vegetated Street Canyon - Laura Bassi Street

LB is a 2 lanes 700 m long road, surrounded by an almost regular deployment of deciduous trees facing small private houses or apartments. Its orientation is north-south at a displacement angle of 24° to east from north. Being a residential area, the road is open to private vehicular traffic as well as some minor bus tracks. Being the inter-distance between facing buildings, the mean street width  $W_{LB} \simeq 25$  m accounts for the lanes width and the residential front gardens. The building skyline rapidly changes through the street, passing from 2 stores private houses



**Figure 3.6:** Top (a) and frontal (b) views of LB.

to 4-5 stores buildings. Despite it, a representative mean height  $H_{LB} \simeq 17$  m is retrieved and used to compute the street aspect ratio  $AR_{LB} = H_{LB}/W_{LB}=0.7$ . Fig. 3.6 gives an insight of the street from top and frontal perspectives. Top view in Fig. 3.6a also shows an overlook of

## CHAPTER 3. THE "BOLOGNA PROJECT": THE EXPERIMENTAL FIELD CAMPAIGNS

the surrounding neighborhood. The neighborhood is a network of parallel and perpendicular roads with similar aspect ratios despite the single geometric parameters may change. In fact, the northern part of LB is populated by 7-8 store buildings that enhance the mean building height. Conversely most of the surrounding streets of the southern area are single store houses. Street width also tends to decrease outside LB, leaving the neighborhood aspect ratio almost invariant. The majority of the street and neighborhood vegetation is composed of deciduous trees belonging to the *Platanus Acerifolia* Mil family, a hybrid of *Platanus Orientalis* and *Platanus Occidentalis* types, widely spread in European urban habitats. The average height of the branch-free trunk is 5 m and the spherical shaped crown extends up to 15 m, with a diameter of 5 m. Along the



**Figure 3.7:** Measurement sites locations at the three levels inside and above LB canyon. Colors link the location (dots) to the corresponding measurement site (boxes). Instrumentation at each level is reported on table 3.2. (Source: <https://earth.google.com/web/>).

street, trunks are regularly spaced by approximately 8 m, allowing a small crown superposition. The composition of buildings and vegetation leads to a mean height of the neighborhood  $H_{LB}^n$  of 11 m. To match the measurements collected in MA, a similar set of instrumentation was also installed in LB to quantify the pollutant concentrations at the ground and to reveal the flow and turbulence behaviors inside and above the canyon. The instrumentation was subdivided in three different locations and heights above the ground. Fig. 3.7 displays the locations (dots) of the instrumentation in the street. The dots color is the same as in Fig. 3.5 for MA: green refers to the rooftop, red to the mid-canyon and blue to the ground levels respectively. The

GL is placed on the east side of the road, in a parking spot beneath trees at 3 m (AGL). The ML protrudes from a balcony of an east side building toward the road at 9 m (AGL), in the southern part of the street. The RL during the summer campaign is located on the flat rooftop of a tall building on the west side of the street at 20 m (AGL). During the winter campaign the RL had been lowered to a rooftop balcony at 15 m on a near building due to power sourcing issues. Each site was equipped to ensure the same data type collection of MA, enabling the computation of mean flow and turbulence characteristics at different levels of the canyon, together with the pollutant concentrations at the street surface. The basement of the GL station is again represented by a mobile laboratory of ARPAE (Fig. 3.7, Ground level). The gas analyzer and particulate samplers within it perform continuous measurements of pollutant concentrations such as nitrogen dioxides ( $NO$  and  $NO_2$ ), carbon monoxide ( $CO$ ), ozone ( $O_3$ ), sulfur dioxide ( $SO_2$ ) and particulate matter ( $PM_{10}$  and  $PM_{2.5}$ ). The sampling rates of  $NO$ ,  $NO_2$  and  $CO$ , along with  $O_3$ , are once again set at 0.2 Hz (12 measurements per minute) and automatically averaged over one minute intervals. The interval is discarded if less than 6 measurements are collected within the averaging window.  $SO_2$  is evaluated hourly, while daily amounts are collected for the particulate matter. Every 23 hours, gas analyzers and particle samplers perform an automatic calibration test. Basic meteorological variables are measured at 0.2 Hz and the 1 minute average is stored. A thermohygrometer probe and a cup and vane anemometer are located on the van top to measure air temperature and relative humidity, 2D wind velocity and direction. A sonic anemometer was also set on the van top to collect high frequency measurements of the three wind velocity components, together with the sonic temperature, sampling at 20 Hz. Finally, thermohygrometer and a barometer sampling at 1 Hz are used to access the fast variation of air temperature, relative humidity and pressure. The ML was equipped with a sonic anemometer for the measurement of mean flow velocity and direction and turbulence, and a thermohygrometer for air temperature and relative humidity. As for the GL, the sonic anemometer samples at 20 Hz while the thermohygrometer samples at 1 Hz. The instrumentation was mounted on an ad-hoc metal structure at the edge of a balcony facing the street from the eastern side (Fig. 3.7, Mid-canyon level). To minimize the building facade and balcony perturbation effects on the atmospheric flow, the sonic anemometer was mounted on a branch of the metal structure protruding approximately 2 m from the balcony edge toward the street center. During the summer campaign, the RL was located on the rooftop of one of the tallest building on the west side of the street at 20 m (AGL) (Fig. 3.7, Rooftop level). During the winter campaign, the same level was moved to a lower rooftop balcony on the nearby building at 15 m due to risen technical issues with the power supply. The instrumentation equipment did not change between the two campaigns, so they will be considered as a single site. The site was equipped by a sonic anemometer and a net radiometer. The sonic anemometer differs from the in-canyon ones since it ensures measurement stability over a wider temperature range.

CHAPTER 3. THE "BOLOGNA PROJECT": THE EXPERIMENTAL FIELD CAMPAIGNS

Site	Experimental setup and measurements			Measurements
	Instrumentation	Association	Sample	
Rooftop level (20m AGL)	Sonic anemometer 81000, RM Young Company, Traverse City, Michigan, USA	CNR	10 Hz	wind velocity components, sonic temperature
	Net radiometer CNR4, Kipp and Zonen, Delft, Netherlands	DIFA-UNIBO	1 min	Solar radiation components, radiative temperature
Mid-canyon level (9m AGL)	Sonic anemometer Windmaster 3D, Gill, Lymington, Hampshire, UK	DIFA-UNIBO	20 Hz	wind velocity components, sonic temperature
	Thermohygrometer HCS2S3-L, Campbell Scientific, Logan, Utah, USA	DIFA-UNIBO	1 Hz	air temperature, relative humidity
Ground level (3m AGL)	Sonic anemometer Windmaster 3D, Gill, Lymington, Hampshire, UK	DIFA-UNIBO	20 Hz	wind velocity components, sonic temperature
	Thermohygrometer HCS2S3-L, Campbell Scientific, Logan, Utah, USA	DIFA-UNIBO	1 Hz	air temperature, relative humidity
Ground level (3m AGL)	Barometer PTB110, Vaisala, Helsinki, Finland	DIFA-UNIBO	1 Hz	air pressure
	Gas analyzer T300, T200, T100 Teledyne API, San Diego, California, USA	ARPAE	1 min	carbon monoxide, nitrogen oxides and sulfur dioxide concentrations
Ground level (3m AGL)	Gas analyzer 49i, Thermo Fischer Scientific, Rodano, Italy	ARPAE	1 min	ozone concentration
	Particle sampler Swam 5a, Fai Instruments, Fonte Nuova, Italy	ARPAE	1 day	particulates concentration
Ground level (3m AGL)	Cup and vane anemometer, DNA301.1 and DNA310.1, LSI-Lastem, Milano, Italy	ARPAE	1 min	wind velocity and direction
	Thermohygrometer HMP230, EXP815, LSI-Lastem, Milano, Italy	ARPAE	1 min	air temperature, relative humidity

Table 3.2: Table summarizing the instrumentation setup deployed in LB.

Nevertheless it has a reduced sampling rate (10 Hz). The net radiometer collected solar radiation data, storing the 1 minute average and retrieving the radiative temperature from them. The sonic anemometer was mounted at the top of the metal pole of a tripod positioned in the middle of the rooftop, about 3 m above the floor. The net radiometer was mounted on a branch protruding in the south direction. A summary of the instrumentation deployed at each site of LB, together with location, model specification, affiliation, sampling rate and measured variables is reported in Tab. 3.2. A more exhaustive description of the instrumentation technical specifications is given in Appendix A.

### 3.2 Supporting Instrumentation

Supporting monitoring sites are spread all over the city, located at points (a), (b), (d), (f) and (g) in Fig. 3.3. Apart from site (g), the others are part of the permanent air quality and meteorological monitoring network of ARPAE. Therefore, the instrumentation deployed in each site is conformed to what is logged in the mobile laboratories. Sites (b) and (d), respectively named PSF and GM (Fig. 3.8), are part of the network for monitoring the air quality in the city. The monitoring stations follow the European standards on pollutant measurements. PSF is an urban traffic monitoring site, located at the namesake junction hosting one of the 12 ancient city gates through the walls. Traffic is very intense in this area since it is embedded in



**Figure 3.8:** PSF (a) and GM (b) air quality monitoring sites.

the 6 lanes circulatory road of the city. A one way street connects the junction to the business core of the historical center, while the main public road connecting the Emilia-Romagna region capitals leaves the junction toward the east suburbs, passing the main hospital of Bologna. GM is classified as an urban background monitoring site, located inside the namesake and largest park of the city. The park extends for 260000 m<sup>2</sup>, and it is completely closed to motored vehicles. The monitoring sites are equipped with both gas analyzer and particulate samplers.

### CHAPTER 3. THE "BOLOGNA PROJECT": THE EXPERIMENTAL FIELD CAMPAIGNS

---

They both measure  $PM_{10}$ ,  $PM_{2.5}$  and  $NO_x$ . PSF adds measurements of  $CO$  and  $BTX$ , while at GM  $O_3$  is sampled, coherently to the different scope of each site. Since ARPAE is a regional public agency, the collected data are available, already checked and averaged according to the European legislation. Therefore, particulate matters are available as daily average, while gases are hourly averaged.

Sites (a) and (f) in Fig. 3.3, respectively named SI and AT, are part of the meteorological network in the city. SI is considered as an urban meteorological site. The station is composed of a cup and vane anemometer, a thermohygrometer probe, a barometer, a pluviometer and a net radiometer (for the scope of this work we will only consider the anemometer and the thermohygrometer). It is located on the rooftop of the headquarter of ARPAE in SI, at 35 m (AGL). AT is a



**Figure 3.9:** The Vaisala Ceilometer CL31 located on the rooftop of the Physics and Astronomy department in IS.

synoptic meteorological site. The station is located on the top of the AT at approximately 100 m (AGL) and equipped with a cup and vane anemometer and a thermohygrometer. Horizontal wind speed, wind direction, air temperature and relative humidity are collected at both sites and the one-hour average is stored. The ARPAE meteorological stations enable the estimation of the background flow velocity and the air temperature and relative humidity, i.e. the quantities needed to characterize the air mass flowing in the UBL. Finally, site (g) in Fig. 3.3 depicts the location of a ceilometer (Fig. 3.9), property of DIFA-UNIBO, placed on the rooftop of the Physics and Astronomy department in IS. The instrumentation allows to estimate the UBL height and its evolution in time. The measurements are retrieved from the backscattered signal of a laser beam emitted by the ceilometer at a wavelength centered at 910 nm. The boundary layer height data are then stored every 16 s.

Site	Experimental setup and measurements			
	Instrumentation	Association	Sample	Measurements
Silvani Street (35m AGL)	Cup and vane anemometer WMS301, Vaisala, Helsinki, Finland	ARPAE	30 min	wind velocity and direction
	Thermohygrometer HMP230, Vaisala, Helsinki, Finland	ARPAE	30 min	air temperature, relative humidity
Asinelli Tower (100m AGL)	Cup and vane anemometer Vr20 and Dv20, CAE, Bologna, Italy	ARPAE	60 min	wind velocity and direction
	Thermohygrometer THS, CAE, Bologna, Italy	ARPAE	60 min	air temperature, relative humidity
Porta San Felice	Gas analyzer T300, Teledyne API,San Diego, California, USA	ARPAE	60 min	carbon monoxide concentration
	Gas analyzer T200 Teledyne API,San Diego, California, USA	ARPAE	60 min	nitrogen oxides concentration
	Gas analyzer Chromatotech, Val de Virvee, France	ARPAE	60 min	BTX concentration
	Particle sampler Swam 5a, Fai Instruments, Fonte Nuova, Italy	ARPAE	1 day	particulates concentration
	Gas analyzer T300 Teledyne API,San Diego, California, USA	ARPAE	60 min	carbon monoxide concentration
Giardini Margherita	Gas analyzer 49i, Thermo Fischer Scientific, Rodano, Italy	ARPAE	60 min	ozone concentration
	Particle sampler Swam 5a, Fai Instruments, Fonte Nuova, Italy	ARPAE	1 day	particulates concentration
Innerio Street	Ceilometer CL31 Vaisala, Helsinki, Finland	DIFA-UNIBO	16 sec	boundary-layer height

**Table 3.3:** Table summarizing the instrumentation setup deployed at the supporting sites.

## CHAPTER 3. THE "BOLOGNA PROJECT": THE EXPERIMENTAL FIELD CAMPAIGNS

---

A summary of the instrumentation deployed at each ARPAE and DIFA-UNIBO monitoring site, along with location, model specification, affiliation, sampling rate and measured variables is reported in Tab. 3.3. A more exhaustive description of the instrumentation technical specifications is given in Appendix A.

### 3.3 Summary and Conclusions

In this section, the experimental field campaigns have been presented, focusing on the characterization of the field domains and the instrumentation deployed. It worth recalling that two experimental field campaigns have been performed, investigating both summer (07/08/2017-26/09/2017) and winter (16/01/2018-14/02/2018) seasons. The field campaigns investigations were supported and financed by the iSCAPE project.

The city of Bologna, host of the campaigns, has been described revealing its hot-spot condition regarding air pollution, as a consequence of the low natural ventilation provided by its geographical collocation within the Po Valley. The network of narrow street canyons that composes the city center is known to exacerbate this low ventilation condition, worsening the air pollution problem. To investigate the ventilation processes in presence and absence of vegetation, and to reveal their impacts on pollutant removal, the two street canyons of MA and LB have been selected as main sites of the experimental field campaigns. The street canyons description focused on the instrumentation deployed at three different levels inside and above each canyon to measure mean flow and turbulence characteristics, along with air pollutants. The instrumental setup was then completed by the permanent monitoring station in the city, establishing the supporting measurement sites necessary to evaluate the background flow conditions.

## Chapter 4

# Data Processing and Methodology

In this Chapter, data processing and methodology will be discussed to introduce the investigations evaluated in this thesis, including both data analysis and numerical simulations. The Chapter will be subdivided in two main branches. First, it will be explained the treatment and use of data from the field campaigns, from the initial processing concerning the data cleaning to the explanation of the methodology adopted for the investigation. Second, the methodology will pose the basement for the data analysis and numerical investigation; therefore, the numerical model will be described to introduce its computation logic, focusing on the vegetation parametrization and the simulation setup. In particular, after the data cleaning, a suitable period identification is performed by means of synoptic conditions analysis. Exchange processes diagnostic quantities are defined and characterized to introduce the type of analysis at the core of this thesis. Eventually, a focus on the numerical model is given.

### 4.1 Data processing

#### 4.1.1 Experimental protocol and despiking procedure

Data self-consistence of each instrumentation type is ensured by a former laboratory test comparison between them to ensure the validity of the calibration. Moreover, the same test is also performed in a real but controlled environment. Data collected during the campaigns were preliminary checked to detect and remove out-of-range data or instrumental fails. This procedure is based on typical local ranges so that the specific quantities under investigations are retrieved if the following conditions are satisfied:

- wind velocity components  $|(u, v, w)| \leq 20 \text{ m s}^{-1}$
- temperature (both sonic and real):  $|T| \leq 50^\circ\text{C}$
- relative humidity: ranges in 0 – 100%

Values above thresholds are replaced with the nearest finite value along the time series. The same procedure is applied to not-a-number and infinite values. If the consecutive “wrong values” equal (or exceed) the averaging period (5 minutes) they are simply replaced with non-values and the interval is rejected. Sonic data are then despiked, following a procedure similar to the method proposed by Højstrup (1993). This technique assumes that each interval within the dataset is a Gaussian distribution of independent data for which means ( $\bar{x}$ ) and standard deviations ( $\sigma$ ) are calculated. Values above a defined threshold ( $C \cdot \sigma$ ) are marked as spikes. The discriminant factor of the threshold  $C$  is taken equal to 3.5 following both Vickers and Mahrt (1997) and Schmid et al. (2000). The interval’s dimension is chosen to be 5 minutes, in agreement with Vickers and Mahrt (1997), which ensures to gather most of the variance without losing the Gaussian assumption. The despiking procedure is only applied once per interval and spikes are replaced by the mean value of the interval calculated without the spike.

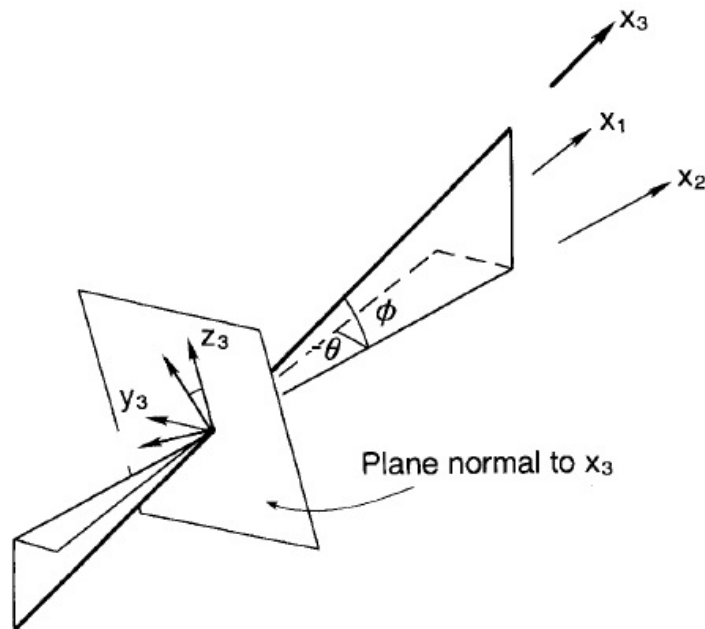


**Figure 4.1:** Three dimensional coordinate rotations for alignment of coordinate axes to the flow field over sloping terrain. Modified from figure 6.20 of Kaimal and Finnigan (1994).

#### 4.1.2 Coordinate system rotation

The despiked horizontal wind components are rotated following McMillen (1988) to compute the velocity along the streamline and then the turbulent fluxes. The method is based on a double rotation around the mean wind vector  $\vec{u} = (\bar{u}_1, \bar{v}_1, \bar{w}_1)$ . The averaging window depends on the spatial grid and the average time, therefore all quantities have been averaged in time over a

period of 5 minutes. The whole transformation refers to the diagram in figure (4.1). The first transformation swings the  $x_1$  and  $y_1$  axes around  $z_1$  to produce a new set of axes  $(x_2, y_2, z_2)$  with  $x_2$  in the plane spanned by  $\vec{u}$  and  $z_1$ :

$$\begin{aligned} u_2 &= u_1 \cos \psi + v_1 \sin \chi \\ v_2 &= -u_1 \sin \psi + v_1 \cos \chi \\ w_2 &= w_1 \\ \psi &= \tan^{-1}(\bar{v}_1/\bar{u}_1); \end{aligned}$$

where  $\chi$  is the angle along the projection of the mean stream on the instrumental plane. This way, the coordinate system is oriented along with the mean stream direction, computing a rotation in  $\chi$ . As a consequence, the rotation constrains advection to be null ( $\bar{v}_2 = 0$ ) and the main stream to project along  $\bar{u}_2$ , letting  $\bar{w}_2 = \bar{w}_1$ . The second rotation maintains  $\bar{v}_2 = 0$ , swinging  $x_2$  and  $z_2$  of the elevation angle from the surface  $\phi$  into new directions  $(x_3, y_3, z_3)$ . So  $x_3$  is the direction of the streamline,  $y_3$  is the cross-streamline direction and  $z_3$  is the vertical normal to the inclined surface:

$$\begin{aligned} u_3 &= u_2 \cos \phi + w_2 \sin \phi \\ v_3 &= v_2 \\ w_3 &= -u_2 \sin \phi + w_2 \cos \phi \\ \phi &= \tan^{-1}(\bar{w}_2/\bar{u}_2). \end{aligned}$$

Since the elevation angle is small the variation between the first to the second rotation is negligible. After the whole rotation procedure, the final velocity vector is  $\bar{u}_f = (\bar{u}_3, 0, 0)$ . Once data have been despiked and rotated, both mean flow quantities and kinematic turbulent fluxes are computed at all levels inside and above the canyon. To ensure a general robustness of the analysis, without losing small scales processes, all quantities have been averaged in time over a period of 5 minutes.

## 4.2 Data analysis

### 4.2.1 The period selection based on the analysis of synoptic conditions

Long-lasting experimental field campaigns enable to continuously collect local data throughout different meteorological synoptic conditions. Large scale horizontal gradients induce the synoptic circulation and drive the small scale dynamics. In a close environment such as the Po Valley (see Sect. 3.1), these large scale gradients are easily inhibited by the presence of the mountain chains. This inhibition is more visible when the region is not perturbed by fronts or instabilities,

## CHAPTER 4. DATA PROCESSING AND METHODOLOGY

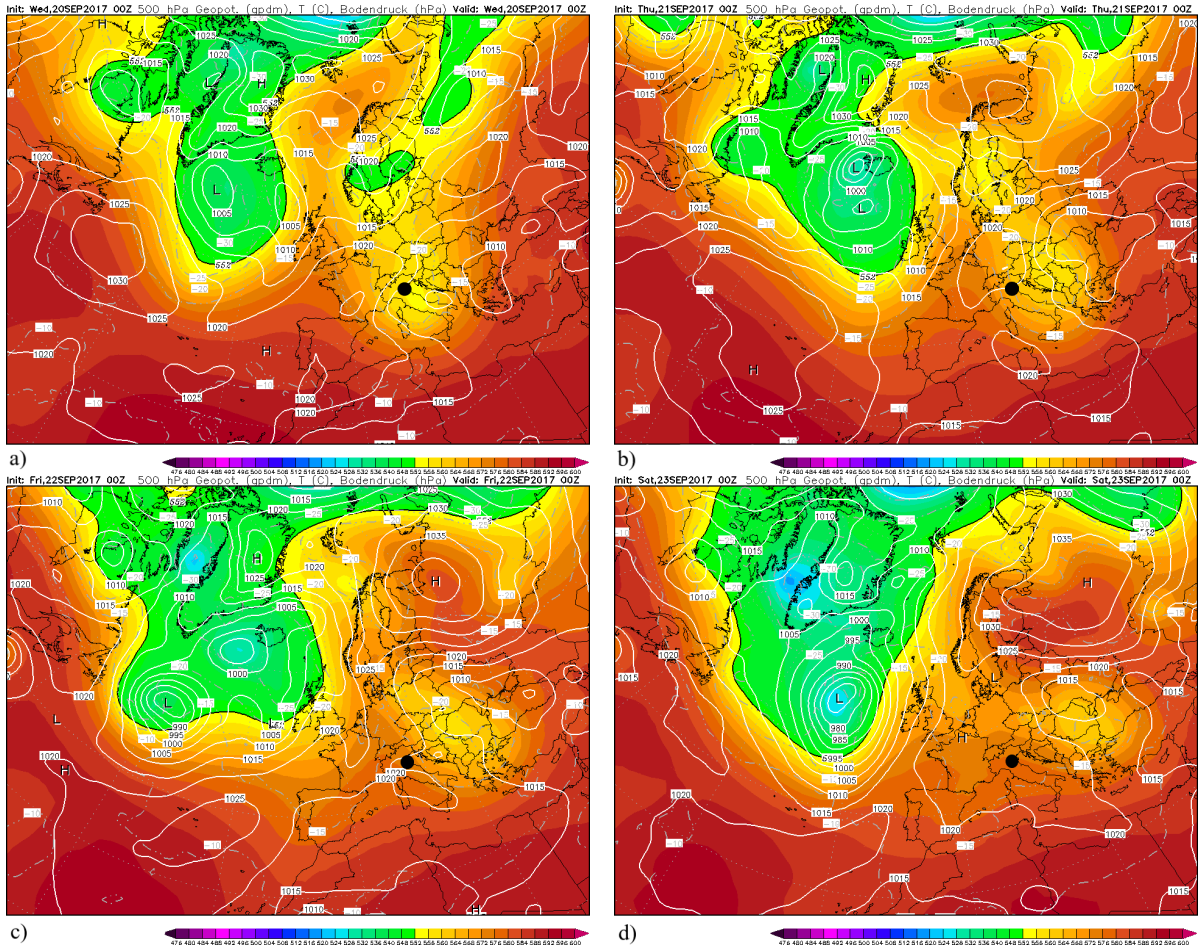


**Figure 4.2:** GFS analysis of the surface isobars (white lines) superimposed on the geopotential at 500 hPa (colormap). Each panel shows the midnight UTC of a single day within the summer period. Bologna is identified by the black dot.

and leads to the development of local circulations.

Local circulation flows are driven by small scale gradients and perturbed by the network of obstacles of an urban environment. The transport of momentum, heat and other scalars like mass and moisture, are regulated by local mean flow gradients and turbulent processes (Bitter and Hanna, 2003). Given that the aim of this work is to assess the behavior of turbulent exchange processes in street canyons and the role of vegetation on local circulations, it is fundamental to ensure that local circulation can establish and be perturbed as little as possible. Suitable periods have been selected, one from each campaign, when weak synoptic conditions are found. These periods are identified following an analysis of synoptic maps and soundings. The first gives an overview on the horizontal patterns, in order to avoid instabilities or frontal passages. The second retrieves the wind velocity along the atmospheric column and ensures no local instabilities are present.

A period of 4 consecutive days (20-23 September 2017) was selected during the summer campaign. During this period, a detected weak thermal stability is related to the passage of high pressure conditions on the Po Valley (Fig. 4.2). The intrusion of the high pressure, especially from September 21 (Fig. 4.2(b)), ensures a weak but permanent thermal stability in Southern Europe. Under this conditions, the wind speed is weak at least locally or in the atmospheric portion closer to the surface (Fig. 4.3). After September 21, the wind speed in the whole boundary

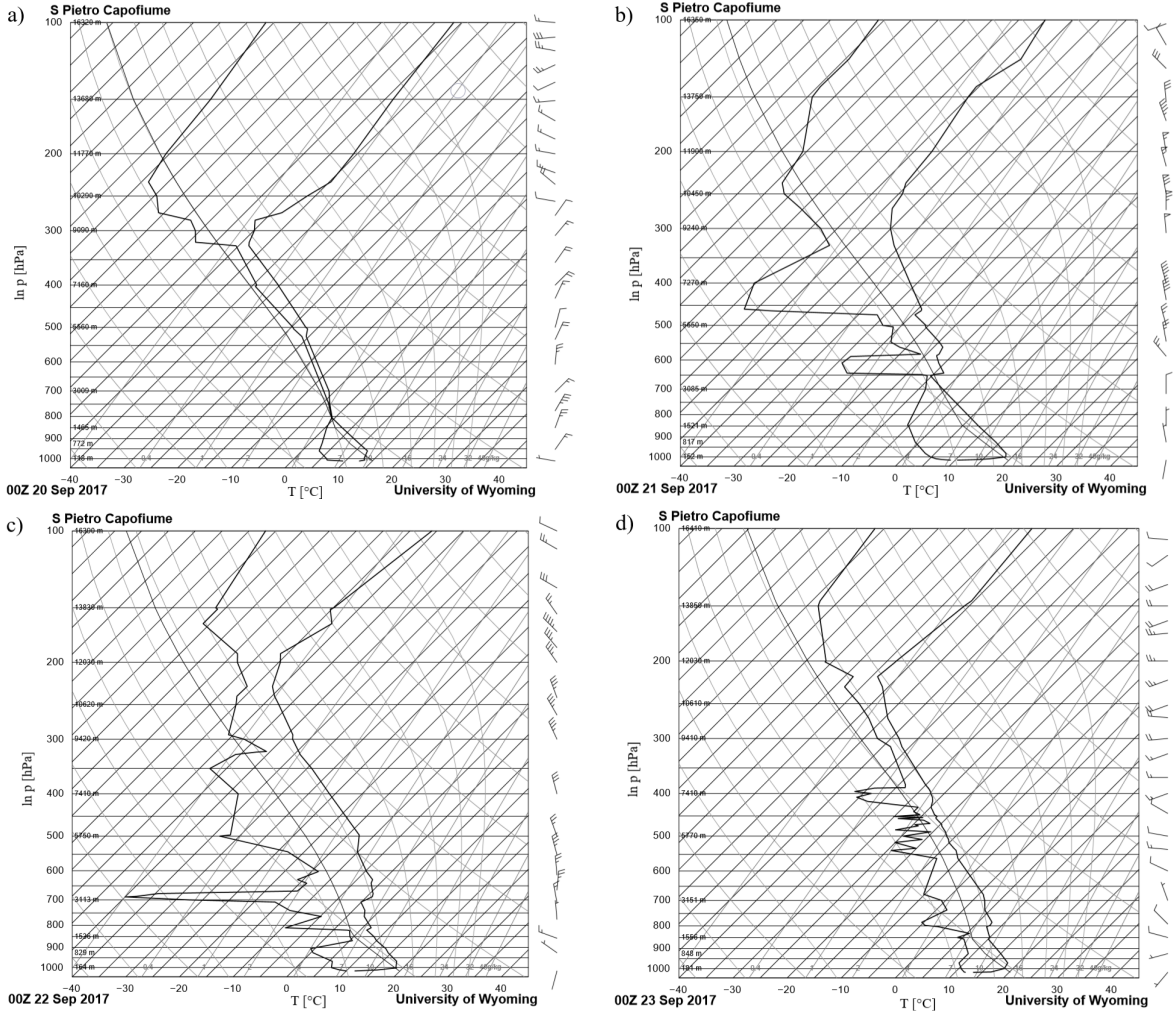


**Figure 4.3:** Wind velocity, air temperature and dew point temperature profiles retrieved from sounding data measured during (a) 20, (b) 21, (c) 22 and (d) 23 September from San Pietro in Capofiume, a small village 30 km to the north-east of Bologna (Data source: University of Wyoming, <http://weather.uwyo.edu/upperair/sounding.html>).

layer (up to  $z=3000$  m) is weak. Thermal stability and clear sky conditions are also ensured by the small CAPEs (Convective Available Potential Energy) retrieved from the air temperature profiles. CAPE ranges between 0 and 5.1 evaluated during September 21 (Fig. 4.2(b)), meaning

## CHAPTER 4. DATA PROCESSING AND METHODOLOGY

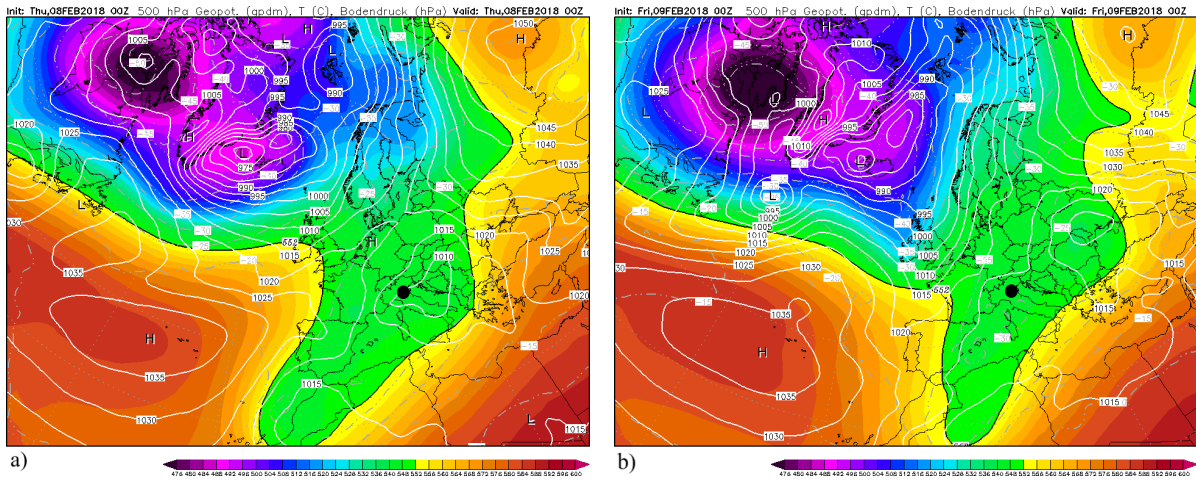


**Figure 4.4:** GFS analysis of the surface isobars (white lines) superimposed on the geopotential at 500 hPa (colormap). Each panel shows the midnight UTC of a single day within the winter period. Bologna is identified by the black dot.

almost no energy is available for convection in the atmosphere. To summarize, with neither convection activity nor large scale instabilities, the local circulation can establish and develop during the selected period (20-23 September 2017), as it will be described in Sect. 5.

During winter, thermally stable conditions are difficult to found for more consecutive days. Moreover, the 2018 winter season in northern Italy has been largely perturbed, with consec-

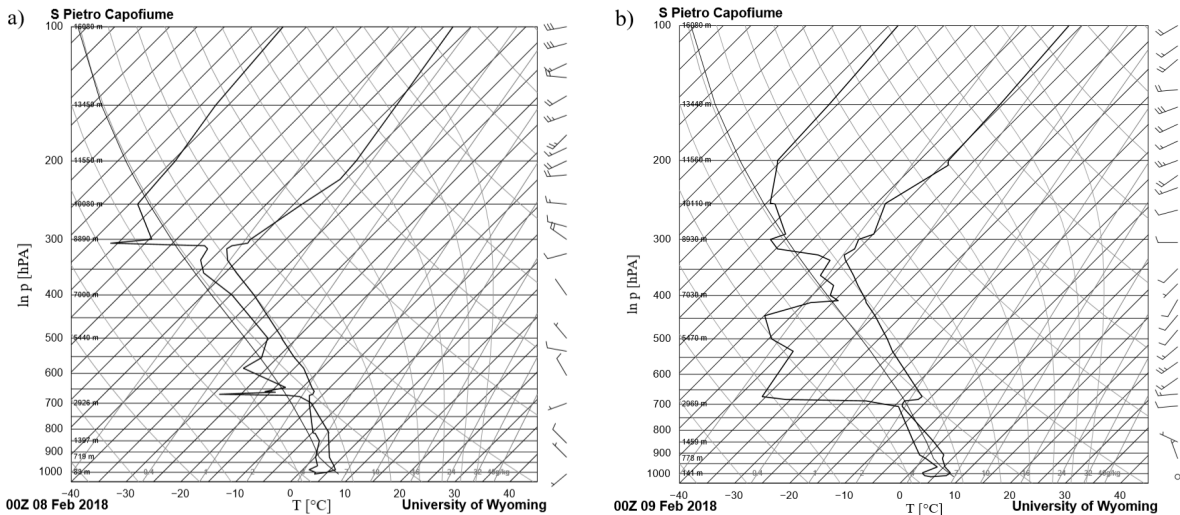


**Figure 4.5:** Wind velocity, air temperature and dew point temperature profiles retrieved from sounding data measured during (a) 08 and (b) 09 February from San Pietro in Capofiume, a small village 30 km to the north-east of Bologna (Data source: University of Wyoming, <http://weather.uwyo.edu/upperair/sounding.html>).

utive periods of heavy rains and snows. Within the campaign only few consecutive days were found to be in clear sky conditions and slightly stable stability. Among them, days 08 and 09 of February were constantly stable (Fig. 4.4). Both days were under a very weak surface low pressure coupled to a geopotential branch extending from the polar vortex. This geopotential branch is also wide enough to involve the whole Europe and perdure almost unperturbed for both days. These synoptic conditions are not ideal but sufficient to weaken the wind velocity along the profile (Fig. 4.5) up to 9000 m. Local circulations can develop among an atmospheric depth much larger than the whole boundary layer depth. Moreover, the different wind directions of the weak velocity depth from the atmosphere above ensures a strong decoupling of the local and SL from the large scale flow. Thermal stability and clear sky conditions are again ensured by the small CAPEs retrieved from the air temperature profiles. CAPE ranges between 0 and 18.2 evaluated during the 09 February (Fig. 4.2(b)), meaning almost no energy is available for convection in the atmosphere. To summarize also during winter period, the local circulation can establish and develop among the chosen period (08-09 February 2018), as it will be described in Sect. 5, since neither convection activity nor large scale instabilities are detected.

#### 4.2.2 Exchange processes: time scales and rates

In Sect. 2.3, the widely used time scales associated with the exchange processes in street canyon have been presented. As it was described, these time scales always directly involve the pollutant concentrations or the emission rate from the pollutant source, and can be independent on the flow circulation developing in the canopies. However one goal of this thesis is to evaluate new time scales which can be a characteristic of the exchange processes between the UCL and the atmosphere above it. As a consequence, our new time scales are chosen to be characterized by the flow and turbulent fields and to be independent on the pollutant concentrations or emission sources, in opposition to the literature described in Sect. 2.3. With this choice, these time scales and the subsequent diagnostic quantities derived from them will be used to assess the pollutant concentration removal only associated to the atmospheric exchange processes, without falling into self-correlation problems. To fulfill this aim, it is fundamental to characterize both flow and turbulent fields in connection with the urban morphology of the investigated area.

Following the classification proposed by Oke (1987), flows in street canyons of typical European cities belong to the skimming flow regime (Ratti et al. 2002; Di Sabatino et al. 2010), where turbulence dominates local exchange processes (Oke 1988; Louka et al. 2000). As already reviewed in Sect. 2.3, turbulent kinematic fluxes regulate the transfer of momentum, heat and other scalars within and above the street canyon. During periods of weak synoptic forcing, turbulent fluxes become the main driver of the atmospheric circulation and recirculation flows inside the canyon (Britter and Hanna, 2003). Given that one element of the work is to derive new original diagnostic time scales for real urban flows in a street canyon, it worths to assess

## CHAPTER 4. DATA PROCESSING AND METHODOLOGY

the circulation within it. As an example, Fig. 4.6 displays the wind velocity streamlines on a 2D cross-section of the MA. It was evaluated from a CFD simulation in the analyzed street canyon obtained using input and boundary conditions extracted from measured data and considering background winds perpendicular (Fig. 4.6a) and parallel (Fig. 4.6b) to the canyon orientation. As sketched on Fig. 4.6, the background flow passing above the city is characterized by a wind speed  $U_b$  and an air potential temperature  $\theta_b$ . The vertical TKMFes are the key parameters regulating the local turbulent exchanges between the mean flow and the in-canyon structures (Klein and Galvez, 2015). As sketched in Fig. 4.6, the vertical TKMF at the RL ( $\overline{w'u'}|_H$ ) drives fresh air in the canyon through the ShL while the inside canyon one ( $\overline{w'u'}|_S$ ) creates mixing and swirling motions. Theoretically, horizontal TKMFes have also to be considered as a mean for vector or scalar transport within the canyon (Klein and Galvez, 2015), but they are not calculated since the focus of this study is only directed to the vertical removal capacity. When the mean flow above the canyon is weak, thermal aspects are also important. In this case,

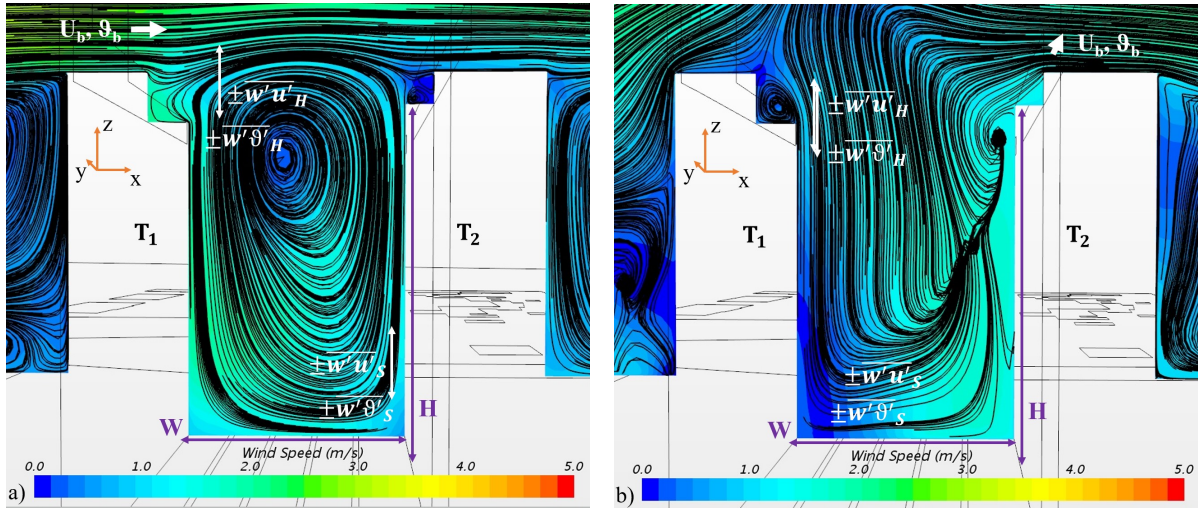


**Figure 4.6:** Wind velocity streamlines retrieved from CFD simulations of MA, in condition of background wind direction perpendicular (a) and parallel (b) to the canyon orientation.  $H$  and  $W$  are the mean building height and width of the canyon,  $T_1$  and  $T_2$  the building facade temperatures,  $U_b$  and  $\theta_b$  the background wind speed and air potential temperature,  $\overline{w'u'}$  and  $\overline{w'\theta'}$  the TKMF and TKSHEF respectively evaluated inside the canyon (GL and ML, subscript S) and at the RL (subscript H).

the differential heating of the opposite building facades ( $T_1 \neq T_2$ ) induces a swirly circulation (Dallman et al., 2014). The differential heating also affects the turbulent heat transport, mixing and thermal stratification within and above the canyon (Nazarian et al., 2017), leading to a modification of the exchange processes efficacy on pollutant removal (Nazarian et al., 2018). As already assessed in Sect. 2.3, it is therefore fundamental to consider both effects not to misjudge flow and turbulence behaviors and effectiveness for exchange processes (Cheng et al., 2009b).

The momentum and heat cascades from the mean flow to turbulence dictate the time scales of exchange processes, which in turn are constrained by the canyon geometry. These time scales are new local factors dependent on both local (canopy scale) and non local (city scale) quantities. The new four different time scales can be evaluated, distinguishing inertial and thermal processes, rooftop and in-canyon locations. Time scales are defined as the time required for momentum and heat to be vertically exchanged between two atmospheric layers. At the RL, they describe the time taken by the external flow to infiltrate the canyon through momentum transport and heat loss. Inside the canyon, time scales assess the mixing efficacy of fresh air with stagnant air and the upward particle removal time from the street.

These new time scales are derived using the Buckingham Theorem (BT), a key property of the similarity theory (Durst, 2008)<sup>1</sup>. The BT states that if a certain number of variables can be related in a physically meaningful equation, then a set of parameters can be constructed from the original variables. The theorem provides a method for computing sets of parameters from the given variables, even if the form of the equation is still unknown. These variables can then be combined with the appropriate powers given through the theorem application to retrieve the final equation. Following the previous considerations on the mean flow and turbulence importance for the in-canyon circulation, the momentum and heat time scales at the RL

$$\tau_d^H = f(\overline{w'u'}|_H, H, W, L, \frac{\Delta U_b}{\Delta z}) \quad (4.1a)$$

$$\tau_h^H = f(\overline{w'\theta'}|_H, H, W, L, \frac{\Delta \theta_b}{\Delta z}) \quad (4.1b)$$

are considered to be functions respectively of the TKMF  $\overline{w'u'}|_H$  ( $\text{m}^2\text{s}^{-2}$ ), the TKSHF  $\overline{w'\theta'}|_H$  ( $\text{mKs}^{-1}$ ) taken at the RL, the thermal stratification (represented by the vertical gradient of the mean speed  $\Delta U_b/\Delta z$  ( $\text{s}^{-1}$ ) and potential temperature  $\Delta \theta_b/\Delta z$  ( $\text{Ks}^{-1}$ )) of the background flow impinging on the canyon and the geometric parameters  $H$  (m) the mean buildings height,  $W$  (m) the mean street width, and  $L$  (m) the street length. Making use of the BT on both Eq. (4.1a) and (4.1b), following the example given in Appendix B, the time scales become:

$$\tau_d^H = \frac{H^3}{\overline{w'u'}|_H W} \frac{\Delta U_b}{\Delta z} \quad (4.2a)$$

$$\tau_h^H = \frac{H^3}{\overline{w'\theta'}|_H W} \frac{\Delta \theta_b}{\Delta z}. \quad (4.2b)$$

Equations (4.2a) and (4.2b) represent only one of the possible solutions of the BT due to the presence of arbitrary coefficients, as described in Appendix A. Time scales increase as the canyon

---

<sup>1</sup>An example application of the BT is presented in Appendix B.

height increases, as well as the thermal stratification increases, with the latter inhibiting mixing. Conversely, time scales decrease as canyon width increases, as well as the fluxes intensities increase. The equations Eq. (4.2a) and (4.2b) do not depend on  $L$  since time scales are based only on vertical transport or vertical flow variation. These quantities are confined on the bi-dimensional plane defined by the vertical and cross-canyon directions and delimited by the geometric parameter  $H$  and  $W$  of the canyon. Therefore, they are not supposed to be an extensive variable of canyon length.

Time scales inside the canyon describe the required time for exchange processes to mix fresh air coming from the rooftop interface with the stagnant air of the canopy. Time scales inside the canyon are functions of the merging flow from the ShL into the inner circulation, and present the following dependencies:

$$\tau_d^S = f(\overline{w'u'}|_S, W, L, H, u_*^H) \quad (4.3a)$$

$$\tau_h^S = f(\overline{w'\theta'}|_S, W, L, H, u_*^H, \theta_*^H), \quad (4.3b)$$

where the fluxes are computed inside the canyon (GL and ML, subscript S),  $W$ ,  $L$  and  $H$  are the geometric parameters, while the friction velocity  $u_*^H = (\overline{w'u'}|_H^2 + \overline{w'v'}|_H^2)^{1/4}$  ( $\text{ms}^{-1}$ ) and temperature  $\theta_*^H = \frac{\overline{w'\theta'}|_H}{u_*^H}$  (K) are constant values computed at the RL for each wind direction configuration. As for the rooftop ones, these time scales depend on the momentum and heat transport provided by the in-canyon momentum  $\overline{w'u'}|_S$  ( $\text{m}^2\text{s}^{-2}$ ) and heat  $\overline{w'\theta'}|_S$  ( $\text{mKs}^{-1}$ ) fluxes, which dictate the mixing time of the canopy, and are constrained by the canyon geometry. The fresh air is driven in the canopy by the momentum and heat transfers sustaining the circulation within the canyon and modulated by the shear layer intensity, the latter parametrised by the friction velocity  $u_*^H$  ( $\text{ms}^{-1}$ ) and temperature  $\theta_*^H$  (K). Using again the BT, with the procedure in Appendix B, Eq. (4.3a) and (4.3b) become:

$$\tau_d^S = \frac{H^2 u_*^H}{\overline{w'u'}|_S W} \quad (4.4a)$$

$$\tau_h^S = \frac{H^2 \theta_*^H}{\overline{w'\theta'}|_S W}. \quad (4.4b)$$

Equations (4.4a) and (4.4b) describe the time associated to momentum and heat transport within the canyon. These time scales increase in stagnant conditions, that occur when air is trapped within the canyon, and decrease when mixing with fresh air entered from the RL is favored by the exchange processes. Time scales do not depend on  $L$ , neither it was for the time scales evaluated at the RL.  $\tau_h^S$  in Eq. (4.4b) does not depend on  $u_*^H$  either because friction velocity contribution is provided by  $\theta_*^H$ .

The ratios between the time scales evaluated inside and above the canyon provide the following relations:

$$\eta_d = \frac{\tau_d^S}{\tau_d^H} \quad (4.5a)$$

$$\eta_h = \frac{\tau_h^S}{\tau_h^H}. \quad (4.5b)$$

These ratios provide information about the rate of mixing of fresh and stagnant air within the canyon, by comparing turbulent exchange efficacy at different heights. As long as  $\tau^H > \tau^S$ , the air within the canyon is supposed to efficiently mix with fresh air from the rooftop. The air within the canyon is well mixed. Momentum and heat are efficiently transported toward higher levels and exchanged with the free atmosphere. When  $\tau^H < \tau^S$ , mixing inside the canyon is less efficient than the rooftop one. Turbulent structures in the canyon are not prone to transport momentum and heat, enhancing stagnant conditions. At the RL, a well mixed air mass is separated from the inner canyon, behaving as a cap for vertical exchanges. Air in the canyon stagnates trapped within the canopy. Since Eq. (4.5a) and (4.5b) provide information about the refreshing properties of the canyon, they will be referred to as transport or exchange rates. The aim of this study is to prove that these diagnostic quantities are useful to characterize the exchange processes and to interpret pollutant removal from real urban street canyons.

### 4.2.3 Pollutant concentration normalization

Pollutant concentrations in real environments are strongly affected by several aspects such as the canyon geometry, the wind velocity above the canopy, local flow structures and the source emission rates. Particularly, the source treatment can be challenging due to the different composition and time dependency of emission sources, and the presence of multiple sources especially during the winter period when domestic heating is a non negligible emission component. Unfortunately, the estimation of domestic heating emission is still a challenge as well as the availability of heat consumption databases from the public administrations. Therefore emissions are estimated considering vehicular traffic as the only source of pollutant concentrations inside the canyon. This approximation is good for the summer period, when the cooling systems are a small emissions source compared to traffic, but it is a bad approximation during winter. To minimize the heating system contribution to the overall emission, we select the carbon monoxide  $CO$  as pollutant tracer for this investigation, since  $CO$  is considered a criteria to estimate pollutant emitted by internal combustion engines (Winkler et al., 2018).  $CO$  emissions from vehicular traffic is retrieved from the analysis of the fleet composition of the vehicles passed through the canyons during the analyzed periods. Traffic counts were obtained from counting

## CHAPTER 4. DATA PROCESSING AND METHODOLOGY

stations based on inductive loops technology located at the main traffic junctions within the city. The inductive loops compute the traffic rate as the number of vehicles passing through the streets every 5 minutes, the time resolution of the instrumentation. These traffic rates give a clear footprint on pollutant concentrations, as shown in Fig. 4.7 where the 5-minute averaged  $CO$  concentrations are shown along with the traffic rates through MA (Fig. 4.7(a)) and LB (Fig. 4.7(b)). MA shows low traffic rates during nighttime. During daytime, although vehicular traffic is constrained by the traffic restriction warrant, there is constant bustle of buses affecting emissions. As a consequence, traffic rates are only slowly decreasing after the morning rush hour until the nighttime cutoff. No evening rush hour has been measured. Traffic counts are sensibly lower in LB due to the location of the street in a residential area of the city. Despite it, traffic remains sustained during daytime, showing good footprints of both morning and evening rush hours especially during the first two days.  $CO$  concentrations follow a tendency which is similar to the traffic rates in both streets. Concentrations displaying a bimodal behavior are evident especially in LB, where a two rush hours are indeed detected. In MA,  $CO$  concentrations generally reach the daily maxima at the sunset despite a true rush hour is not detected. Motivation can be multiple. The increase of  $CO$  emissions for example can be involved by a variation in the traffic composition, with more polluting vehicles. Sunset periods are also associated with weak wind speed due to the inversion of the local circulation. As a consequence, ventilation within the canopy can reduce its intensity, letting the pollutants stagnate and the concentrations increase. In analogy to the summer period, traffic counts and  $CO$  concentrations in each street canyon are compared during the selected days of the winter campaign. The overall behavior of both

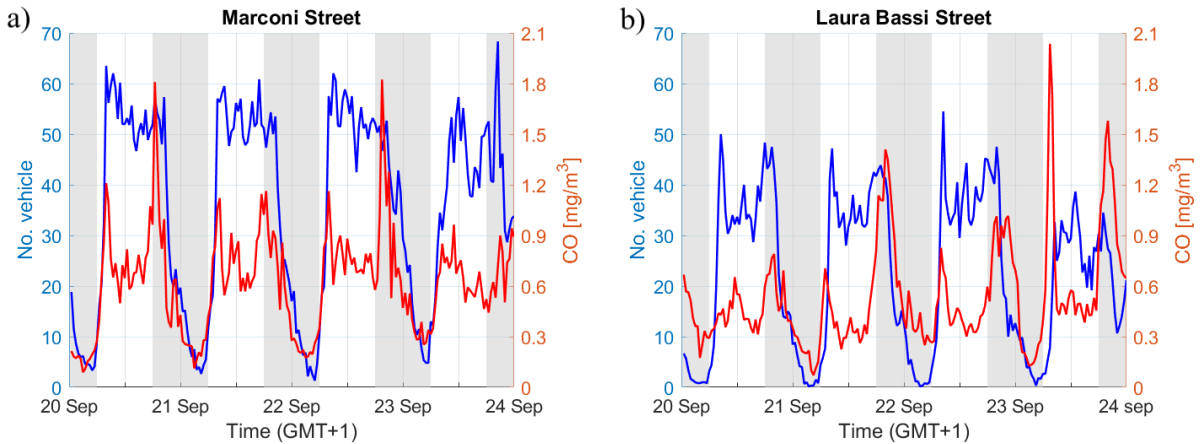


**Figure 4.7:** Comparison between  $CO$  concentrations (red line) measured in (a) MA and (b) LB and the respective traffic rates (blue line) expressed as the number of cars passing through the street during the summer period. Data are averaged over a 30 minutes window. The shadowed areas highlight nighttime periods. On average sun rises at 6:00 AM and sets at 18:00 PM (GMT+1).

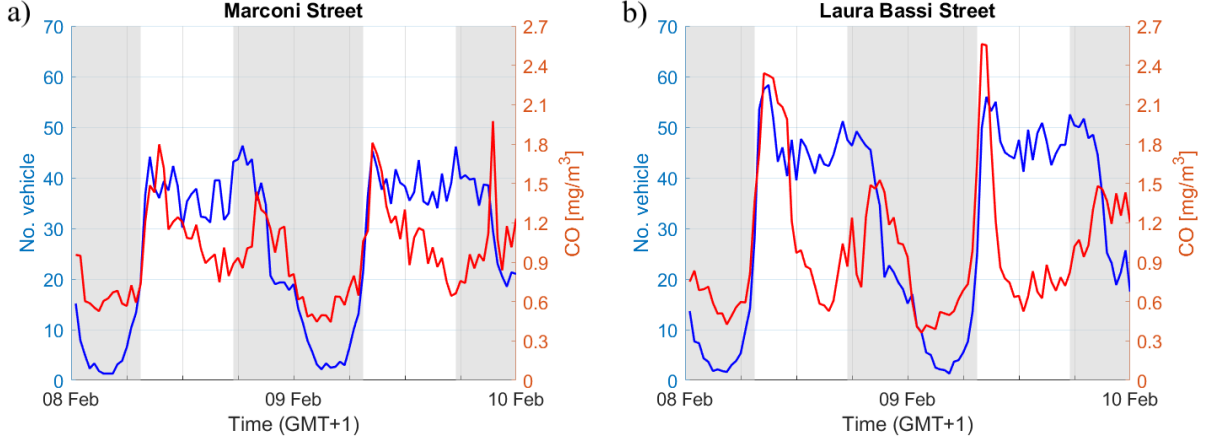


**Figure 4.8:** Comparison between  $CO$  concentrations (red line) measured in (a) MA and (b) LB and the respective traffic rates (blue line) expressed as the number of cars passing through the street during the winter period. Data are averaged over a 30 minutes window. The shadowed areas highlight nighttime periods. On average sun rises at 7:30 AM and sets at 17:30 PM (GMT+1).

quantities is similar to what already found during the summer period, but some differences are easy to detect. Traffic rates during the supposed rush hours show a more similar day-to-day behavior, even in LB.  $CO$  concentrations are maxima in the early morning, and as for the traffic rates, and are somehow larger in LB than MA. This last behavior is quite unexpected but it must be tackled in view to correctly estimate the impact of local atmospheric processes on pollutant concentrations. It is therefore fundamental to normalize the measured  $CO$  concentrations, to remove the local emission rate variability, geometrical effects and mean flow dependency, similarly to Kubilay et al. (2017). Measurements are therefore normalized with a reference concentration  $CO_0$  defined as:

$$CO_0 = \frac{Q_e}{HWU_H}, \quad (4.6)$$

where  $Q_e$  ( $\text{g s}^{-1}$ ) is the pollutant source rate,  $U_H$  ( $\text{ms}^{-1}$ ) is the wind speed measured at the canyon top,  $H$  (m) is the mean building height and  $W$  (m) is the mean street width. While  $U_H$ ,  $H$  and  $W$  are directly computed or extrapolated from data, an algorithm has been developed to estimate the source rate  $Q_e$ . First, the traffic counts are classified by vehicle type (motorcycle, light vehicles, heavy vehicles, buses), fuel type (gasoline, diesel, liquefied petroleum gas, compressed natural gas) and EURO technology classes. The number of buses passing through MA and LB is directly retrieved from the bus schedule of Bologna<sup>2</sup>. The local fleet composition is

<sup>2</sup>Available on the web site of the regional transport company at <https://www.tper.it/>

extracted from the regional inventory of circulating vehicles<sup>3</sup> and used to divide the remaining vehicular traffic following the vehicular type classification. Pollutant emission rates ( $\text{g km}^{-1}$ ) per class (vehicle, fuel and EURO technology) are estimated from the European Monitoring and Evaluation Program of the European Environment Agency (EMEP/EEA) air pollutant emission inventory for each vehicle category (Ntziachristos et al., 2009). Pollutant emission rates are finally converted in pollutant source rates  $Q_e$  ( $\text{g s}^{-1}$ ) applying a representative vehicle mean urban speed of  $19 \text{ km h}^{-1}$  (Ntziachristos et al., 2009) as a conversion factor. The normalized  $CO$  concentrations, named  $CO^+$ , are simply retrieved from the ratio between the measured concentrations  $CO$  in each street canyon and the reference concentration  $CO_0$  from Eq. (4.6).

### 4.3 Numerical simulations

The numerical evaluation part of this work is tackled using Quick Urban & Industrial Complex (QUIC) dispersion modeling system. QUIC is a fast-response model that runs on a laptop, combining a mass-conserved wind solver (QUIC-URB) with a Lagrangian random-walk dispersion model (QUIC-PLUME). The QUIC system was primarily developed to rapidly tackle impulsive problems such as accidental releases of substances within the urban environment. Its primary scope was to obtain a reliable but approximated result of an atmospheric dynamics problem in the smallest time possible, in order to be used as an operative nowcasting model to tackle emergency situations. Since the model first application, it has been improved to update and improve the approximations used to solve the complex interaction between the atmospheric flows and the terrain obstacles, without increasing the computational costs. Today it is used to rapidly diagnose flow and turbulence characteristics in complex urban and vegetated environments.

In the context of this thesis work, QUIC is preferred among the most widely adopted and computationally costly CFD models because it combines high computation performances to the evaluation of approximated but consistent results. The small computational costs enable to perform a wide ensemble of simulations for every given case study in few hours, allowing to capture all the different shades of the problem. This last consideration is extremely valuable in real environments, where homogeneous and stationary conditions are rarely achieved and sustained for long periods.

#### 4.3.1 QUIC-URB model description

QUIC-URB is a 3D wind solver that uses a mass consistent wind model to resolve the wind field around obstacles for a representative time interval (Singh et al., 2008). Mass consistency method forces the initial wind velocity field  $\mathbf{u}_0 = (u_0 \hat{i} + v_0 \hat{j} + w_0 \hat{k})$  generated from the input

---

<sup>3</sup>Available as an open data on the Italian Car Club (ACI) web site (<http://www.aci.it/laci/studi-e-ricerche/dati-e-statistiche/open-data.html>)

conditions and the non divergent final velocity field  $\mathbf{u}_f = (u_f \hat{i} + v_f \hat{j} + w_f \hat{k})$  to minimize their differences. The theoretical formalism of this method was developed by Sasaki (1958, 1970a,b), and proceeds as follows. From the input parameters, an initial wind velocity field  $\mathbf{u}_0$  is generated at each grid point of the model, using a set of empirical parametrizations to account for the flow physics around and within the various obstacles. From this initial velocity field the final velocity field  $\mathbf{u}_f$ , result of the solver, is obtained applying the constrain given in Eq. (4.7).

$$E(u_f, v_f, w_f, \lambda_m) = \int_{V_c} \left[ \alpha_1^2 (u_f - u_0)^2 + \alpha_1^2 (v_f - v_0)^2 + \alpha_2^2 (w_f - w_0)^2 + \lambda_m \left( \frac{\partial u_f}{\partial x} + \frac{\partial v_f}{\partial y} + \frac{\partial w_f}{\partial z} \right) \right] dx dy dz, \quad (4.7)$$

where  $\lambda_m$  ( $s^{-1}$ ) are Lagrange multipliers,  $V_c$  ( $m^3$ ) is the cell grid volume and  $\alpha_i^2$  ( $s^2 m^{-2}$ ) are weighting factors (Gaussian precision moduli). As previously introduced, Eq. (4.7) forces to minimize the variance of the difference between the initial and the final velocity fields. The associated Euler-Lagrange equations whose solution minimizes Eq. (4.7) are

$$u_f = u_0 + \alpha_1^{-2} \frac{\partial \lambda_m}{\partial x} \quad (4.8a)$$

$$v_f = v_0 + \alpha_1^{-2} \frac{\partial \lambda_m}{\partial y} \quad (4.8b)$$

$$w_f = w_0 + \alpha_2^{-2} \frac{\partial \lambda_m}{\partial z}. \quad (4.8c)$$

The boundary conditions applied to these equations impose the derivative of  $\lambda_m$  in the normal direction to be null at the solid boundaries ( $\partial \lambda_m / \partial n = 0$ ) and  $\lambda_m = 0$  at the inflow/outflow boundaries. These different choices at different boundaries are motivated by the mass transport associated with the velocity crossing a boundary. A non null adjustment of the velocity component normal to the boundary implies a mass amount has crossed the boundary. This condition is inconvenient if the boundary is solid and therefore  $\partial \lambda_m / \partial n = 0$  is the better choice. Conversely, at non solid interfaces, mass exchange can develop and, as a consequence,  $\lambda_m = 0$  is used when dealing with inflow/outflow (or flow-through) boundaries.

A Poisson equation can be found after differentiating and combining Eq. (4.8a), (4.8b) and (4.8c) into the continuity equation  $\nabla \cdot \mathbf{u} = 0$  (Sherman, 1978) to force the mass conservation in the final velocity field:

$$\frac{\partial^2 \lambda_m}{\partial x^2} + \frac{\partial^2 \lambda_m}{\partial y^2} + \left( \frac{\alpha_1}{\alpha_2} \right)^2 \frac{\partial^2 \lambda_m}{\partial z^2} = -2\alpha_1^2 \left( \frac{\partial u_0}{\partial x} + \frac{\partial v_0}{\partial y} + \frac{\partial w_0}{\partial z} \right). \quad (4.9)$$

Eq. (4.9) is solved in QUIC-URB through an iterative successive over-relaxation solver on a non-uniform staggered grid where velocities are face centered values and Lagrange multipliers are called center quantities (Singh et al., 2008).

Input values and parameters are set through an intuitive interface. Wind velocity and direction can be set through a single profile coming from an external source, multiple profiles coming from multiple sources or from the output of a mesoscale model such as the Weather Research and Forecasting (WRF) model. In the current investigation, the single profile is the only input choice adopted, so it will be illustrated alone. Three different wind profiles can be chosen, along with an user profile built point-by-point. The selected option was a simple logarithmic profile following the wall law, but other options could have been a power law profile or a urban canopy one. An insight on the input conditions will be given in Sect. 4.3.4.

To complete the current presentation of the model, the parametrizations used to simulate the

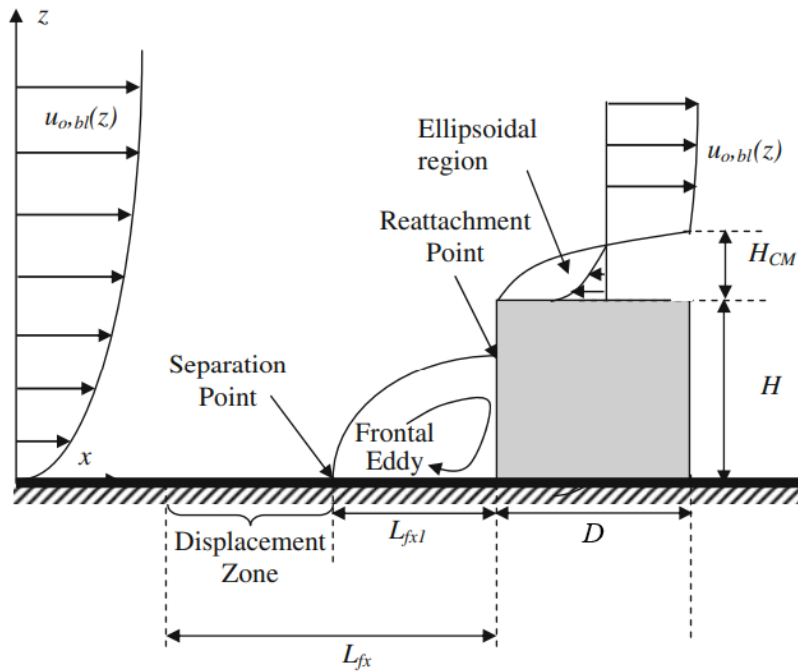


**Figure 4.9:** 2D simplified schematic of the interaction of an incident boundary layer flow with the front face of a rectangular obstacle and the initial wind field for the rooftop recirculation scheme. In the upwind region, the boundary layer first adjusts to the adverse pressure gradient associated with the obstacle in the displacement zone where wind speeds are retarded. This zone is followed by flow separation and the formation of a frontal eddy. In the rooftop region, the model produces a monotonically decreasing profile with high velocities (opposite in direction to the incident boundary layer) near the roof and zero velocity at the core of the recirculation region. Above the vortex core, the velocities are specified to be the same as the upstream incident boundary layer. (Source: Gowardhan et al. (2010))

initial wind velocity field are briefly described in the following paragraphs.

### Upwind cavity algorithm

The upwind cavity volume is the region of the model domain located upwind to a single building where the upstream flow adjusts to the pressure gradient induced by the building. The cavity is an ellipsoid quarter with  $L_{fx}$  (m) (cavity length) and  $H$  (m) (building height) respectively half the major and minor axes. The cavity length is evaluated as

$$L_{fx} = \frac{1.5D/H}{1 + 0.8D/H},$$

where  $D$  is the building width and the constant values are retrieved from wind tunnel investigations. The cavity is in turn divided into a displacement zone and a vortex region with separate parametrizations for the velocity within separate ellipsoidal cavities (Gowardhan et al., 2010). The vortex region has a domain volume of length  $L_{fx1}$  (m) where the interaction between the upstream flow and the building generates a frontal eddy (Fig. 4.9) and the wind speed reverses its direction. Similarly to the cavity region, the length scale of the vortex region is defined as

$$L_{fx1} = \frac{0.6D/H}{1 + 0.8D/H}.$$

The streamwise  $u_0$  ( $\text{ms}^{-1}$ ) and vertical  $w_0$  ( $\text{ms}^{-1}$ ) velocity components, normalized with the streamwise velocity component at the building height  $u_0(H)$  ( $\text{ms}^{-1}$ ), are

$$\begin{aligned} \frac{u_0}{u_0(H)} &= \left( -0.6 \cos \left( \frac{\pi z_f}{0.5H} + 0.05 \right) \right) \left( -0.6 \sin \left( \frac{\pi x_f}{L_{fx1}} \right) \right) \\ \frac{w_0}{u_0(H)} &= \left( -0.1 \cos \left( \frac{\pi x_f}{L_{fx1}} + 0.05 \right) \right), \end{aligned}$$

where  $x_f$  (m) and  $z_f$  (m) are respectively the streamwise distance from the building edge and the vertical distance from the building base. The displacement zone length is defined as  $L_{fx} - L_{fx1}$  (m) and accounts for the flow responding to the approaching building a recirculation zone. Within this volume, the flow velocity components follow the unperturbed upwind ones but reduced by a factor 0.4 to better match the experimental data (Gowardhan et al., 2010).

### Rooftop recirculation algorithm

The recirculation region is an ellipsoidal volume above the building rooftop where the flow can produce small vortices as the wind interacts with the obstacle roughness. This region extends by a length  $L_{CM} = 0.9R$  (m) in the streamwise direction and  $H_{CM} = 0.22R$  (m) in the vertical from the rooftop, where  $R = B_S^{2/3} B_L^{1/3}$  (m) is a length scale depending on the shorter  $B_S$  (m)

and longer  $B_L$  (m) building height or width dimensions. If  $L_{CM} \geq D$  the recirculation region extends to the whole rooftop, otherwise it reattaches (Fig. 4.9). An initial velocity profile is imposed in the recirculation region, so that

$$u_0(z) = -u_{0,bl}(z) \left| \frac{H - z + H_{CM}}{H_{CM}} \right|,$$

where  $u_0$  ( $\text{ms}^{-1}$ ) and  $u_{0,bl}$  ( $\text{ms}^{-1}$ ) are respectively the streamwise velocity in the region and that of the upwind flow. This initial profile ensures the velocity to decrease from the rooftop to the end of the recirculation region balancing the upwind flow at the region edge (Fig. 4.9). The wind velocity in the region shows a decreasing profile and a reverse direction to the upwind flow. A slight modification of this simple algorithm ensures a good performance of the simulation also when the upwind flow is not orthogonal to the building. Above the rooftop either of a solid obstacle or a cavity, the wind velocity profile is defined by the displaced wall law

$$U_0(z) = \frac{u_*}{0.4} \left( \ln \frac{z - d}{z_0} + \psi \left( \frac{z}{L_O} \right) \right),$$

where  $u_*$  ( $\text{ms}^{-1}$ ) is the friction velocity,  $z_0$  (m) is the roughness length,  $d$  (m) is the displacement height and  $\psi$  is the stability function dependent on the Obukhov length  $L_O$  ( $\text{m}^{-1}$ ).

### Street canyon and wake algorithms

Street canyon and wake algorithms have been firstly developed by [Rockle \(1990\)](#) and modified by [Singh et al. \(2008\)](#). The use of the street canyon or the wake algorithm is discriminated by the [Oke \(1987\)](#) flow regime classification, simplified by [Rockle \(1990\)](#) to avoid the unstable wake interference regime. The street canyon algorithm therefore applies when a skimming flow regime is detected while the wake algorithm approximate the isolated building. The discriminant factor between the two regimes is given by

$$\frac{W^*}{H} = \frac{1.8 \frac{W}{H}}{\left( \frac{L}{H} \right)^{0.3} \left( 1 + 0.24 \frac{W}{H} \right)},$$

where  $W^*$  (m) is the length of recirculation cavity in the wake of an isolated building,  $W$ ,  $H$  and  $D$  are the mean street width, mean buildings height and mean building width respectively. If  $W < W^*$  the street canyon parametrization is implemented, otherwise the wake algorithm is used. The street canyon algorithm is based on three velocity parametrizations characterizing three different volumes of the whole street canyon. A central volume of the canopy, is laterally and vertically bounded by prismatic volumes identifying mixing or shear regions where the horizontal or vertical transports create turbulent diffusion. Considering an upwind flow perpendicular to the canyon, the central volume is characterized by a reverse flow extending from

the surface to the last cell below the rooftop height (Fig. 4.10). Initial streamwise and vertical normalized velocity components for this central volume of the canyon are given by

$$\frac{u_0(x, y, z)}{u_0(H)} = -0.3 \frac{x_{can}}{0.5W} \left( \frac{W - x_{can}}{0.5W} \right) \left[ 1 - \frac{|y_{can}|}{\delta_{SC}(x_{can})/2} \right]^p \quad (4.10a)$$

$$\frac{w_0(x, y, z)}{u_0(H)} = - \left| \frac{1}{2} \left( 1 - \frac{x_{can}}{0.5W} \right) \right| \left( 1 - \frac{W - x_{can}}{0.5W} \right), \quad (4.10b)$$

where  $x_{can}$  (m) is the distance from the backwall of the upwind building,  $y_{can}$  (m) is the cross canyon direction,  $\delta_{SC}(x_{can}) = W - 2\delta_{lw}(x_{can})$  and  $p$  is an empirical factor. When the upwind flow is non orthogonal, the flow is decomposed into normal and a parallel velocity components to the canyon orientation. The normal component within the canopy is then computed with Eq. (4.10a), while the parallel is left unchanged from the upwind flow, describing a channeling velocity behavior. The cross canyon term of Eq. (4.10a) accounts for the lateral diffusion that involves the lateral volume reducing the velocity in the cross direction. The flow in the lateral and



**Figure 4.10:** Schematic illustrating the flow regions and initial velocity fields associated with the street canyon parametrization in the vertical plane. (Source: [Gowardhan et al. \(2010\)](#))

top canyon volumes is modeled as a mixing or ShL, accounting for the linear growth of the layers with the downstream distance and having a velocity profile with a hyperbolic tangent shape ([Pope, 2000](#)). The vertical volume (Fig. 4.10) extends from the upstream to the downstream building and inside the canyon at a small angle from the upstream building and penetrate the canyon a  $\delta_{vw} |_{x_{can}=W} = 0.2W$  (m) ( $x_{can}$  (m) is the canyon normal direction). Within this region the initial velocity is defined as

$$\frac{u_0(x, y, z)}{U_H} = \frac{\tanh [(\delta_{vw}(x_{can}) - z_{can})/\delta_{vw}(x_{can})]}{\tanh(1.0)},$$

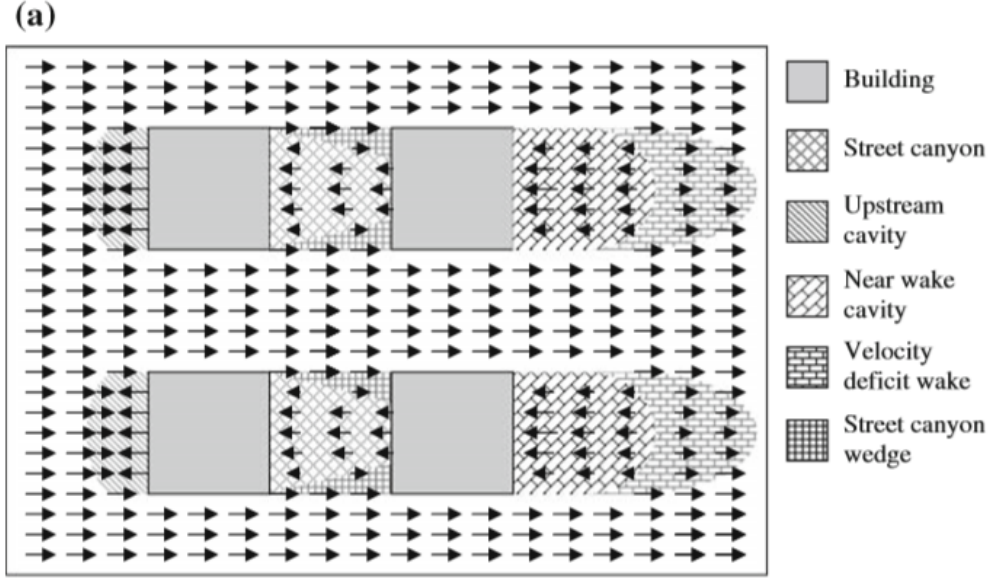


**Figure 4.11:** Schematic illustrating the flow regions and initial velocity fields associated with the street canyon parametrization in the horizontal plane. (Source: [Gowardhan et al. \(2010\)](#))

where  $U_H$  ( $\text{ms}^{-1}$ ) is the reference velocity in the streamwise direction at the rooftop obtained from a displaced logarithmic profile,  $z_{can}$  (m) is the vertical canyon direction and  $\delta_{vw}|_{x_{can}} = 0.2x_{can}$  (m) is the linear approximation of the volume penetration depth. The lateral volume (Fig. 4.11) has the same shape of the vertical with maximum horizontal penetration width  $\delta_{lw}|_{x_{can}=W} = 0.2W$  (m). Within this region the initial velocity is defined as

$$\frac{u_0(x, y, z)}{u_{0,bl}(z)} = 0.3 \frac{\tanh[Y_{lw}/\delta_{lw}(x_{can})]}{\tanh(1.0)},$$

where  $u_{0,bl}(z)$  ( $\text{ms}^{-1}$ ) is the upwind velocity profile,  $\delta_{lw}|_{x_{can}} = 0.2x_{can}$  (m) is the width of the lateral volume and  $Y_{lw} = |y_{can}| - \delta_{SC}(x_{can})/2$  (m) is the isoline delimiting the street canyon volume penetration into lateral volume.

Downwind to the street canyon or an isolated building a wake region develops as a turbulent layer ([Kaplan and Dinar, 1996](#)). The wake region develops as the upwind cavity region, with a near and a far volume based on the same principle but defined with a single velocity profile. The near volume has a streamwise dimension

$$L_w = W^* \sqrt{\left(1 - \left(\frac{z_{can}}{H}\right)^2\right) \left(1 - \left(\frac{y_{can}}{W}\right)^2\right) - 0.5D}$$

where the wind flow direction is reversed with respect to the upwind flow. The wake region streamwise length is defined as  $3W^*$  and within this region the velocity is deflected with respect

to the upwind flow and defined as

$$u_0(z) = u_{0,bl}(z) \left( 1 - \left( \frac{L_w}{x_{can}} \right)^{1.5} \right).$$

Vertical and horizontal views of the wake, the street canyon, the upstream cavity, the near wake cavity, the velocity deficit wave, the street canyon wedge and the rooftop recirculation regions, along with the initial velocity field within them, are shown in Fig. 4.10 and 4.11 respectively.

### Sidewall recirculation algorithm

Sidewall recirculation vortices develop on the side of the buildings due to the flow separation at the boundary. This region is found to be originated by the pressure and friction generated by the building on the flow field and it has been observed by means of laboratory and numerical simulations (Hayati et al., 2017). Nevertheless, its dynamics is generally difficult to capture, as more commonly used CFD models fail to predict it, so the sidewall recirculation algorithm option is not a default one in QUIC-URB. This recirculation region is present only when the flow has a minimum angle of  $\pm 10^\circ$  with respect to the building (Hayati et al., 2017). The volume involved in the recirculation region accounts for multiple interaction of other sidewall regions generated by near buildings. The region has an elliptical shape defined by a downwind length  $L_c = 0.9R$  and width  $W_c = 0.22R$ . Within this volume the velocity is reversed with respect to the upwind flow direction and scales linearly from the reference wind speed near the wall to zero at the edge of the ellipse (Hayati et al., 2017).

### 4.3.2 QUIC-PLUME model description

QUIC-PLUME is a Lagrangian dispersion model where the fluid particles move following the instantaneous wind. It is a Langevin model, meaning the stochastic incremental changes in velocity are time integrated to obtain the flow trajectory. The flow particle trajectories are in turn perturbed by turbulence that adds a random contribution to the velocity components (Williams et al., 2004) as follows:

$$\begin{aligned} x_j &= x_{j-1} + \bar{u}\Delta t + \frac{u'_{j-1} + u'_j}{2} \Delta t \\ y_j &= y_{j-1} + \bar{v}\Delta t + \frac{v'_{j-1} + v'_j}{2} \Delta t \\ z_j &= z_{j-1} + \bar{w}\Delta t + \frac{w'_{j-1} + w'_j}{2} \Delta t. \end{aligned}$$

The particle positions at the current and at the previous time step  $\Delta t$  are respectively  $x_j$ ,  $y_j$ ,  $z_j$  and  $x_{j-1}$ ,  $y_{j-1}$ ,  $z_{j-1}$ .  $\bar{u}$ ,  $\bar{v}$  and  $\bar{w}$  are the mean wind velocity components,  $u'$ ,  $v'$  and  $w'$  the

## CHAPTER 4. DATA PROCESSING AND METHODOLOGY

---

velocity components fluctuation at the current (subscript  $j$ ) and previous (subscript  $j - 1$ ) time step. The fluctuations are indeed calculated as differential increments  $du$ ,  $dv$  and  $dw$  of the previous step:

$$\begin{aligned}u'_j &= u'_{j-1} + du \\v'_j &= v'_{j-1} + dv \\w'_j &= w'_{j-1} + dw.\end{aligned}$$

The differential increments depend on several turbulent related quantities all scaling on the friction velocity  $u_*$  ( $\text{ms}^{-1}$ ). These quantities are the three velocity variances  $\sigma_u = 2u_*$ ,  $\sigma_v = 2u_*$  and  $\sigma_w = 1.3u_*$ , the dissipation rate  $\epsilon = u_*^3/(0.4(z + z_0))$  and the shear stress component  $\tau_{uw} = u_*^2(1 - z/z_m)^{3/2} \approx u_*^2$  ( $z_m$  (m) is the mixed layer depth). The initial fluctuation components are also defined from  $u_*$  as

$$\begin{aligned}u'_0 &= \sigma_u dW_1 \\v'_0 &= \sigma_v dW_2 \\w'_0 &= \sigma_w dW_3,\end{aligned}$$

where  $dW_i$  is an uncorrelated normally distributed variable with mean 0 and standard deviation 1. It is therefore evident the dependency on  $u_*$  of the turbulence behavior. The friction velocity is defined as the combination of local and non-local contributions as

$$u_* = u_*^{local} + \underbrace{u_*^{hor} + u_*^{vert}}_{non-local}$$

The local friction velocity scales directly with the vertical gradient of the final velocity field  $\partial u/\partial z$  ( $\text{s}^{-1}$ ) calculated with QUIC-URB:

$$u_*^{local} = 0.4(\Delta z + z_0) \frac{\partial u}{\partial z}$$

where  $\Delta z + z_0$  (m) is the vertical distance from the first solid boundary. Non-local mixing accounts for the mixing generated in building wake and cavity regions by the mean flow interacting with the obstacles (Williams et al., 2004). Extra mixing production, and subsequent turbulent transport, can be detected either from the side and the top of the obstacle. Therefore, two contributions are added to the total mixing to detect the horizontal mixing ( $u_*^{hor}$ ) produced by vertical axis eddies, and vertical mixing ( $u_*^{vert}$ ) produced by eddies that brought material down from higher winds above the cavity or wake.  $u_*^{hor}$  and  $u_*^{vert}$  are estimated from the time scale associated to the horizontal ( $T_H$ ) and vertical ( $T_V$ ) mass transport respectively in the wake and

cavity regions as

$$u_*^{hor} = C_H \frac{T_H}{\max(T_H) + \max(T_V)} \Delta u_r^{hor}$$

$$u_*^{vert} = C_V \frac{T_V}{\max(T_H) + \max(T_V)} \Delta u_r^{vert},$$

where  $C_{H,V}$  are proportionality constant,  $\Delta u_r^{hor}$  ( $\text{ms}^{-1}$ ) is the centerline velocity difference in the horizontal direction and  $\Delta u_r^{vert}$  ( $\text{ms}^{-1}$ ) is the reference velocity in the vertical direction. Outside the parametrized regions (wake, cavity and recirculation zones)  $u_*$  is calculated reversing the wall law velocity profile, using an iterative method which should ensure the friction velocity to be constant along the profile. The major limitations of this last technique are the a-priori assumption of the logarithmic shape of the mass conserved velocity profile and the divergence of the iteration method if  $u_*$  is not considered as constant. A simple correction was introduced in the code to avoid this inconvenience, as presented in the next paragraph.

### Modified friction velocity computation

The a-priori logarithmic assumption of the mass conserved velocity profile can be a too strong constraint in an urban environment. Despite this, having an iterative condition to evaluate if the profile is effectively logarithmic certifies the good choice of the assumption. Therefore the correction we apply will focus only on the non logarithmic cases, i.e. when the iterative method does not converge. In this scenario  $u_*$  is calculated as the local value, without any a-priori assumption:

$$u_* = 0.4(z_1 + z_0) \frac{\Delta u}{\Delta z} / \psi,$$

where  $z_1$  is the first grid point above a surface which is not involved in any of the previously described parametrizations. The strength of this computation is that you give a value to  $u_*$  associated to the mass conserved unperturbed flow, without addressing the shape of its profile. Tests performed on idealized and real domains of this corrected method are presented in Sect. 7.1.

### 4.3.3 Vegetation Parametrization

Vegetation mostly spread through the neighborhoods has been described in Sect. 3.1.2. Within the model, vegetation consists in a single type of trees pictured as cylinders of constant height  $H_v=15$  m and diameter  $d_v=5$  m, typical of the full grown trees during summertime. Within these volumes, the wind velocity profile is forced to follow Cionco (1965)

$$U(z) = U_{H_v} \exp \left[ a \left( \frac{z}{H_v} - 1 \right) \right], \quad (4.11)$$

## CHAPTER 4. DATA PROCESSING AND METHODOLOGY

---

where  $U_{H_v}$  ( $\text{ms}^{-1}$ ) is the velocity above the top of the cylinder and  $a$  is the attenuation coefficient. The attenuation coefficient is estimated from measurements, reversing the Eq. (4.11)

$$a = \frac{\ln(\bar{U}(z)/\bar{U}_H)}{z/H - 1}, \quad (4.12)$$

where  $\bar{U}(z)$  ( $\text{ms}^{-1}$ ) is the average wind speed within RL during the analyzed period and  $\bar{U}_H$  ( $\text{ms}^{-1}$ ) is the average wind speed at the RL of LB during the analyzed period. The retrieved attenuation coefficient takes the value  $a=(1.7\pm 0.3)$ . To check the reliability of the coefficient value,  $a$  is used to calculate the vegetative drag coefficient  $C_v$  of an isolated tree in the domain. The integral of the difference between the mass conserved velocity profiles in a bare domain and within a tree retrieved from the same input conditions, gives a good estimation of the total drag force  $F_{tot}$  generated by the tree on the wind. From basic laws of fluid mechanics, the drag force is proportional to the unperturbed wind velocity through a drag coefficient, which in this case is relative to the vegetation. From this law,  $C_v$  is retrieved as

$$C_v = \frac{2F_{tot}}{\rho A_f^v U_{tot}^2},$$

where  $\rho$  ( $\text{kgm}^{-3}$ ) is the air density,  $A_f^v$  ( $\text{m}^2$ ) is the frontal area of the tree and  $U_{tot}$  is the unperturbed wind velocity integrated along the profile. Using this method,  $C_v=(0.24\pm 0.4)$  in agreement with [Jeanjean et al. \(2017\)](#) and [Di Sabatino et al. \(2015\)](#), who found a value for  $C_v$  equal to 0.25 for the same tree species.  $C_v$  is then used to evaluate the vegetation porosity as

$$P = (1 - C_v/1.08)^{1/1.8},$$

as defined by [Guan et al. \(2003\)](#). Trees are found to be largely porous medium with  $P=(0.56\pm 0.05)$ . Both the porosity and the vegetation drag coefficient are used to calculate the total area fraction coefficients following [Kent et al. \(2017\)](#), as it will be shown in Sect. 4.3.4. Here we will only focus on the computation of the vegetation planar and frontal area  $A_p^v$  ( $\text{m}^2$ ) and  $A_f^v$  ( $\text{m}^2$ ).  $A_p^v$  is defined as the circumference (radius  $r=2.5$  m) area times the number  $n$  of trees in the domain, while  $A_f^v$  is taken as the maximum cylinder cross section

$$\begin{aligned} A_p^v &= \pi \cdot r^2 \cdot n \\ A_f^v &= H_v \cdot 2r \cdot n. \end{aligned}$$

Vegetation areas will be used in the following section to compute the total area fraction coefficients.

#### 4.3.4 Model setup

The street canyons described in Sect. 3.1.1 and Sect. 3.1.2 are the reference streets representing their respective neighborhoods. These neighborhoods are used as domain for the QUIC simulations, which are displayed in Fig. 4.12. The domains share the same size ( $x=1000$  m,  $y=1300$



Figure 4.12: (a) MA and (b) LB domains.

m and  $z=200$  m) and resolution ( $dx=2$  m,  $dy=2$  m and  $dz$  increases exponentially with  $z$  by a factor 0.15 from the surface value  $dz_0=1$  m), for a total domain size of  $32'500'000$  cells. Despite the large number of cells discretizing the domain, each QUIC-URB-QUIC-PLUME coupled simulation will take approximately 5 minutes. As described presenting the model in Sect. 4.3.1, the chosen input profile is defined as logarithmic

$$U(z) = \frac{U_{ref}(\ln((z + z_0)/z_0) + \psi(z/L_0))}{\ln((z_{ref} + z_0)/z_0)},$$

from a reference velocity  $U_{ref}$  measured at SI at the reference height  $z_{ref}=40$  m. The wind directions associated with the velocity profile are given as ensembles of directions of  $\Delta\phi=40^\circ$  across the perpendicular and parallel wind directions with respect to MA and LB orientations. For example, if we consider winds blowing from east (with respect to the reference canyon orientation) we will set a direction ensemble between  $70^\circ$  and  $110^\circ$  with a resolution of  $5^\circ$ . The roughness length  $z_0$  (m) is defined, according to Macdonald et al. (1998), as

$$\frac{z_0}{H} = \left(1 - \frac{d}{H}\right) \exp \left[ - \left(0.5\beta k^{-2} C_d \lambda_f \left(1 - \frac{d}{H}\right)\right)^{-0.5} \right], \quad (4.13)$$

Algorithm/Parameter	Type/Value
Rooftop surfaces roughness ( $z_0$ )	0.1 m (Hayati et al., 2019)
Street canyon algorithm	Rockle with Fackrell cavity length (Gowardhan et al. 2010; Hayati et al. 2019)
Wake algorithm	Modified Rockled
Blended region algorithm	On (Gowardhan et al. 2010; Hayati et al. 2019)
Rooftop algorithm	Recirculation (Gowardhan et al. 2010; Hayati et al. 2019)
Upwind cavity algorithm	High-rise MVP model (Gowardhan et al. 2010; Hayati et al. 2019)
Side wall algorithm	On (Hayati et al. 2017)
Domain size	1000x1300x200 m
Resolution	2x2x1(exponential variation)

**Table 4.1:** Setup configuration for the QUIC simulations.

where the displacement height  $d$  (m) and the frontal area fraction coefficient  $\lambda_f$  are modified according to Kent et al. (2017) to account for the vegetation,  $\beta=1$ ,  $k=0.4$  is the Von Karman constant,  $H$  is the mean building height and  $C_d$  is the drag coefficient associated to the solid obstacles and taken equal to 1 as previously used in European cities (Ratti et al. 2002; Di Sabatino et al. 2010). As mentioned, also the displacement height  $d$  depends on the vegetation since it is proportional to the planar area fraction coefficient  $\lambda_p$  that in turn depends on  $A_p^v$  (Kent et al., 2017). The total planar and frontal area fraction coefficients are defined by Kent et al. (2017) as

$$A_f = A_f^b + \frac{C_v}{C_d} A_f^v$$

$$A_p = A_p^b + (1 - P) A_p^v,$$

where  $A_f^b$  (m<sup>2</sup>) and  $A_p^b$  (m<sup>2</sup>) are the frontal and planar areas associated with the solid obstacles (buildings) and  $A_f^v$  (m<sup>2</sup>) and  $A_p^v$  (m<sup>2</sup>) are the frontal and planar areas associated to the vegetation and defined in Sect. 4.3.3. The building planar area is retrieved directly from the domain as the sum of the areas of the building rooftop, considered as flat. The building frontal area is

calculated as

$$A_f^b = \sum_i \frac{h_i \cdot l_i \cdot \Delta_j}{\bar{\Delta}},$$

where  $h_i$  are the single building heights,  $l_i$  are the single building widths under the assumption that all buildings have square facades,  $\Delta$  is the domain length and  $\bar{\Delta}$  is the mean domain length. The subscript  $i$  is the building counter,  $j$  the inlet wind approaching direction (and domain entryway). The assumption over  $l_i$  is necessary since the only information on building facades

Quantity	Marconi	Laura Bassi
$A_t$	1300000 m <sup>2</sup>	1300000 m <sup>2</sup>
$A_p$	560909 m <sup>2</sup>	271808 m <sup>2</sup>
$A_f$	686692 m <sup>2</sup> (N-S)	329478 m <sup>2</sup> (N-S)
	888779 m <sup>2</sup> (E-W)	407249 m <sup>2</sup> (E-W)
	787736 m <sup>2</sup> (SW)	368364 m <sup>2</sup> (SW)
$\lambda_p$	0.4315	0.2089
$\lambda_f$	0.5282 (N-S)	0.2519 (N-S)
	0.6837 (E-W)	0.3117 (E-W)
	0.6060 (SW)	0.2818 (SW)
$d$	10.8890 m	4.6462 m
$z_0$	1.1195 m (N-S)	1.5113 m (N-S)
	1.3300 m (E-W)	1.7524 m (E-W)
	1.2625 m (SW)	1.6316 m (SW)

**Table 4.2:** Setup quantities for Marconi and Laura Bassi domains. Between brackets is reported the inlet wind direction considered (when important).

is the total area, from which it is impossible to retrieve the shape. However, the normalized domain length  $\Delta/\bar{\Delta}$  smooths the uncertainty on  $A_f$  adding or removing a compensating factor due to the different length of the domain along the x and y axes. Therefore,  $A_f^b$  changes with the inlet wind direction, but maintains the same value for opposite wind directions (e.g. north and south, east and west). From these information on the areas, the planar and frontal area coefficients  $\lambda_p$  and  $\lambda_f$  are retrieved as by definition

$$\lambda_f = \frac{A_f^b + C_v/C_d A_f^v}{A_t}$$

$$\lambda_p = \frac{A_p^b + (1 - P)A_p^v}{A_t},$$

where  $A_t$  ( $\text{m}^2$ ) is the total area of the domain.  $\lambda_p$  is then used to compute the displacement height  $d$  as defined by [Macdonald et al. \(1998\)](#)

$$d = H \left[ 1 + 4.43^{-\lambda_p} (\lambda_p - 1) \right].$$

Tab. 4.2 stores the values computed for the defined quantities.

QUIC-PLUME needs input values to compute realistic turbulent quantities. Reference surface temperatures are retrieved from the ground level thermohygrometers deployed in the streets. Reference air temperature and humidity are taken from SI. Eventually, the boundary layer height is measured with the ceilometer located in IS. A list of the parametrizations used in the model is given in Tab. 4.1.

### 4.4 Summary and Conclusions

In this chapter, the approach to data analysis and modeling was described. Data processing has been briefly described to define the experimental protocol used to check, clean and (for wind velocity components) rotate the measured data. After an initial check on the reliable ranges of the raw data, data gaps and unmeasured values have been replaced by the mean on the 5-minute interval they are included in. 5-minute interval which has also been chosen as averaging period to ensure the robustness of the results without losing the quick turbulent events. A despiking procedure has been performed to remove the outliers from the high resolution sonic anemometer data, which has subsequently been double rotated to align the coordinate system to the wind streamline direction.

Following the data processing, the methodology for the data analysis has been presented. First the most suitable period has been identified for both experimental field campaigns, based on the choice of weak synoptic conditions characterized by thermal stability at large scale and small local wind speed in the UBL. Then the analysis method has been described, introducing the diagnostic time scales and exchange rates that will characterize the analysis of the exchange processes and their implications on normalized  $CO$  concentrations removal. The time scales have been defined as the mixing times associated with the momentum and heat exchanges between different atmospheric layers within the canopy and throughout the rooftop interface. The exchange rates have been defined as the ratios between the time scales within the canopy and the ones above it, addressing the mixing efficacy of momentum and heat in the SL. The exchange rates have also been identified as describing factors of pollutant removal from the UCL. To evaluate the previous hypothesis, the pollutant concentration has been normalized to remove the emission source, mean flow and geometrical contributions on the measurements. The whole methodology will be used for the data analysis in Sect. 6

After the methodology for the data analysis, the approximated CFD model QUIC used to eval-

uate the numerical investigation of this study have been introduced. Both its main components, i.e. QUIC-URB and QUIC-PLUME, have been described, focusing on the physical principles that regulates their functioning and on the algorithms required to combine reliable results to high computational performances. Being the focus of the numerical investigation, a dedicated section has been used to fully describe the parametrization of vegetation in the model, which is represented as porous cylinder where the wind speed profile is attenuated by the flow-leaves interactions.

Finally, the model setup for the numerical investigations has been given. To enhance the reliability of the simulations, the most updated algorithms and parametrizations in QUIC have been used, along with the choice of simulating a large domain around the reference MA and LB canyons to capture the neighborhood scale dynamics. Wind direction ensembles have been chosen to be representative of each input wind directions, to better capture most of the variability associated to the measured wind direction oscillations. Given the described model and setup, the results from the numerical simulations will be shown in Sect. 7.



## Chapter 5

# Results and Discussion: Observations and Campaign Comparison

In this chapter, an overview of the campaigns results is presented and detailed focusing on the mean characteristics of the background flow, local circulation, turbulence and air quality in the two reference street canyons. The mean behaviors of the most representative meteorological and air quality variables will be presented to characterize the reference street canyons and surrounding neighborhoods during both the investigated seasons. A preliminary inter-seasonal comparison is also presented, to address the seasonal dependency of the investigated quantities. For what concern air quality, the pollutant concentrations are compared with the permanent monitoring network data to assess the impact of a close environment, such as the urban canyon, to the measured concentrations. The background flow will be compared to the local in-canyon mean meteorological characteristics, to address the implication of the investigated environment on the mean atmospheric flows. Meteorological and turbulent data measured within the reference canyons will focus on the weak synoptic periods defined in Sect. 4.2.1, so that summer campaign data corresponds to the 20-23 September and winter campaign data to 08-09 February, to assess the local flow and turbulence characteristics and behaviors during weak synoptic conditions. Conversely, to have a more complete and general assessment of the city scale dynamics, it worths to present a comparison of the selected period characteristics with the mean campaign ones.

## 5.1 Mean Characteristics of the Summer Campaign

### 5.1.1 Pollutant Concentrations

Characteristic pollutant concentrations for the whole campaigns are presented by means of boxplot and usefull statistics (summarized in Tab. 5.1 and 5.2 for the summer and winter cam-

**CHAPTER 5. RESULTS AND DISCUSSION: OBSERVATIONS AND CAMPAIGN COMPARISON**

	Quantity	Mean	Std	Pct25	Pct50	Pct75
Marconi Street	$NO_2$ [ $\mu\text{gm}^{-3}$ ]	53	38	23	46	75
	$CO$ [ $\text{mgm}^{-3}$ ]	0.4	0.3	0.2	0.3	0.5
	$O_3$ [ $\mu\text{gm}^{-3}$ ]	52	30	28	50	72
	$PM_{10}$ [ $\mu\text{gm}^{-3}$ ]	19	7	15	19	23
	$PM_{2.5}$ [ $\mu\text{gm}^{-3}$ ]	9	3	7	9	11
	$T$ [ $^\circ$ ]	22	5	18	22	25
Laura Bassi Street	$NO_2$ [ $\mu\text{gm}^{-3}$ ]	25	32	12	19	32
	$CO$ [ $\text{mgm}^{-3}$ ]	0.3	0.2	0.2	0.3	0.4
	$O_3$ [ $\mu\text{gm}^{-3}$ ]	61	36	35	57	81
	$PM_{10}$ [ $\mu\text{gm}^{-3}$ ]	16	6	11	17	21
	$PM_{2.5}$ [ $\mu\text{gm}^{-3}$ ]	9	4	5	9	12
	$T$ [ $^\circ$ ]	23	6	18	22	27
Porta San Felice	$NO_2$ [ $\mu\text{gm}^{-3}$ ]	30	14	20	29	39
	$CO$ [ $\text{mgm}^{-3}$ ]	0.5	0.14	0.4	0.5	0.6
	$PM_{10}$ [ $\mu\text{gm}^{-3}$ ]	16	6	11	15	20
	$PM_{2.5}$ [ $\mu\text{gm}^{-3}$ ]	9	3	6	9	11
Giardini Margherita	$NO_2$ [ $\mu\text{gm}^{-3}$ ]	12	8	6	10	17
	$O_3$ [ $\mu\text{gm}^{-3}$ ]	70	36	42	67	95
	$PM_{10}$ [ $\mu\text{gm}^{-3}$ ]	14	6	10	14	18
	$PM_{2.5}$ [ $\mu\text{gm}^{-3}$ ]	8	5	5	8	13
Silvani Street	$T$ [ $^\circ$ ]	23	5	18	23	27

**Table 5.1:** Significant statistics for the air quality and air temperature within the reference SCs and the supporting monitoring sites during the summer campaign. Left to right: mean, standard deviation, 25<sup>th</sup> percentile, 50<sup>th</sup> percentile, 75<sup>th</sup> percentile

paigns respectively), to assess their general behaviors. In this section, the focus will be on the summer campaign, while Sect. 5.2 will deal with the winter one. Fig. 5.1 shows the boxplots of the most common pollutants related to urban environment emissions (traffic, domestic heating and cooling systems) and particulates. As for the nature of the single pollutant,  $CO$  concentrations represent a footprint of traffic emissions (Winkler et al., 2018), while  $NO_2$  and  $O_3$  concentrations also assess the importance of background concentrations on local measurements.  $CO$  concentrations (Fig. 5.1b) within the two street canyons are very similar, with an expected wider range toward large concentrations in the case of MA probably due to the larger amount of traffic during the season (example been provided in Fig. 4.7). On a traffic related pollutant like  $CO$  it seems that the street canyon aspect ratio have a smaller impact, at least on the distribution median, with respect to the traffic count. In fact, PSF boxplot shows larger concentrations, following a larger amount of traffic (the station is along the main city center

## 5.1. MEAN CHARACTERISTICS OF THE SUMMER CAMPAIGN

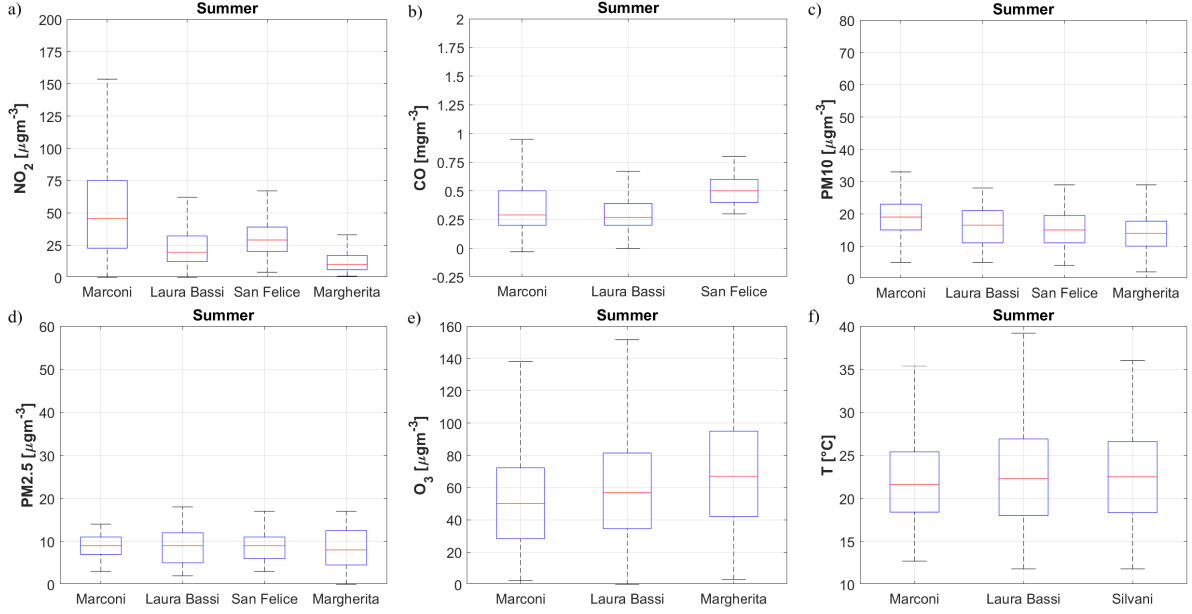


**Figure 5.1:** Boxplot of the summer campaign (a)  $NO_2$ , (b)  $CO$ , (c)  $PM_{10}$ , (d)  $PM_{2.5}$ , (e)  $O_3$  concentrations and (f) air temperature  $T$  within the reference canyons and the supporting sites.

roadway). A different behavior is retrieved for  $NO_2$  concentration; indeed its large atmospheric residence time is enough for the street geometry to play a key role in enhancing the measured concentrations in MA (Fig. 5.1a). Despite the open environment, LB shares similar values of  $NO_2$  concentrations with PSF, certifying itself as an urban traffic site. The geometry effect of the street canyon is evident comparing the discrepancies between MA and PSF in  $NO_2$  and  $CO$  concentrations, i.e. background concentrations against traffic footprint. Despite the a lower traffic rate, the stagnant condition imposed by the closed geometry impacts on the  $NO_2$  mea-

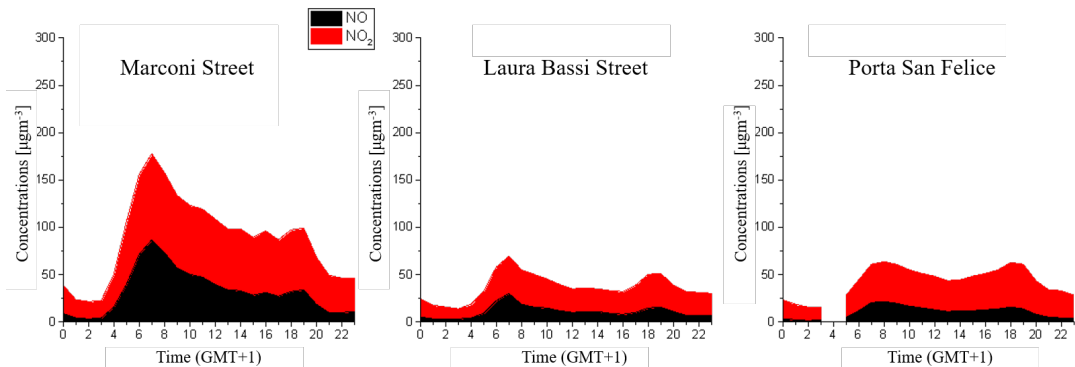


**Figure 5.2:** Typical day for  $NO$  and  $NO_2$  concentrations in MA, LB and PSF during the summer campaign.

## CHAPTER 5. RESULTS AND DISCUSSION: OBSERVATIONS AND CAMPAIGN COMPARISON

measurements. A similar behavior is retrieved also for  $PM_{10}$  (Fig. 5.1c), whose particles are more strictly related to traffic than for  $PM_{2.5}$  (Fig. 5.1d), that is generally more prone to react with other compounds.  $PM_{2.5}$  is also affected by the volatile organic compounds, which explains the large values in LB and GM. As expected, ozone concentrations (Fig. 5.1e) show the opposite behavior of  $NO_2$  concentrations, due to the ozone reactions cycle involving  $NO_x$  both in the destruction and creation processes. An insight on the  $O_3$  cycle during summertime is provided through the typical day analysis. Fig. 5.2 shows the comparison between  $NO$  and  $NO_2$  typical day concentrations in MA, LB and PSF. As it emerged from the boxplot analysis, LB behaves

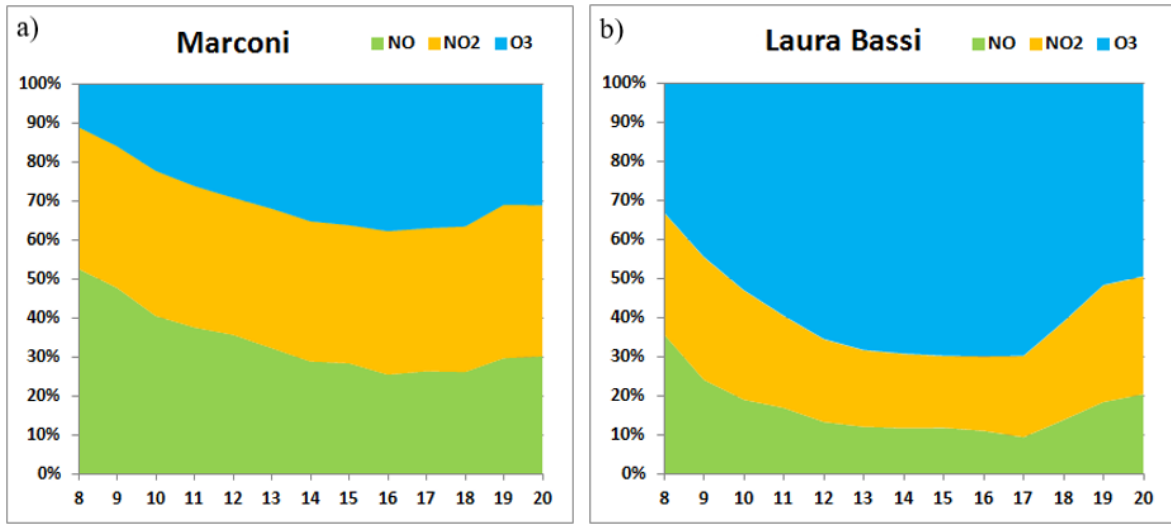
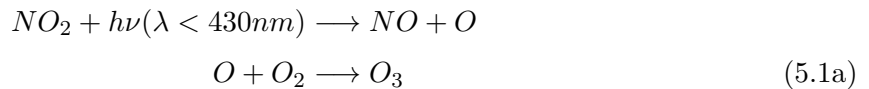


**Figure 5.3:** Typical relative concentrations of  $NO$ ,  $NO_2$  and  $O_3$  in (a) MA and (b) LB during the summer campaign.

like an urban traffic station for what concern both primary  $NO$  and secondary  $NO_2$  nitrogen oxides compounds, while in MA the geometry is such that concentrations are almost twice the PSF ones. Moreover, while the morning rush hour is clearly evident in all the three locations, the evening one is definitively less intense or almost absent, confirming what emerged from the traffic counts description (Sect. 4.2.3). Knowing the typical daily evolution of the nitrogen oxides concentrations, it is easier to understand the behavior of  $O_3$  ones. Ozone cycle directly depends on both  $NO$  and  $NO_2$  since



are the production (Eq. (5.1a) and destruction (Eq. (5.1b)) reactions establishing the lifetime of  $O_3$  in atmosphere. The bulk evidence from the cycle is the inverse proportionality between  $NO_2$  and  $O_3$  concentrations. The implication of these reactions on the  $O_3$  typical concentrations is evident in Fig. 5.3 where  $NO$ ,  $NO_2$  and  $O_3$  typical relative concentrations are compared. In both panels, the 100% is the total cumulative concentration of the three compound and each area corresponds to the cumulative relative contribution of each compound one to the total. In MA (Fig. 5.3a) the ozone production-destruction cycle is shifted toward destruction due to the large availability of  $NO$ . Conversely, in LB (Fig. 5.3b) ozone production is more efficient and nitrogen oxides concentrations remain small. Since in both streets the amount of  $NO_2$  concentrations is fixed approximately to the 30% of the total cumulative concentration, the ozone cycle is entirely directed by  $NO$  (production-destruction ozone cycle related to the volatile organic compounds is not investigated since the lasts are embedded in  $PM_{2.5}$  measurement).

### 5.1.2 Background and Mean Flow Fields Characteristics

Wind roses in Fig. 5.4 show the general behavior of the background flow (SI) and the mean flow fields (MA and LB) within the canyons. Within the canopies, wind is directed along the canopy orientations. The prevalent direction is from south, but the wind velocity intensities are weak (always below  $2 \text{ ms}^{-1}$ ). The other prevalent direction in MA is from north, where wind speed also reaches large intensities. Background wind velocity field flowing at the city scale has

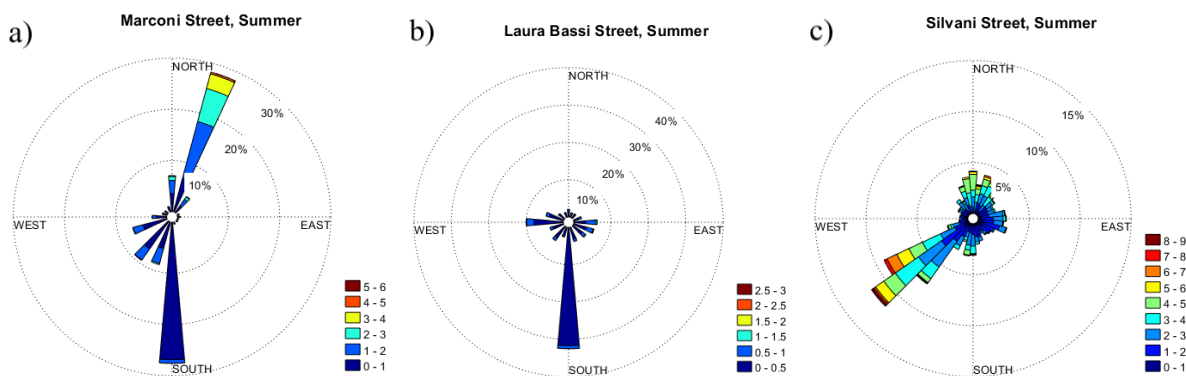


**Figure 5.4:** Wind roses of the summer campaign within (a) MA, (b) LB and (c) on the supporting site of SI.

a strong predominance from southwest. This direction identifies a local flow typical of Bologna, where the wind is flowing from the Reno Valley (a small valley created by the Reno river in the southwest of the southern hill chain) to the plain. A minor contribution to the wind rose is retrieved from north, when the winds come from the Po Valley toward the city.

A brief overview on air temperature is also displayed in Fig. 5.1f, where the canyons are compared with the background temperatures, with very poor differences. In fact, the three sites show

## CHAPTER 5. RESULTS AND DISCUSSION: OBSERVATIONS AND CAMPAIGN COMPARISON

similar medians and percentiles, with LB showing the largest variability probably as a result of air trapping and shadowing effect by the trees.

### 5.1.3 Local Flow Field and Turbulence

Local flow field on urban environments is the result of the unperturbed boundary layer flow interacting with the enhanced drag force and roughness generated in a city. This local field, i.e. background flow, involves the whole city in an atmospheric layer developing above the UCL, where the irregular pattern of obstacles drives the flow apart, generating very local circulations. An insight of the background flow field is displayed in Fig. 5.5, where the measurements taken at the background monitoring sites of SI and AT are compared with the ones collected at the street RLs. Wind speeds close to the canopy interface (cyan and green bullets in Fig. 5.5a)

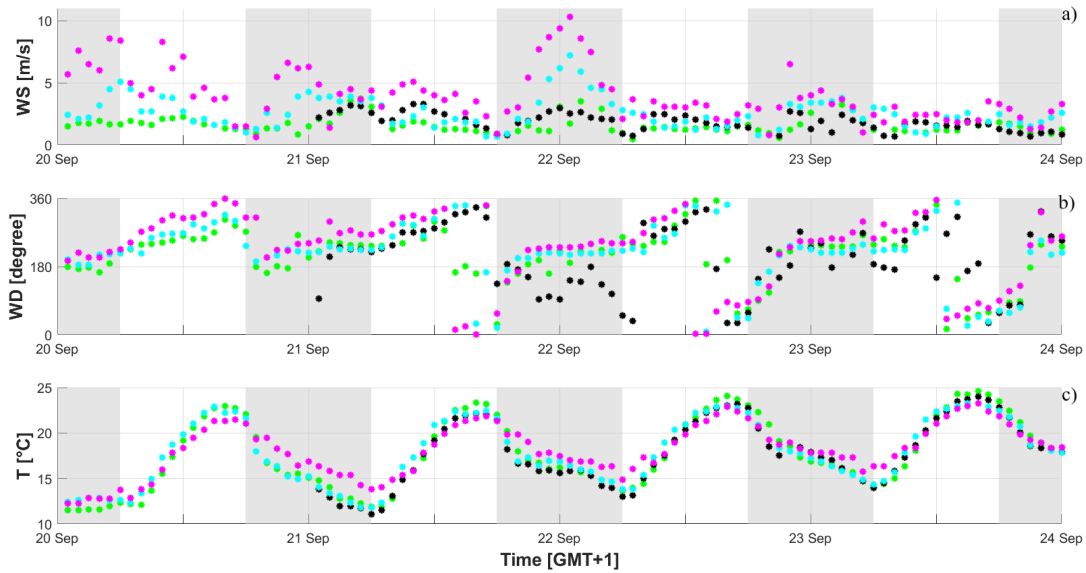


**Figure 5.5:** 1 hour average wind speed (a), wind direction (b) and temperature (c) measured above the UCL. Colors indicate the following sites: (●) AT at 100 m agl, (●) SI at 35 m agl, (●) RL at 33 m agl in MA and (●) RL at 20 m agl in LB. The shadowed areas highlight nighttime periods. On average sun rises at 06:00 AM and sets at 18:00 PM (GMT+1).

are constantly smaller ( $< 5 \text{ ms}^{-1}$ ) than the average summer value (Fig. 5.4c), apart from the intense maximum during the night between the 22 and 23 of September probably related to a low-level jet behavior of the nocturnal flow. Wind directions (Fig. 2.1b) are typical of a local valley circulation, showing well defined downslope/downvalley flows coming from the hill chain that southerly bounds the city (southerly parallel background wind direction to the canyon orientation) during the nighttime and a continuous wind rotation during the daytime, with predominating upslope/upvalley flows coming from the northern plain (northerly parallel background wind direction to the canyon orientation). Finally, air temperature shows the typical

## 5.1. MEAN CHARACTERISTICS OF THE SUMMER CAMPAIGN

evolution of a stable clear sky day, with daytime vertical homogeneity and nighttime inverse stratification, the last intense enough to generate a vertical gradient up to 4°C. Maximum temperature are reached during the early afternoon (03:00-04:00 PM, GMT+1).

During weak synoptic conditions, the vertical TKMF developing at the canopy interface drives the IC within the canyons (Britter and Hanna, 2003), especially when the geometry prevents the channeling of the mean flow, e.g. when the background wind direction is perpendicular to the canyon orientation. The mean flow vertical structure within the canopy shapes as displayed in Fig. 5.6. Profiles are well mixed within both canopies, with the largest gradients in MA both

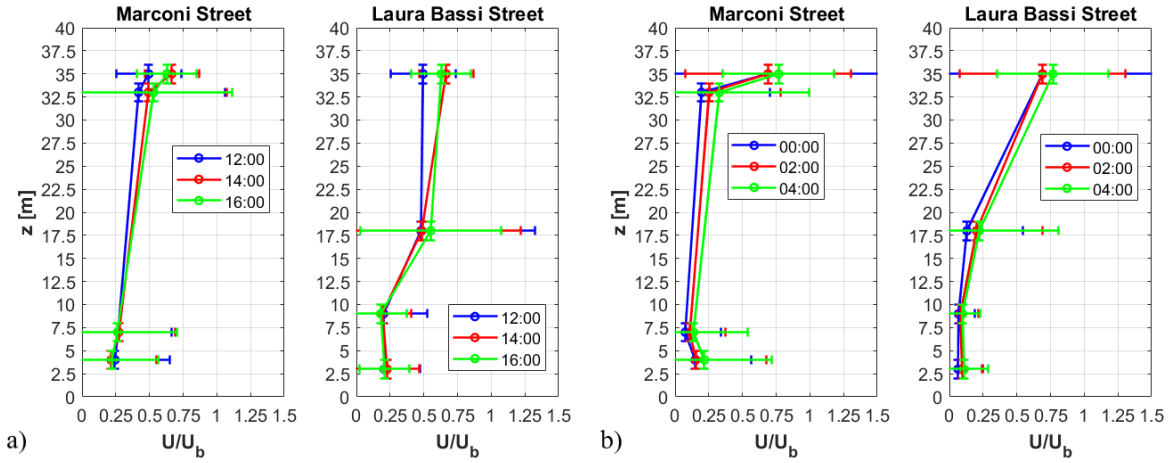


**Figure 5.6:** Daytime (a) and nighttime (b) typical wind speed profiles in MA and LB relative to the period 20-23 September. Measurements are taken from the respective GLs, MLs and RLs and coupled with SI. Profiles are the hourly average over the investigated period taken at the 12:00, 14:00 and 16:00 GMT+1 during the day and the 00:00, 02:00 and 04:00 GMT+1 during the night.

during day and night. Stationarity also dominates the evolution of the canyon profile, while above the interface a small variability is retrieved. The largest vertical gradient is found in Laura Bassi between the canopy and its rooftop, especially during daytime when the UCL and the upper UBL seems to be decoupled. Above the canopy a certain flow stratification is always present during nighttime, leading to a strong gradient between the canopy representative speed and the background flow in the UBL. This behavior is verified also by the time evolution of the wind speed during the analyzed period (Fig. 5.7), where the wind speed intensities at the RL are closer to the background flow (Fig. 5.5a) than the respective GL and ML within the canopies. In both canopies, but especially in LB (Fig. 5.7b), wind speed at the rooftop is larger than the in-canyon ones, where homogeneity conditions dominate the air volumes. Daytime hours show the largest velocity value of the time series, caused by the convection induced by the warm surfaces. During nighttime, wind speeds are generally smaller, but at the RL the impact of the nocturnal flow over the city enhances the velocity values at the interfaces, decoupling them from

## CHAPTER 5. RESULTS AND DISCUSSION: OBSERVATIONS AND CAMPAIGN COMPARISON

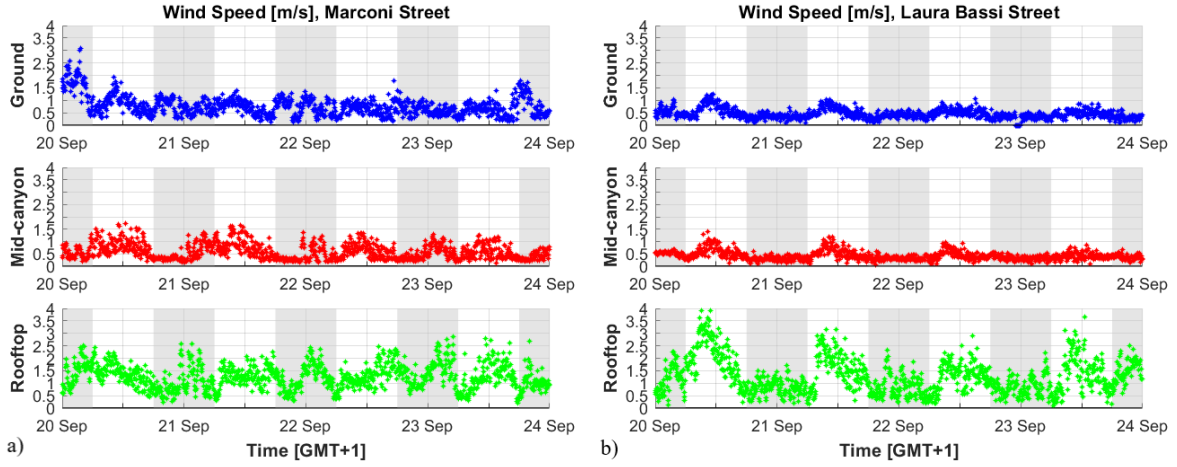


**Figure 5.7:** Time evolution of the wind speed in (a) MA and (b) LB during the period 20-23 September. Measurements are taken from the respective GLs (blue), MLs (red) and RLs (green) of the canyons. The shadowed areas highlight nighttime periods. On average sun rises at 06:00 AM and sets at 18:00 PM (GMT+1).

the in-canyon circulations. A strong impact on the in-canyon circulation can be produced by the air temperature within the cavity volumes and by the horizontal gradients between opposite building facades. Fig 5.8a shows the evolution of air temperatures within and at the interface of MA and LB. Within each canyon, temperature is homogeneous, revealing the impact of mixing during the whole period. Mixing extends to the canyon rooftop during daytime, while during

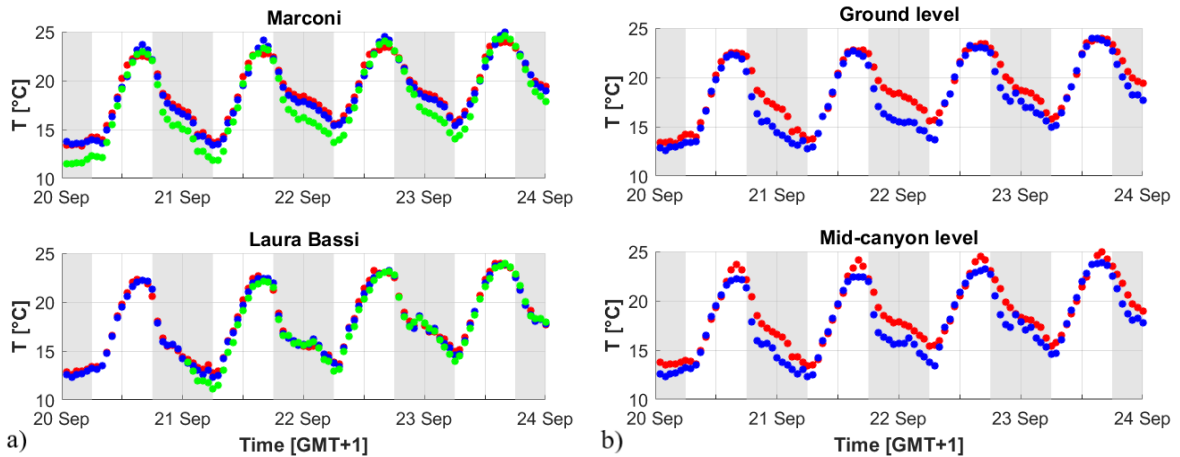


**Figure 5.8:** Time evolution of the air temperature (a) in MA and LB, and their in-canyon comparison (b) during the period 20-23 September. Measurements are taken from the respective GLs (blue), MLs (red) and RLs (green) of the canyons. In (b) red asterisks correspond to MA, the blue ones to LB. The shadowed areas highlight nighttime periods. On average sun rises at 06:00 AM and sets at 18:00 PM (GMT+1).

the nights a small inversion appears only in MA. This last difference between the canyons can be caused by the morphology of neighborhood surrounding background flow, or by the geometry of the canyon. Single houses with gardens all around them, and lateral junctions, are sources of horizontal entrainment, causing an increase of mixing with the air coming from outside the canopy. The geometry of the canyon is such that its mean aspect ratio lets the flow be at the edge between the skimming flow regime and the wake interference (Oke, 1987). Exchanges with the free atmosphere are enhanced by the cavity overtune, increasing the column mixing. Fig. 5.8b shows the comparison between the in-canyon measurements of the two sites. During daytime, differences between air temperatures are almost negligible. In this case the shadow effect of the trees in LB do not impact on the air temperature, but it can decrease the radiation absorption by the surface. This phenomenon leads to the nocturnal differences. The heat loss by the surface is proportional to the daytime absorption. Therefore, the shadowing effect seems to reduce the nocturnal heat emission and consequently the air temperature. Definitely, a local heat island effect develops between the city center and the surrounding residential areas, with temperature contrasts up to 2°C.

The presence of continuously flowing background winds enables the development of the ICn within the canopy (Barlow et al., 2004), with the consequent formation of mechanically generated turbulent structures. Superimposed to the IC, the differential heating between opposite building facades of the canopy induces a horizontal temperature gradient, that establishes a TC (Dallman et al., 2014). Fig. 5.9 and 5.10 show the TKMF and the TKSHF at the canonic three levels of MA and LB. At the RLs, the fluxes are influenced and constrained by the mean flow. TKMFes inside the canyons are generally smaller than at the rooftop ones due to the morpholog-

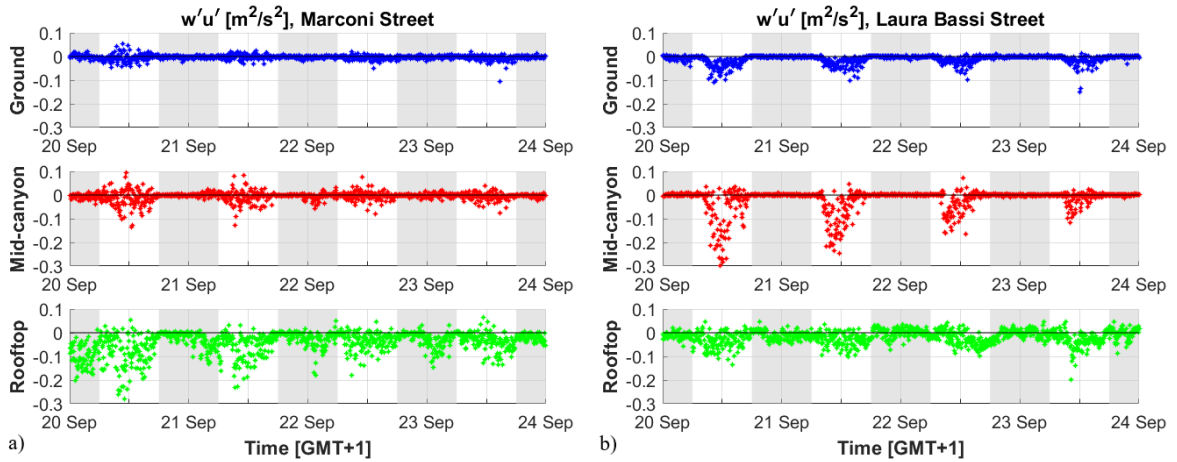


**Figure 5.9:** Time evolution of the TKMF measured in (a) MA and (b) LB during the period 20-23 September. Measurements are taken from the respective GLs (blue), MLs (red) and RLs (green) of the canyons. The shadowed areas highlight nighttime periods. On average sun rises at 06:00 AM and sets at 18:00 PM (GMT+1).

CHAPTER 5. RESULTS AND DISCUSSION: OBSERVATIONS AND CAMPAIGN COMPARISON

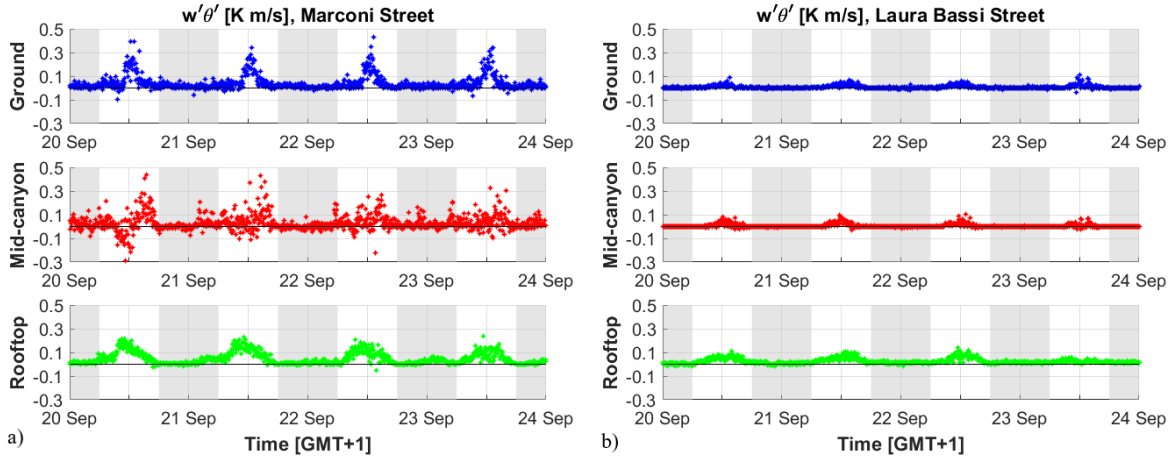


**Figure 5.10:** Time evolution of the TKS HF measured in (a) MA and (b) LB during the period 20-23 September. Measurements are taken from the respective GLs (blue), MLs (red) and RLs (green) of the canyons. The shadowed areas highlight nighttime periods. On average sun rises at 06:00 AM and sets at 18:00 PM (GMT+1).

ical restriction on mean flow. At RLs, TKMFes are predominantly negative, driving momentum inside the canopy and sustaining the IC. Within the canopies, fluxes are more chaotic, randomly oscillating between positive and negative values. Daily patterns are more evident in LB, where the vegetation seems to lower the transport intensity during night and to enhance the maximum daytime values. Conversely, the TKS HFes inside the canyon are strengthened by the presence of multiple artificial surfaces prone to release heat during both daytime and nighttime.

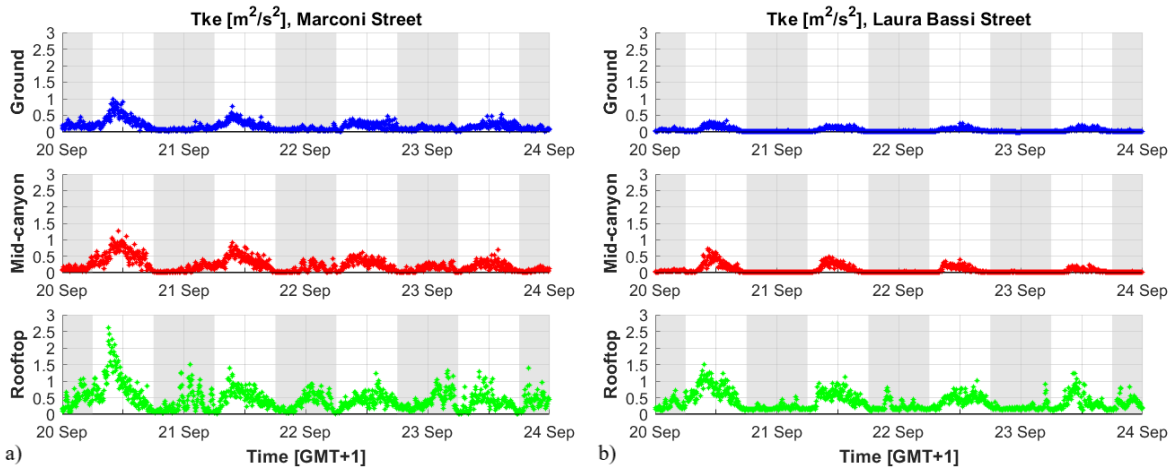


**Figure 5.11:** Time evolution of the  $Tke$  measured in (a) MA and (b) LB during the period 20-23 September. Measurements are taken from the respective GLs (blue), MLs (red) and RLs (green) of the canyons. The shadowed areas highlight nighttime periods. On average sun rises at 06:00 AM and sets at 18:00 PM (GMT+1).

Maximum intensities are gained during daytime, while during the nights they are weakened by thermal stratification, but never overturned, implying no changes in the direction of the heat exchange. The overall smaller values retrieved in LB can be a consequence of a morphology open to lateral infiltration that removes heat from the street and the vegetation shadowing effect that reduces the heat transport from the surfaces. Also the  $Tke$  in Fig. 5.11 confirms the large amounts of turbulent production at the RLs and homogeneity within the canopies. TKE is particularly weak within LB canyon during night, while at the RL it is similar to MA one. Similar are also the stability conditions computed at the RLs and characteristics of the canopy (Fig. 5.12). Stability is addressed using the adimensional parameter  $H - d/L_O$  dependent on

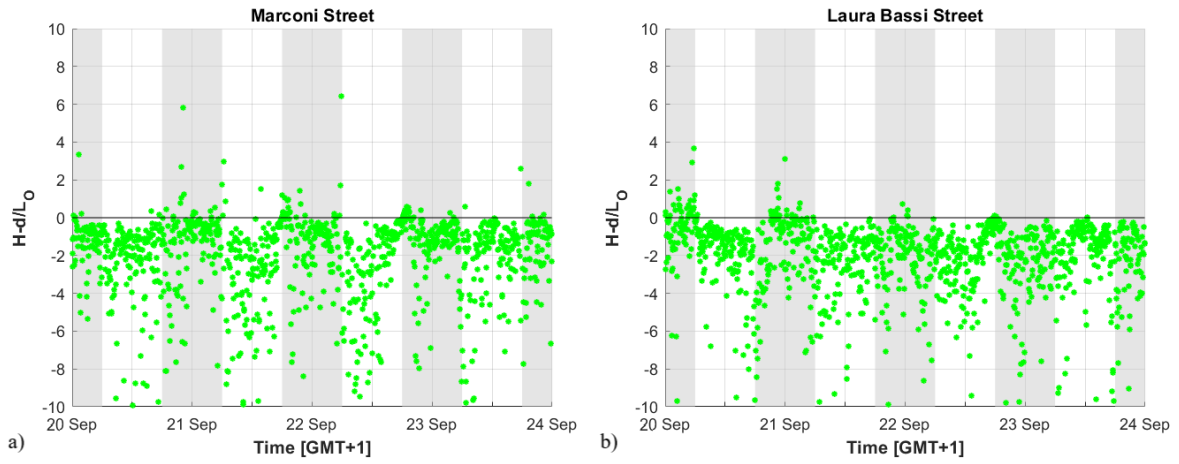


**Figure 5.12:** Time evolution of the stability parameter  $H - d/L_O$  measured in (a) MA and (b) LB at the RLs of the canyons during the period 20-23 September. The shadowed areas highlight nighttime periods. On average sun rises at 06:00 AM and sets at 18:00 PM (GMT+1).

the mean building height of the street  $H$  (m), the displacement height  $d$  (m) and the Obukhov length  $L_O$  (m). Following the classification determined by Rotach (1995), the stability parameter describes near-neutral conditions when  $-0.05 < H - d/L_O < 0.05$  and strongly unstable ones when  $H - d/L_O < -0.5$ . In the analyzed period, strongly unstable conditions dominate the whole time series, even during nighttime, sustaining the mixing efficacy of the canopy even after the solar energy cut-off at sunset.

### Normalized $CO$ concentrations

During the analyzed period (20-23 September 2017), particular focus have been posed on  $CO$  concentrations, to use them as the passive tracer the mean flow and turbulent motions transport through the canopy. To avoid the vehicular traffic, the geometry and the background flow footprints from the  $CO$  concentrations, measured data where first normalized following the procedure described in Sect. 4.2.3. As a result, the normalized carbon monoxide concentrations

## CHAPTER 5. RESULTS AND DISCUSSION: OBSERVATIONS AND CAMPAIGN COMPARISON

$CO^+$  are retrieved for both MA and LB and compared in Fig. 5.13. Apart from the last day

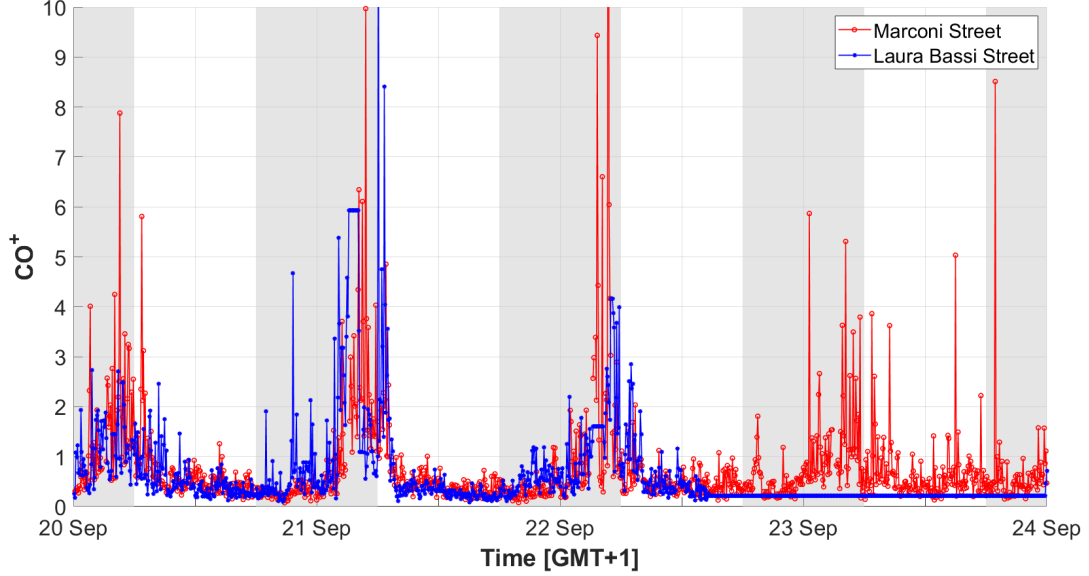


**Figure 5.13:** Time evolution of the 5-minute average normalized carbon monoxide concentrations  $CO^+$  in MA (red) and LB (blue) during the analyzed period (20-23 September). The shadowed areas highlight nighttime periods. On average sun rises at 6:00 AM and sets at 18:00 PM (GMT+1).

and a half, when traffic data in LB were not available, the  $CO^+$  concentrations in the canyons are very much similar for the whole period. Removing the source effect, along with geometry and background flow, possible differences between the sites have flattened, leaving only the local circulation dependency. As a result, the  $CO^+$  in the two canyons are very similar. Normalized concentrations are small during daytime, and slightly larger after sunset, also showing stronger oscillations. The larger concentration peaks are retrieved before sunrises, when the circulation is weakening and the nocturnal stability above the canopy has reached its maximum intensity (Fig. 5.5c). This stratification inhibits the turbulent heat transport at RLs (green line in Fig. 5.10) and reduces the efficacy of the exchange processes with the canyon (Li et al. 2015, 2016), causing an increase of  $CO^+$  concentration (Fig. 5.13). Consequently, the pollutant dispersion is inhibited and  $CO^+$  concentrations can rise again, despite the low emission levels. The oscillations in the time series can derive from multiple factors, depending on the main flow (wind velocity and direction changes, temperature rise or drop, vertical or lateral entrainment) or turbulence variations and their interactions with the complex geometry of the canyon and its intersections. To certify the normalized  $CO^+$  concentrations are no longer dependent on the emission source  $Q_e$  and the wind speed at the canyons RLs  $U_H$ , scatterplots in Fig. 5.14 are shown. In both canyons, the resulting  $CO^+$  concentrations are independent on canyon geometry, mean wind at the canyon top (Fig. 5.14b-d) and traffic emissions (Fig. 5.14a-c). Therefore, normalized  $CO^+$

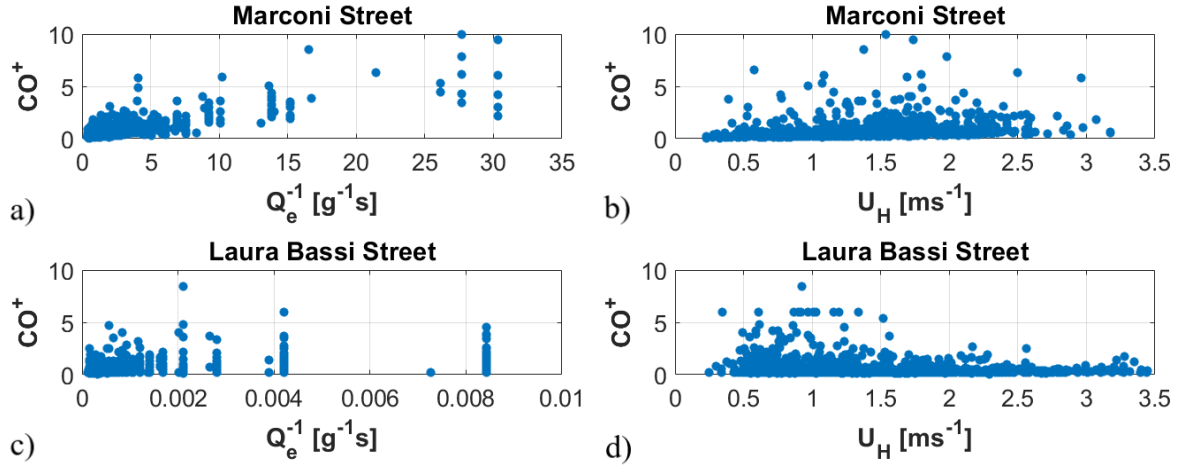


**Figure 5.14:** Normalized  $CO^+$  concentration as function of the emission source  $Q_e$  in (a) MA and (c) LB, and the rooftop wind speed  $U_H$  in (b) and (d) respectively.

concentrations are verified to depend only on local circulations, with transport governed by turbulent processes.

## 5.2 Mean Characteristics of the Winter Campaign

### 5.2.1 Pollutant Concentrations

Pollutant concentration behaviors during winter are similar to the summer ones, meaning that the differences between site couples for the same pollutant are almost equal to what was retrieved for the summer campaign. A summary of the significant statistics for each pollutant distribution

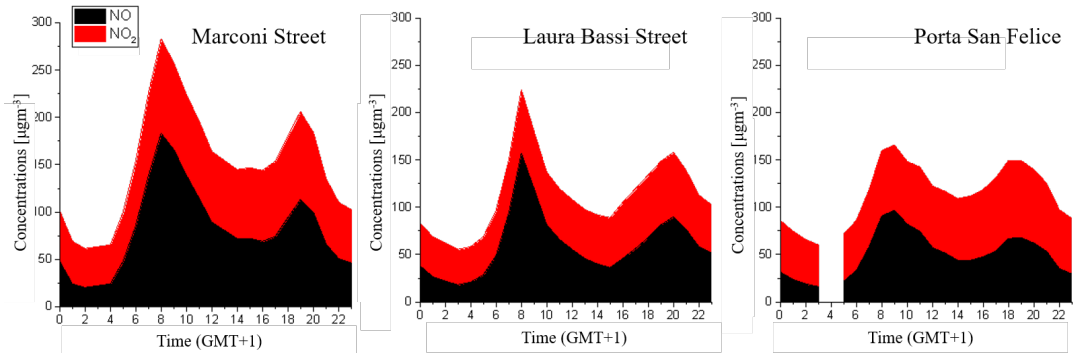


**Figure 5.15:** Typical day for  $NO$  and  $NO_2$  concentrations in MA, LB and PSF during the winter campaign.

is reported in Tab. 5.2. One difference is represented by  $CO$  concentrations (Fig. 5.16b) where all sites medians and percentiles share the same values, despite PSF range is less wide. The

## CHAPTER 5. RESULTS AND DISCUSSION: OBSERVATIONS AND CAMPAIGN COMPARISON

other clear difference with the summer period is represented by the almost always negligible values of the ozone concentrations due to the large amount of  $NO$  (Fig. 5.15) and solar radiation necessary to catalyze the cycle (Eq. (5.1a)).  $NO_2$  (Fig. 5.16a) and  $PM_{10}$  (Fig. 5.16c) exacerbate

	Quantity	Mean	Std	Pct25	Pct50	Pct75
Marconi Street	$NO_2$ [ $\mu\text{gm}^{-3}$ ]	68	32	48	63	82
	$CO$ [ $\text{mgm}^{-3}$ ]	0.9	0.4	0.6	0.8	1.06
	$O_3$ [ $\mu\text{gm}^{-3}$ ]	11	12	3	5	13
	$PM_{10}$ [ $\mu\text{gm}^{-3}$ ]	44	22	32	44	53
	$PM_{2.5}$ [ $\mu\text{gm}^{-3}$ ]	26	16	13	25	34
	$T$ [ $^\circ$ ]	7	2	5	6	8
Laura Bassi Street	$NO_2$ [ $\mu\text{gm}^{-3}$ ]	52	16	42	51	61
	$CO$ [ $\text{mgm}^{-3}$ ]	0.9	0.5	0.6	0.8	1.0
	$O_3$ [ $\mu\text{gm}^{-3}$ ]	11	14	2	4	15
	$PM_{10}$ [ $\mu\text{gm}^{-3}$ ]	34	18	19	32	43
	$PM_{2.5}$ [ $\mu\text{gm}^{-3}$ ]	23	14	12	23	29
	$T$ [ $^\circ$ ]	6	3	4	5	8
Porta San Felice	$NO_2$ [ $\mu\text{gm}^{-3}$ ]	63	17	50	63	75
	$CO$ [ $\text{mgm}^{-3}$ ]	0.9	0.3	0.6	0.7	1.0
	$PM_{10}$ [ $\mu\text{gm}^{-3}$ ]	36	20	24	37	45
	$PM_{2.5}$ [ $\mu\text{gm}^{-3}$ ]	26	15	15	27	33
Giardini Margherita	$NO_2$ [ $\mu\text{gm}^{-3}$ ]	41	16	32	43	52
	$O_3$ [ $\mu\text{gm}^{-3}$ ]	11	16	1	3	15
	$PM_{10}$ [ $\mu\text{gm}^{-3}$ ]	31	21	14	33	41
	$PM_{2.5}$ [ $\mu\text{gm}^{-3}$ ]	26	16	15	26	33
Silvani Street	$T$ [ $^\circ$ ]	6	3	4	5	8

**Table 5.2:** Significant statistics for the air quality and air temperature within the reference SCs and the supporting monitoring sites during the winter campaign. Left to right: mean, standard deviation, 25<sup>th</sup> percentile, 50<sup>th</sup> percentile, 75<sup>th</sup> percentile.

the impact of geometry in MA already described for the summer campaign, enlarging the gap with LB. Large amounts of  $PM_{10}$  and  $PM_{2.5}$  are retrieved, even in LB and GM where the volatile organic compounds are reduced by the absence of the vegetation leaves. In both street canyons the large  $NO_2$  concentrations typical of urban areas tend to produce  $O_3$  under warm and sunny conditions not so common during winter. Therefore, once  $O_3$  is degraded by  $NO$ ,  $NO_2$  can rise but the ozone production mechanisms is inhibited by the poor solar radiation. Since its primary source is vehicular traffic,  $NO$  concentrations remain large at all sites (Fig. 5.15), accounting for the largest portion of the whole nitrogen dioxides.  $NO$  concentrations have a clear footprint from traffic data, showing bimodal distributions in all sites in connection with

## 5.2. MEAN CHARACTERISTICS OF THE WINTER CAMPAIGN

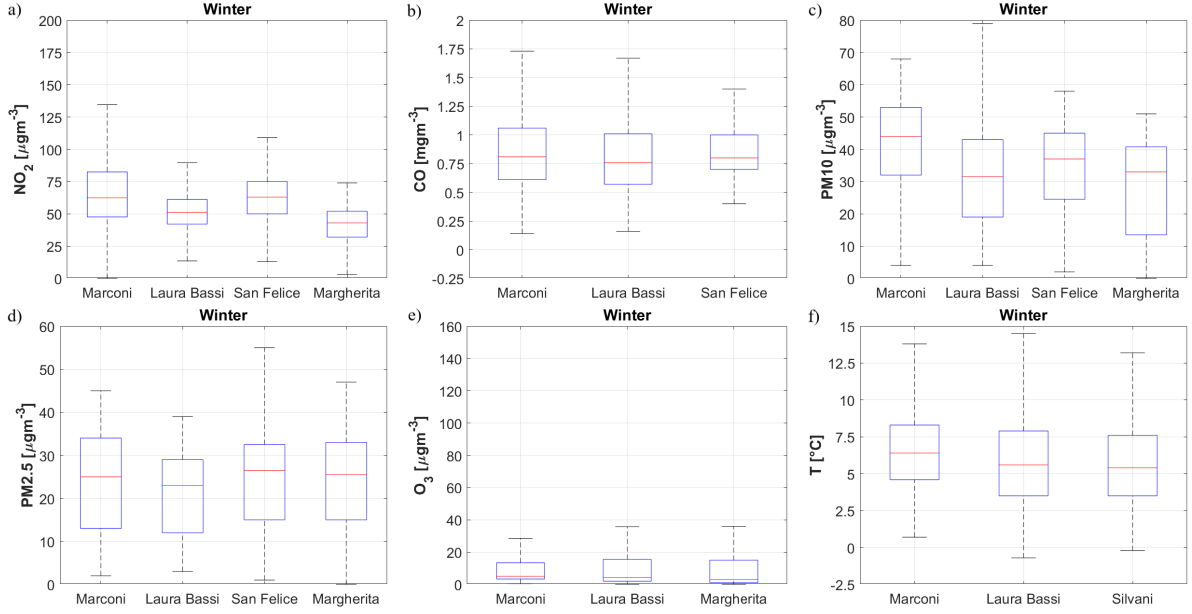


**Figure 5.16:** Boxplot of the winter campaign (a)  $NO_2$ , (b)  $CO$ , (c)  $PM_{10}$ , (d)  $PM_{2.5}$ , (e)  $O_3$  concentrations and (f) air temperature  $T$  within the reference canyons and the supporting sites.

the rush hours. Concentrations are also clearly larger in LB and PSF than the counterparts during the summer campaign, but in MA they are similar. This last similarity can be explained by the large influence of canyon geometry in a close and narrow street like MA with respect to cases like LB, where the wide street full of intersections creates an horizontal recirculation which is inhibited during wintertime.

### 5.2.2 Background and Mean Flow Fields Characteristics

As for the summer campaign, Fig. 5.17 shows the wind roses in MA, LB and SI, accounting for the mean canopy and background flow fields. Again the prevailing directions in the canopies are along the canyon orientations (almost north to south), but several occurrences of winds flowing from lateral streets are retrieved. Wind speeds remain small ( $<2 \text{ ms}^{-1}$ ) except when the wind flows from north in MA, although this pattern is less evident than the summer one. Background flows are indeed equally directed with respect to the summer ones, with prevailing directions from southwest. Wind speeds are generally weaker than during summer.

Air temperature boxplots for the winter period are displayed in Fig. 5.16f. Again, differences between the canopy and the background flow are small, but it is clear a certain shift in MA toward larger values, caused by an average and local urban heat island effect, evident even within different areas of the same city.

## CHAPTER 5. RESULTS AND DISCUSSION: OBSERVATIONS AND CAMPAIGN COMPARISON

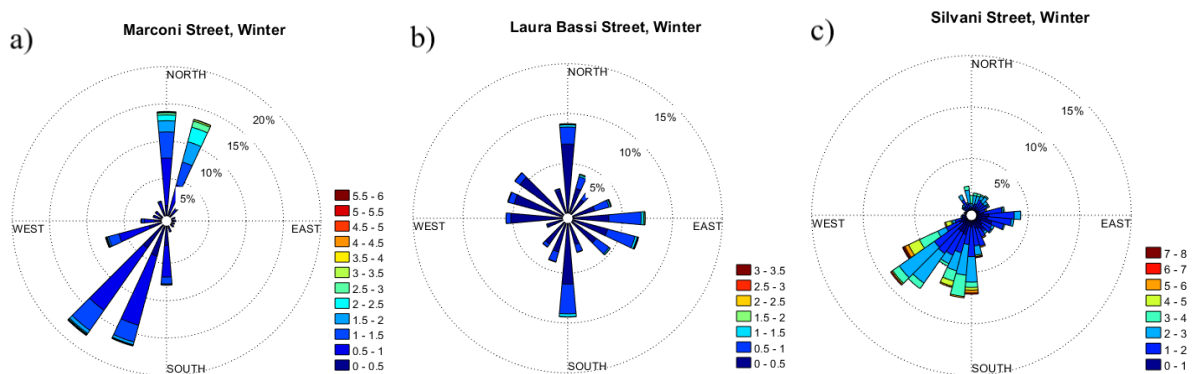


**Figure 5.17:** Wind roses of the winter campaign within (a) MA, (b) LB and (c) on the supporting site of SI.

### 5.2.3 Local Flow Field and Turbulence

Large scale stability during winter is hard to find due to high number of perturbations that can detach from the persistent low pressure system in the polar region (Fig. 4.4). The chosen days are the best solution we can afford in a very unstable winter, but show some similarity with the summer period especially when dealing with the city scale flow (Fig. 5.18). To facilitate the seasonal comparison, the values of wind velocity, turbulent kinematic fluxes and stability parameter measured at the winter LB RL location (15 m agl) are also linearly extrapolated to

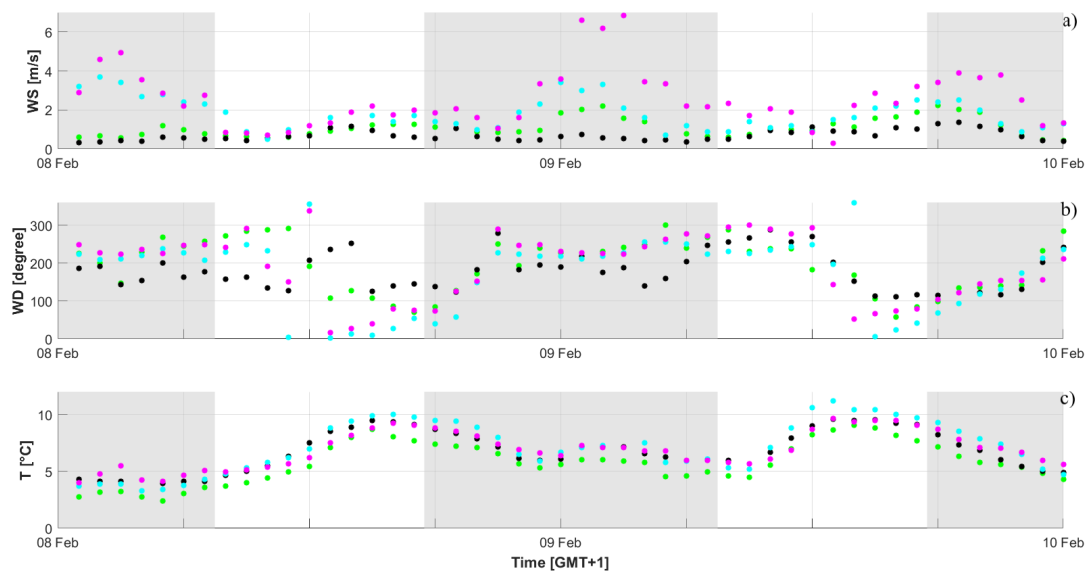


**Figure 5.18:** 1 hour average wind speed (a), wind direction (b) and temperature (c) measured above the canopy layer. Colors indicate the following sites: (●) AT at 100 m agl, (●) SI at 35 m agl, (●) RL at 33 m agl in MA and (●) RL at 18 m agl in LB. The shadowed areas highlight nighttime periods. On average sun rises at 07:30 AM and sets at 17:30 PM (GMT+1).

## 5.2. MEAN CHARACTERISTICS OF THE WINTER CAMPAIGN

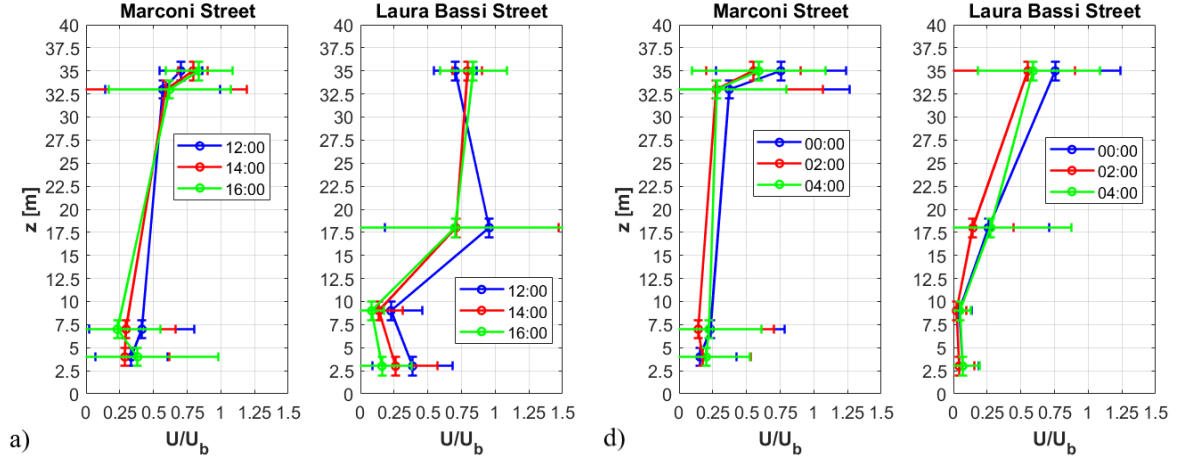


**Figure 5.19:** Daytime (a) and nighttime (b) typical wind speed profiles in MA and LB relative to the period 08-09 February. Measurements are taken from the respective GLs (blue), MLs (red) and RLs (green) of the canyons. Profiles are the hourly average over the investigated period taken at the 12:00, 14:00 and 16:00 GMT+1 during the day and the 00:00, 02:00 and 04:00 GMT+1 during the night.

the height of the summer RL location (18 m agl). Wind speed above the city (Fig. 5.18a) is generally weak especially during daytime, when the wind speeds never exceed  $3 \text{ ms}^{-1}$ . During nighttime, the farther the wind is measured away from the rooftop, the larger the wind speed turns out to be. Despite the atmosphere requires a small amount of time to readjust from the last perturbation to the stable condition characteristics of the chosen period, a city scale

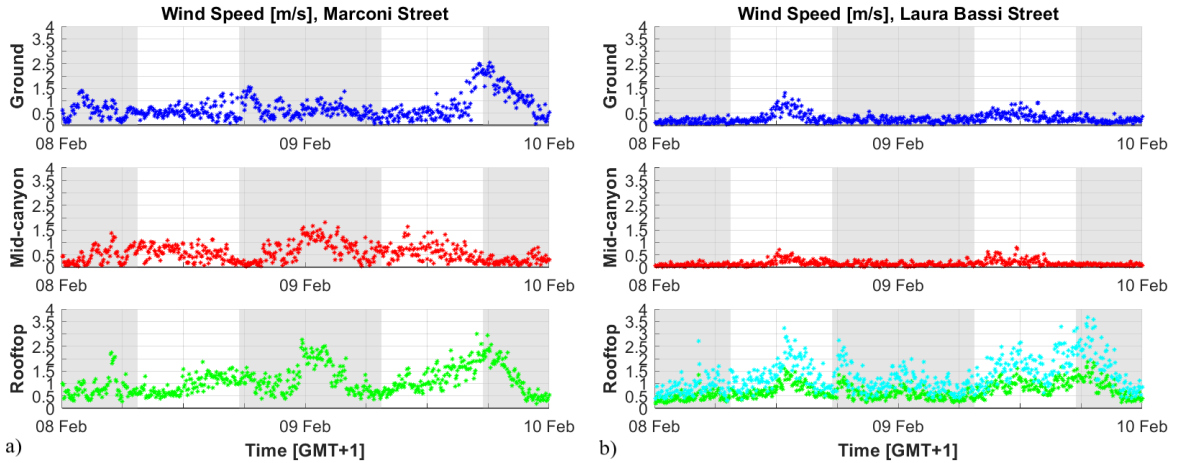


**Figure 5.20:** Time evolution of the wind speed in (a) MA and (b) LB during the period 08-09 February. Measurements are taken from the respective GLs (blue), MLs (red), RLs (green) and extrapolated rooftop levels (cyan, specific for LB) of the canyons. The shadowed areas highlight nighttime periods. On average sun rises at 07:30 AM and sets at 17:30 PM (GMT+1).

## CHAPTER 5. RESULTS AND DISCUSSION: OBSERVATIONS AND CAMPAIGN COMPARISON

valley circulation develops (Fig. 5.18b). During nighttime, the wind direction is constantly from southwest, and this condition persists during the early morning when the weak solar radiation needs time to break the nocturnal stability. During daytime, the wind is not constant, but the most common direction is from east, meaning wind perpendicular to the street canyon. Temperatures (Fig. 5.18c) follow the typical daily evolution, but there is no nighttime inversion. Wind profiles in Fig. 5.19 show some of the characteristics already observed during summer. MA shows persistent mixing conditions in the whole canyon during both day and night. LB shows a certain vertical gradient inside the canopy during daytime and a decoupling from the atmosphere above, the latter persisting for the whole day and night. The time evolution of the wind speed in MA (Fig. 5.20a) also confirms the mixed conditions between the canopy and its rooftop. In LB, the stratification is more evident especially during daytime, when the wind speed at the GL doubles the ML one (Fig. 5.20b). Slight decoupling is evident at the RL (both the true and the extrapolated one) where the flow is more similar to the city scale one than to the canyon. Homogeneous conditions are retrieved also from the air temperature signals (Fig. 5.21),

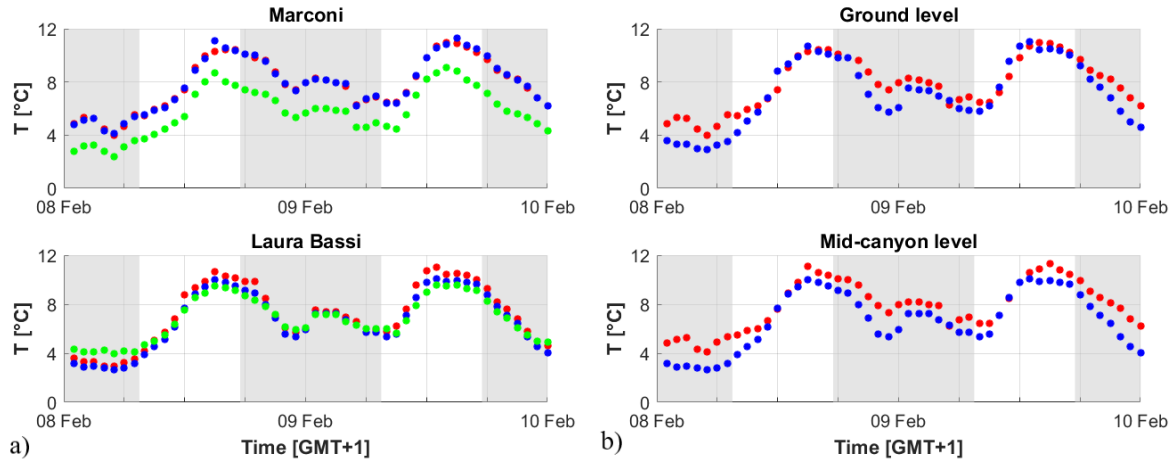


**Figure 5.21:** Time evolution of the air temperature (a) in MA and LB, and their in-canyon comparison (b) during the period 08-09 February. Measurements are taken from the respective GLs (blue), MLs (red) and RLs (green) of the canyons. In (b) red asterisks correspond to MA, the blue ones to LB. The shadowed areas highlight nighttime periods. On average sun rises at 07:30 AM and sets at 17:30 PM (GMT+1).

but the coupling between in-canyons and rooftops seems to be opposite in the two reference streets. Mixing within the canopy is always present, especially in MA where the two signals are completely superimposed (Fig. 5.21a). However, the RL in MA is completely detached, showing the same evolution but with 1-2°C less than the GL and ML temperatures. The heat storage and release processes developed by the buildings and the stagnant air within the canyon preserve the mixed condition. On the other hand, the strength of convective processes is less effective especially above the canopy, where thermal stratification plays a role in regulating air

## 5.2. MEAN CHARACTERISTICS OF THE WINTER CAMPAIGN

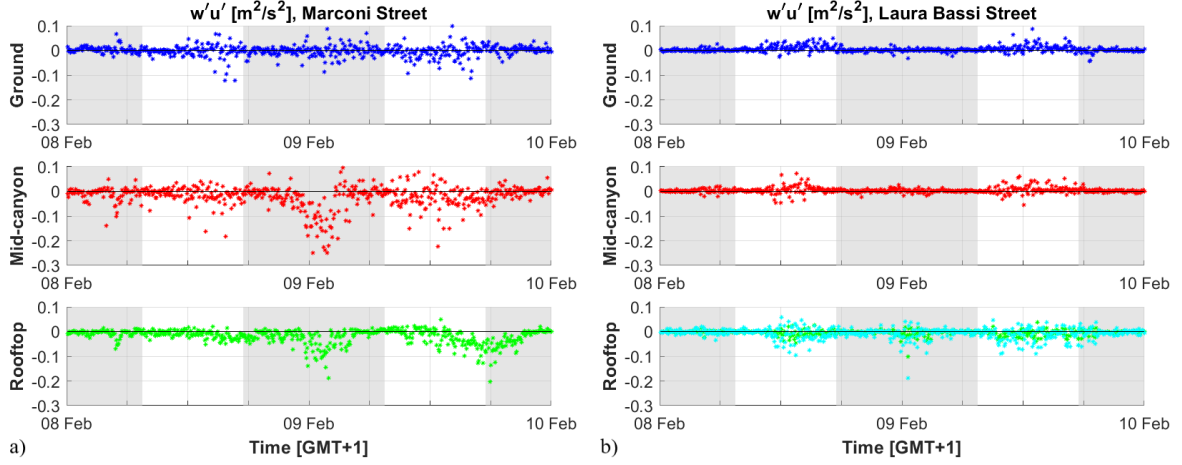


**Figure 5.22:** Time evolution of the TKMF measured in (a) MA and (b) LB during the period 08-09 February. Measurements are taken from the respective GLs (blue), MLs (red), RLs (green) and extrapolated rooftop levels (cyan, specific for LB) of the canyons. The shadowed areas highlight nighttime periods. On average sun rises at 07:30 AM and sets at 17:30 PM (GMT+1).

temperature. LB maintains a clear homogeneity along the profile and during the whole period, as it was already established during the summer period (Fig. 5.8a). Temperature differences between the GLs and the MLs of the two street canyons are smaller than the summer one, but are present also during daytime. Heat release by the buildings, together with the domestic systems heating emissions, seems to have a stronger footprint on MA temperatures, where the density of building packaging is larger. The nighttime urban heat island effect is still present

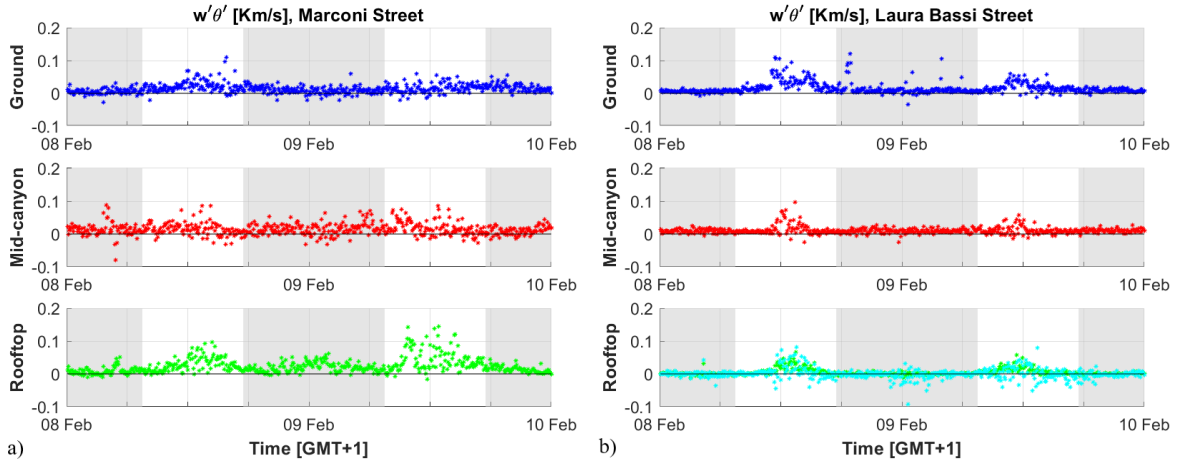


**Figure 5.23:** Time evolution of the TKS HF measured in (a) MA and (b) LB during the period 08-09 February. Measurements are taken from the respective GLs (blue), MLs (red), RLs (green) and extrapolated rooftop levels (cyan, specific for LB) of the canyons. The shadowed areas highlight nighttime periods. On average sun rises at 07:30 AM and sets at 17:30 PM (GMT+1).

CHAPTER 5. RESULTS AND DISCUSSION: OBSERVATIONS AND CAMPAIGN COMPARISON

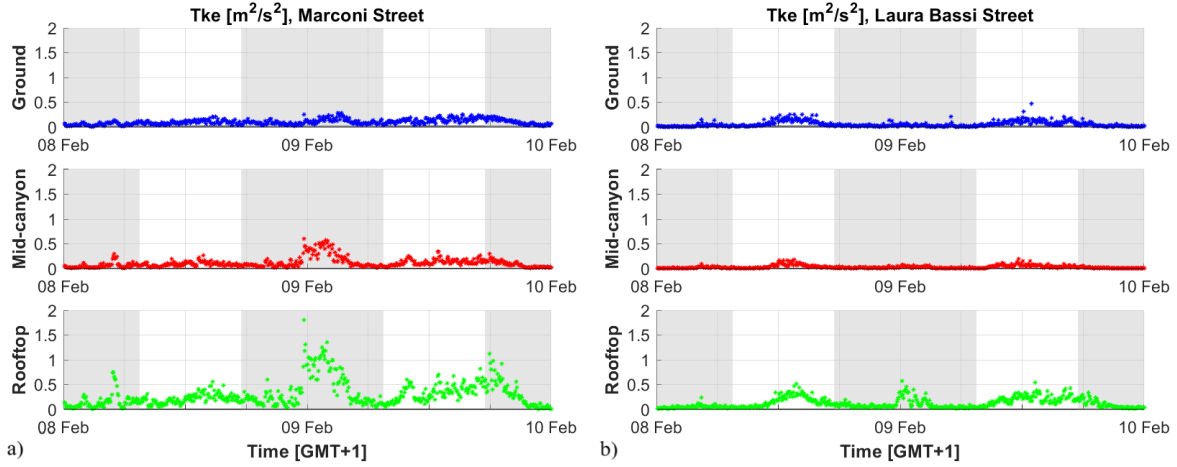


**Figure 5.24:** Time evolution of the  $Tke$  measured in (a) MA and (b) LB during the period 08-09 February. Measurements are taken from the respective GLs (blue), MLs (red), RLs (green) and extrapolated rooftop level (cyan, specific for LB) of the canyons. The shadowed areas highlight nighttime periods. On average sun rises at 07:30 AM and sets at 17:30 PM (GMT+1).

with an intensity similar to the summer one (Fig. 5.8b).

As already introduced describing the summer campaign period, TKMFes are responsible for inducing and sustaining the IC within the canyon, while the TKSHFes have an impact on the thermal aspects and induced dynamics. In a real environment, both aspects contribute to the local transport of pollutants (Dallman et al., 2014). Both TKMF (Fig. 5.22) and TKSHF (Fig. 5.23) measured during the winter period are weaker than during the summer ones. Fluxes

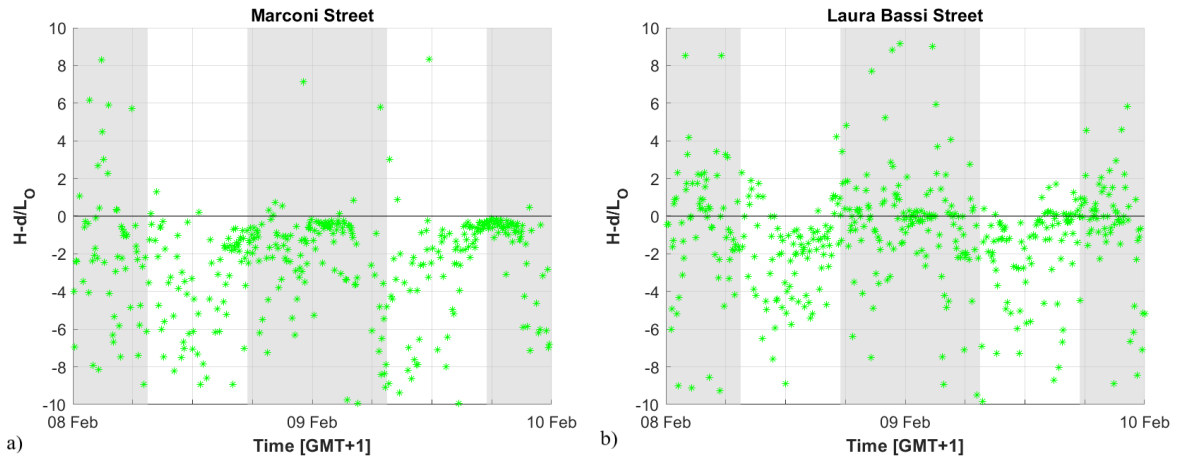


**Figure 5.25:** Time evolution of the stability parameter  $H - d/L_O$  measured in (a) MA and (b) LB during the period 08-09 February. Measurements are taken from the respective RLs (green) of the canyons. The shadowed areas highlight nighttime periods. On average sun rises at 07:30 AM and sets at 17:30 PM (GMT+1).

randomly change directions within both canopies, while at the RLs a certain diurnal pattern is retrieved, especially for the TKSHFes where the large intensity measured during daytimes are balanced by an almost total suppression during nighttime. These behaviors in the fluxes are consequences of the small amounts of TKE (Fig. 5.24) and radiative energy available during the analyzed period. TKE is almost negligible within both canopies, especially during the nighttime in LB. A certain pattern is retrieved at the RLs, but especially in MA it is perturbed by a strong maximum observed within the night between the 08 and the 09 of February. Then the atmospheric flow above the rooftop penetrates the canyon leaving a clear footprint at ML. The inhibition of the turbulent related quantities, with respect of the values observed during summertime, can be partially explained by the stability; the parameter  $H - d/L_O$  (Fig. 5.25) shows less instability with respect to the summer counterparts, especially in LB. Relatively stable conditions are also retrieved during nighttime in LB (which was not the case during the summer period, see Fig. 5.12), while in MA a persistent weak or strong instability is always retrieved, as the large amount of heat release in the canyon by the human activity contributes to sustain surface convection and mixing, lowering the atmospheric stability.

### Normalized $CO$ concentrations

As already discussed for the summer campaign, the  $CO$  concentrations have been chosen to be the passive tracer for the current investigation. Therefore, the measured  $CO$  concentrations are

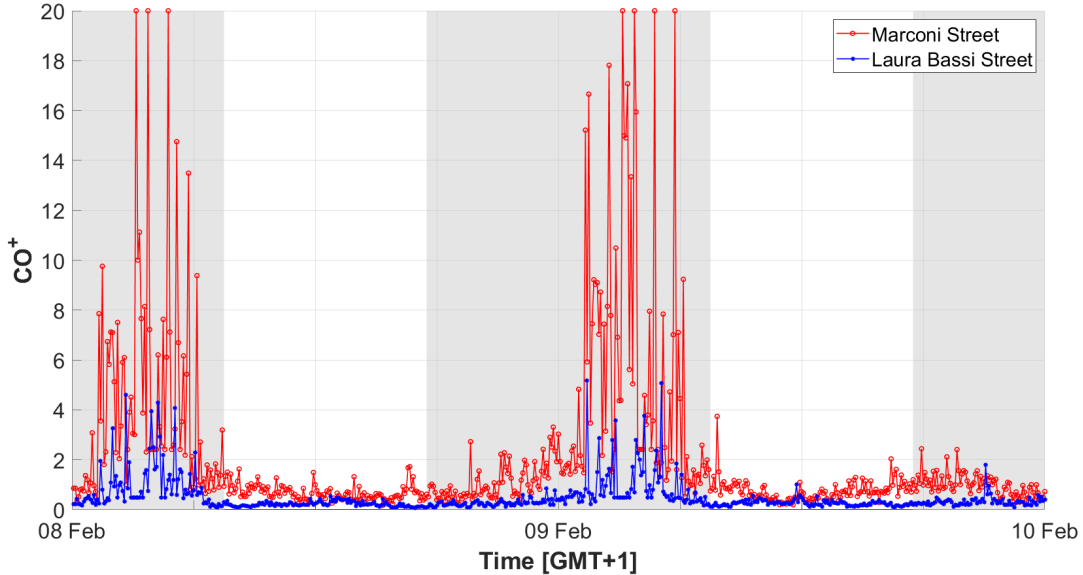


**Figure 5.26:** Time evolution of the 5-minute average normalized carbon monoxide concentrations  $CO^+$  in MA (red) and LB (blue) during the analyzed period (08-09 February). The shadowed areas highlight nighttime periods. On average sun rises at 7:30 AM and sets at 17:30 PM (GMT+1).

## CHAPTER 5. RESULTS AND DISCUSSION: OBSERVATIONS AND CAMPAIGN COMPARISON

normalized following the procedure described in Sect. 4.2.3 also during the winter period (08-09 February). The normalized  $CO^+$  concentrations are shown in Fig. 5.26. MA and LB show the same evolution, but large differences in term of magnitudes. As for the summer period, the  $CO^+$  maximum is reached during the second part of the night and extinguished before sunrise. Daytime hours are more homogeneous and flatten to the minimum background values. For the largest portion of the analyzed period,  $CO^+$  concentrations in MA are more than twice as large as that measured in LB. In a way, this discrepancy is unexpected, since the similarity found during summer (Fig. 5.13). Nevertheless, a densely built area like MA and its neighborhood can be more prone to entrap the air within the canopy with respect to a more open environment like the residential area of LB. Stagnant conditions are exacerbated in MA by the emissions derived from the domestic heating systems, which are less easily diffused than LB because of the building dense displacement and not accounted in the normalization.

As for the summer period, to verify the robustness of the normalized  $CO^+$  against the emission source  $Q_e$  (provided by the traffic) and the wind speed at the RL  $U_H$ , comparisons between those quantities are presented in Fig. 5.27. In both canyons, the resulting  $CO^+$  are found to be independent on traffic emissions (Fig. 5.27a-c) and wind speed at the respective canyon RLs (Fig. 5.27b-d). Therefore, normalized  $CO^+$  concentrations are only dependent on local circulation factors such as turbulent transport.

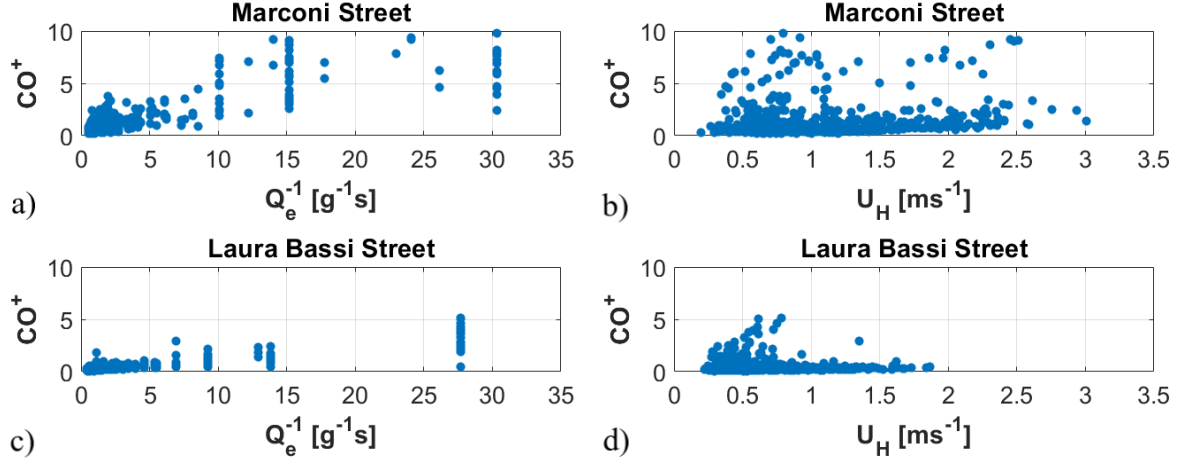


**Figure 5.27:** Normalized  $CO^+$  concentration as function of the emission source  $Q_e$  in (a) Marconi Street and (c) LB, and the rooftop wind speed  $U_H$  in (b) and (d) respectively.

### 5.3 Summary and Conclusions

In this chapter, a characterization of the summer and winter campaign was presented, focusing on the main observations extracted from the measured data. Both canyons have been charac-

terized in terms of air quality and typical meteorological patterns and then focusing on some aspects more crucial for the following investigations, as the normalized pollutant concentration evolution, the local circulation features and turbulent behavior. The seasonality and street canyons comparisons have highlighted the similar and dissimilar behaviors of the reference canyons. In particular, the behavior of the different pollutants certifies the importance of the street canyon effect in both locations (especially in MA), while the seasonality exacerbates the different impacts of multiple emission sources and local atmospheric conditions on the pollutant concentrations. Local atmospheric conditions that indeed show the larger importance of the location rather than the seasonality. Similarity evolution of the mean flow and turbulent related quantities have been retrieved comparing summer and winter periods under weak synoptic forcing, both within and above the canopy, where the majority of the inter-seasonal differences are caused by the different amounts of available energy in the environment. On the contrary, the different morphology and presence of vegetation of the two street canyons have supported regimes of sustained turbulence and mixing in MA, less intense in LB. Atmospheric stability has also forced a seasonality footprint on local flow and turbulent behaviors, weakening the winter wind speed, mechanical and thermal related turbulence magnitudes, while enhancing the same quantities intensity favoring summertime convection and mixing. The results obtained from these observations will provide a baseline for the next chapter analyses on the local characteristics of the urban flows, with the aim of revealing interesting diagnoses on the turbulent exchange processes and their impact on air quality.



## Chapter 6

# Results and Discussion: Exchange Processes between the Canopy Layer and the Urban Boundary Layer

In this chapter, this thesis will describe the results concerning the very local investigation on exchange processes described in Sect. 4.2.2 and vegetation impact on local ventilation, using the experimental campaign data. References to the results of the previous chapter will be required for a better interpretation of the exchange processes behaviors in terms of local flow and turbulence characteristics.

Local features of flow field and turbulent structures are strictly dependent on the background wind direction with respect to the canyon orientation. Single or multiple bi-dimensional vortices can develop within the canopy when the background wind direction is perpendicular to the canyon. Conversely, when wind direction is horizontally tilted, the vortices assume a tri-dimensional helical shape which resembles the structure of a channeled flow when background wind direction is parallel to the canyon orientation. To separate these scenarios, three cases are defined to investigate different wind direction effects. The first accounts for wind East-West Perpendicular (EWP) to the street canyon (angles ranging  $70^\circ - 110^\circ$  for wind coming from east and  $250^\circ - 290^\circ$  from west), the second for the longitudinal north-to-south direction corresponding to the Northerly Parallel (NP) flow (with angles ranging  $-20^\circ - 20^\circ$ ) and the last for longitudinal south-to-north direction corresponding to the Southerly Parallel (SP) flow (with angles in the range  $160^\circ - 200^\circ$ ). All ranges are referred as to the canyon orientation (see Sect. 3.1.1 and Sect. 3.1.2 to the street canyon descriptions). This classification will be largely used through the current and next chapter, to properly interpret the obtained results.

## 6.1 Exchange Processes: Time Scales and Rates

### 6.1.1 Time Scales Evaluation

As defined in Sect. 4.2.2, time scales represent the amount of time required for an exchange process to develop. Time scales are computed at all levels within the canopies and at the rooftop to assess the different speed of the processes. Both canyons were investigated during the summer (20-23 September), using the 5-minute average of the time scales evaluated using Eq. (4.1a) and (4.1b) within the canyons (GL and ML) and Eq. (4.2a) and (4.2b) at the RL. For each time scale (mechanical and thermal at each site), a normalized probability distribution is computed and displayed in Fig. 6.1 and 6.2 respectively identifying MA and LB measurement sites. To improve the readability of the graphs, bin dimensions have been set to 500 s. The distributions

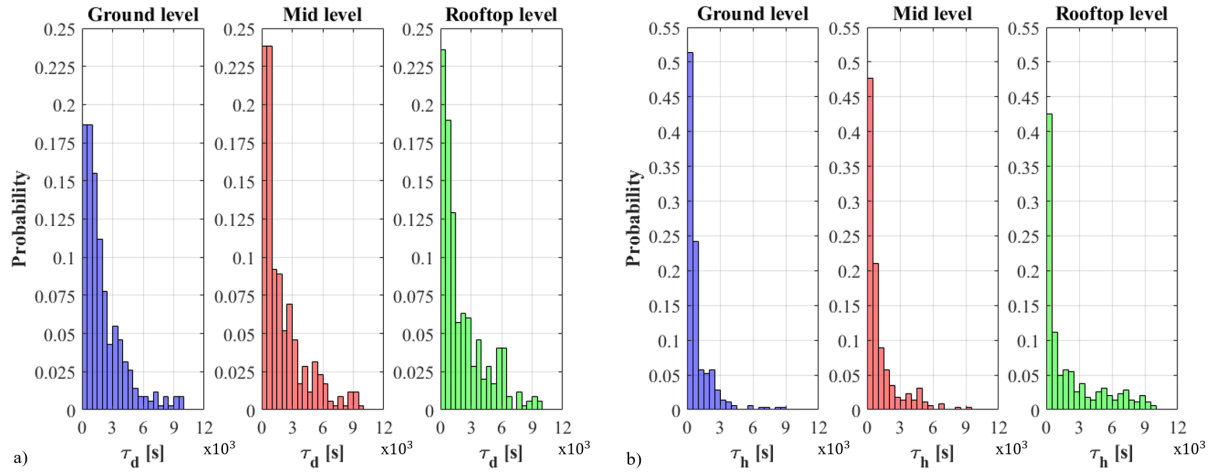


**Figure 6.1:** Normalized density distributions of the 5 minutes average  $\tau_d$  (a) and  $\tau_h$  (b) data inside and above MA during the analyzed period (20-23 September 2017). All the wind direction cases are considered together at each level.

in both canyons present similar shapes, with modes occurring within the first or the first two bins, and long directional tails where occurrences rapidly decrease (with the only exception of  $\tau_d$  in MA, Fig. 6.1a, where the occurrences decrease is smooth). This similarity is the result of a succession of mixed conditions determined by large mechanical and heat transports. When dealing with the RL, mixed conditions can also be induced by small background flow gradients, that decrease stratification and enhance the vertical transport. Fast developing exchange processes are retrieved as the mode of the distributions. Time scales increase when turbulent fluxes are suppressed or overpowered by larger scale gradients. In this last scenario, exchange processes are decreasing their velocity almost monotonically and exponentially, but some extremely slow events have been detected especially within MA canyon (Fig. 6.1a, Ground and Mid level panels). The tails of the distributions are more populated in MA (Fig. 6.1) than in LB (Fig. 6.2),

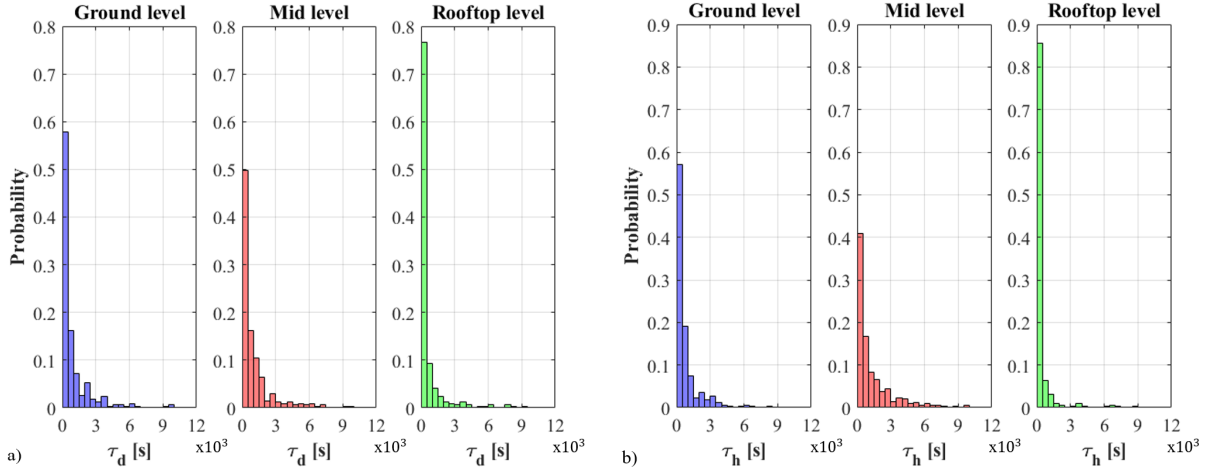


**Figure 6.2:** Normalized density distributions of the 5 minutes average  $\tau_d$  (a) and  $\tau_h$  (b) data inside and above LB during the analyzed period (20-23 September 2017). All the wind direction cases are considered together at each level.

where the distributions are strongly peaked on the modes. In LB local atmospheric and morphological conditions seem to stimulate the development of fast exchange processes with a frequency which is almost always above the 50% of each distribution (apart from Mid level in Fig. 6.2b). Exchanges are much faster than in MA, and there are also less occurrences of extremely slow events. Data distributions in both canyons can be approximated through a probability density function generally used to study the turnover time associated to extreme meteorological events in climatic series. The probability density function that better approximates the shape of the

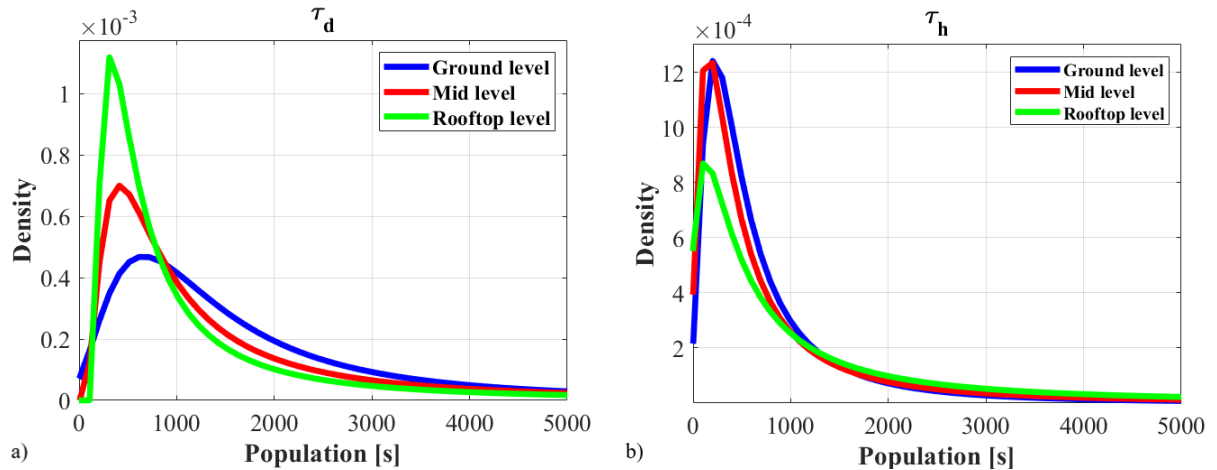


**Figure 6.3:** Generalized extreme value density functions of  $\tau_d$  (a) and  $\tau_h$  (b) distributions in Fig. 6.1 inside and above MA during the analyzed period (20-23 September 2017). All the wind direction cases are considered together at each level.

**CHAPTER 6. RESULTS AND DISCUSSION: EXCHANGE PROCESSES BETWEEN THE CANOPY LAYER AND THE URBAN BOUNDARY LAYER**

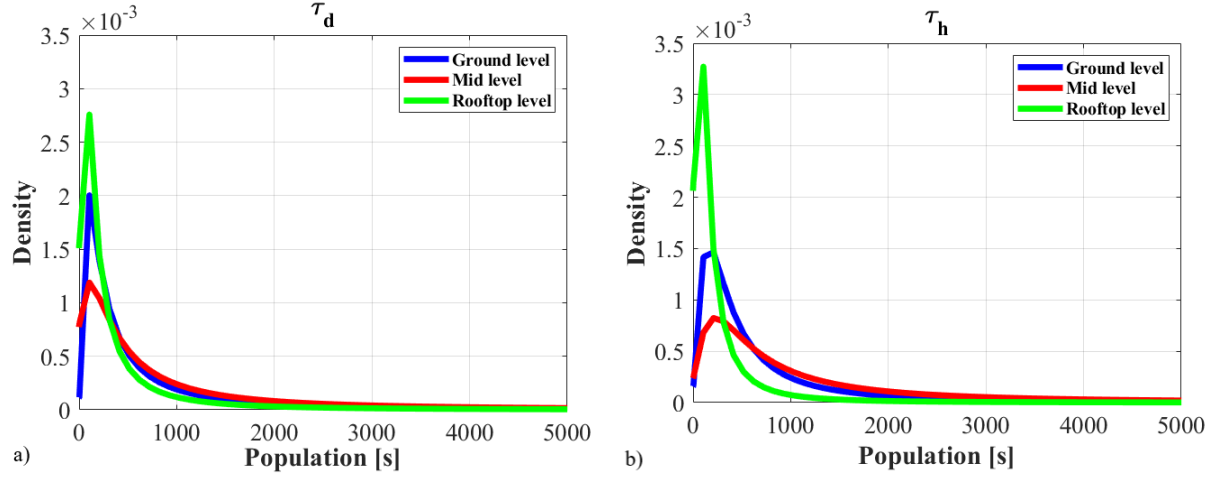


**Figure 6.4:** Generalized extreme value density functions of  $\tau_d$  (a) and  $\tau_h$  (b) distributions in Fig. 6.2 inside and above LB during the analyzed period (20-23 September 2017). All the wind direction cases are considered together at each level.

distributions is the Generalized Extreme Value (GEV)<sup>1</sup> function, whose use can be extended to general asymmetrical tailed distributions (Kotz and Nadarajah, 2000). The GEVs enable the estimation of the modes of the various distributions, together with the directional spread. The same fit is proposed also when the data are discriminated following the wind direction classification and modes related to MA and LB, as shown in Tab. 6.1 and 6.2 respectively. The mode associated errors are estimated as the 10% of the retrieved mode values. The Overall column in Tab. 6.1 and 6.2 stores the modes retrieved from Fig. 6.3 and 6.4. The behavior of  $\tau_d$  in MA is a direct consequence of the flux evolution (Fig. 5.9a), since the TKMF is larger at the RL than inside the canyon. On the other hand,  $\tau_h$  at the RL is smaller than inside the canyon despite the TKSHF is typically more intense inside the canopy. TKSHFs inside the canyon can overpower the rooftop one, since the differential heating of building facades during the day can contribute as an additional heat source increasing the vertical transport (Cheng et al., 2009b). Nevertheless, the background vertical temperature gradients can be weak enough for the time scale computed at the RL to remain small. Comparing the timescales, thermal exchange processes are faster than the mechanical ones. Thermal processes are also more homogeneous within the canopy, where heat is well mixed.  $\tau_d$  and  $\tau_h$  also show different behaviors at GL. The TKMF at the GL can be strongly inhibited by the mechanical friction of the surface roughness (Kastner-Klein and Rotach, 2004), enhancing  $\tau_d$  to a value that is almost twice the ML and almost three times the RL values respectively. This is also evident from Fig. 6.3a where the GL distribution is clearly shifted toward larger values.  $\tau_h$  at the GL is affected by the TKSHF emitted from the surface, which causes a decrease in the time scale enhancing mixing of heat

<sup>1</sup>A brief description of the Generalized Extreme Value distributions is given in Appendix C

## 6.1. EXCHANGE PROCESSES: TIME SCALES AND RATES

		Marconi Street time scales [s]			
		Overall	N Parallel	S Parallel	Perpendicular
$\tau_d$	Ground level	$720 \pm 70$	$310 \pm 30$	$1000 \pm 100$	$620 \pm 60$
	Mid-canyon level	$410 \pm 40$	$310 \pm 30$	$830 \pm 80$	$310 \pm 30$
	Rooftop level	$250 \pm 30$	$310 \pm 30$	$1300 \pm 100$	$210 \pm 20$
$\tau_h$	Ground level	$210 \pm 20$	$160 \pm 20$	$160 \pm 10$	$200 \pm 20$
	Mid-canyon level	$210 \pm 20$	$110 \pm 10$	$310 \pm 30$	$200 \pm 20$
	Rooftop level	$160 \pm 20$	$110 \pm 10$	$720 \pm 70$	$100 \pm 10$

**Table 6.1:** Table summarizing the characteristic time scales  $\tau$  in MA derived from the modes of the probability density functions computed for the whole period overall flow, NP, SP and EWP background wind direction cases.

and pollutants (Li et al., 2012). This condition of surface mixing persists during nighttime (Fig. 5.10a), reducing the spread of the time scale distribution (Fig. 6.3b, Ground level). The same distribution is retrieved for  $\tau_h$  at ML (Fig. 6.3b, Mid level), due to the heat emission from the buildings facades, which enhances the thermal mixing of the canopy. GEV distributions related to LB are displayed in Fig. 6.4. The behavior of time scales in LB seem to oppose that of MA. The Overall values of  $\tau_d$  are more homogeneous than  $\tau_h$ . The roughness effects typical of the GL of MA is not found in LB, as a possible consequence of the lateral entrainment that enhances the turbulence. Moreover, the GL flow is subjected to the acceleration due to the increased pressure generated by the tree crown.  $\tau_h$  varies with the level inside and above the canyon. At the GL, the thermal related time scale is very small despite TKSHFes are smoothed by the tree shadowing effect (Fig. 5.10). The ML is the slowest of the Overall  $\tau_h$  values, probably smoothed by the small volume where the flow and turbulence develop. The RL is similar to that retrieved in MA, since there are not much horizontal differences in term of TKSHFes (Fig. 5.10). The modes from the GEV distributions for each wind direction are stored in Tab. 6.1 and 6.2 (N Parallel, S Parallel and Perpendicular columns). In MA,  $\tau$  follows the distributions identified in Fig. 6.1, in agreement with the probability density functions obtained by Lo and Ngan (2017) with their Lagrangian model. When the background wind is NP to the canyon, the air column is well mixed within and above the canyon by the turbulent transport and the heat release from the surfaces. Modes retrieved from SP background wind direction show the larger time scale values among the different wind direction cases, corresponding to small and rapidly changing TKMF and TKSHF. In these conditions, exchange processes develop at different time scales, as identified from the mode stored in the S Parallel column of Tab. 6.1. A certain difference is also evident in  $\tau_d$  and  $\tau_h$  for the EWP background wind direction. Mechanical time scales are small in the upper part of the canyon, while roughness is still efficient in inhibiting the TKMF at the GL, enhancing  $\tau_d$ .  $\tau_h$  is again homogeneous inside the canyon and faster at the RL. The

**CHAPTER 6. RESULTS AND DISCUSSION: EXCHANGE PROCESSES BETWEEN THE CANOPY LAYER AND THE URBAN BOUNDARY LAYER**

		Laura Bassi Street time scales [s]			
		Overall	N Parallel	S Parallel	Perpendicular
$\tau_d$	Ground level	100 ± 10	50 ± 5	210 ± 20	100 ± 10
	Mid-canyon level	110 ± 10	67 ± 7	200 ± 20	110 ± 10
	Rooftop level	110 ± 10	90 ± 9	100 ± 10	83 ± 8
$\tau_h$	Ground level	78 ± 8	160 ± 20	180 ± 20	140 ± 10
	Mid-canyon level	210 ± 20	95 ± 10	370 ± 40	110 ± 10
	Rooftop level	100 ± 10	41 ± 4	80 ± 8	92 ± 9

**Table 6.2:** Table summarizing the characteristic time scales  $\tau$  in LB derived from the modes of the probability density functions computed for the whole period overall flow, NP, SP and EWP background wind direction cases.

homogeneity retrieved in LB, for the Overall  $\tau_d$  case, is slightly less evident for the specific wind direction intervals (Tab. 6.2). Nevertheless, the canopy is still homogeneous, creating a small decoupling with the RL and the atmosphere above it. Differently classified  $\tau_h$  oppose the Overall behavior. The GL is generally interested by the slowest time scales during NP and EWP wind directions, which are typical of the daytime hours and when the shadowing effects can minimize the heat storage by the ground. During SP wind direction, typical of the nighttime, the ML time scale is larger and mostly accounting for the condition where the exchange processes are slow. The RL time scales are similar to  $\tau_d$  values and faster than the in-canyon ones.

Modes of the mechanical time scales for EWP background wind direction (table 6.1) can be compared with recirculation and pollutant removal times from literature. The vortex recirculation time  $T = H/u_*$ , generally used in CFD simulations to identify the time scale of turbulent motions in street canyon, computed for EWP background wind directions, ranges between 90 and 490 s, with a mean value of 200 s.  $\tau_d$  calculated for EWP background wind direction at the RL ( $\tau_d^{p,r}=210$  s) is also in agreement with Salizzoni et al. (2009) pollutant removal time  $T=200$  s computed with the current investigation parameters.  $\tau_d^{p,r}$  aligns also with Lo and Ngan (2017) Lagrangian time scales, re-computed for the aspect ratio of the current investigation, which range between 198s and 269s.

### 6.1.2 Exchange Rates Evaluation

Equations (4.5a) and (4.5b) describe the turbulent mixing and transport rates of atmospheric particles inside the canyon, considering separately mechanical and thermal processes.  $\eta < 1$  describes an advantageous condition for momentum and heat transport toward higher levels and exchange with the free atmosphere. Exchange processes are faster within the canopy than at the rooftop, and momentum and heat are pushed toward the upper layers of the canopy.

When  $\eta > 1$ , mixing inside the canyon is less efficient and air is trapped within the canyon. Momentum and heat are efficiently exchanged only in the upper part of the canopy, forcing a recirculation mechanisms toward the ground. Fig. 6.5 and 6.6 show the distribution of  $\eta$  defined in Eq. (4.5a) and (4.5b) in MA and LB respectively. Values of  $\eta$  are averaged over a 30-minute interval to ensure the robustness of the following analysis, and distribution bins are 0.5 units wide.  $\eta$  is referred to the GL when it is calculated as the ratio between  $\tau$  evaluated at the RL and the GL, or to ML when the ratio includes  $\tau$  evaluated at the RL and the ML. The

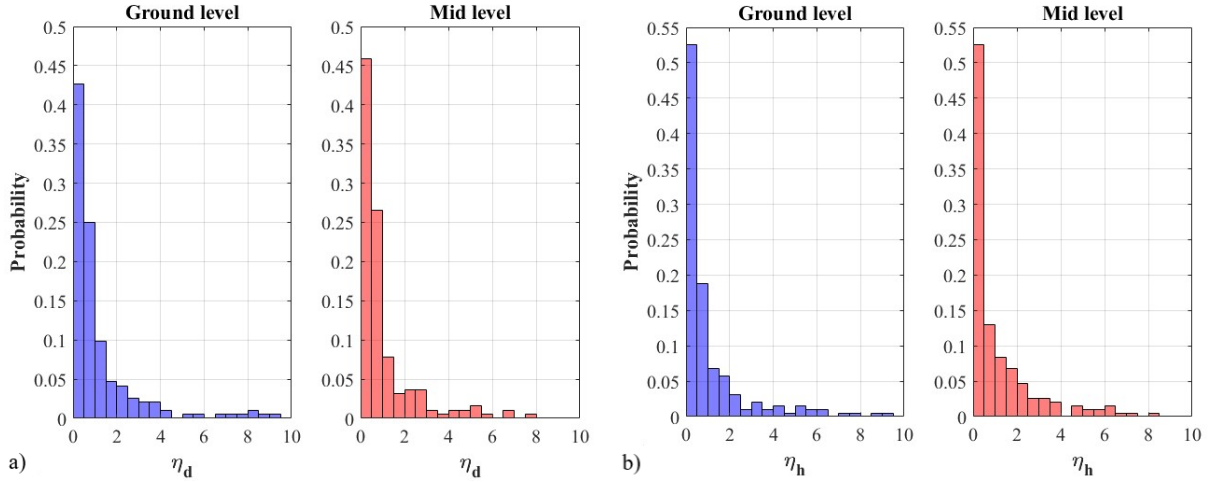


**Figure 6.5:** Normalized density distributions of  $\eta_d$  (a) and  $\eta_h$  (b) data inside and above MA during the analyzed period (20-23 September 2017). All the wind direction cases are considered together at each level.

$\eta$  frequencies evaluated in MA (Fig. 6.5) are clearly shifted toward the first two bins of the distributions, describing a scenario whose cumulative probability is about the 50-75% of the total. In this scenario  $\eta$  is less than 1, and exchange processes developing within the canopy are faster than the one involving the canyon top, describing favorable conditions for momentum and heat transport away from the inner part of the canopy. The remaining 25-50% accounts for the disadvantageous scenario where  $\eta > 1$  and exchange processes within the canopy are slower than the one at the rooftop and momentum and heat are trapped close to the ground. The most disadvantageous scenario from these distributions is represented by the  $\eta_d$  in LB (Fig. 6.6a), where there is an almost perfect balance in the occurrences of favorable and unfavorable mixing conditions. These considerations are verified not considering the  $\eta_h$  in LB, which distributions show almost the opposite behaviors with respect to the others (Fig. 6.6b). This anomalous behavior will be addressed lately in this section.

As done for the time scales,  $\eta$  distributions can be fitted by the GEV curves. Tab. 6.3 stores the modes of the of the GEVs in MA again considering separately mechanical and thermal processes, and the wind direction classification already adopted in Tab. 6.1 and 6.2. Modes in the Overall

**CHAPTER 6. RESULTS AND DISCUSSION: EXCHANGE PROCESSES BETWEEN THE CANOPY LAYER AND THE URBAN BOUNDARY LAYER**

		Marconi Street exchange ratios			
		Overall	N Parallel	S Parallel	Perpendicular
$\eta_d$	Ground level	$0.65 \pm 0.07$	$0.46 \pm 0.05$	$0.12 \pm 0.012$	$0.47 \pm 0.05$
	Mid-canyon level	$0.75 \pm 0.08$	$0.34 \pm 0.03$	$0.22 \pm 0.02$	$0.34 \pm 0.03$
$\eta_h$	Ground level	$0.67 \pm 0.07$	$0.47 \pm 0.05$	$0.15 \pm 0.015$	$0.25 \pm 0.03$
	Mid-canyon level	$0.58 \pm 0.06$	$0.59 \pm 0.06$	$0.10 \pm 0.01$	$0.12 \pm 0.012$

**Table 6.3:** Table summarizing the characteristic exchange rates  $\eta$  in MA derived from the modes of the probability density functions computed for the whole period overall flow, NP, SP and EWP background wind direction cases.

column assesses the mean behavior of the distribution fits when no wind direction classification is applied and shows a certain homogeneity within the canopy and between mechanical and thermal processes, with the latter slightly more efficient than the first. When the wind direction classification is applied, the efficacy of the exchange processes increases in each case with respect to the overall one, especially when the background flow is SP to the canyon. This efficiency retrieved in south parallel condition is favored by the large  $\tau$  measured at the RL (Tab. 6.1). NP and EWP conditions are equally efficient when dealing with mechanical processes. For thermal processes, the EWP background wind direction is almost equal to the SP one.  $\eta$  distributions evaluated in LB (Fig. 6.6) are wider and less peaked than the MA ones. Thermal processes probabilities follow a smooth decrease with the increasing bins, and a considerable portion of the distribution occupies the last quartile of them, particularly evident for the ML

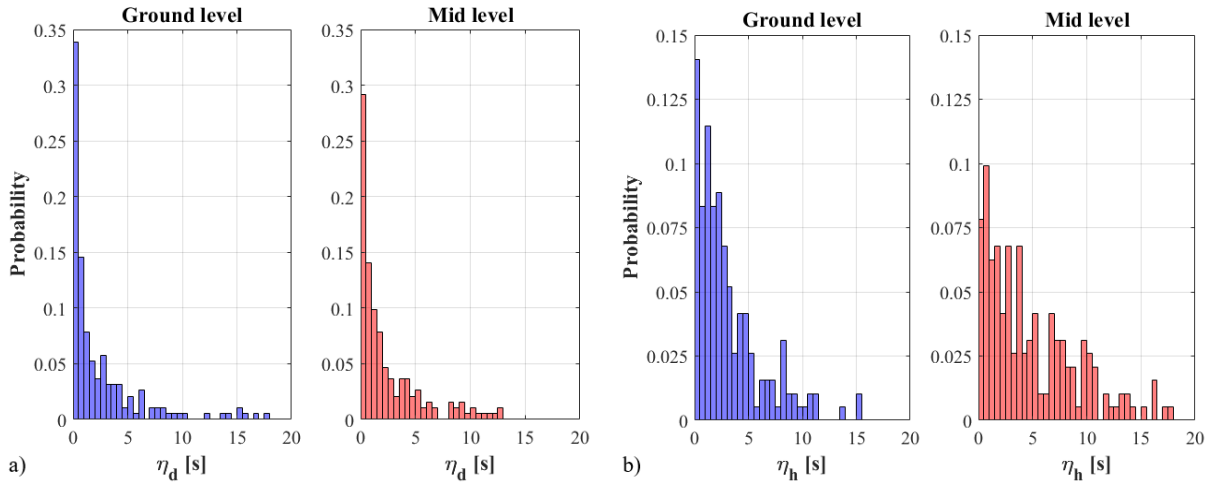


**Figure 6.6:** Normalized density distributions of  $\eta_d$  (a) and  $\eta_h$  (b) data inside and above LB during the analyzed period (20-23 September 2017). All the wind direction cases are considered together at each level.

		Laura Bassi Street exchange ratios			
		Overall	N Parallel	S Parallel	Perpendicular
$\eta_d$	Ground level	$0.28 \pm 0.03$	$0.20 \pm 0.02$	$0.11 \pm 0.011$	$0.16 \pm 0.016$
	Mid-canyon level	$0.39 \pm 0.04$	$10.00 \pm 1.00$	$0.15 \pm 0.015$	$0.16 \pm 0.016$
$\eta_h$	Ground level	$0.24 \pm 0.02$	$7.40 \pm 0.70$	$1.80 \pm 0.18$	$1.20 \pm 0.12$
	Mid-canyon level	$0.22 \pm 0.02$	$7.50 \pm 0.80$	$2.00 \pm 0.20$	$1.50 \pm 0.15$

**Table 6.4:** Table summarizing the characteristic exchange rates  $\eta$  in LB derived from the modes of the probability density functions computed for the whole period overall flow, NP, SP and EWP background wind direction cases.

distribution (Fig. 6.6b). The probability of having stagnant conditions within the canopy is much larger than in MA, despite LB is wider and with a favorable aspect ratio. Differences with MA arise from the different behaviors of momentum and heat fluxes in the two street canyons (Fig. 5.9b and 5.10b). During night periods, both fluxes in LB are almost null within the canopy while at the rooftop they are still on the same order of magnitude of the daytime ones. Therefore, in-canyon time scales are generally larger during nighttime than both the daytime ones and the ones evaluated at the RL. However, daytime TKMFes are generally larger within the canopy and the exchange rates are strongly influenced by it. Except for ML north parallel conditions, mechanical exchange rates show strongly efficient modes for each wind direction case and for the overall scenario (Tab. 6.4). On the contrary, TKSHFes are always increasing with the increasing level from the ground. As a consequence, for large fractions of the day, disadvantageous conditions are established and exchange processes are strongly inhibited. Tab. 6.4 supports again the distribution behaviors, depicting disadvantageous scenarios for all wind direction cases. Only the overall condition of  $\eta_h$  shows a strong efficacy, accounting for intermediate scenarios between the analyzed wind directions.

### 6.1.3 Comparison between the Exchange Rates and the Normalized Pollutant Concentrations

In the previous analysis of this chapter, mechanical and thermal processes have been kept separate to investigate the characteristics exchange processes related to the IC and TC that can develop within a real canopy. However, the circulation drivers can change during the day, following variations of some mean atmospheric properties, such as the background wind direction and speed, or the radiative budget through a modification of the incoming solar radiation with the solar path. These variations can cause a change of the circulation type and intensity, which can be sudden and evanescent. Another aspect to be taken into account is the mutual development of the two circulations at the same time. In a real urban environment, it is generally common

## CHAPTER 6. RESULTS AND DISCUSSION: EXCHANGE PROCESSES BETWEEN THE CANOPY LAYER AND THE URBAN BOUNDARY LAYER

to have both drivers of the two circulations active at the same time, i.e. a mean flow above the canopy, from which turbulent momentum transport can drive and sustain the IC in the canopy, and the horizontal temperature gradient between opposite building facades that induces the TC. It is therefore important not only to establish a criterion to identify the circulation type, but also to assess if the dominant one is sufficiently stronger to overpower the other. The knowledge of the dominant circulation at the evaluation time is fundamental to understand which exchange process is the most active, i.e. which process drives the exchanges between the canopy and the atmosphere above.

The dominant circulation developing within the canopy has an impact on the pollutant concentrations removal from the canopy. Under the assumption of mass transport behaving as momentum and heat transports, pollutant concentrations are expected to follow the exchange rates. Since exchange rates provide information about the refreshing properties of the canyon, it is legitimate to assume  $CO^+$  concentrations to be driven by the efficacy of the exchange processes at different levels inside and above the canopy. Depending on the most effective circulation, the corresponding  $\eta$  would be the best choice to assess the  $CO^+$  concentration behavior. To strengthen the assumption of mass transport behaving as the momentum and heat ones, a qualitative analysis is presented and supported by Fig. 6.7 where the  $CO^+$  concentration distributions in MA and LB are fitted by their most likely curves. As already evaluated for time

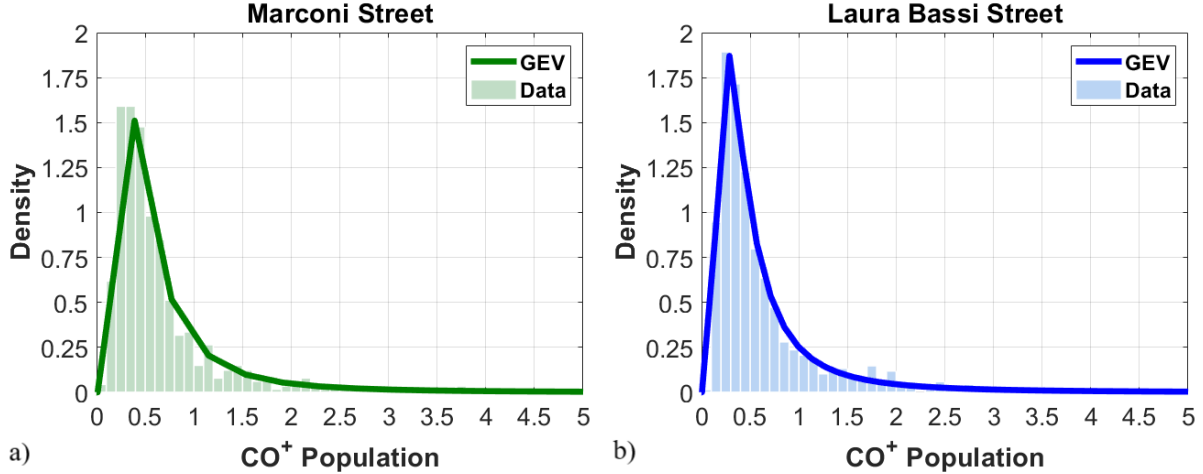


**Figure 6.7:** Data distributions and relative fits for the normalized  $CO^+$  concentrations in (a) MA and (b) LB.

scales and exchange rates, also  $CO^+$  concentrations follow a GEV distribution. Distributions in the street canyons are very similar, as established from the time series in Fig. 5.1, with LB showing more events in the mode value than MA that shows a larger spread around the peak. The fact that  $CO^+$  concentrations follow a GEV distribution is a qualitative verification of their behaviors similar to the exchange processes diagnostic quantities. Therefore it is legitimate to

suppose the mass concentration of a passive tracer to be regulated by the turbulent exchange processes evaluated within this chapter.

To discern the importance of the IC over the TC, the buoyancy parameter has been introduced by Dallman et al. (2014) and described in Sect. 2.2.1, Eq. (2.6), as the ratio between horizontal buoyancy and background wind speed

$$B = \frac{g\alpha H\Delta T}{U_b^2 \left(1 + \left(\frac{H}{L}\right)^2\right)}, \quad (6.1)$$

where  $g$  ( $\text{ms}^{-2}$ ) is the gravitational acceleration,  $\alpha = \bar{T}^{-1}$  ( $\text{K}^{-1}$ ) is the thermal expansion coefficient equal to the mean canyon temperature (evaluated as the mean between the measured temperatures at GL and ML),  $\Delta T$  (K) is the temperature difference between opposite building facades within the canyon. Eq. (6.1) is calculated for the whole period and compared to its critical value  $B_c$  (Fig. 6.8), defined as the threshold separating IC and TC regimes and retrieved from both street canyons by displaying the wind speed ratio between the in-canopy and the background wind speed  $U_C/U_b$  as a function of  $B$ .  $U_C$  ( $\text{ms}^{-1}$ ) identifies either MA (subscript *ma*) or LB (subscript *lb*) mean canopy wind speed. The critical value  $B_c$  is evaluated directly from data, considering as  $U_C$  the average between the GL and the ML measured wind speeds in both canopies, while  $U_b$  is taken from SI monitoring site. Being a threshold between two regimes,  $B_c$  must identify a change in the behavior of  $U_C/U_b$  with  $B$ . The wind speed ratio is supposed to be constant with  $B$  until the in-canopy circulation is inertial, since the in canyon velocity is expected to scale only with the background velocity. Conversely, when the circulation

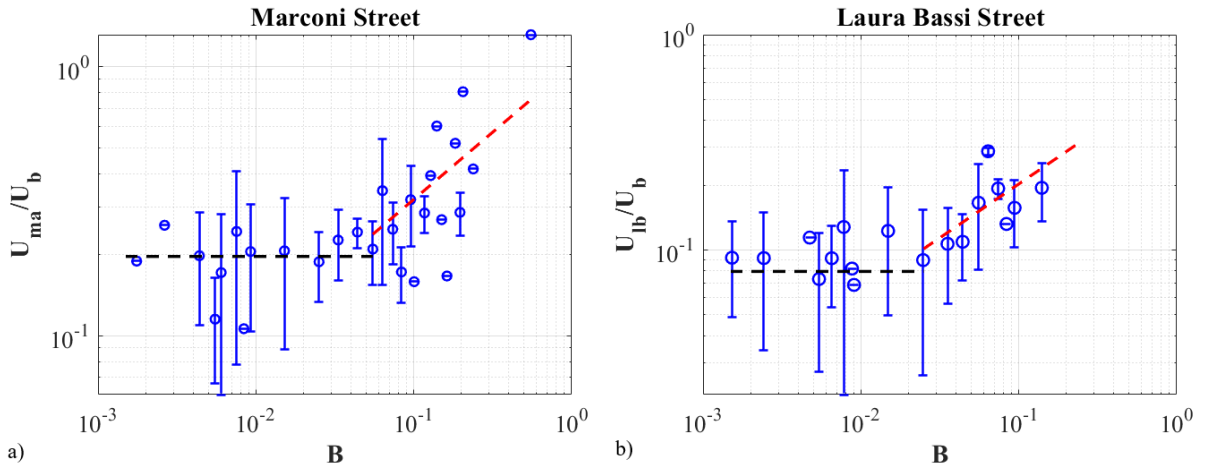


**Figure 6.8:** Wind speed ratios  $U_C/U_b$  as a function of  $B$  in (a) MA and (b) LB. Wind speed ratios are averaged over  $B$  bins and the errorbars represent the standard deviation computed in each bin. Dashed lines are the trends from which Eq. (6.2) are extrapolated, black the one associated with the IC and red the one associated with the TC.

## CHAPTER 6. RESULTS AND DISCUSSION: EXCHANGE PROCESSES BETWEEN THE CANOPY LAYER AND THE URBAN BOUNDARY LAYER

---

becomes thermally driven, the wind speed ratio has to depend on  $B$ , which in turn depends on the circulation drivers, i.e. the horizontal temperature gradient between opposite building facades. Fig. 6.8 shows that the critical value of the buoyancy parameter is slightly dependent on the local morphology, since it changes from a value  $B_c \approx 0.03$  in LB to a value  $B_c \approx 0.06$  in MA, in agreement with the common value retrieved from the literature of approximately 0.05. From the distributions in Fig. 6.8, two different trends per street canyon are extrapolated, identifying the inertial and the thermal circulation regimes. From the trends in Fig. 6.8, an approximate dependency of the wind speed ratios from  $B$  is extrapolated and reported in Eq. (6.2)

$$\frac{U_C}{U_b} \sim \begin{cases} C_1, & \text{if } B < B_c \\ C_2 \cdot B^{1/2}, & \text{if } B > B_c, \end{cases} \quad (6.2)$$

where the proportionality constants  $C_1$  and  $C_2$  are evaluated from Fig. 6.8 and are found to be equal to 0.20 and 0.41 respectively in MA and 0.08 and 0.64 in LB. Once the critical values of the buoyancy parameter are retrieved, the time evolution of  $B$  is used to identify IC and TC regimes. Fig. 6.9 shows the evolution of  $B$  in MA and LB while the respective thresholds are highlighted with the black dashed lines. The common behavior of the canopies is found to develop following the IC regime during daytime and late night hours, while the TC is dominant across sunset when the differential heating between opposite facades is maximized. In LB, the TC is also present around sunrise while in MA the late night IC is still predominant. This difference between street canyons can be explained by the maintenance of nocturnal conditions in MA due to the difficulty of the weak sunbeams of the early morning in breaking the nocturnal mixing of the inner canopy. Conversely, in LB sunbeams can easily reach the buildings even in the early morning despite the shadowing effects of the trees. Once the regime is identified, a total exchange rate  $\eta_t$  is defined as follows

$$\eta_t = \begin{cases} \eta_d, & \text{if } B < B_c \\ \eta_h, & \text{if } B > B_c, \end{cases} \quad (6.3)$$

so that it accounts for the heat exchanges when the circulation is thermal and the momentum exchange when the circulation is inertial.  $\eta_t$  describes the total behavior of the exchange processes related to street canyon circulation and will be used to assess the mass removal of a passive tracer like  $CO^+$ . Fig. 6.10 shows the comparison between  $\eta_t$  and the  $CO^+$  concentrations in MA at both GL and ML within the canopy. The  $\eta_t$  evolution follows the diurnal path of  $CO^+$  concentrations especially during the first three days, with maximum at sunrise and minimum during the early night. The agreement is almost lost during the last day at both GL and ML due to the unusual longer lasting predominance of the TC during the daytime. Large oscillations in  $\eta_t$  are instead consequences of the large variability in the TKMF (Fig. 5.9

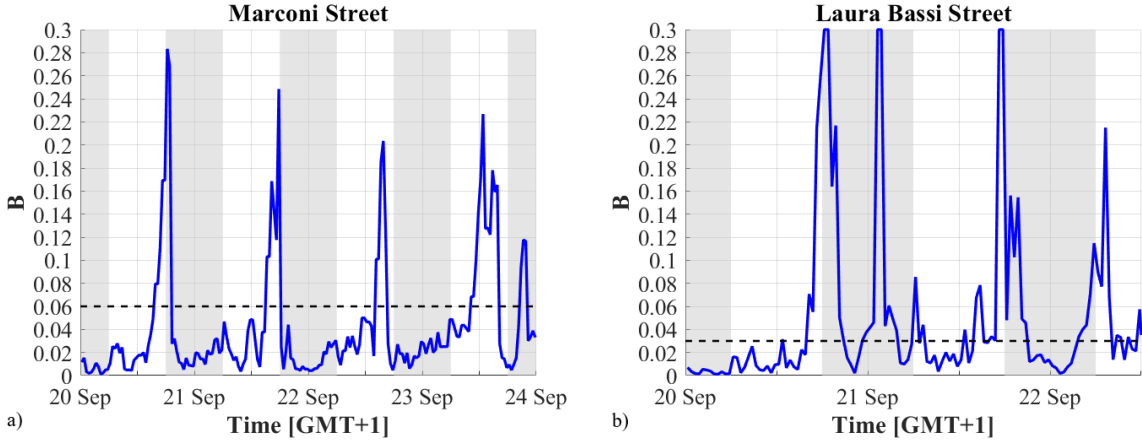


**Figure 6.9:** Time evolution of the buoyancy parameter  $B$  defined by Eq. (6.1) in (a) MA and (b) LB. The dashed lines highlight the critical values  $B_c$ . The shadowed areas highlight nighttime periods. On average sun rises at 6:00 AM and sets at 18:00 PM (GMT+1)

and the TKSHF 5.10), which evolution show more rapid oscillations than for a bulk quantity like  $CO^+$  concentration. Peaks of  $CO^+$  concentrations are retrieved when  $B$  is close to  $B_c$ , i.e. when there is not a predominance of one in-canyon circulation on the other. This behavior can also explain why  $\eta_t$  peaks are generally larger than  $CO^+$  concentrations. Conversely, when close to transition between IC and TC, both exchange processes can also be equally important (Dallman et al., 2014). When a circulation is well established ( $B \gg B_c$  or  $B \ll B_c$ ),  $CO^+$  concentrations are small and well described by  $\eta_t$ . Fig. 6.11 shows the comparison between  $\eta_t$  and the  $CO^+$  concentrations evolution in LB at the GL and ML of the canopy. As already found for MA comparison,  $\eta_t$  and  $CO^+$  concentrations show a really good agreement during the day-

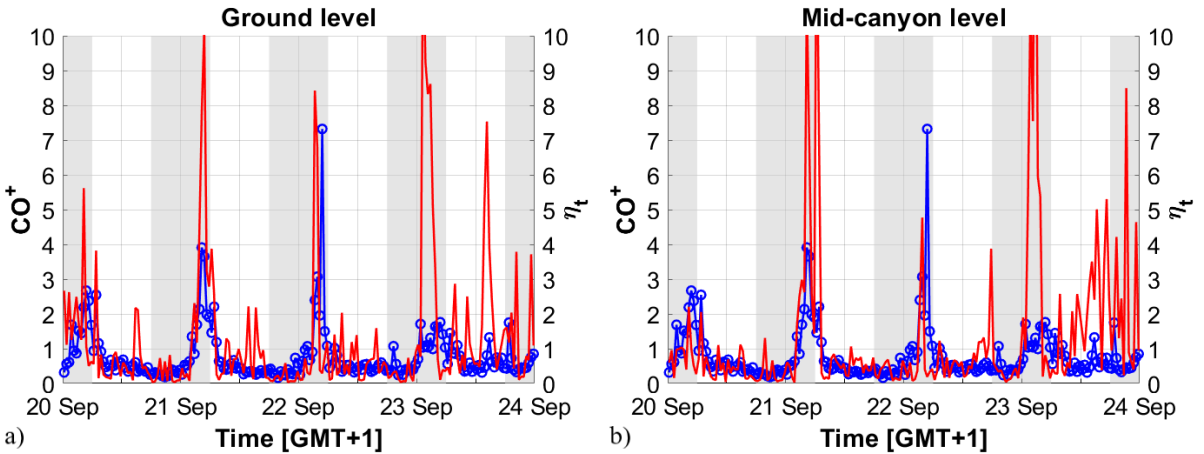


**Figure 6.10:** Evolution comparison between  $CO^+$  (blue) and  $\eta_t$  (red) for (a) the GL to RL and (b) the ML to RL exchange rates in MA.

**CHAPTER 6. RESULTS AND DISCUSSION: EXCHANGE PROCESSES BETWEEN THE CANOPY LAYER AND THE URBAN BOUNDARY LAYER**

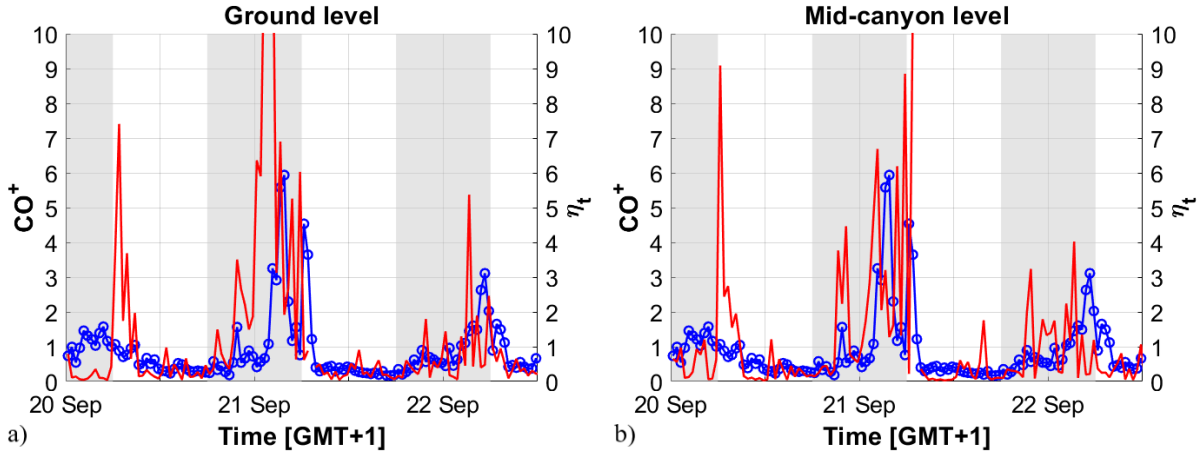


**Figure 6.11:** Evolution comparison between  $CO^+$  (blue) and  $\eta_t$  (red) for (a) the GL to RL and (b) the ML to RL exchange rates in LB.

time hours, when the concentrations are flattened to their minimum value by efficient turbulent transport mechanisms. During nighttime,  $\eta_t$  seems to anticipate and overestimate the pollutant concentrations probably because there is a certain delay time between the establishment of the nocturnal regime and the impact it may have on  $CO^+$  concentrations. In analogy to MA,  $\eta_t$  is again more oscillating than  $CO^+$  concentrations due to the rapid variation in the fluxes evolution (Fig. 5.9b and 5.10b), while secondary peaks can be related to transitional intervals between the two circulations. Definitely, exchange processes based on both IC and TC can be good tools to assess passive pollutant concentrations evolution within an urban canopy.

**6.1.4 The Circulation Regime Identification: use of New Parametrizations to Compare Different Street Canyon Flow Characteristics**

The buoyancy parameter  $B$  was found to be a useful and simple tool to identify the circulation regime within a street canyon (Sect. 2.2.1). The evaluation of this parameter was performed by Dallman et al. (2014) in the semi-idealized environment shown in Fig. 6.12. A semi-idealized environment term is used to identify those investigations taken in real environments, such as the sloping park in Fig. 6.12, which are deliberately modified by artificial ideal objects that replicate real obstacles, like the containers representing two lines of buildings. This way a semi-idealized street canyon is built and it is subjected to real atmospheric phenomena. Such operative domains are generally in the middle between laboratory and field experiments since they introduce a certain degree of control (e.g. the building shape, dimension and location, the street canyon aspect ratio) in a real environment. A comparison of the behaviors of Dallman et al. (2014) parameter between their and the current analysis is shown. The analysis also gives the opportunity to test new and modified parametrizations on in-canyon flow characteristics that can enhance

the current comparability and propose themselves as simple way to compare street canyons with different aspect ratio. Following the current investigations, only three different street canyons will be compared, but the hope is to give a hint for further extension. The applicability of the

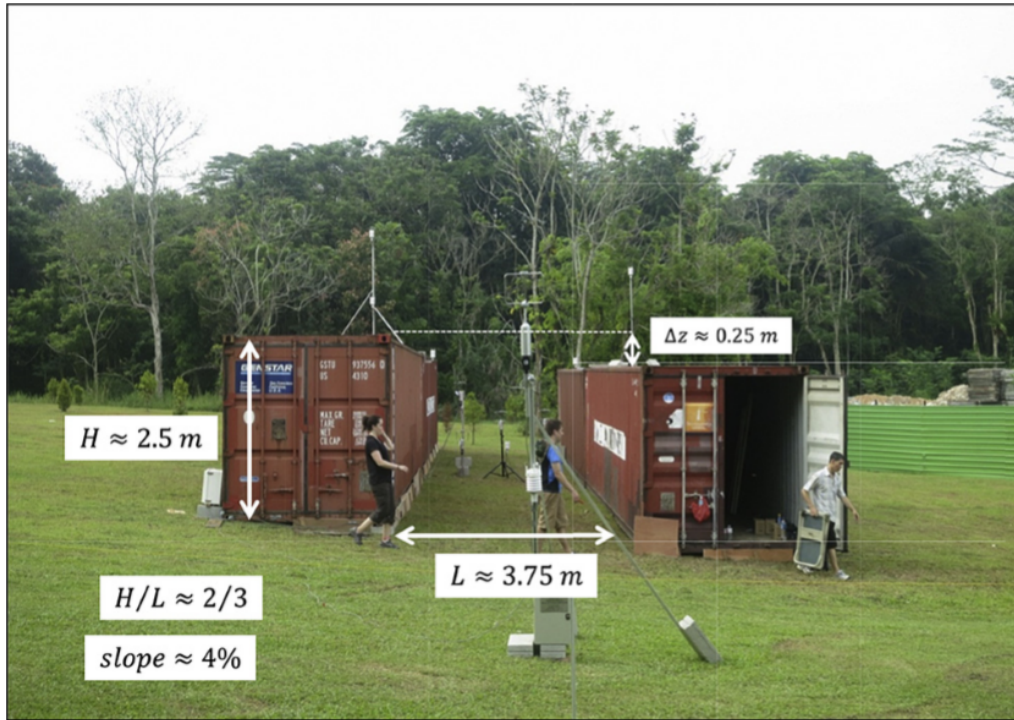


**Figure 6.12:** Experiment setup, with aspect ratio shown. The view is looking towards north (Source: [Dallman et al. \(2014\)](#)).

soon to be proposed parametrizations seems to be given by the aspect ratio, which in turn is the key parameter to identify the flow regime developing within the canopy. From geometrical considerations on both MA and LB discussed in Sect. 4.2.2, it was established that both street canyons inner circulations follow the skimming flow regime introduced by [Oke \(1987\)](#). The classification made by [Oke \(1987\)](#) was based only on the street canyon aspect ratio in an idealized isothermal street canyon without vegetation but it will be considered as reliable for both the analyzed street canyons and the [Dallman et al. \(2014\)](#) one. In fact all the streets in Bologna and [Dallman et al. \(2014\)](#) street canyons have an aspect ratio larger than 0.7, the [Oke \(1987\)](#) threshold for the skimming flow regime to develop. This first analogy ensures a certain comparability between the three canyons and was considered as a basic condition among which defining the parametrizations and fulfill the comparisons. Another hint from literature toward the enhancement of canyons comparability is given by [Soulhac et al. \(2008\)](#) where the wind speed ratio between the in-canyon and the background wind speed was found to be a linear decreasing function of the aspect ratio  $H/W$  when this last parameter is larger than 0.5. On the basis of this analysis, a simple scaling is proposed to compare wind speed ratios obtained

## CHAPTER 6. RESULTS AND DISCUSSION: EXCHANGE PROCESSES BETWEEN THE CANOPY LAYER AND THE URBAN BOUNDARY LAYER

---

for different street canyons, depending only on an aspect ratio rescaling as shown in Eq. (6.5a). In the equation,  $W_{Da}$  and  $H_{Da}$  (m) are the mean width and height of [Dallman et al. \(2014\)](#) canyon extracted from Fig. 6.12,  $W_C$  and  $H_C$  (m) are the current analysis mean width and height in either MA or LB and  $U_C^m/U_b^m$  is the modified wind speed ratio rescaled on [Dallman et al. \(2014\)](#) street canyon geometry. At last, [Solazzo and Britter \(2007\)](#) proposed a simple parametrization to obtain the middle canyon temperature  $T_c$  (K) knowing the temperature at one building facade ( $T_w$  in K) and the ambient temperature ( $T_a$  in K) outside the canopy as

$$T_c = R \frac{H}{W} (T_w - T_a) + T_a, \quad (6.4)$$

where the value of  $R = (T_c - T_a)/(T_w - T_a) = 0.11$  was retrieved independently for street canyons of different aspect ratios in the range  $0.5 < H/W < 5.0$ . Since in the current analysis the important quantity is the horizontal temperature gradient between opposite building facades, Eq. (6.4) was modified to compute the modified discrete horizontal temperature gradient  $\Delta T^m$  (K) assuming the middle canyon temperature to be the mean between the temperatures at the opposite building facades ( $T_1$  and  $T_2$  in K, measured respectively at GL and ML). The modified [Solazzo and Britter \(2007\)](#) parametrization is then given in Eq. (6.5b), where  $T_a$  (K) is the ambient temperature measured outside the canopy in SI monitoring site.

$$\frac{U_C^m}{U_b^m} = \frac{H_C}{W_C} \frac{W_{Da}}{H_{Da}} \frac{U_C}{U_b} \quad (6.5a)$$

$$\Delta T^m = \left( 0.22 \frac{H_{Da}}{W_{Da}} - 2 \right) (T_1 - T_a), \quad (6.5b)$$

Both wind speed ratios and the buoyancy parameter in Eq. (6.2) and (6.1) are rescaled using Eq. (6.5a) and (6.5b) and compared to the [Dallman et al. \(2014\)](#) data in Fig. 6.13. Evident is the different behavior of the parametrizations in the two street canyons. While MA (Fig. 6.13a) shows a very good match with [Dallman et al. \(2014\)](#) data, in LB (Fig. 6.13b) the parametrizations are not able to fill the gap associated with the different aspect ratios. The reasons behind the still remaining discrepancy in LB can be various. First, the street aspect ratio is similar to [Dallman et al. \(2014\)](#) one, so the corrections applied to the data are minimum. Second, the presence of intra-building flow infiltration in LB can cause a modification of the flow regime, changing the complexity of the environment and lowering the comparability. Third, the presence of trees must be taken into account somehow, since they are only present in LB. The latter point of the list is the one to be tackled, since the first two require a different approach not dependent on measured data, which would go beyond the scope of this analysis. To account for the presence of trees, without increasing the complexity and the nature of the proposed parametrization, different geometrical parameters will be used to describe LB aspect ratio. Ef-

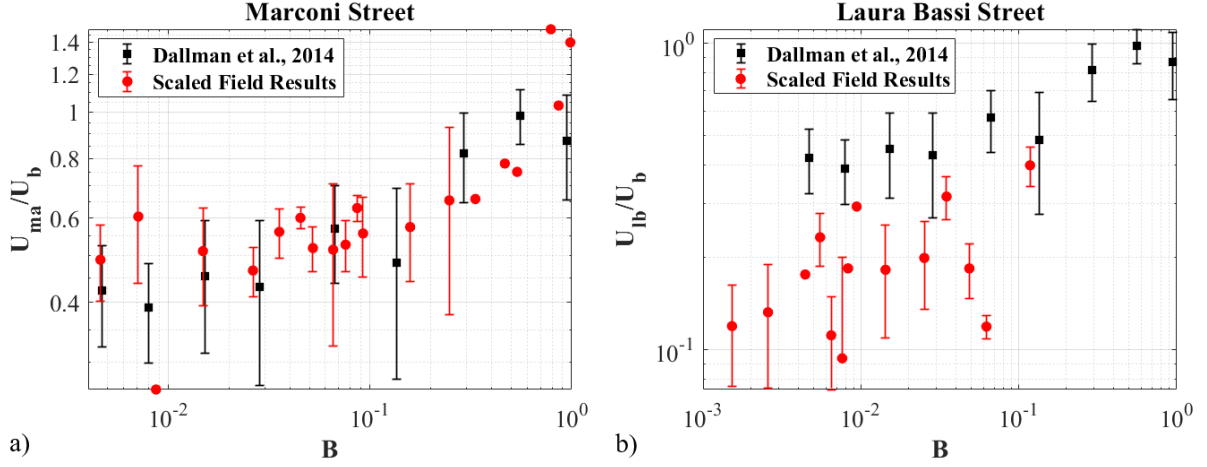


**Figure 6.13:** Wind speed ratios  $U_C/U_b$  as a function of  $B$  in (a) MA and (b) LB modified according to Eq. (6.5a) and (6.5b) to compare with Dallman et al. (2014). Wind speed ratios are averaged over  $B$  bins and the errorbars represent the standard deviation computed in each bin.

fective geometrical parameters are introduced to redefine the mean street canyon width  $W_{eff}$  (m) as the mean distance between opposite trees and the mean street canyon height  $H_{eff}$  (m) as the mean trees height. These new geometry is found to give  $H_{eff} = 15$  m and  $W_{eff} = 11$  m,

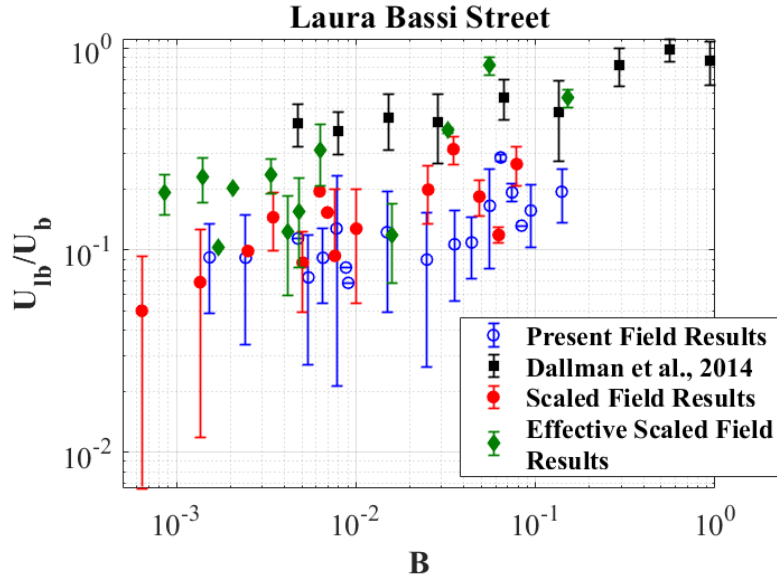


**Figure 6.14:** Wind speed ratios  $U_C/U_b$  as a function of  $B$  in LB modified according to Eq. (6.5a) and (6.5b) to account for the effective aspect ratio defined considering trees instead of buildings to compare with Dallman et al. (2014). Wind speed ratios are averaged over  $B$  bins and the errorbars represent the standard deviation computed in each bin.

## CHAPTER 6. RESULTS AND DISCUSSION: EXCHANGE PROCESSES BETWEEN THE CANOPY LAYER AND THE URBAN BOUNDARY LAYER

---

leading to an effective aspect ratio  $H_{eff}/W_{eff} = 1.36$ . The basic assumption for this evaluation is to consider the trees as solid obstacles like buildings, so that they become the boundaries of the street canyon. Although this approximation is certainly rough because for example it does not account for the tree crown porosity or the trunk, it is a simple solution to account for the presence of trees. Substituting the effective geometrical parameters in Eq. (6.5a) and (6.5b), the wind speed ratio as a function of the buoyancy parameter displays as in Fig. 6.14 with the previous scaling (Fig. 6.13b) and the real results. The comparison is still far from being as good as in MA (Fig. 6.13a) but there are improvement taking the effective geometry. Scaled data are closer to Dallman et al. (2014) ones despite the distinction between the IC and TC regimes is deteriorated especially in the vicinity of the transition value, as somehow the reduced canopy air volume imposed by the trees dismantles the circulation differences. As anticipated, the introduced correction to account for the presence of the trees is weak but simple, and gives better results than the case where trees are totally neglected. A discrepancy remains due to the presence of the tree contribution within the measurements of wind speed and air temperatures taken within the canopy. To magnify the comparability it will probably be necessary to introduce further parametrization in these two variables to account for the tree impact on both flow field and temperature.

### 6.2 The Impact of Trees on Exchange Processes Variables: a Multi-Seasonal Comparative Analysis

In Sect. 3.1 and during the introduction of this chapter, it was highlighted the importance of the canopy atmospheric stability and the background wind direction with respect to the canyon orientation in driving the circulation regimes within the canopy. In Sect. 4.2.2, the background wind direction was stressed to be a fundamental indicator of the circulatory motion within the canyon, as retrieved from literature. Atmospheric stability is also important in determining the strength and characteristics of mean flow and turbulent structures within the canopy. To compare summer and winter campaign's mean flow and turbulence during the weak synoptic periods it is therefore fundamental to classify different regimes based on atmospheric stability and background wind direction. This way, mean flow and turbulence within the canopy are independent on both atmospheric stability and background wind direction, enabling the comparison to better highlight the possible impact of tree crowns. The background wind direction classification was defined at the beginning of this chapter and used throughout the presented analysis, but it presents a slight modification to the EWP wind direction. In fact, the EWP wind direction is further divided in East Perpendicular (EP) and West Perpendicular (WP) to search for possible discrepancies in having the monitoring site on the windward or leeward building rooftop of the canyon. The atmospheric stability classification relies on the stability

6.2. THE IMPACT OF TREES ON EXCHANGE PROCESSES VARIABLES: A  
MULTI-SEASONAL COMPARATIVE ANALYSIS

Wind Direction	Canopy Levels	Near-Neutral Stability			
		$U_s/U_w$	$\overline{w'u'_s}/\overline{w'u'_w}$	$\overline{w'\theta'_s}/\overline{w'\theta'_w}$	$Tke_s/Tke_w$
Northerly Parallel	Ground	$0.59 \pm 0.02$	$0.19 \pm 0.02$	$0.13 \pm 0.01$	$0.21 \pm 0.02$
	Mid-canyon	$1.39 \pm 0.02$	$0.36 \pm 0.03$	$0.25 \pm 0.01$	$0.23 \pm 0.01$
	Rooftop	$0.85 \pm 0.01$	$0.64 \pm 0.02$	$0.10 \pm 0.01$	$0.99 \pm 0.06$
Southerly Parallel	Ground	$1.96 \pm 0.03$	$2.22 \pm 0.08$	$0.67 \pm 0.02$	$1.78 \pm 0.17$
	Mid-canyon	$3.18 \pm 0.04$	$2.68 \pm 0.18$	$0.42 \pm 0.01$	$1.3 \pm 0.2$
	Rooftop	$2.15 \pm 0.02$	$1.18 \pm 0.03$	$0.15 \pm 0.02$	$3.2 \pm 0.3$
Westerly Perpendicular	Ground	$0.75 \pm 0.01$	$1.17 \pm 0.04$	$1.34 \pm 0.05$	$1.35 \pm 0.14$
	Mid-canyon	$0.69 \pm 0.01$	$1.52 \pm 0.15$	$2.91 \pm 0.06$	$1.2 \pm 0.2$
	Rooftop	$0.77 \pm 0.02$	$1.02 \pm 0.04$	$0.21 \pm 0.02$	$1.7 \pm 0.1$
Easterly Perpendicular	Ground	$1.16 \pm 0.01$	$3.21 \pm 0.03$	$1.51 \pm 0.01$	$1.53 \pm 0.09$
	Mid-canyon	$1.28 \pm 0.01$	$8.52 \pm 0.11$	$1.93 \pm 0.02$	$2.0 \pm 0.2$
	Rooftop	$1.23 \pm 0.01$	$3.96 \pm 0.02$	$0.59 \pm 0.02$	$1.94 \pm 0.02$

**Table 6.5:** Ratios between the summer (subscript  $s$ ) and the winter (subscript  $w$ ) mean wind speed, TKMF, TKSHF and  $Tke$  for different background wind direction classes under near-neutral atmospheric stability condition at the three levels of LB.

parameter  $H - d/L_O$  used by Rotach (1995) and first presented in Sect. 3.3. Applying this two classifications on the summer (20-23 September) and winter (08-09 February) weak synoptic periods, four wind direction classes are obtained for both near-neutral stability and strongly unstable stability cases. The comparison is applied only on LB, since this is an effort to evaluate the impact of tree crowns from measured data. As previously highlighted, the classification makes mean flow and turbulence to become independent on local atmospheric stability and background wind direction, but by construction they are also independent on the canyon geometry (because it is a multi-seasonal comparison of data retrieved in the same canopy) and large scale conditions (since the focus is only given to the weak synoptic periods retrieved in Sect. 4.2.1). With good approximation, the comparison between summer and winter periods gives an indication of the impact of the tree crowns on the canyon flow and ventilation characteristics thanks to the seasonality of the crown leaves. Therefore, percentage attenuation (or enhancement) coefficients of the mean wind speed, TKMF, TKSHF and  $Tke$  associated with the presence of the tree crowns are calculated as the ratio between the summer and winter quantities. The coefficient values for near-neutral stability are reported in Tab. 6.5 for each class of background wind direction. Tab. 6.6 stores the coefficients for the strongly unstable condition. The tabled coefficients do not show a predominance of attenuation or enhancement related to the tree crown, but there is a strong dependency on the background wind direction for what concern having the attenuation or enhancement effects, and a dependency on atmospheric sta-

**CHAPTER 6. RESULTS AND DISCUSSION: EXCHANGE PROCESSES  
BETWEEN THE CANOPY LAYER AND THE URBAN BOUNDARY LAYER**

Wind Direction	Canopy Levels	Strongly Unstable Stability			
		$U_s/U_w$	$\overline{w'u'_s}/\overline{w'u'_w}$	$\overline{w'\theta'_s}/\overline{w'\theta'_w}$	$Tke_s/Tke_w$
Northerly Parallel	Ground	$0.68 \pm 0.01$	$0.57 \pm 0.02$	$0.42 \pm 0.01$	$0.33 \pm 0.01$
	Mid-canyon	$0.61 \pm 0.01$	$0.52 \pm 0.02$	$0.28 \pm 0.01$	$0.17 \pm 0.01$
	Rooftop	$0.48 \pm 0.01$	$0.65 \pm 0.02$	$1.04 \pm 0.02$	$0.35 \pm 0.01$
Southerly Parallel	Ground	$1.08 \pm 0.02$	$4.6 \pm 0.2$	$1.19 \pm 0.06$	$1.27 \pm 0.06$
	Mid-canyon	$1.02 \pm 0.03$	$10.8 \pm 0.8$	$0.55 \pm 0.03$	$1.48 \pm 0.13$
	Rooftop	$1.31 \pm 0.04$	$1.87 \pm 0.07$	$3.22 \pm 0.13$	$1.39 \pm 0.04$
Westerly Perpendicular	Ground	$0.62 \pm 0.01$	$0.58 \pm 0.01$	$0.27 \pm 0.01$	$0.25 \pm 0.01$
	Mid-canyon	$0.62 \pm 0.01$	$0.75 \pm 0.02$	$0.29 \pm 0.01$	$0.11 \pm 0.01$
	Rooftop	$0.46 \pm 0.01$	$0.60 \pm 0.01$	$1.63 \pm 0.02$	$0.44 \pm 0.01$
Easterly Perpendicular	Ground	$0.99 \pm 0.01$	$2.85 \pm 0.02$	$1.33 \pm 0.01$	$1.00 \pm 0.01$
	Mid-canyon	$1.04 \pm 0.01$	$10.82 \pm 0.08$	$1.87 \pm 0.01$	$1.09 \pm 0.01$
	Rooftop	$0.91 \pm 0.01$	$2.37 \pm 0.01$	$5.61 \pm 0.03$	$0.88 \pm 0.01$

**Table 6.6:** Ratios between the summer (subscript  $s$ ) and the winter (subscript  $w$ ) mean wind speed, TKMF, TKSHF and  $Tke$  for different background wind direction classes under strongly unstable atmospheric stability condition at the three levels of LB.

bility for the magnitude of these effects. During strongly unstable conditions (Tab. 6.6), mean flow and turbulence are more strictly related. Within this stability condition, both mean flow and turbulence are attenuated by the tree crown when the background wind direction is NP and WP to the canyon orientation, while they are enhanced during SP and EP conditions. In terms of mean wind speed, the described behavior is retrieved also when atmospheric stability is near-neutral. The opposite behavior of the EP and WP conditions can be explained in terms of mean flow and turbulence attenuation along the descending branch of the supposed in-canyon vortex circulation, and an enhancement along the ascending branch. When the background wind direction is EP, the monitoring sites within the canopy are located close to the leeward wall where the ascending branch of the circulation is developing. There the flow is subjected to the pressure increase due to the tree crown volume which reduces the flow section, producing an acceleration. This behavior is more evident during near-neutral stability conditions, when the flow is not forced by unstable vertical motions. Conversely, when the background wind direction is WP, the monitoring sites within the canopy are located close to the windward wall where the descending branch of the circulation is developing. The flow is entering in the canyon from the atmosphere above directly interacting with the porous crown of the tree, reducing its speed by blocking the flow. Local atmospheric instabilities are also responsible for the turbulent fluxes and energy reduction in this wind direction case, since they somehow increase the turbulent dissipation. On the other hand, when atmospheric stability is near neutral, turbulent fluxes and

energy increase as the tree crown favors momentum and energy cascades from the mean flow to the turbulent structures. These last transport processes between mean and turbulent fields are commonly retrieved for all wind directions in near-neutral condition, except for the NP one where the attenuation is almost always the dominant factor. The flow behavior retrieved at the RL follows the in-canyon coefficients, but it is more critical to understand since the atmospheric flows at the top of the canyon is affected by the whole neighborhood perturbations. Of difficult interpretation is also the difference between southerly and NP background wind direction cases. The helical shape of the circulation does not allow to know whether a measure is taken on an ascending or descending branch.

### 6.3 Summary and Conclusions

In this chapter, the methodology described in Sect. 4.2.2 is applied to describe the behaviors of the diagnostic quantities related to the exchange processes and to establish the role of turbulent transport as a key mechanism for exchange processes has been investigated characterizing the mechanical and heat effects of the flow structures in real urban street canyons. New time scales quantify the velocity associated with mixing and exchange processes related to mechanical and thermal aspects of the in-canyon circulations at three different levels inside and above MA and LB. These quantities shape into asymmetrical tailed distributions that can be approximated by GEV functions, whose modes is the most likely value of the investigated time scale (overall and in dependency on different background wind directions). The mechanical time scales  $\tau_d$  in MA vary within and above the canyon, with values evaluated at the RL smaller than the ones evaluated at lower levels. Thermal time scales  $\tau_h$ , sustained by the heat released from the street and the building facades, are smaller and more homogeneous than the mechanical ones. The time scales also vary with background wind direction. When the background wind is NP or EWP to the canyon orientation, both times scales are smaller and more homogeneous among different levels inside and above the canyon. During SP background wind direction, time scales increase as the momentum and heat fluxes are inhibited. Time scales in LB behave very differently from MA ones.  $\tau_d$  are homogeneous within and above the canyon, as the presence of vegetation and the lateral flow entrainment mix the mechanical exchange velocity by affecting the mechanical production of turbulence. The irregular building and street insolation, caused by the shadowing effect of the trees, affects the mixing properties of the canopy leading to heterogeneous  $\tau_h$  values. As for the MA case, the time scales retrieved in LB vary with background wind direction.  $\tau_d$  remain homogeneous within the canopy even considering different wind directions, but the RL is slightly decoupled, showing increasing (NP) or decreasing (SP and EWP) mixing times. The overall behavior of  $\tau_h$  is only supported during SP wind directions, while the shadowing effect of trees is found to affect the GL more than the ML during NP and EWP ones.

## CHAPTER 6. RESULTS AND DISCUSSION: EXCHANGE PROCESSES BETWEEN THE CANOPY LAYER AND THE URBAN BOUNDARY LAYER

---

The exchange rates associated with mechanical ( $\eta_d$ ) and thermal ( $\eta_h$ ) processes evaluate the in-canyon flow capability to exchange momentum and heat with the atmosphere above. Both MA and LB are found to be favourable environment for exchange processes to develop for approximately the 50 – 75% of the rates cases, but the long tails of the distributions describe scenarios where the exchanges are totally suppressed, particularly common in LB. The only exception is retrieved for  $\eta_h$  in LB, where the vegetation inhibits the exchanges at the surface by lowering the TKS HF. As the exchange rates modes agree in describing efficient mixing characteristics in MA for all the wind direction cases and for mechanical processes in LB, the  $\eta_h$  in LB mostly describe very poor mixing and and heat exchange.

From the combination of  $\eta_d$  and  $\eta_h$ , a total exchange rate  $\eta_t$  is evaluated to assess the normalized  $CO^+$  concentrations removal capacity of the canyon. The buoyancy parameter  $B$  retrieved from [Dallman et al. \(2014\)](#) has been used as distinguishing factor to combine the mechanical and thermal rates into the total one. The comparisons between  $\eta_t$  and  $CO^+$  show a very good agreement in both canopies, verifying the a priori hypothesis of mass transport to be driven by momentum or heat transports, depending on the most dominant in-canyon circulation.

Furthermore, the validation of the reproducibility of [Dallman et al. \(2014\)](#) in-canyon circulation detection on the current investigated canyons enabled the introduction of simple parametrizations for in-canyon wind speed and temperature horizontal gradient as functions of the mean canyon aspect ratio  $H/W$ . These parametrizations allow to estimate and compare flow characteristics in real street canyons with different aspect ratios, if the airflow within the canyon behaves as expected by the skimming flow regime.

Finally a multi-seasonal analysis is presented to retrieve attenuation and enhancement coefficients associated to the impact the tree crowns have on the mean flow and turbulent characteristics under different stability conditions. Both mean flow and turbulent momentum transport depend strongly on the background wind direction for what discern attenuation and enhancement impacts, and depend on atmospheric stability for the magnitude of the coefficients. Attenuation coefficients are retrieved for the mean flow when background wind directions are NP and WP. The relationship applies also to the turbulent quantities when dealing with strongly unstable conditions, while a general enhancement is retrieved when atmospheric stability is near-neutral. The results from this last analysis will provide an useful verification for the numerical investigations of the following chapter.

## Chapter 7

# Results and Discussion: Modeling the Impacts of Trees on the Exchange Processes

In this chapter, the results obtained from the numerical investigation using the QUIC model will be presented to simulate the impact of trees on the ventilation, enriching the characterization of the exchange processes in the real urban environment described in Chapter 3 and already investigated in Chapter 5 and 6. After a short description of the modification method (see Sect. 4.3.2) application, the improved model will be tested on the MA and LB domain among different input wind conditions, classified by wind direction ensemble, and verified with the measured data retrieved from the summer campaign. Comparative studies among three different wind direction ensembles will be presented to evaluate the impact of trees in the urban neighborhoods surrounding MA and LB, focusing on the topological differences of the urban structures within it and the morphological dependency of the exchange processes when trees are added or removed from the domain.

### 7.1 Qualitative Code Verification: $u_*$ associated to the Unperturbed Flow

As described in Sect. 4.3.2, the friction velocity  $u_*$  is the fundamental variable at the basis of the computation of the initial turbulent field. The variable is computed at each grid point of the domain from the sum of a local, directly related to the mass conserved mean flow, and a non-local parts. The value of  $u_*$  already accounts for the various parametrizations that characterize the model and, as said, the mass conservation constraint. When dealing with such complex domains, as in typical European urban environments, the mean flow dynamics is strongly perturbed by

CHAPTER 7. RESULTS AND DISCUSSION: MODELING THE IMPACTS OF TREES ON THE EXCHANGE PROCESSES

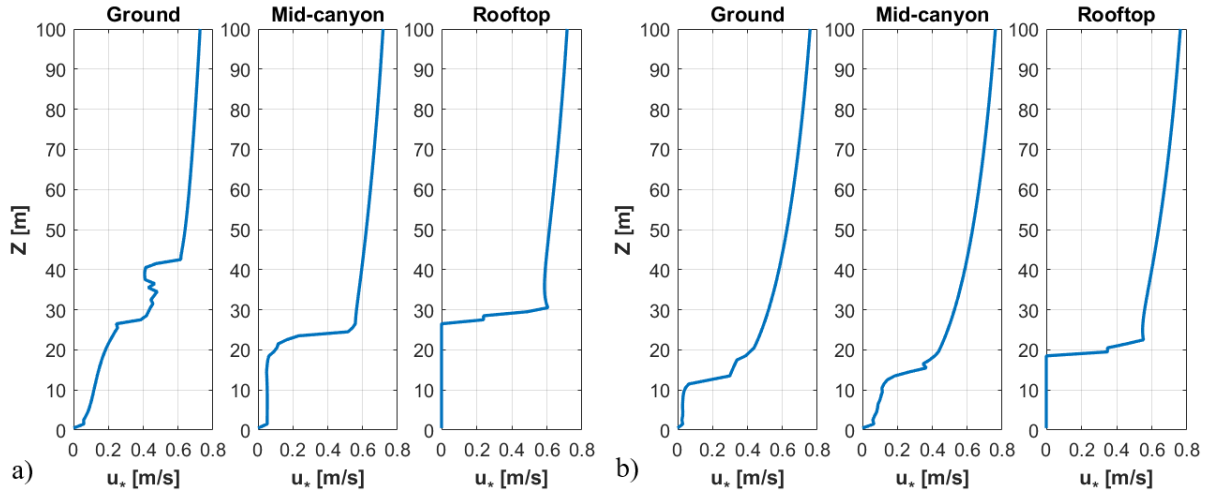


**Figure 7.1:** Simulated  $u_*$  in (a) MA and (b) LB at the three monitoring levels as it was computed by the original version of the model.

the local morphology within the UCL. The effect of these perturbations involves also the whole UBL, modifying the mean flow and turbulent fields. As a consequence, the wind speed profile in the UBL is not expected to follow a logarithmic profile anymore. Therefore, forcing the flow to be logarithmic to compute  $u_*$  from the wall law induces errors in the estimation of  $u_*$  as described in Sect. 4.3.2. An example of the  $u_*$  profile in MA and LB is given in Fig. 7.1 to better visualize the inaccuracy of the model in its original version. Potential problems related to the simulated  $u_*$  arise from the magnitude and the discrepancy between UCL and UBL above. Above the canopies, there is a strong discontinuity in the  $u_*$  values which is actually physical

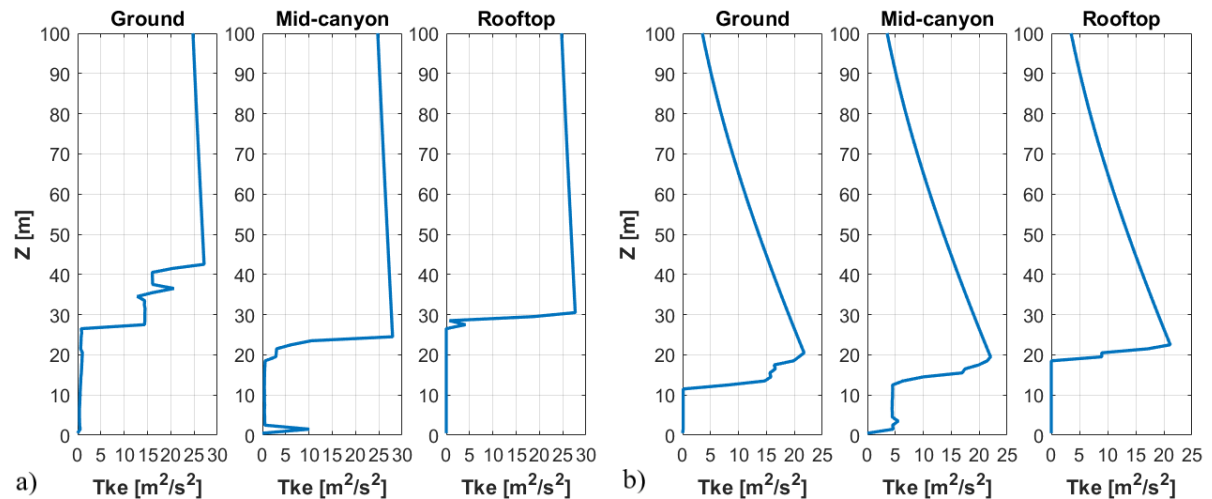


**Figure 7.2:** Simulated  $Tke$  in (a) MA and (b) LB at the three monitoring levels as it was computed by the original version of the model.

## 7.1. QUALITATIVE CODE VERIFICATION: $U_*$ ASSOCIATED TO THE UNPERTURBED FLOW

if a ShL dynamics is present. However,  $u_*$  is expected to be constant above and smaller than the retrieved value in the ShL due to the expected logarithmic decrease of wind velocity with the height (which supposes a constant  $u_*$ ). The magnitude of  $u_*$  is instead increasing with the

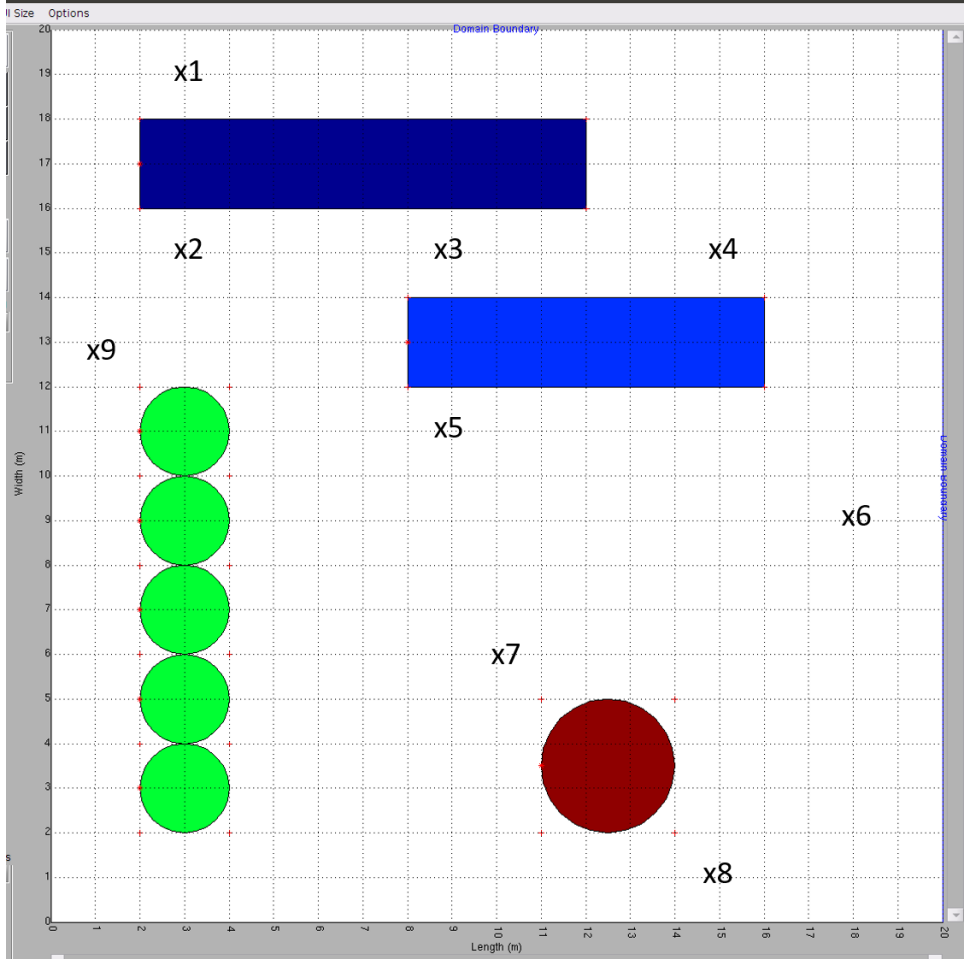


**Figure 7.3:** Simple domain for testing the newly computed  $u_*$ .  $x_i$  identify the locations where the simulated  $u_*$  profiles are taken, and represent specific morphological structures depending on the input wind direction. Domain size ( $X \times Y \times Z$ ): 20x20x100 m; Domain resolution: 1x1x0.5 m. Dark blue building size: 10x2x20 m; light blue building size: 8x2x25 m; red tower size (diameter  $d$  and height  $h$ ):  $d=3$  m,  $h=50$  m; trees sizes:  $d=2$  m,  $h=15$  m, attenuation coefficient  $a=1.7$ .

increasing height and the single values are suspiciously large when compared with the wind speed they are retrieved from. The input reference wind speed used to simulate the  $u_*$  profiles are the same used for the central value of the EP wind direction ensembles ( $wd=90^\circ$ ) in both MA (Sect. 7.2.2) and LB (Sect. 7.2.1). This reference values are taken from SI at  $z_{ref}=40$  m and are  $u_{ref}=1.9 \text{ ms}^{-1}$  and  $u_{ref}=2 \text{ ms}^{-1}$  respectively for MA and LB cases. The most critical effect of this overestimation is a bad evaluation of the turbulent quantities derived from  $u_*$ , especially  $Tke$ . An example of  $Tke$  simulated from the same reference input values of Fig.

## CHAPTER 7. RESULTS AND DISCUSSION: MODELING THE IMPACTS OF TREES ON THE EXCHANGE PROCESSES

---

Input Variables for the Test Cases				
Case	$u_{ref}$	$z_{ref}$	$wd_{ref}$	$(1/LO)_{ref}$
1	1 ms <sup>-1</sup>	10 m	0°	0 m <sup>-1</sup>
2	5 ms <sup>-1</sup>	10 m	0°	0 m <sup>-1</sup>
3	10 ms <sup>-1</sup>	10 m	0°	0 m <sup>-1</sup>
4	5 ms <sup>-1</sup>	10 m	315°	0 m <sup>-1</sup>
5	5 ms <sup>-1</sup>	10 m	270°	0 m <sup>-1</sup>
6	5 ms <sup>-1</sup>	10 m	315°	-1 m <sup>-1</sup>
7	5 ms <sup>-1</sup>	10 m	315°	0.1 m <sup>-1</sup>

**Table 7.1:** Input variables for the seven test cases used to assess the reliability of the new  $u_*$  computation.

7.1 is given in Fig. 7.2. As it is clear just from a visual verification, *The* simulated values above the canopies are completely wrong and from the code debugging the overestimation of  $u_*$  was found to be the reason. Therefore, a new computation of  $u_*$  is given as described in Sect. 4.3.2. To test the efficacy of the new  $u_*$  computation, a simple domain was built to perform a qualitative verification. The domain (Fig. 7.3) was built in order to include several remarkable morphological features typical of real domains, such as isolated buildings, street canyons and trees. Each morphological element is well spaced from the others, ensuring to avoid flow perturbations from superimposition effects. A total of seven test cases have been performed to evaluate the new  $u_*$  computation results among the original version of the model, all giving a substantial improvement. The test cases aim to stress different aspect of a flow field such as the wind speed, the wind direction and the atmospheric stability. The specification of the test cases are reported in Tab. 7.1, but only results from Case 2 will be discussed because the same considerations can be extended to the other six. Given the input wind direction of Case 2, the locations  $x_i$  of the retrieved profiles from the test domain are representative of:

- ( $x_1$ ) the upwind cavity of the first approaching single building line;
- ( $x_2$ ) the downwind or wake cavity behind a single building line;
- ( $x_3$ ) the street canyon cavity with an aspect ratio  $H/W=11$ ;
- ( $x_4$ ) the upwind cavity of a non isolated building line next to a street canyon;
- ( $x_5$ ) the wake cavity of a street canyon;
- ( $x_6$ ) an area of free surface where the perturbed flow has already readjusted from the previous perturbations;
- ( $x_7$ ) the upwind cavity of a single isolated tower;

## 7.1. QUALITATIVE CODE VERIFICATION: $U_*$ ASSOCIATED TO THE UNPERTURBED FLOW

- ( $x_8$ ) the wake cavity of a single isolated tower;
- ( $x_9$ ) the proximity of a vegetated area.

These locations represent possible environmental geometries that contribute to perturb the input wind speed profile. Using the input variables of Case 2, the simulation produces the  $u_*$  field. From this field, the wrong values (terminology used to indicate the supposed wrong values that are replaced by the new computation) of  $u_*$  are stored in Tab. 7.2 together with the newly computed  $u_*$  and the wind speeds retrieved from the same grid points. The qualitative check on the new  $u_*$  is ensured by the fact that the new  $u_*$  is always of the same order of magnitude of the corresponding wind speed, differently from the original  $u_*$  which values are two orders larger. Despite among 80000 grid points only 6 have given wrong  $u_*$  values, the impact on the single location profiles is evident (Fig. 7.4). With the original model evaluation, the mean  $u_*$  calculated at surface (avoiding the parametrized volumes) and used to generate the  $u_*$  profile outside the UCL is retrieved to be  $\bar{u}_* = 1.3 \text{ ms}^{-1}$ . With the new method, the mean  $u_*$  is equal to  $0.4 \text{ ms}^{-1}$ . The  $u_*$  profiles in Fig. 7.4 shows the discrepancies between

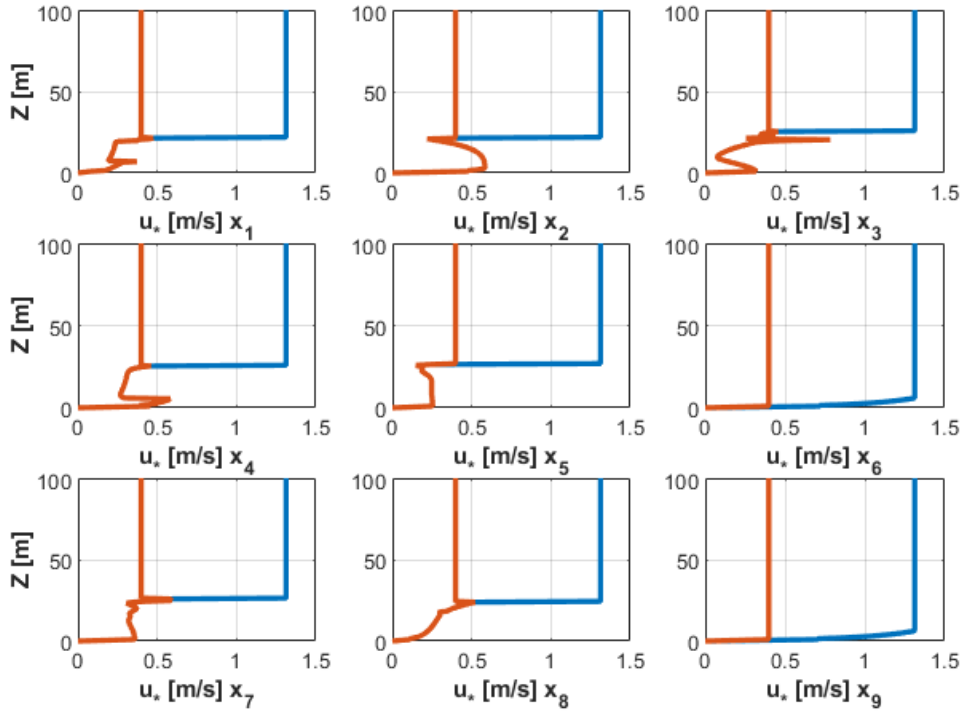


**Figure 7.4:** Simulated  $u_*$  profiles with the original QUIC (blue line) and the new computation (red line) for the Case 2 (Tab. 7.1). Each panel shows one location from the list (Fig. 7.3).

the original and the new computation methods. As shown, the correction involves the whole UBL, since within the canopy the computation method is independent on the flow type. All locations shares the same behavior with a constant decrease of  $u_*$  above the UCL of  $0.9 \text{ ms}^{-1}$ .

**CHAPTER 7. RESULTS AND DISCUSSION: MODELING THE IMPACTS OF TREES ON THE EXCHANGE PROCESSES**

Wrong friction velocity $u_*$	Retrieved values from Case 2	
	New friction velocity $u_*$	Corresponding wind speed $U$
35.55 ms <sup>-1</sup>	0.13 ms <sup>-1</sup>	0.22 ms <sup>-1</sup>
5.77 ms <sup>-1</sup>	0.13 ms <sup>-1</sup>	0.036 ms <sup>-1</sup>
16.07 ms <sup>-1</sup>	0.078 ms <sup>-1</sup>	0.10 ms <sup>-1</sup>
19.18 ms <sup>-1</sup>	0.067 ms <sup>-1</sup>	0.12 ms <sup>-1</sup>
30.07 ms <sup>-1</sup>	0.13 ms <sup>-1</sup>	0.19 ms <sup>-1</sup>
17.76 ms <sup>-1</sup>	0.13 ms <sup>-1</sup>	0.11 ms <sup>-1</sup>

**Table 7.2:** Retrieved wrong  $u_*$  values, together with the newly computed ones with the updated method and the corresponding wind speeds for each grid point.

With the correction applied,  $u_*$  in the whole UBL is more consistent with the profile retrieved within the UCL. Testing all the cases of Tab. 7.1, the use of the new computation is strengthened. Some general observations can be made. Most of the wrong  $u_*$  values are found to be at the edges of parametrized domain volumes or along long building sides when the wind direction is parallel to them. The location and number of the wrong  $u_*$  changes according only to the input wind direction since it follows the location of the parametrized volumes. Wrong  $u_*$  values do not seem to be related to presence of vegetation in the domain, neither the domain size. They increase with the decreasing atmospheric stability and vertical resolution. All these observations provide a qualitative verification of the better quality of the new computation with respect to the original model.

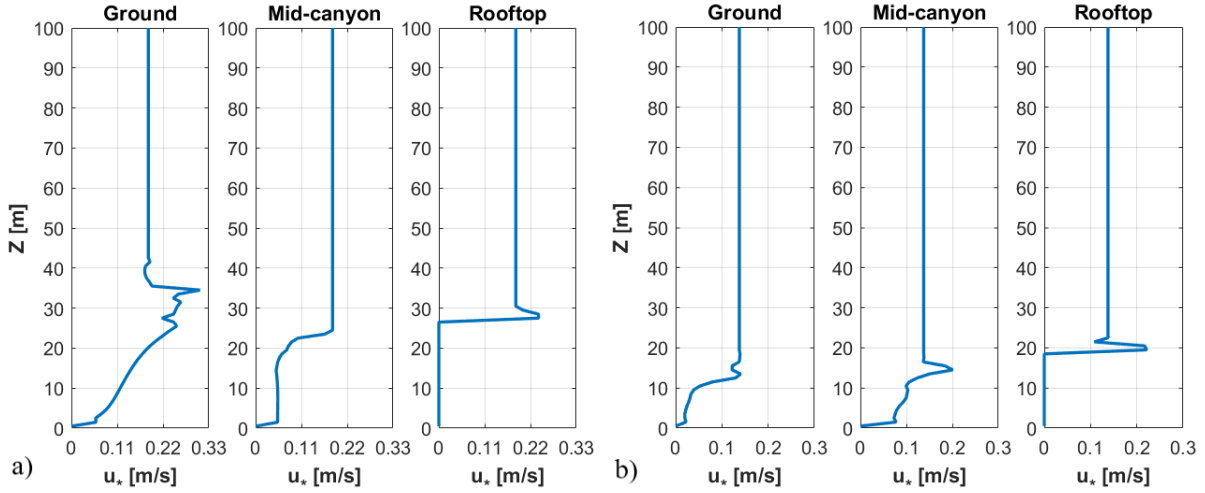
Retrieved values from Marconi (input as in Sect. 7.2.2)		
	Wrong friction velocity $u_*$	New friction velocity $u_*$
Wrong Minimum	0.13 ms <sup>-1</sup>	0.0037 ms <sup>-1</sup>
Wrong Maximum	10.13 ms <sup>-1</sup>	0.069 ms <sup>-1</sup>
Wrong Mean	5.72 ms <sup>-1</sup>	0.053 ms <sup>-1</sup>
Mean	1.27 ms <sup>-1</sup>	0.19 ms <sup>-1</sup>

Retrieved values from Laura Bassi (input as in Sect. 7.2.1)		
	Wrong friction velocity $u_*$	New friction velocity $u_*$
Wrong Minimum	0.15 ms <sup>-1</sup>	0.0050 ms <sup>-1</sup>
Wrong Maximum	14.20 ms <sup>-1</sup>	0.12 ms <sup>-1</sup>
Wrong Mean	5.67 ms <sup>-1</sup>	0.050 ms <sup>-1</sup>
Mean	1.22 ms <sup>-1</sup>	0.14 ms <sup>-1</sup>

**Table 7.3:** Retrieved wrong  $u_*$  values, together with the newly computed ones with the updated method in MA and LB neighborhoods.

7.1. QUALITATIVE CODE VERIFICATION:  $U_*$  ASSOCIATED TO THE UNPERTURBED FLOW



**Figure 7.5:** Simulated  $u_*$  in (a) MA and (b) LB at the three monitoring levels using the new computation for  $u_*$ .

The new computation of  $u_*$  is implemented also for the investigated domain of MA and LB neighborhoods. Tab. 7.3 stores the minimum, maximum and mean wrong values (and their corrections) together with the mean  $u_*$  over the domains considering either the wrong or the newly computed values. Particularly, the difference in the mean  $u_*$  ensures to qualify the good behavior of the new computation even for complex domains. Using the new mean  $u_*$  values, the  $u_*$  profiles have been re-evaluated at each monitoring level within and above MA and LB (Fig. 7.5). As evaluated for the simple domain, there is more agreement between the  $u_*$  values computed in the UCL and in the UBL above. Both MA and LB show this feature at each

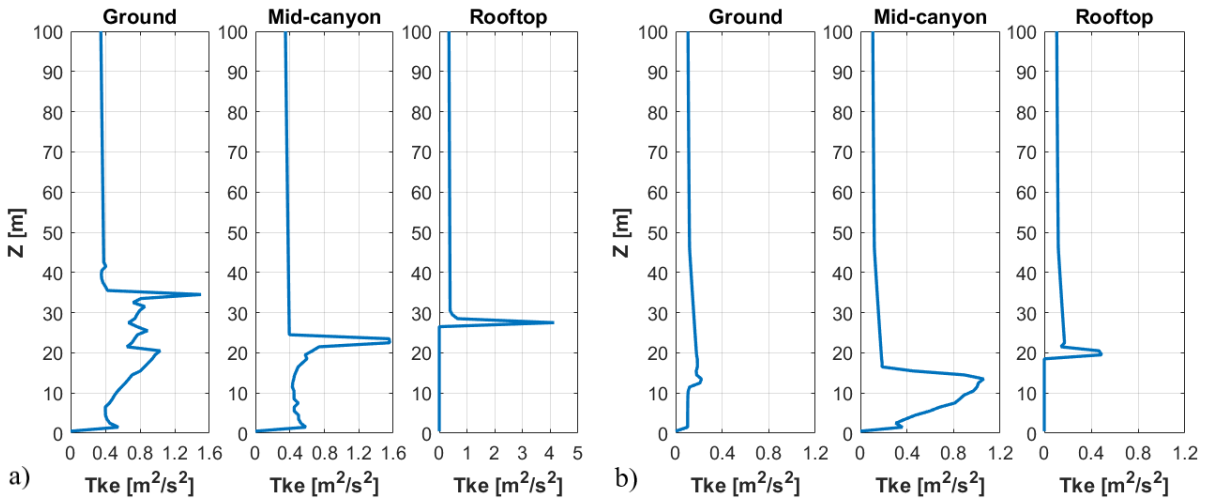


**Figure 7.6:** Simulated  $Tke$  in (a) MA and (b) LB at the three monitoring levels using the new computation for  $u_*$ .

## CHAPTER 7. RESULTS AND DISCUSSION: MODELING THE IMPACTS OF TREES ON THE EXCHANGE PROCESSES

---

monitoring level. As a consequence, the  $Tke$  profiles (Fig. 7.6) are largely attenuated and more realistic with respect to the original QUIC evaluation (Fig. 7.2). Large values are still retrieved at the RL of MA (Fig. 7.6a) but it is an overall feature of the three locations to simulate a ShL dynamics which at rooftop is intensified by the presence of a solid boundary caused by the mass conservation constraint applied by the model. Therefore the new computation method to evaluate  $u_*$  is implemented and used to perform the simulation results displayed in the rest of this chapter.

### 7.2 Model Verification among Different Wind Direction Ensembles

The QUIC verification is performed on wind speed ( $U$ ), TKMF ( $|\overline{w'u'}|$ ) and TKE ( $Tke$ ) profiles for both street canyons. The four wind direction intervals defined in Chapter 6 are used for the verification. For each interval, a simulated wind direction ensemble is generated, producing a profile every  $5^\circ$ . Therefore, each wind direction ensemble is a collection of 9 profiles for each quantity whose reliability has to be verified among the measured data retrieved during the campaign. Since the aim of this chapter is to establish the role of vegetation in street canyons, we will focus only on replicating summer conditions which can be compared with the weak synoptic period defined in Sect. 4.2.1. Each simulated wind direction ensemble tries to replicate a small period of one hour in the measured dataset, when the measured wind direction above the canopy are approximately constant (in the same direction defined for each ensemble). Input conditions are defined as described in Sect. 4.3.4 and they are therefore averaged over the selected one hour periods to enhance the verification robustness. A simulated profile per quantity is given at each canyon level, since their locations are horizontally displaced. An attempt to simulate the mean behavior of the canyon is also provided calculating the profiles at the canyon center and comparing them with all the canyon stations (and the supporting ones when dealing with wind speed). Each simulated profile is calculated from an average of horizontal arrays of cells around the location of the measurement stations, to smoothen possible simulation spikes of the single cell.

#### 7.2.1 Vegetated Street Canyon - Laura Bassi Street

##### Input Wind Direction Parallel from East to the Street Canyon Orientation

Fig. 7.7 shows the simulated profiles ensembles for the case of EP wind directions  $wd$  ( $70^\circ \leq wd \leq 110^\circ$ ) to LB orientation. They are representative of the period 22:00-23:00 of the 22/09/2017 and compared with data from each measurement site within and above the canyon, averaged over this selected period. The reference wind speed  $u_{ref}=2.0 \text{ ms}^{-1}$  for the input logarithmic

## 7.2. MODEL VERIFICATION AMONG DIFFERENT WIND DIRECTION ENSEMBLES

profile of the model is retrieved from SI monitoring site at the reference height  $z_{ref}=40$  m. The roughness length is set at  $z_0=1.75$  m according to table 4.2, while the Obukhov length is calculated at the canyon RL and its inverse is  $1/L_O=0$  m<sup>-1</sup>. The vegetation attenuation coefficient

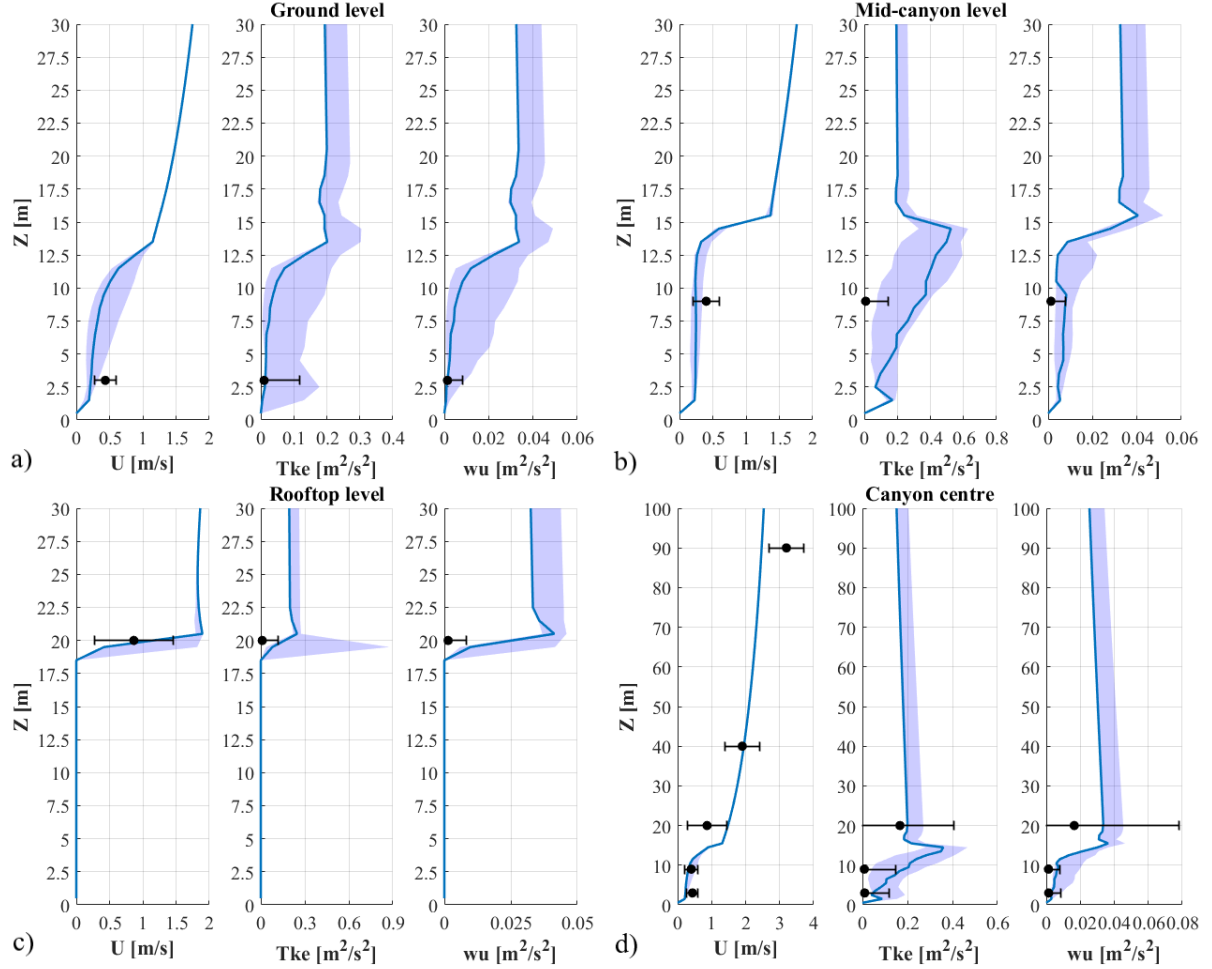


**Figure 7.7:** Simulated  $U$ ,  $Tke$  and  $|\overline{w'u'}|$  at (a) GL, (b) ML, (c) RL and (d) canyon center locations for the EP wind direction ensemble in LB. The blue profile represents the 90° wind direction to the canyon orientation, while the shadowed area is the wind direction ensemble. The black dots and error bars refer to the averaged measured value and standard deviation within the selected period.

is calculated from Eq. (4.12) and is set at  $a=1.7$ . From the thermohygrometers data at each level, the atmospheric profile of temperature and relative humidity are retrieved, considering both UCL and UBL above. The whole UBL is found to be isothermal at  $T=288.4$  K with small oscillation of the relative humidity around the input value  $RH=60\%$ . The boundary layer height ( $h_{BL}=480$  m) is still decreasing to typical nocturnal values.

The agreement between simulated and measured data is acceptable for both wind speed and

## CHAPTER 7. RESULTS AND DISCUSSION: MODELING THE IMPACTS OF TREES ON THE EXCHANGE PROCESSES

---

turbulence related quantities. Within the canyon, wind speed is underestimated by the model, but still within the error bars. This behavior can be consequence of the wind acceleration due to the reduced air volume and increased pressure between the tree crown and the surface (at GL) or the building facade (at ML) not sufficiently accounted by the model. TKE and TKMF within the canyon are well captured, despite a certain overestimation at ML. Turbulent related quantities are less in agreement with data for what concern the RL (Fig. 7.7c). Since measurements are taken directly above the rooftop, the profiles are cut at the building height. Despite the good agreement for wind speed values, turbulence is roughly overestimated, describing a turbulent layer which does not find confirmation in the measured data. Despite these small disagreements, data from measurements are well simulated by the model. Agreement is still good if a single representative profile is computed for the canyon (Fig. 7.7d). These last profiles are not meant to match perfectly the data, but to assess how representative could measurements be of the flow behavior. Poor agreement was expected inside the canopy, where local morphological features and the vicinity of trees may have a role in the modification of the profile. However, the agreement is good for both mean flow and turbulent quantities, confirming the results found at each measurement site. Wind speed is also compared to SI and AT monitoring sites to assess the flow behavior at larger scale. SI is perfectly represented, verifying the logarithmic shape of the wind velocity profile outside the canopy layer. However, wind speed at AT is poorly captured. This behavior can be the consequence of the possible perturbations of the logarithmic profile by the larger scale flow, which enhances the wind speed in the upper part of the UBL.

### Input Wind Direction Perpendicular from West to the Street Canyon Orientation

Profiles simulated for the WP wind direction ensemble ( $250^\circ \leq wd \leq 290^\circ$ ) to LB orientation are displayed in Fig. 7.8, representing the interval 09:00-10:00 of the 21/09/2017. Reference wind speed  $u_{ref}=2.1 \text{ ms}^{-1}$  for the input profile is again collected at SI monitoring site at  $z_{ref}=40 \text{ m}$ . As for the EP case,  $z_0=1.75 \text{ m}$  and  $a=1.7$ . The inverse Obukhov length is  $1/L_O=-0.0242 \text{ m}^{-1}$ , describing a near neutral stability condition. Temperature is uniform inside the canopy ( $T_c=292 \text{ K}$ ) and almost equal to the ambient temperature  $T_a=291 \text{ K}$ . Relative humidity ranges between the  $RH_c=50\%$  of the canopy to the  $RH_a=40\%$  at the AT monitoring site. A rising boundary layer reaches a height of  $h_{BL}=750 \text{ m}$ .

Fig. 7.8 shows an even better agreement between simulations and measurements than the EP ensemble. Each profile stays within the error bar of the measurements, even considering the canyon center panel in Fig. 7.8d. However, a certain underestimation can be found inside the canopy (Fig. 7.8a-b) where both wind speed and TKMF are smaller than the measurements. Wind speed is slightly underestimated by the model (Fig. 7.8a-b) as it was already found for the EP wind direction ensemble (Fig. 7.7a-b). The reduced air volume between the tree crown and the ground or the building facade increases the local pressure and produces an acceleration

## 7.2. MODEL VERIFICATION AMONG DIFFERENT WIND DIRECTION ENSEMBLES

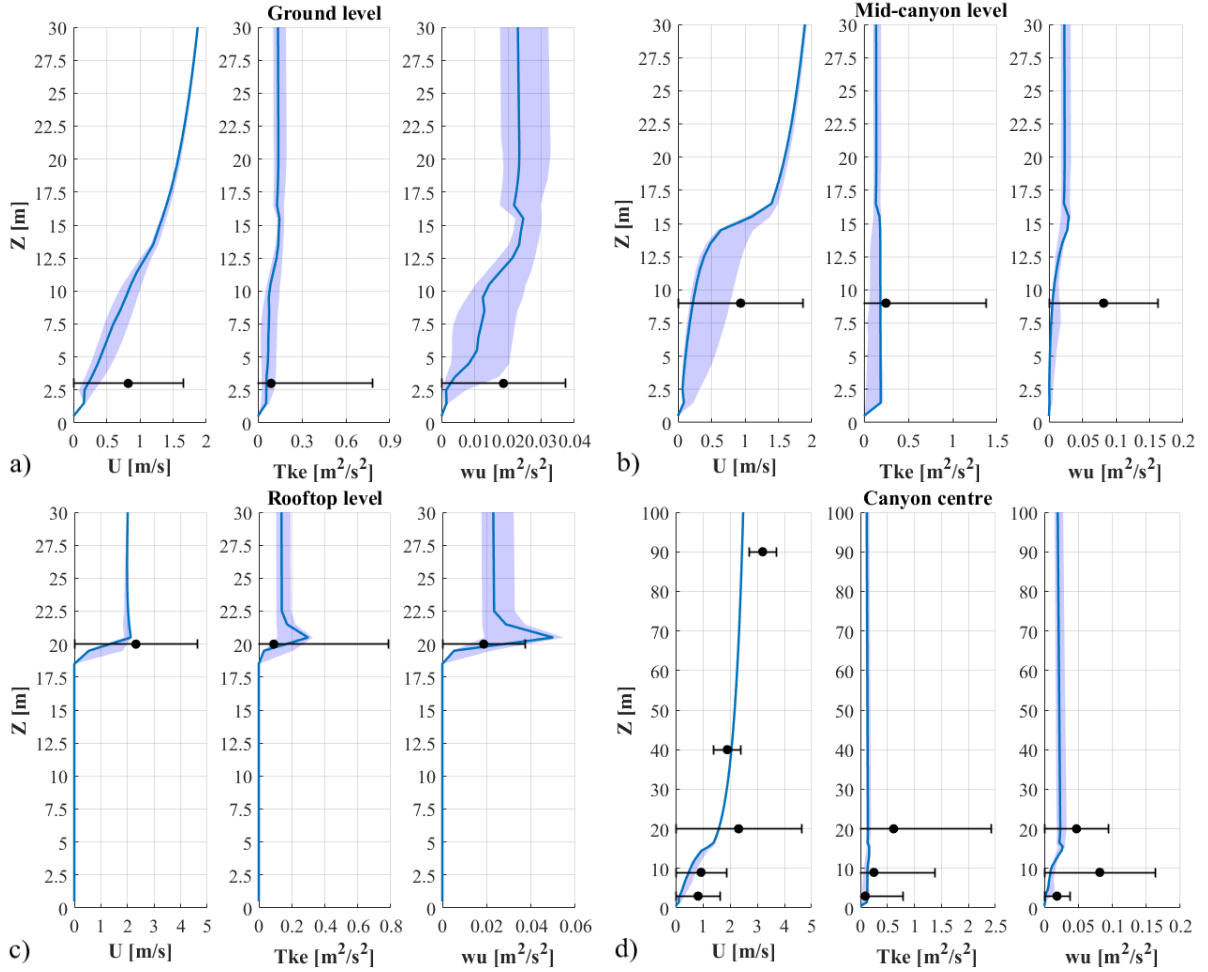


**Figure 7.8:** Simulated  $U$ ,  $Tke$  and  $|\overline{w'u'}|$  at (a) GL, (b) ML, (c) RL and (d) canyon center locations for the WP wind direction ensemble in LB. The blue profile represents the  $270^\circ$  wind direction to the canyon orientation, while the shadowed area is the wind direction ensemble. The black dots and error bars refer to the averaged measured value and standard deviation within the selected period.

in the wind speed which is not well captured by the model. Turbulent related quantities are instead well captured at the GL (Fig. 7.8a) but overestimated at the ML (Fig. 7.8b) where the dissipation seems to be the dominant effect. Again in the proximity of a boundary, like surface or the building facade, the model estimations are poor, but still within the range of confidence of the data. The wind speed is instead well captured above the UCL (Fig. 7.8d) and it is in good agreement with data retrieved from SI. The wind speed at AT is slightly outside the range simulated by the model, but the error can be due to the rough approximation that imposes the input velocity profile to follow the logarithmic wall law. As usual this approximation for the input profile is as accurate as the measurements used to compute the input profile, or to

## CHAPTER 7. RESULTS AND DISCUSSION: MODELING THE IMPACTS OF TREES ON THE EXCHANGE PROCESSES

compare the simulation result, are taken outside the RSL, where the drag force of the buildings modifies the wind speed profile. The RL remains the most difficult location for the mean flow and turbulence to be replicated due to the interaction with the roughness elements of the rooftops surface, that the model evaluates as homogeneous whereas in the real environment it is not.

### Input Wind Direction Parallel from North to the Street Canyon Orientation

Simulated profiles for the NP wind direction ensemble ( $-20^\circ \leq wd \leq 20^\circ$ ) to the reference LB orientation are shown in Fig. 7.9. They refer to the period 16:00-17:00 of the 22/09/2017 when the reference wind speed at SI monitoring site was  $u_{ref}=1.5 \text{ ms}^{-1}$ . The vegetation attenuation

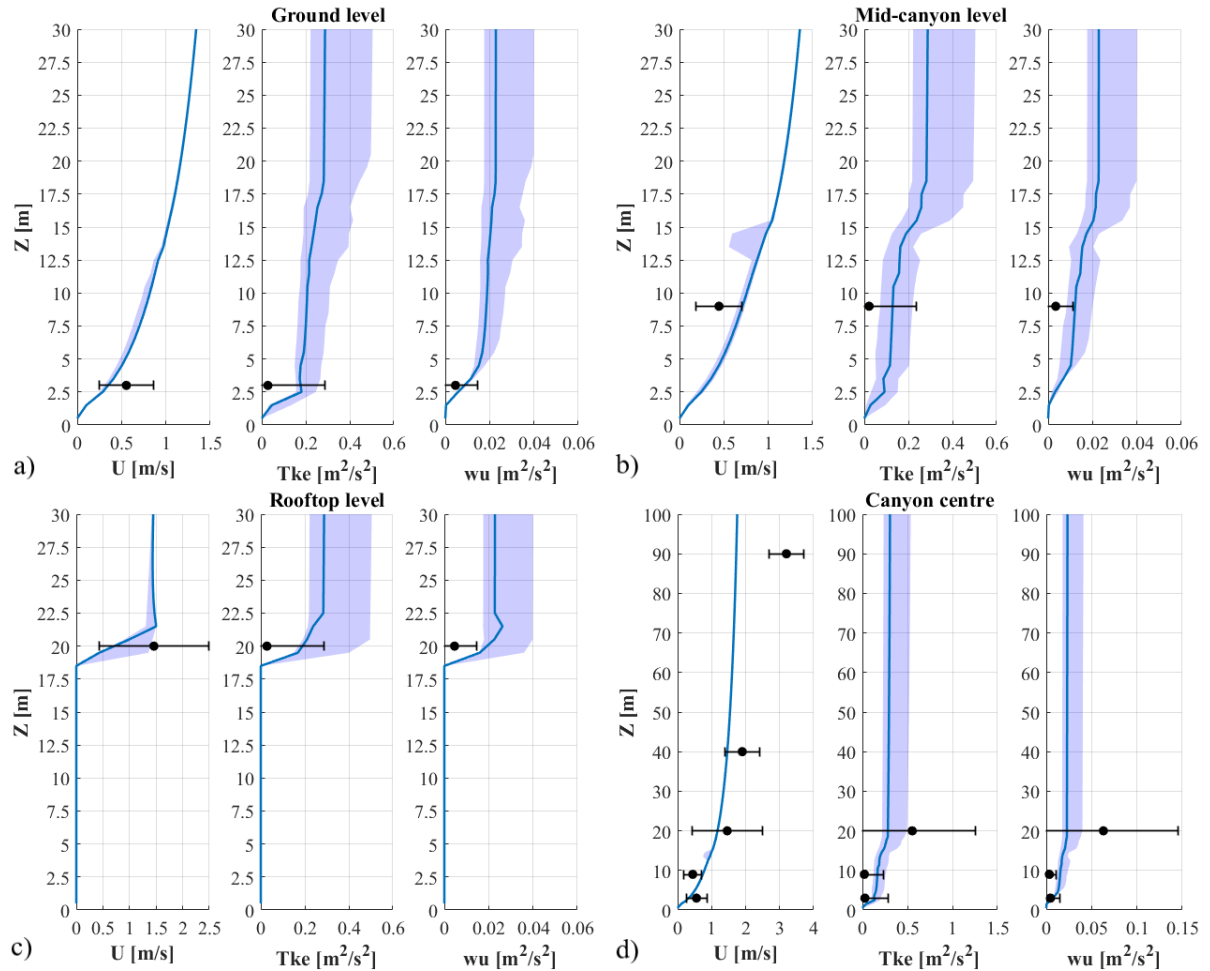


**Figure 7.9:** Simulated  $U$ ,  $Tke$  and  $|\overline{w'u'}|$  at (a) GL, (b) ML, (c) RL and (d) canyon center locations for the NP wind direction ensemble in LB. The blue profile represents the  $0^\circ$  wind direction to the canyon orientation, while the shadowed area is the wind direction ensemble. The black dots and error bars refer to the averaged measured value and standard deviation within the selected period.

## 7.2. MODEL VERIFICATION AMONG DIFFERENT WIND DIRECTION ENSEMBLES

coefficient is always  $a=1.7$ , while  $z_0=1.51$  m according to table 4.2. The inverse of the Obukhov length ( $1/L_O=-0.0223$  m<sup>-1</sup>) accounts for a near neutral condition. The in-canyon temperature ( $T_c=296$  K) is slightly larger than the ambient ( $T_a=295$  K), while relative humidity decreases from  $RH_c=43\%$  to  $RH_a=33\%$  from the canyon surface to the AT monitoring site. The boundary layer height ( $h_{BL}=1336$  m) is typical of daytime hours.

TKE and TKMF are overestimated in comparison with the data from measurements. Once again the proximity of a boundary, like the surface or the building facade, is poorly represented by the model, but still within the range of confidence of the data. Moreover the channelling effect of the flow parallel to the street canyon, somehow enhances the turbulence production of both TKE and TKMF. The mean wind speed is underestimated at the GL (Fig. 7.9a) due to the poor representation of the flow acceleration between the tree crown and the surface. Conversely, the wind speed is overestimated at ML (Fig. 7.9b). The channelling effect at the street surface is underestimated, since the trunk portion of the tree can create a flow acceleration not captured by the model. Nevertheless, the speed reduction due to the enhanced roughness of the small environment between the tree crown and the building facades is instead interpreted by the model as a simple sidewall on which the flow can accelerate due to the increased volume pressure. In both cases, wind speed profiles are independent of wind direction, as a consequence of the channeling behavior of the flow. The canyon center profiles (Fig. 7.9d) overestimate the daytime typical behavior of the mean flow and turbulence accounting for well mixed air and small gradients, larger than what it is resembled by data from measurements. This last poor comparison is indeed a consequence of the sum of the problematic already described for the single sensors locations, and it is expected to increase due to the bulk estimation of the center canyon profile. Nevertheless the data from measurements stay within the wind direction ensembles retrieved from the model.

### Input Wind Direction Parallel from South to the Street Canyon Orientation

Fig. 7.10 shows the simulated profiles for the SP wind direction ensemble ( $160^\circ \leq wd \leq 200^\circ$ ) to the LB orientation, referring to the period 03:00-04:00 of the 22/09/2017. This last scenario presents some differences with the previously analyzed ones. Reference wind speed is more intense ( $u_{ref}=5.3$  ms<sup>-1</sup>) due to the possible development of a nocturnal jet at the city scale. An inverse thermal stratification affects the UBL above the canopy, where a  $\Delta T=2$  K is retrieved between 40 m and 100 m. Nevertheless, air within the canopy and at the rooftop interface remains mixed due to the heat loss from the building facades, and a weak unstable condition develops inside the canyon ( $1/L_O=-0.0816$  m<sup>-1</sup>). The result is a strong thermal and stability decoupling between the UCL and the UBL above it. Relative humidity does not follow the temperature inversion and ranges between the  $RH_c=69\%$  value inside the canyon to  $RH_a=50\%$  at the AT monitoring site. A boundary layer height of  $h_{BL}=455$  m is retrieved.

## CHAPTER 7. RESULTS AND DISCUSSION: MODELING THE IMPACTS OF TREES ON THE EXCHANGE PROCESSES

Wind speeds inside the canyon and at RL are in slight good agreement with measurements, with the same behavior already described for the previous wind directions. Turbulent related quantities show peculiar profiles, with large magnitudes inside the canopy and a rapid decrease where the temperature gradient becomes positive. Moving toward the canyon center, the TKE maximum moves closer to the street surface, while TKMF maximum remains confined in the lower half of the canyon. Near the buildings facades (Fig. 7.10b), turbulence maxima are re-

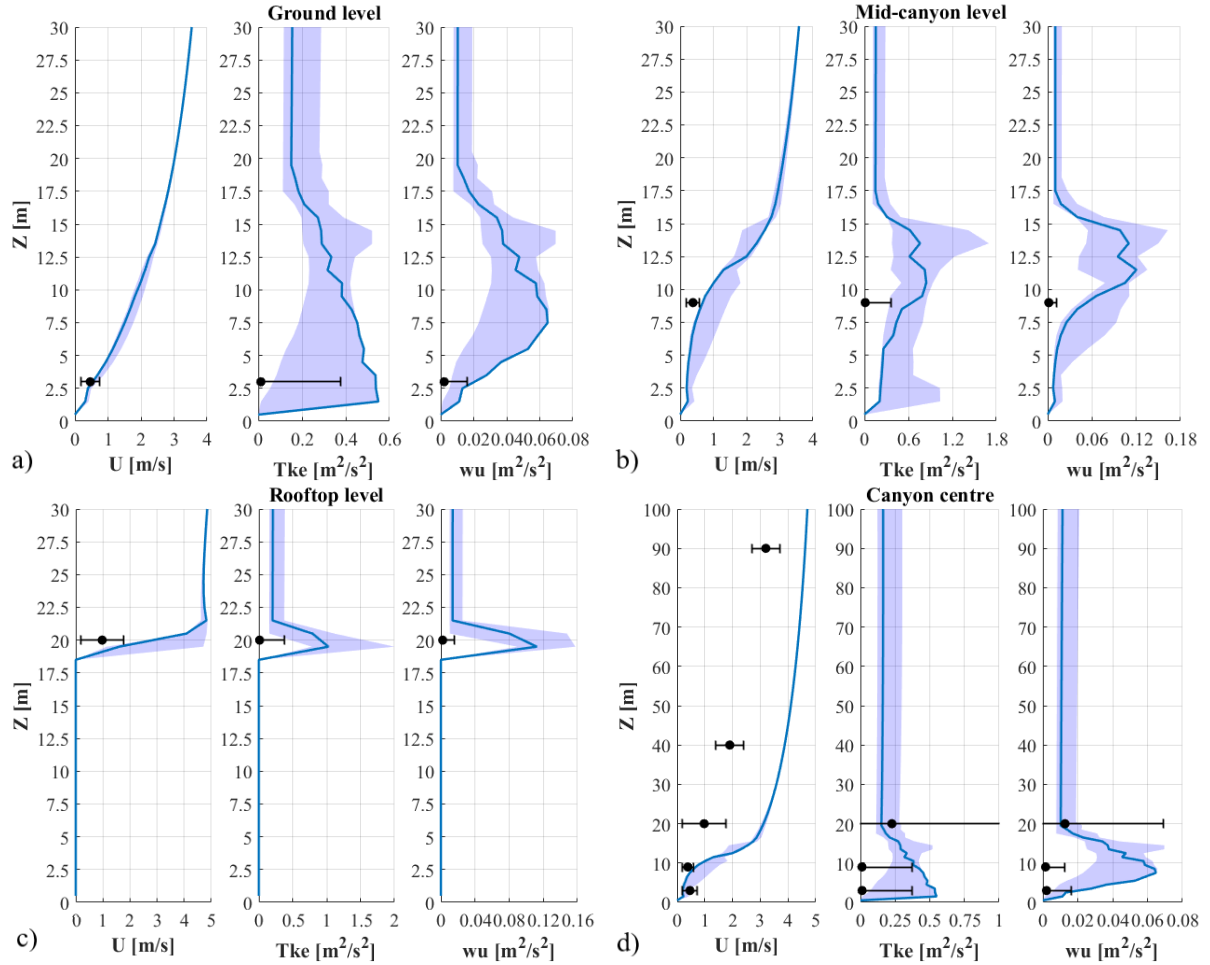


**Figure 7.10:** Simulated  $U$ ,  $Tke$  and  $|w'u'|$  at (a) GL, (b) ML, (c) RL and (d) canyon center locations for the SP wind direction ensemble in LB. The blue profile represents the 180° wind direction to the canyon orientation, while the shadowed area is the wind direction ensemble. The black dots and error bars refer to the averaged measured value and standard deviation within the selected period.

trieved close to the mean rooftop height, creating a small upper canyon circulation confined between the buildings and the trees. Simulations always overestimate the data from measurements, probably because of the overestimation of the local unstable conditions impact on the flow, or the mutual presence of a stable stratification on top of an unstable layer. This last

suggestio maybe caused by the limitations involved using an approximated/operational model instead of a more "sofisticated" but computationally costly one. Nevertheless, as the profiles are mostly within the measurements error bars, the use of QUIC is justified by the good balance between the results reliability and the small computational costs of the simulations.

### 7.2.2 Non Vegetated Street Canyon - Marconi Street

#### Input Wind Direction Perpendicular from East to the Street Canyon Orientation

Profiles simulated for the EP wind direction ensemble ( $70^\circ \leq wd \leq 110^\circ$ ) to MA orientation are displayed in Fig. 7.11, relative to the measured period 17:00-18:00 of the 22/09/2017. The reference wind speed for the logarithmic input profile, retrieved from SI monitoring site is  $u_{ref}=1.9$   $\text{ms}^{-1}$  at the already know reference height  $z_{ref}=40$  m. As stored in Tab. 4.2, the roughness length for the EP wind direction case is  $z_0=1.33$  m, while the vegetation attenuation coefficient is  $a=1.7$ . Neutral conditions within the canopy are ensured by the measured inverse Obukhov length  $1/L_O=0$   $\text{m}^{-1}$ . A temperature gradient is retrieved between the canopy temperature  $T_c=296$  K and the atmospheric temperature  $T_a=294$  K above the canopy. Relative humidity shows a (decreasing) vertical gradient too from the canopy value  $RH_c=42\%$  to the ambient relative humidity  $RH_a=35\%$ . The boundary layer height is retrieved from the ceilometer data and has an average value within the period  $h_{BL}=975$  m.

Fig. 7.11a shows the GL comparison between the data from measurements and the simulated profile ensembles. Despite turbulent characteristics are well captured by the model, wind speed is completely underestimated. The complexity associated with the simulation the street surface in MA is a typical issue for the EWP wind direction configurations (see Fig. 7.12) and it is due to the poor representation of the surface dynamics next the lateral boundaries of deep and narrow street canyons, as the one under investigation. In these areas, it is common to observe secondary recirculation vortices which are difficult to replicate, especially with a simple model such as QUIC. Moreover, the presence of *portici*, the galleries covering the sidewalks, contribute to increase the complexity of the local morphology, decreasing the comparability with the model, which does not account for these structural features of the buildings. Despite this discrepancy, the simulations well represent the data from measurements, even considering the canyon center case (Fig. 7.11d), except for the turbulent quantities at the RL. Both the simulated TKMF and TKE profiles capture a ShL dynamics not retrieved from measurements, which are therefore overestimated. It is also possible that the RL is embedded in a recirculation area, induced by the complex morphology of the rooftop itself, which is not captured by the model. Nevertheless, the wind speed is correctly simulated, meaning that at least the mean flow is well represented. Turbulence within the canopy is also overestimated by the model at both GL and ML. Due to the depth of the canyon, the intensity of the observed circulation is small and the turbulence associated with it is very small too. In this context, the model overestimates the TKE and

## CHAPTER 7. RESULTS AND DISCUSSION: MODELING THE IMPACTS OF TREES ON THE EXCHANGE PROCESSES

TKMF productions despite the wind speed within the canopy is underestimated. Nevertheless, the model captures most of the dynamics within and above the canopy, as the simulations are mostly within the measurements error bars.

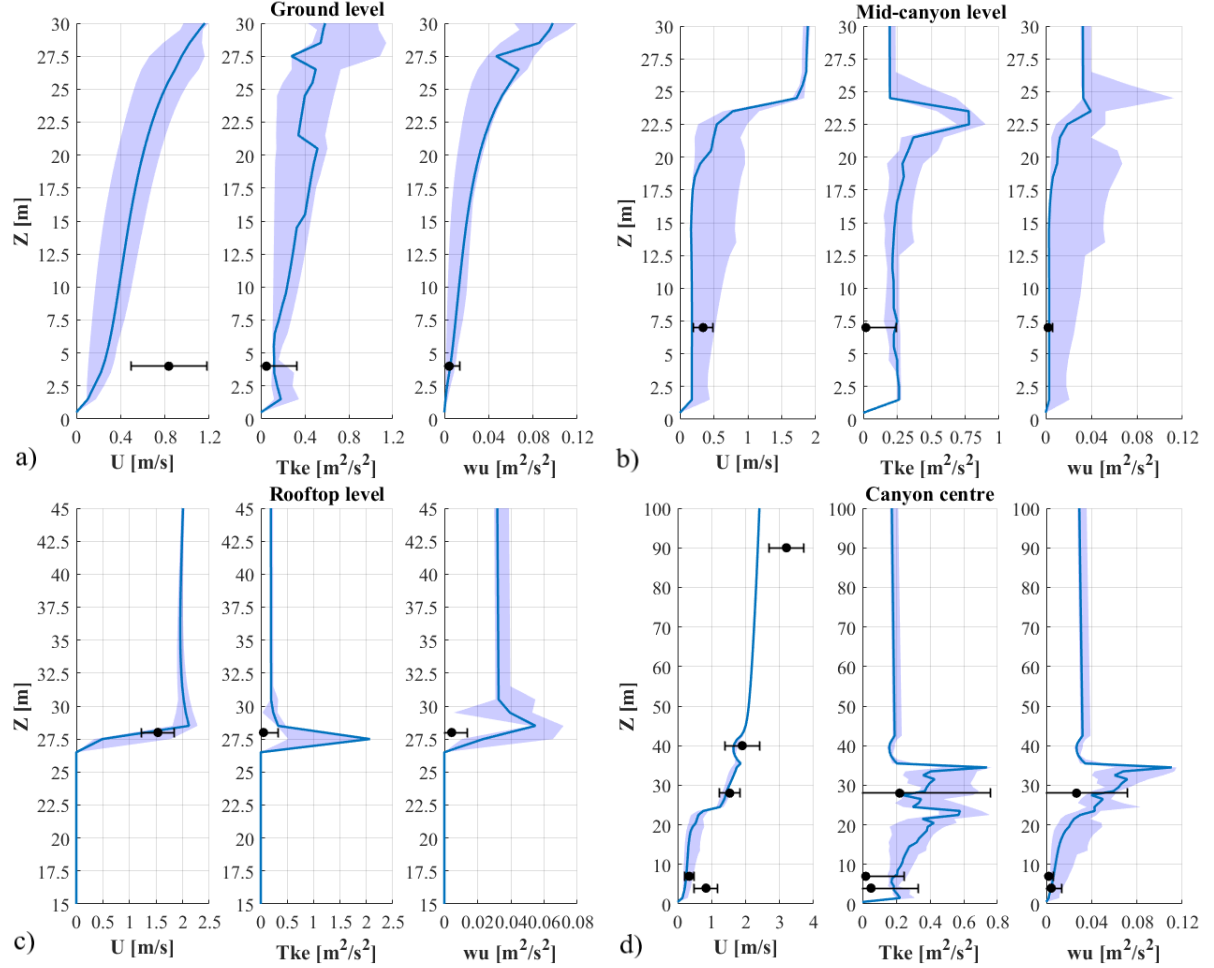


**Figure 7.11:** Simulated  $U$ ,  $Tke$  and  $|\overline{w'u'}|$  at (a) GL, (b) ML, (c) RL and (d) canyon center locations for the EP wind direction ensemble in MA. The blue profile represents the 90° wind direction to the canyon orientation, while the shadowed area is the wind direction ensemble. The black dots and error bars refer to the averaged measured value and standard deviation within the selected period.

### Input Wind Direction Perpendicular from West to the Street Canyon Orientation

Fig. 7.12 shows the simulated profiles ensembles for the case of WP wind directions  $wd$  ( $250^\circ \leq wd \leq 290^\circ$ ) to MA orientation. They are representative of the period 09:00-10:00 of the 20/09/2017 and compared with data from each measurement site within and above the canyon, averaged over this period. The reference wind speed  $u_{ref}=2.9 \text{ ms}^{-1}$  for the input logarithmic

## 7.2. MODEL VERIFICATION AMONG DIFFERENT WIND DIRECTION ENSEMBLES

profile of the model is retrieved from SI monitoring site at the reference height  $z_{ref}=40$  m. The roughness length is set at  $z_0=1.33$  m according to table 4.2, while the Obukhov length is calculated at the canyon rooftop and its inverse is  $1/L_O=-0.0284$  m<sup>-1</sup> describing a near-neutral condition as it was classified by Rotach (1995). The vegetation attenuation coefficient is calculated from Eq. (4.12) and is set at  $a=1.7$ . From the thermohygrometers data at each level, the

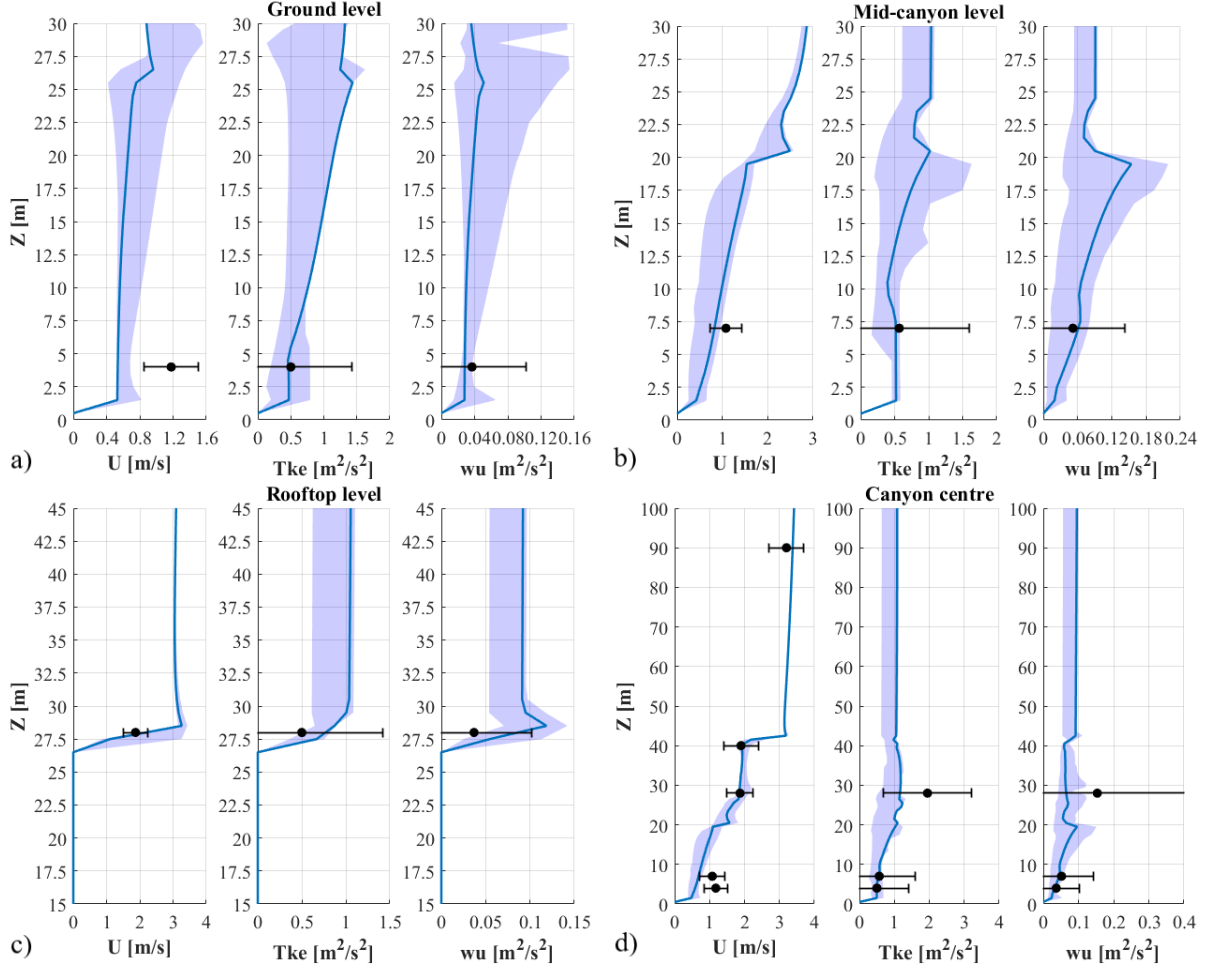


**Figure 7.12:** Simulated  $U$ ,  $Tke$  and  $|\overline{w'u'}|$  at (a) GL, (b) ML, (c) RL and (d) canyon center locations for the WP wind direction ensemble in MA. The blue profile represents the  $270^\circ$  wind direction to the canyon orientation, while the shadowed area is the wind direction ensemble. The black dots and error bar refer to the averaged measured value and standard deviation within the selected period.

atmospheric profiles of temperature and relative humidity are retrieved, considering both UCL and UBL. Air temperature varies slightly with the height, between the in-canyon temperature  $T_c=290$  K and the ambient temperature  $T_a=291.5$  K. Relative humidity shows small oscillations around the input value  $RH=50\%$ . The boundary layer height ( $h_{BL}=750$  m) is similar to the

condition retrieved for the EP wind direction ensemble.

Simulated profiles are in good agreement with the data from measurements at all locations. The only discrepancy is retrieved in the wind speed at the GL location (Fig. 7.12a), as already observed for the EP wind direction ensemble (Fig. 7.11a). In the current case, the underestimation is less pronounced, but it is still present, since the circulation within the canopy is expected to be similar to the EP case. Despite being on the opposite side of the circulation with respect to the EP wind direction case, secondary vortices are still expected to develop. Turbulence quantities are instead well captured by the model, as the measurements data are not as small as during the EP wind direction case. The discrepancy in terms of turbulence intensity between the WP and EP wind directions are a consequence of the different turbulence production at the opposite branches of the canopy circulation. At the RL, turbulent related quantities are still slightly overestimated, but the profiles fall within the measurement error bars, as the ShL dynamics is much less pronounced than during the EP case. The canyon center simulations are able to capture the behaviors of both mean flow and turbulence within and above the canopy.

### Input Wind Direction Parallel from North to the Street Canyon Orientation

The verification procedure for the NP wind direction ensemble ( $-20^\circ \leq wd \leq 20^\circ$ ) to MA orientation is displayed in Fig. 7.13 and represents the interval 10:00-11:00 of the 23/09/2017. The input wind speed profile is defined from the reference wind speed  $u_{ref}=1.1 \text{ ms}^{-1}$  at the reference height  $z_{ref}=40 \text{ m}$  of SI monitoring site. As for the previous cases, the vegetation attenuation coefficient is  $a=1.7$ , while the roughness length is  $z_0=1.12 \text{ m}$ . Neutral atmospheric stability is ensured by the inverse Obukhov length, which was evaluated to be  $1/L_O=0 \text{ m}^{-1}$ . Despite the neutral stability of the canopy, the whole atmospheric column shows a temperature vertical gradient which ensures the canyon temperature  $T_c=293 \text{ K}$  to be smaller than the ambient one  $T_a=296 \text{ K}$  above it. Relative humidity shows the inverse tendency with  $RH_c=54\%$  and  $RH_a=46\%$ . The large temperatures above the canopy enable the boundary layer height to rise to  $h_{BL}=1240 \text{ m}$ .

A good agreement between the simulated profiles and the measurements is found at all locations (Fig. 7.13). Wind speed at GL (Fig. 7.13a) is better represented than the EP cases without deteriorating the agreement with the turbulent quantities. The ML (Fig. 7.13b) shows the worst agreement in terms of wind speed due to a general underestimation of the flow velocity. A poor representation of the wind speed is also found above the canopy at SI ( $z=40 \text{ m}$ ) and AT ( $z=90 \text{ m}$ ) heights (Fig. 7.13d). The vertical gradient of the wind speed from the simulations is too large with respect to what is shown by measurements. As a consequence, a general underestimation of the wind speed within the canopy is obtained at each level (Fig. 7.13). The absence of a displacement in the wind speed profiles within the canopy suggested the channeling behavior of the mean flow, which finds a good agreement with measurements (Fig. 7.13d).

## 7.2. MODEL VERIFICATION AMONG DIFFERENT WIND DIRECTION ENSEMBLES

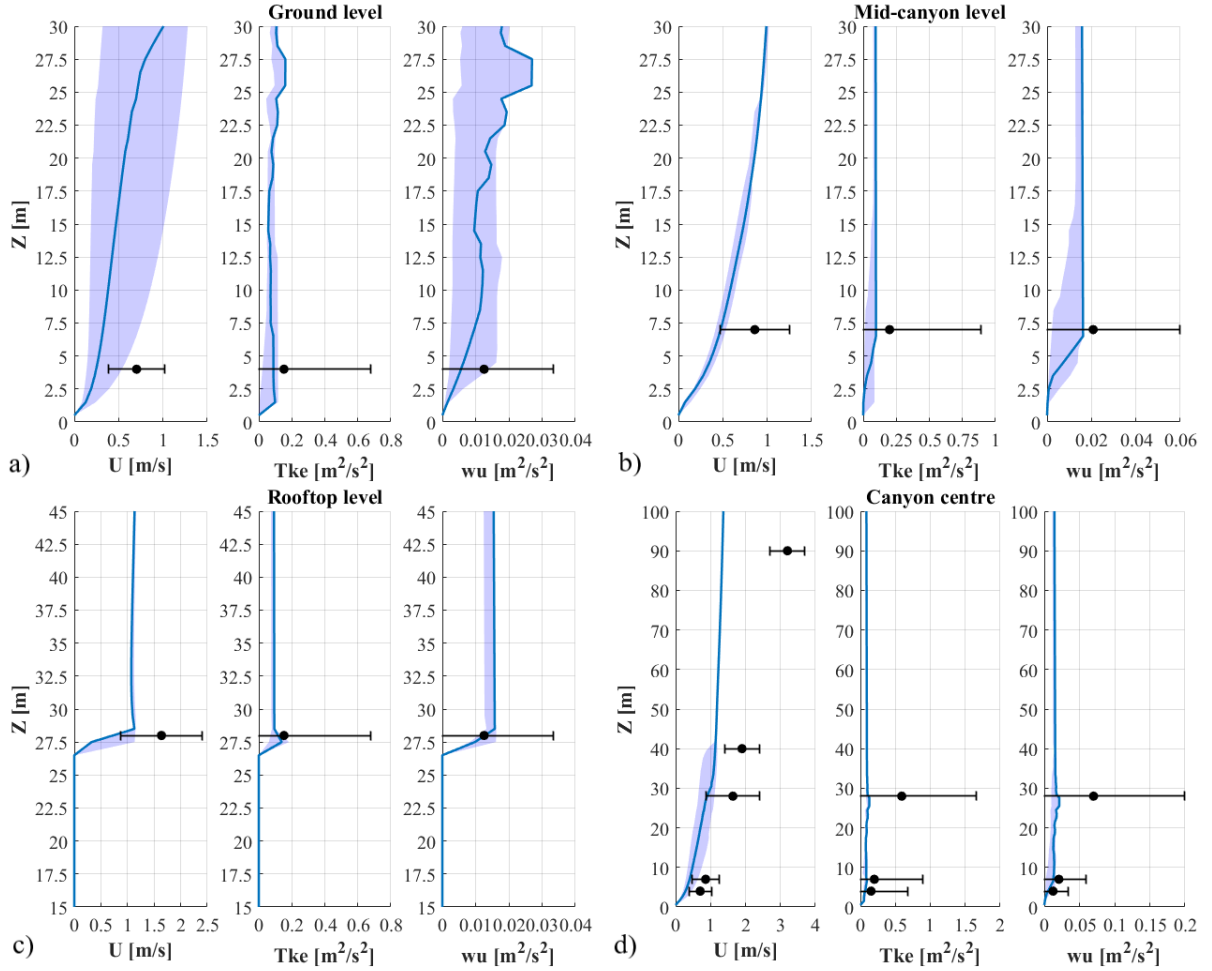


**Figure 7.13:** Simulated  $U$ ,  $Tke$  and  $\overline{|w'u'|}$  at (a) GL, (b) ML, (c) RL and (d) canyon center locations for the NP wind direction ensemble in MA. The blue profile represents the  $0^\circ$  wind direction to the canyon orientation, while the shadowed area is the wind direction ensemble. The black dots and error bars refer to the averaged measured value and standard deviation within the selected period.

### Input Wind Direction Parallel from South to the Street Canyon Orientation

Simulated profiles for the SP wind direction ensemble ( $160^\circ \leq wd \leq 200^\circ$ ) to MA orientation are shown in Fig. 7.14. They refer to the period 05:00-06:00 of the 21/09/2017 when the reference wind speed at SI monitoring site was  $u_{ref}=3.5 \text{ ms}^{-1}$ . The vegetation attenuation coefficient is always  $a=1.7$ , while  $z_0=1.12 \text{ m}$  according to table 4.2. The inverse of the Obukhov length ( $1/L_O=0 \text{ m}^{-1}$ ) accounts for neutral stability in the canyon. The in-canyon temperature ( $T_c=290 \text{ K}$ ) is slightly larger than the ambient ( $T_a=291.5 \text{ K}$ ), while relative humidity decreases from  $RH_c=51\%$  to  $RH_a=44\%$  from the canyon surface to the AT monitoring site. The result is a strong thermal and stability decoupling between the UCL and the UBL above it. The boundary

CHAPTER 7. RESULTS AND DISCUSSION: MODELING THE IMPACTS OF TREES ON THE EXCHANGE PROCESSES

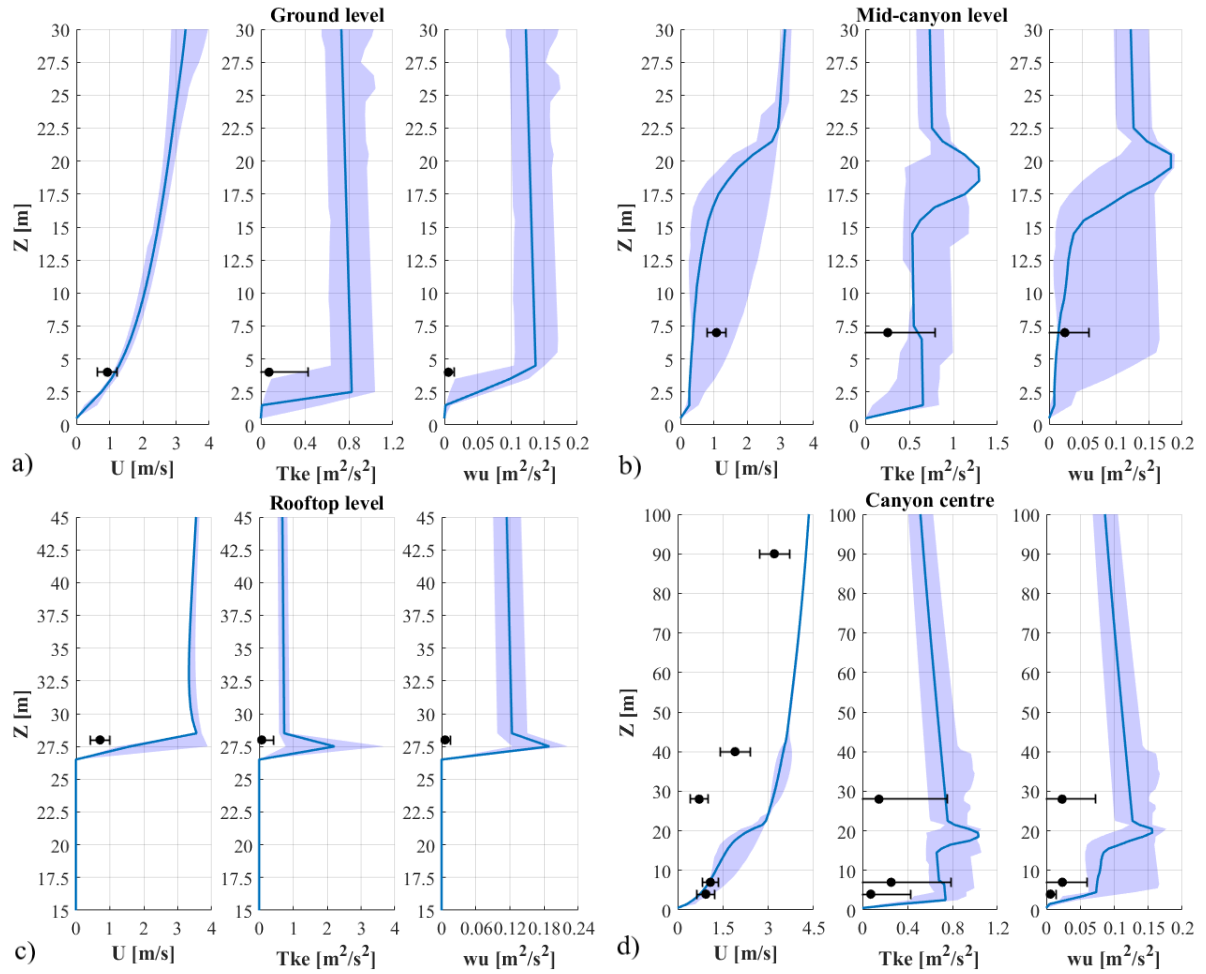


**Figure 7.14:** Simulated  $U$ ,  $Tke$  and  $|\overline{w'u'}|$  at (a) GL, (b) ML, (c) RL and (d) canyon center locations for the SP wind direction ensemble in MA. The blue profile represents the  $180^\circ$  wind direction to the canyon orientation, while the shadowed area is the wind direction ensemble. The black dots and error bars refer to the averaged measured value and standard deviation within the selected period.

layer height ( $h_{BL}=356$  m) is typical of nocturnal hours.

As it was already found for LB case, the SP wind direction ensemble shows the worst agreement between simulated profile and data from measurements for both mean flow and turbulence (Fig. 7.14). The wind speed within the canopy is well captured by the model, but turbulent quantities are overestimated especially at the GL (Fig. 7.14a). The RL is very poorly represented with a large overestimation of both mean flow and turbulent quantities (Fig. 7.14c). The reason behind the overestimation can be found in the strong decoupling between the canopy and the atmosphere above it, as it is shown by the wind speed measurements in Fig. 7.14d. The UBL profile is poorly represented by the model, that cannot capture the decoupled system. As a

### 7.3. THE IMPACT OF TREES IN LAURA BASSI NEIGHBORHOOD UNDER THE INPUT WIND DIRECTION PERPENDICULAR FROM EAST TO THE STREET CANYON ORIENTATION

---

consequence, the driven wind speed at the RL is overestimated as it is overestimated the UBL profile above the canyon. Being directly related to the mean flow, the turbulent quantities at RL are overestimated too.

## 7.3 The Impact of Trees in Laura Bassi Neighborhood under the Input Wind Direction Perpendicular from East to the Street Canyon Orientation

Following the aim of the research, QUIC is used to assess the impact of trees in an urban neighborhood of the city of Bologna, considered as an example of European city among which testing the efficacy of a model developed for typical American cities. The selected simulated area is the residential neighborhood surrounding LB (Fig. 4.12b). The choice is motivated by the presence of measurements which can help to set the input parameters and to have a comparison with the results from simulations, and because this neighborhood more than the one surrounding MA has a large disposal of vegetation in the real scenario (which will be used as reference to test the impact of vegetation). The setup for the reference simulation is the same as for the EP wind direction ensemble verification (Sect. 7.2.1), and follows the morphological parameter implementation of Sect. 4.3.4. Fig. 7.15, 7.16 and 7.17 display two cross sections of the wind speed, TKE and TKMF within LB in the vicinity of the GL (panels a-b) and ML (panels c-d) locations respectively. Each quantity is simulated using the same domain size, resolution and solid obstacles, with the exception of trees, which are present in the real amount in panels a-c and completely removed in panels b-d. The location for the cross sections computation was chosen to evaluate the impact of trees in two of the most representative geometries of real urban environments, i.e. the wake region on the leeward side of a building (panels a-b) and the street canyon (c-d) whose flow develops in the skimming regime of Oke (1987). In the wake region (Fig. 7.15a) the mean flow perturbation generated by the trees results in a wavelike motion, whose period depends on the distance between adjacent trees. This wavelike motion is generated because the flow speed inside the tree is reduced by the drag force exerted by the porous crown. This wind speed reduction propagate vertically above the trees due to the mass conservation, imposing a wavelike motion also in the ISL. Adding trees means adding obstacles which generate a local increase of pressure on the flow field that in turn has to adapt and adjust. This adaptation creates a wavelike motion since the flow is pushed upward when it passes above the tree, or decelerates when it flows through the tree. The wavelike motion can either be a pressure driven wave or a wake generated by the collision between the flow and the trees. Either way, the mass conservation sustains this wavelike motion and allows it to propagate vertically, generating a column of slower wind speed with respect to the surroundings. This wavelike motion is retrieved in the street canyon environment (Fig. 7.15c), but it is characterized by a smaller

## CHAPTER 7. RESULTS AND DISCUSSION: MODELING THE IMPACTS OF TREES ON THE EXCHANGE PROCESSES

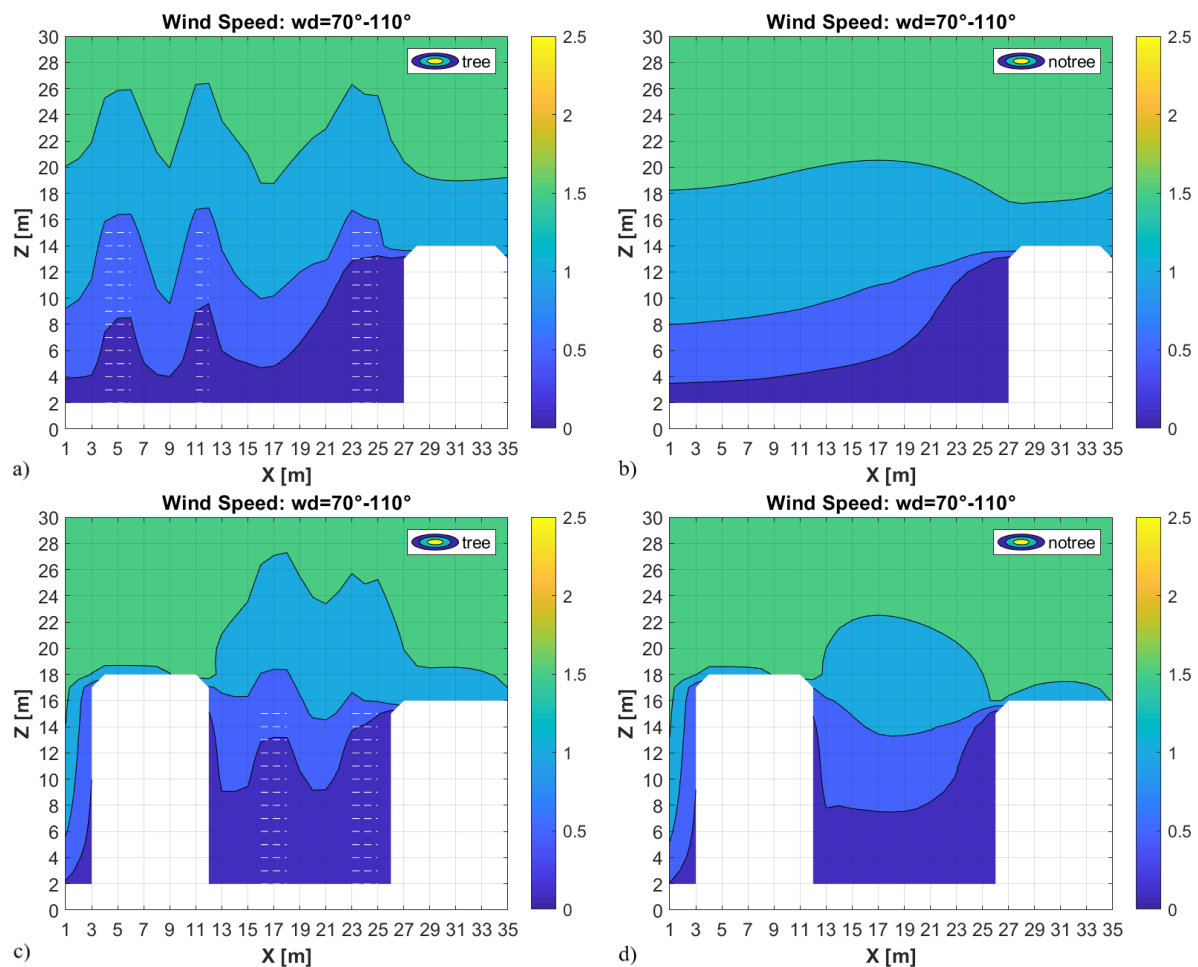


**Figure 7.15:** Cross sections of the wind speed simulated at the GL (a-b) and ML (c-d) monitoring sites of LB. (a-c) simulate the real environment of the street while (b-d) represent the scenario where vegetation has been removed. Solid boundaries are displayed in white, trees are represented as white towers of dashed lines.

intensity. Since the environment is more enclosed by the buildings, the wind speed reduction imposed by the trees is less pronounced compared to the scenario without vegetation (Fig. 7.15d). To summarize, despite the wind speed reduction effect seems to be more pronounced in the wake environment, the overall impact of the trees is a blocking effect on the mean flow (in agreement with previous CFD studies from literature, Sect. 2.4) resulting in a wavelike motion who propagates in the whole UBL.

Scaling directly with the mean flow intensity,  $Tke$  is also modified by the presence of trees (Fig. 7.16). Considering the wake cross section (Fig. 7.16a), the presence of the trees have dual effect.  $Tke$  is weakened close to the street surface within the trees volume as a consequence of the mean flow attenuation.  $Tke$  within the tree top is instead largely increased, while a minimum

### 7.3. THE IMPACT OF TREES IN LAURA BASSI NEIGHBORHOOD UNDER THE INPUT WIND DIRECTION PERPENDICULAR FROM EAST TO THE STREET CANYON ORIENTATION

of  $Tke$  appears above the tree crowns. The tree top increase produces values of  $Tke$  of the same magnitudes of the ones generated in the recirculation zone at the incident building rooftops. With respect to the wind speed modifications, the impact of vegetation on  $Tke$  is limited to the volume occupied by the tree and the closely adjacent areas. A periodicity is also generated but it involves only the vegetated volume. Within the street canyon (Fig. 7.16c-d), the impact of vegetation is more complicated. The overall effect is to decrease the homogeneity and modify the  $Tke$  gradient of the in-canyon field. In the scenario without vegetation (Fig. 7.16d), the  $Tke$  is maximum at the building rooftops, and these large values penetrate the street canyon from the top of the leeward wall. A decreasing  $Tke$  gradient generates in the canopy toward the windward wall, and homogeneous portions of constant  $Tke$  appears obliquely to the canyon

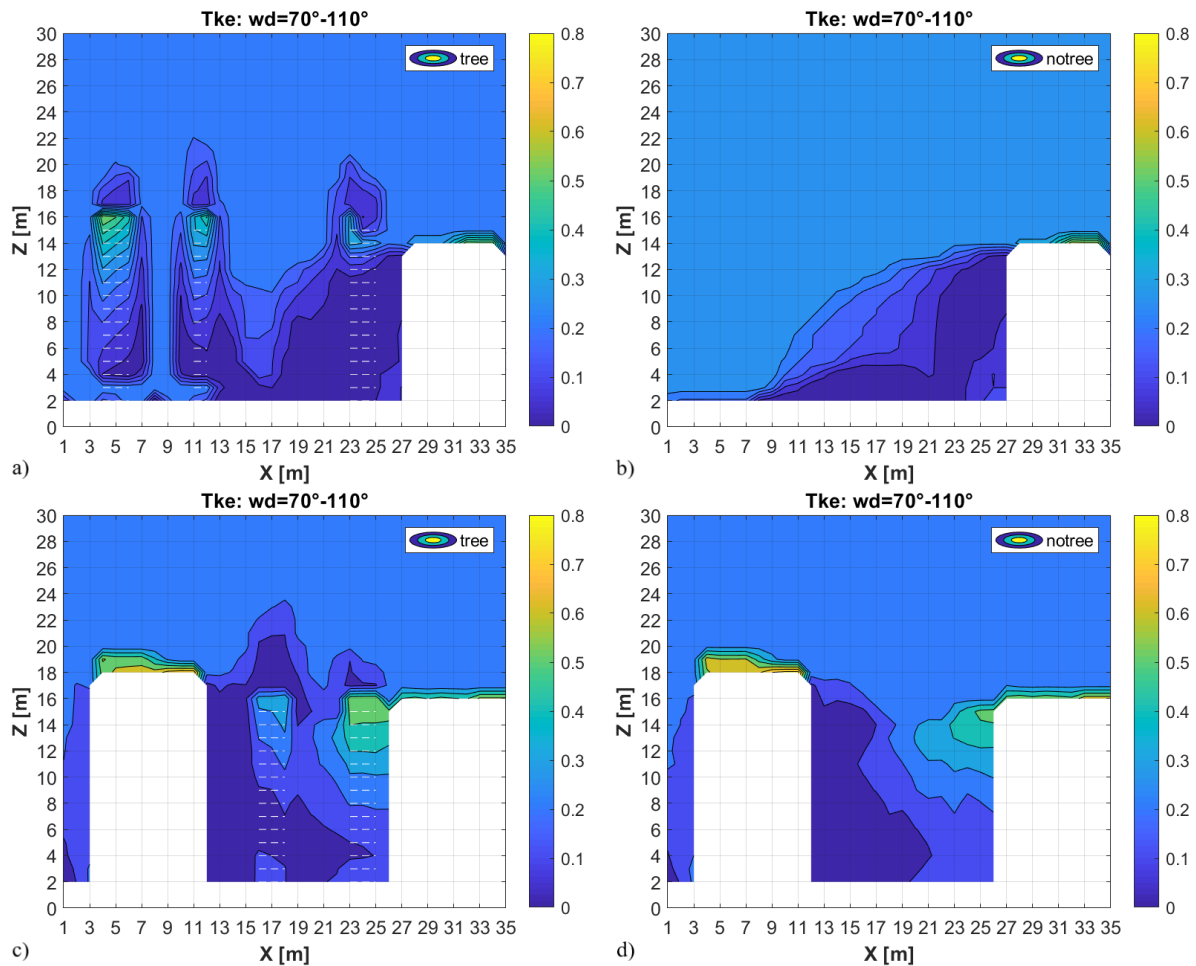


**Figure 7.16:** Cross sections of the  $Tke$  simulated at the GL (a-b) and the ML (c-d) monitoring sites of LB. (a-c) simulate the real environment of the street while (b-d) represent the scenario where vegetation has been removed. Solid boundaries are displayed in white, trees are represented as white towers of dashed lines.

## CHAPTER 7. RESULTS AND DISCUSSION: MODELING THE IMPACTS OF TREES ON THE EXCHANGE PROCESSES

geometrical parameters. When vegetation is introduced in the canopy (Fig. 7.16c), these oblique structures are lost because the trees create zones of small  $Tke$  extending from the tree center, zones of small  $Tke$  increase at the canyon surface and zones of increasing  $Tke$  within the tree tops.  $Tke$  at the leeward wall increases close to the canyon rooftop, while it decreases above the canopy especially close to the windward wall. In this case there is no periodic perturbation, neither a wave motion.

The behavior of the turbulent kinematic momentum flux in the wake regime (Fig. 7.17a-b) is completely equal to its  $Tke$  counterpart. The wake cavity in the scenario with no vegetation (Fig. 7.16b) is highlighted by the wide volume of small  $|\overline{w'u'}|$  and large gradients, which separate the canopy behavior from the outer environment. In the presence of trees (Fig. 7.16a),

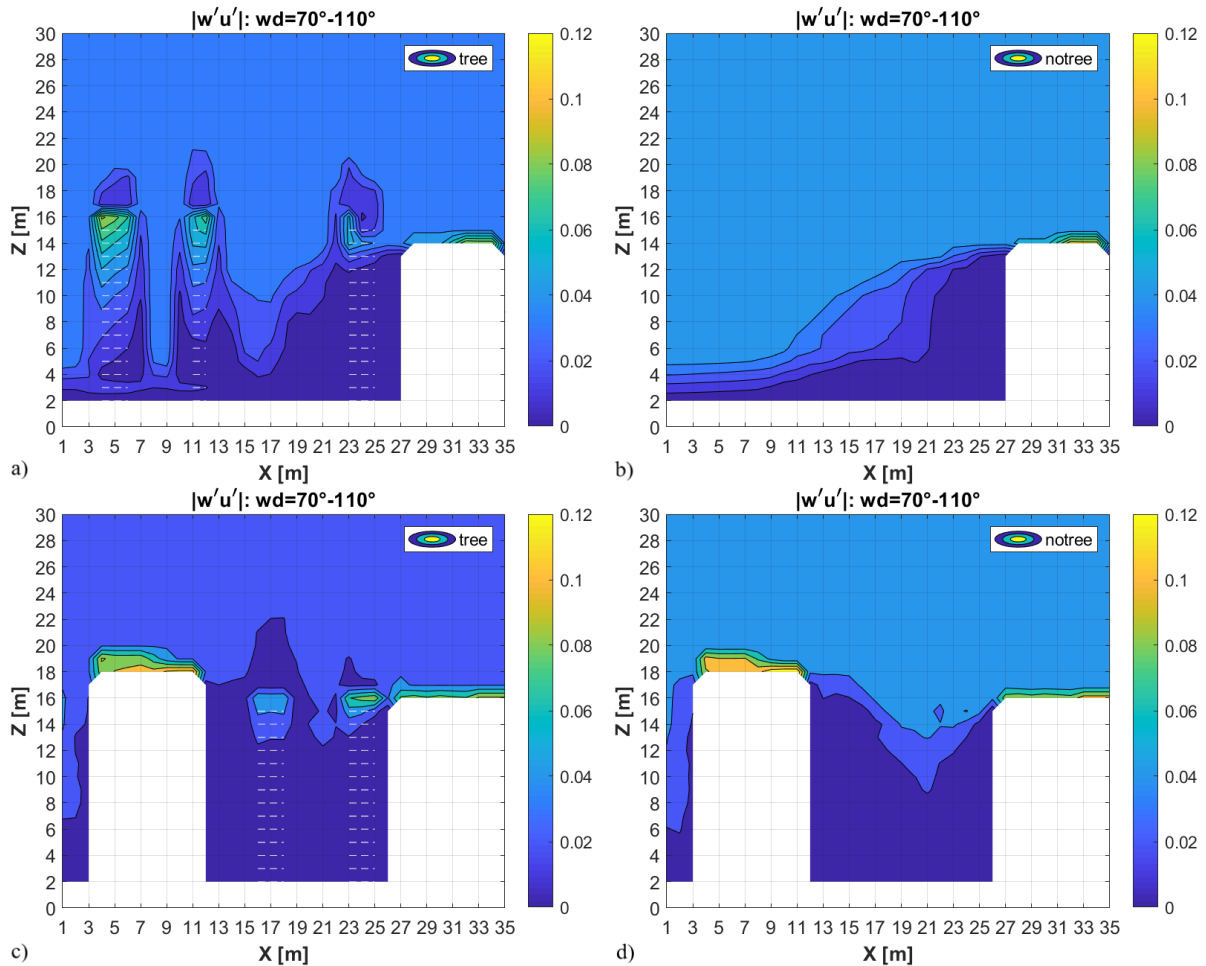


**Figure 7.17:** Cross sections of the TKMF  $|\overline{w'u'}|$  simulated at the GL (a-b) and the ML (c-d) monitoring sites of LB. (a-c) simulate the real environment of the street while (b-d) represent the scenario where vegetation has been removed. Solid boundaries are displayed in white, trees are represented as white towers of dashed lines.

### 7.3. THE IMPACT OF TREES IN LAURA BASSI NEIGHBORHOOD UNDER THE INPUT WIND DIRECTION PERPENDICULAR FROM EAST TO THE STREET CANYON ORIENTATION

---

the wake cavity is extended away from the building, while maxima of  $|\overline{w'u'}|$  are retrieved at the tree top. The impact of vegetation in the street canyon scenario (Fig. 7.16c-d) shows similarities and dissimilarities with the TKE simulations. The behavior of the TKMF in the recirculation zone of the building rooftops in the scenario with no vegetation is similar, but no intense entrainment is retrieved. A certain penetration through the street is also evident in the leeward half of the canopy. This penetration is completely lost when trees are present (Fig. 7.16c), and it is replaced by small values of  $|\overline{w'u'}|$  extending above the canopy. An intensification of the TKMFes within the tree top is induced by the momentum transport from the mean flow colliding with the crown to turbulence. The presence of trees does not seem to produce an effect on the in-canyon momentum flux.

From these qualitative investigation, it is evident the blocking effect of the trees on the mean flow field, while the turbulent quantities show a dual behavior: a dissipation of the turbulent fields at the surface and an increase of them within the trees top. Wavelike motions are also retrieved when dealing with the mean flow, while perturbations on the turbulent fields are more constrained in the vicinity of the trees. More quantitative analyses of the impact of trees are given in the following sections, where the distributions of wind speed, TKE and TKMF from the whole domain are detailed.

#### 7.3.1 Vegetation Impact Distributions and Topological Discretization

To extend the observations made in the previous section to the whole neighborhood and generalize the results for densely vegetated urban areas, an analysis based on the wind speed,  $Tke$  and  $|\overline{w'u'}|$  distributions is presented to evaluate the overall impact of trees in LB neighborhood. The same analysis is also refined to account for the different behavior of specific topological features of the neighborhood, such as differently oriented street canyons or intersections, when the total vegetation amount is modified. The proposed distributions will cover the whole horizontal domain and will be representative of five different layers within the UBL. Distributions are normalized on each total number of occurrences and displayed in a percentage ordinate scale from 0 (0%) to 1 (100%). The first two layers represent the average behavior of the mean flow and turbulent fields at ground and mid-canyon layers of the UCL, within whom the analyzed quantities are averaged. The depth of the layers are 1.5-4.5 m for the ground layer and 5.5-9.5 m for the mid layer. The roof layer (10.5-14.5 m) is the interface layer between the canopy and the UBL above it. Above the rooftop height, a roughness layer (15.5-20.5 m) is generally observed where the flow is adjusting from the perturbation generated by the canopy. The last layer is the inertial layer extending in the depth 25.5-30.5 m. It generally refers to the layer where the flow has already readjusted from the perturbation given by the canopy, but in this case there was no analysis to identify the height where a possible inertial layer develops, so it simply identifies the top layer of the first half of the vertical domain.

## CHAPTER 7. RESULTS AND DISCUSSION: MODELING THE IMPACTS OF TREES ON THE EXCHANGE PROCESSES

To evaluate the distributions, the EP wind direction ensemble input conditions (Sect. 7.2.1) are used. Three different scenarios are investigated, where only the vegetation amount is changed. The real environment simulation is used as Reference Scenario (REF-scen) among which to tests two possible vegetation amount variations. A No Vegetation Scenario (NOVEG-scen) tests the impact of the complete removal of vegetation from the domain. A third scenario accounts for an increase of the total vegetation element number by a 50%, randomly distributed within the domain, but maintaining a reliability in the positioning. This last condition simply allows to have a realistic increase of the tree number, avoiding for example the occlusion of existing streets. This third scenario will be referred as 50% Vegetation Increase Scenario (VEG50-scen). The wind speed distribution considering the whole domain is displayed in Fig. 7.18. The overall impact of

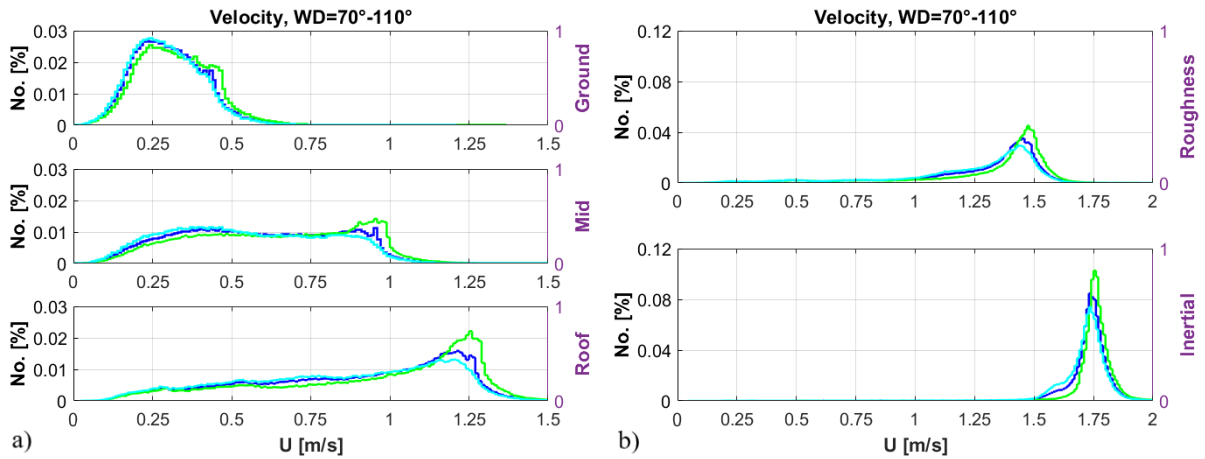


**Figure 7.18:** Wind speed  $U$  distributions evaluated in the (a) UCL and (b) UBL above for the REF-scen (in blue), the NOVEG-scen (in green) and the VEG50-scen (in cyan).

vegetation is to reduce the wind speed especially in the roof layer (Fig. 7.18a), that corresponds to the upper third of the trees. Within the canopy and at the interface the distribution are widespread (Fig. 7.18a), with maximum occurrences skewed toward large wind speed values, especially in the mid and upper portion of the canopy. In these layers, the NOVEG-scen shows a reduction in the number of the small wind speed values ( $U < 0.3 \text{ ms}^{-1}$  at the ground,  $U < 0.5 \text{ ms}^{-1}$  at mid and roof layers) and the appearance or the intensification of an occurrences maximum at large wind speed with respect to the REF-scen. Slight modifications are retrieved in the VEG50-scen with respect to the REF-scen at mid and roof layers, where the behavior is exactly the opposite of the NOVEG-scen variation. At the ground layer, NOVEG-scen and VEG50-scen show no significant differences. Above the canopy (Fig. 7.18b), the wind speed are almost normally distributed, with a tendency of the NOVEG-scen to skew the distributions toward large wind speed values. As the height increases, the discrepancy between the NOVEG-scen and the REF-scen is shaped more like a distribution shift rather than a maximum occurrence skew. The same tendency is retrieved if comparing VEG50-scen to REF-scen, with the distribution shift

### 7.3. THE IMPACT OF TREES IN LAURA BASSI NEIGHBORHOOD UNDER THE INPUT WIND DIRECTION PERPENDICULAR FROM EAST TO THE STREET CANYON ORIENTATION

going toward small wind speed values. As expected, the blocking effect of the trees among the mean flow observed in Sect. 7.3 is confirmed by the distributions in Fig. 7.18. The impact of this wind speed reduction is maximum in the upper portion of the trees, and decreases with the height outside the canopy.

TKE is displayed in Fig. 7.19. To remove the dependency from the wind speed, the TKE is normalized on the square value of the wind speed of each scenario. The contribution given by the tree is evident at all the considered layers. All the  $Tke$  values are normally distributed,

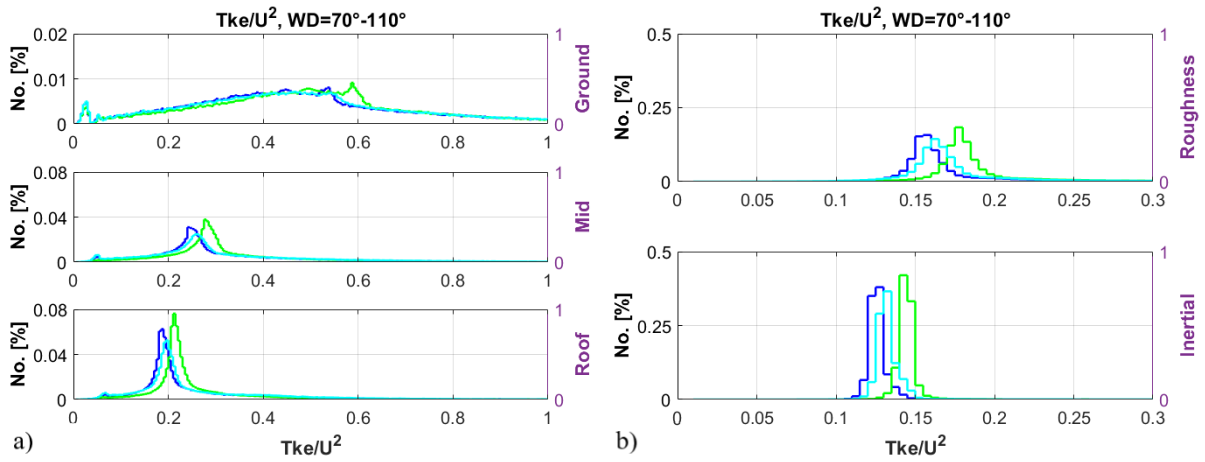


**Figure 7.19:**  $Tke$  distributions, normalized on the squared wind speed  $U$ , evaluated in the (a) UCL and (b) UBL above for the REF-scen (in blue), the NOVEG-scen (in green) and the VEG50-scen (in cyan).

apart from the ground distributions (Fig. 7.19a) that are largely spread, and differences among scenarios are significant only considering the NOVEG-scen. Despite the distributions are almost similar, NOVEG-scen shows a clear  $Tke$  maximum shift toward larger values with respect to both REF-scen and VEG50-scen that are equal. This shift of the NOVEG-scen becomes clearer as the height of the layer increases, reaching the distribution maximum separation outside the canopy (Fig. 7.19b). Outside the canopy, there is also a significant shift between the REF-scen and VEG50-scen distributions, which was only slightly appreciable at the mid and roof layers of the canopy (Fig. 7.19a). In opposition to wind speed results, the  $Tke$  VEG50-scen distributions above the mid layer shows an increase of  $Tke$  with respect to the REF-scen. There seems to be a bimodal behavior of  $Tke$  when the tree number in urban environment is modified.  $Tke$  may increase either removing or adding trees with respect to the REF-scen, describing a largely vegetated urban area. With the current simulation settings, the tree removal gives the larger improvement to the  $Tke$  increase, but there may be a critical tree number by which this situation is overturned.

The TKMF shows a similar behavior to  $Tke$ . Again the  $|\overline{w'u'}|$  values are normalized on the square of the wind speed to ensure a correct comparability between the distributions. The

## CHAPTER 7. RESULTS AND DISCUSSION: MODELING THE IMPACTS OF TREES ON THE EXCHANGE PROCESSES

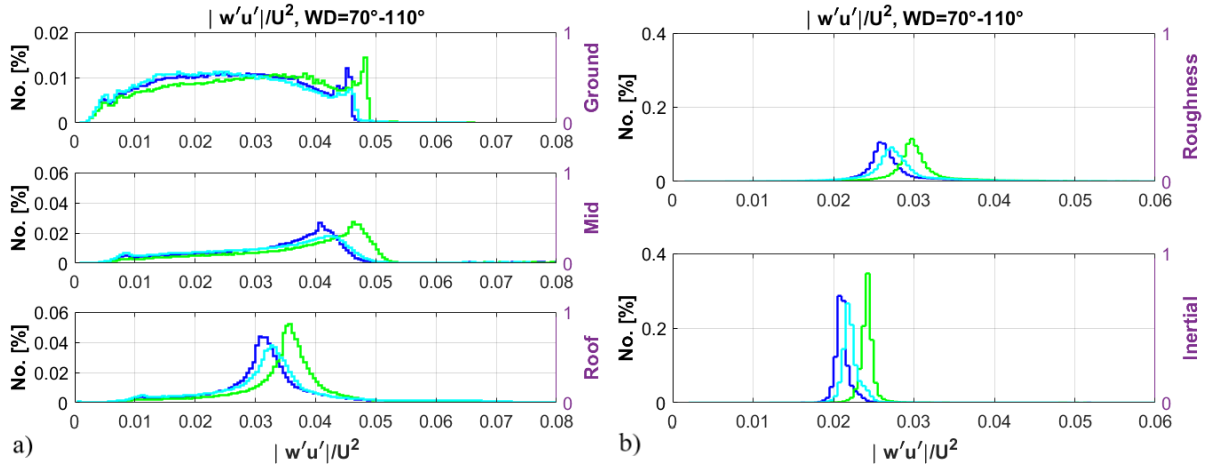


**Figure 7.20:** TKMF  $|\overline{w'u'}|$  distributions, normalized on the squared wind speed  $U$ , evaluated in the (a) UCL and (b) UBL above for the REF-scen (in blue), the NOVEG-scen (in green) and the VEG50-scen (in cyan). Ground layer in (a) has a different ordinate tick to make the distribution differences appreciable.

bimodal behavior already retrieved for the TKE is evident also in the TKMF, where a distribution shift is even clearer. The in-canyon distributions (Fig. 7.20a) follow the wind speed, with wide and skewed distributions in the lower canopy and Gaussian distributions at the roof layer. Distributions also become more narrow and peaked with height, reducing their variances (Fig. 7.20b). The NOVEG-scen is the most suitable scenario for the  $|\overline{w'u'}|$  development, but also VEG50-scen gives a positive trend to the flux increase. As it was for the TKE, with the current simulation settings the tree removal gives the larger improvement to the  $|\overline{w'u'}|$  increase, but there may be a critical tree number by which this statement is overturned.

To highlight the effect of vegetation through the different topological structures of the neighborhood, three topological categories are extracted from the domain. The topological categories are a collection of typical environments within the domain, which are the East-West Oriented Street Canyons (EWcanopy), the North-South Oriented Street Canyons (NScanopy) and the Major Intersections (Intersect). EWcanopy describes the street canyons parallel to the input flow, where a channeling effect is expected. NScanopy represents the perpendicularly oriented street canyons to the input flow, where bidimensional vortices can develop. Finally Intersect is a collection of the main junctions of the domain, where the flow is largely perturbed by horizontal inflows. The categories are a collection of at least ten structures for each class, in order to have a good amount of simulated data to evaluate the distributions. The layers already used for the whole domain distributions are again reproduced for this topological insight. For each category and in each layer, the computed distributions represent the variation factor for each quantity of NOVEG-scen from REF-scen. This variation factor is computed as  $X_{REF-scen}/X_{NOVEG-scen} - 1$ , where  $X$  stays respectively for  $U$ ,  $Tke/U^2$  or  $|\overline{w'u'}|/U^2$ , and

### 7.3. THE IMPACT OF TREES IN LAURA BASSI NEIGHBORHOOD UNDER THE INPUT WIND DIRECTION PERPENDICULAR FROM EAST TO THE STREET CANYON ORIENTATION

the -1 is introduced to center in zero the reduction (negative) and increment (positive) behaviors of the analyzed quantities caused by the vegetation presence. The resulting distributions for the wind speed are displayed in Fig. 7.21. The overall trend of the distributions is to confirm the

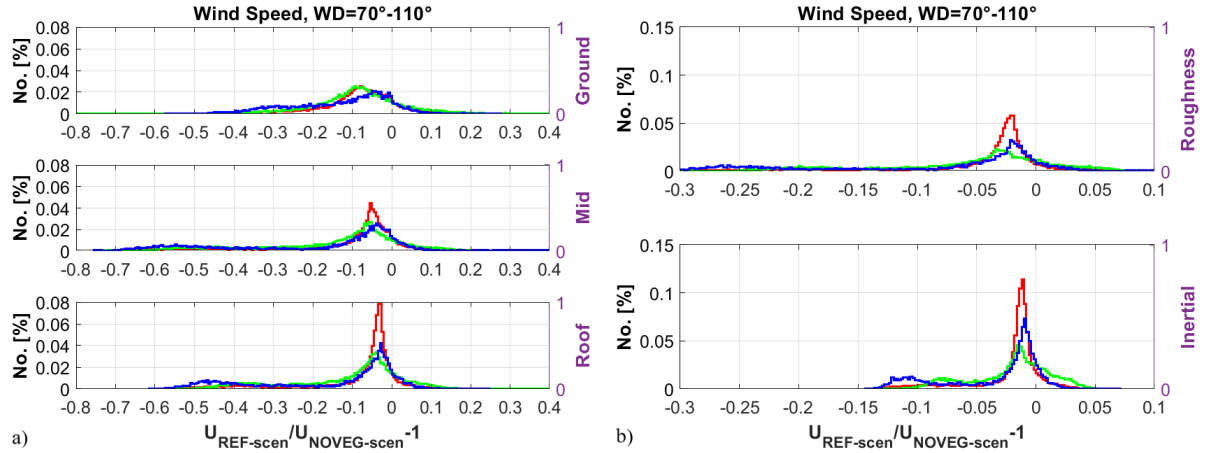


**Figure 7.21:** Wind speed  $U$  variation factor distributions evaluated in the (a) UCL and (b) UBL above for the difference between REF-scen VEG-scen for the EWcanopy (blue), NScanopy (green) and Intersect (red) topological categories.

tendency of the whole domain distributions (Fig. 7.18), with a decrease of wind speed as the trees are introduced in the domain. Within the canopy (Fig. 7.21a), wind speed distributions show some similarities. The majority of the wind speed reduction caused by the vegetation is embedded in the velocity variation factor range 0-0.1, with long tails in each category in the upper portion of the canopy. At the ground layer, wind speeds are almost normally distributed, except for the EWcanopy case, where an important velocity reduction is retrieved to be up to  $-0.35 \div -0.40$ . The largest wind speed reduction seems to occur in the EWcanopy category because of the largest distribution width and despite its distributions maxima are closer to zero with respect to the other two categories. The NScanopy shows a good reduction too, more constrained in the region of the distribution maximum. Less effective is the impact of Intersect, where it is also more difficult to have a large disposal of trees, despite at the roof layer the reduction peak follows the NScanopy category. The Intersect category has a dominant influence outside the canopy (Fig. 7.21b), where the distributions are peaked in the reduction range  $0 \div -0.05$  with a small standard deviation. EWcanopy category follows the roof distribution, showing an increase of the large reduction events at both out-canyon layers. NScanopy shows the largest distribution spread, with several occurrences where the wind speed increases in the presence of trees. The overall blocking effect of the trees on the wind speed is confirmed by the single topological categories, especially when the canopy is parallel to the mean flow direction. Blocking effect is the general behavior also when the mean flow is perpendicular to the street canyon, but some benefits may occur in presence of vegetation. The impact of vegetation on the mean flow in

## CHAPTER 7. RESULTS AND DISCUSSION: MODELING THE IMPACTS OF TREES ON THE EXCHANGE PROCESSES

major junctions becomes more effective outside the canopy.

The normalized turbulent kinetic energy  $\langle Tke \rangle$  (Fig. 7.22) is also analyzed following the topological categorization. The effect of the vegetation among the different categories is similar,

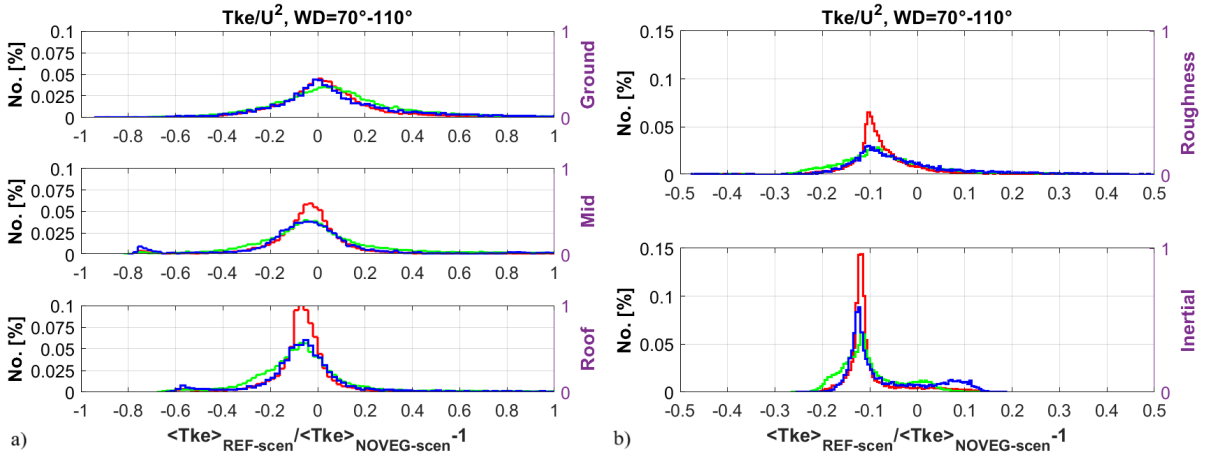


**Figure 7.22:**  $Tke$  variation factor distributions, normalized on the squared wind speed  $U$  ( $\langle Tke \rangle$ ), evaluated in the (a) UCL and (b) UBL above for the difference between REF-scen and NOVEG-scen for the EWcanopy (blue), NScanopy (green) and Intersect (red) topological categories.

but it varies with the layer height. At the ground (Fig. 7.22a), the distributions do not show a certain behavior since  $\langle Tke \rangle$  occurrences are centered in zero and distributed normally. Only the NScanopy category shows a slight tendency to a  $\langle Tke \rangle$  enhancement in the presence of vegetation. In the upper portion of the canopy, the distributions account for a  $\langle Tke \rangle$  reduction, with most of the occurrences spread between 0 and -0.2. All categories show the same normal distribution, with the Intersect more peaked on the median and the NScanopy wider in both negative and positive  $\langle Tke \rangle$  values. A very small mode in the tail of EWcanopy distribution accounts for few large reduction occurrences (approximately -0.75 at the mid layer, approximately -0.55 at the roof one). Outside the canopy the  $\langle Tke \rangle$  reduction imposed by the vegetation presence is still evident but less pronounced. Street canyon distributions in the roughness layer are wide, while the Intersect is more peaked around the mode (-0.1), with more evident tails toward positive variances. Distribution modes in the inertial layer account for an approximated  $\langle Tke \rangle$  reduction of -0.12 with respect to REF-scen, but few unlikely  $\langle Tke \rangle$  intensification events appear within the EWcanopy category. To summarize, the overall impact of trees is a reduction of  $\langle Tke \rangle$  with a commonly retrieved efficacy up to -0.2. The same behavior is highlighted also by the normalized TKMF, as shown by the distributions in Fig. 7.23.

The percentage variation analysis on the topological categories investigated so far is used also to assess the impact of an augmented vegetation amount in LB neighborhood domain with respect

### 7.3. THE IMPACT OF TREES IN LAURA BASSI NEIGHBORHOOD UNDER THE INPUT WIND DIRECTION PERPENDICULAR FROM EAST TO THE STREET CANYON ORIENTATION

to the reference scenario. As previously introduced, the VEG50-scen is a scenario where the

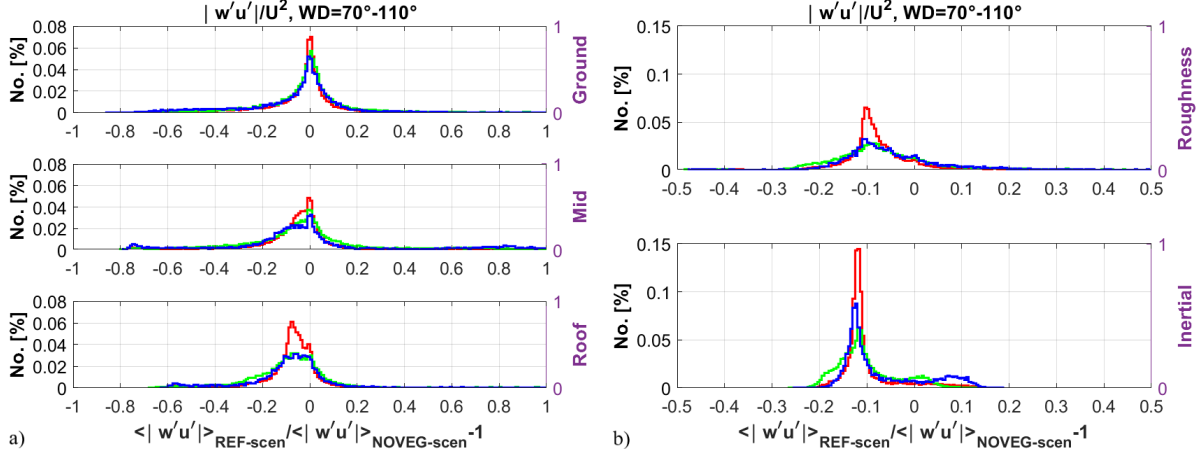


**Figure 7.23:** TKMF  $|\overline{w'u'}|$  variation factor distributions, normalized on the squared wind speed  $U$  ( $\langle |w'u'| \rangle$ ), evaluated in the (a) UCL and (b) UBL above for the difference between REF-scen and NOVEG-scen for the EWcanopy (blue), NScanopy (green) and Intersect (red) topological categories.

number of trees placed in the domain is increased by a 50% with respect to the real amount. The dislocation of the new trees in the domain is random, but it avoids unrealistic disposition. Therefore, the new vegetation does not occlude the streets or overtake a building location, but it simply fills possible gaps in private gardens, parks and along the streets, or introduces vegetation elements in previously bare areas. The impact of the new vegetation is to enhance the complexity of the UCL by increasing the number of obstacles the flow must interact with. Despite the variation in the vegetated area fraction coefficients, the impact of the augmented vegetation on the total roughness of the whole domain is almost negligible. The variation factor is expressed as it was defined for the previous investigation, so that  $X_{REF-scen}/X_{VEG50-scen} - 1$ , where  $X$  stays respectively for  $U$ ,  $Tke/U^2$  or  $|\overline{w'u'}|/U^2$ . Since VEG50-scen accounts an increased vegetated condition, a negative variation factor describes an increase of the variable  $X$  with the increased vegetation, while a positive variation factor describes a reduction of  $X$  with the increased vegetation. The variation factor of the wind speed due to the increased number of trees in the domain is displayed in Fig. 7.24. Since the impact of vegetation on the total roughness is almost negligible, variation on the mean flow intensities are expected to be small, as it is displayed in Fig. 7.24 where the maximum variations are contained in the range of  $\pm 0.025$ . The overall tendency is a reduction of wind speed with the increasing vegetation, but the probability associated to this effect depends on the topological category more than the analyzed layer. Wind speed can be considered normally distributed in each topological category and at each layer. EWcanopy distributions are centered on a zero variation, with only a small skewness toward a wind speed reduction outside the canopy. Therefore the impact of trees on the mean flow

## CHAPTER 7. RESULTS AND DISCUSSION: MODELING THE IMPACTS OF TREES ON THE EXCHANGE PROCESSES

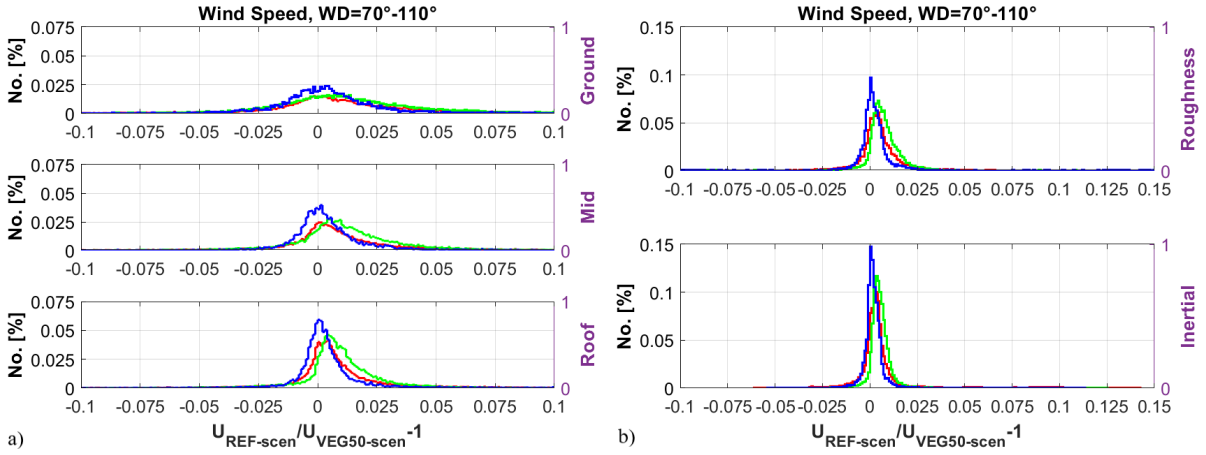


**Figure 7.24:** Wind speed  $U$  variation factor distributions evaluated in the (a) UCL and (b) UBL above for the difference between REF-scen and VEG50-scen for the EWcanopy (blue), NScanopy (green) and Intersect (red) topological categories.

for street canyon parallel to it is completely random. More defined is the NScanopy, where a reduction effect is evident in each layer despite its small magnitude. Intersections contributions stay in the middle between the two street canyons behaviors.

As for the mean flow, also  $\langle Tke \rangle$  variation factors are small and contained within the  $\pm 0.05$  as shown in Fig. 7.25. The overall behavior follows what was already retrieved from the whole domain investigation (Fig. 7.19), with an increase of  $\langle Tke \rangle$  with the increasing number of trees. Some discrepancies are anyway retrieved, especially between different layers and less on

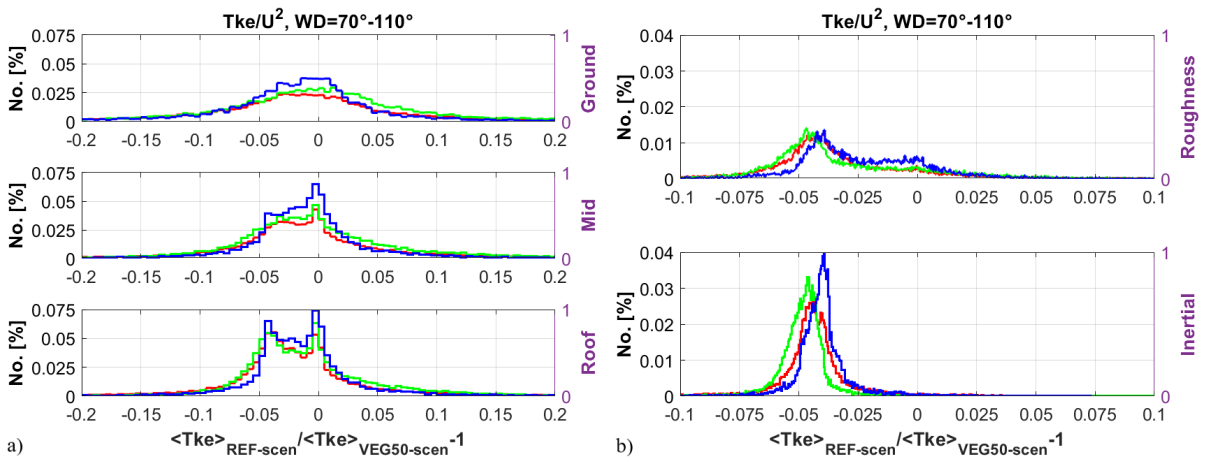


**Figure 7.25:**  $Tke$  variation factor distributions, normalized on the squared wind speed  $U$  ( $\langle Tke \rangle$ ), evaluated in the (a) UCL and (b) UBL above for the difference between REF-scen and VEG50-scen for the EWcanopy (blue), NScanopy (green) and Intersect (red) topological categories.

### 7.3. THE IMPACT OF TREES IN LAURA BASSI NEIGHBORHOOD UNDER THE INPUT WIND DIRECTION PERPENDICULAR FROM EAST TO THE STREET CANYON ORIENTATION

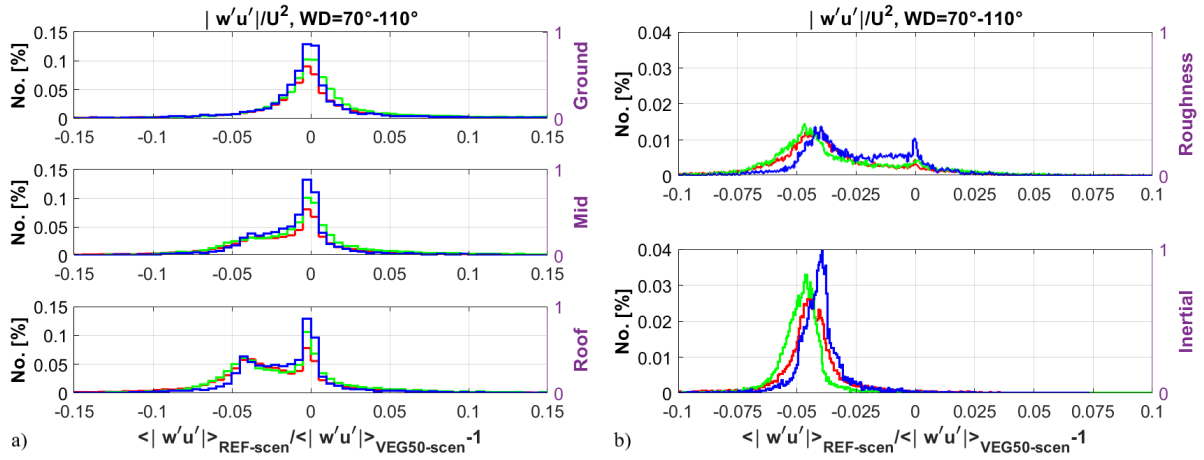


**Figure 7.26:** TKMF  $|\overline{w'u'}|$  variation factor distributions, normalized on the squared wind speed  $U$  ( $\langle |\overline{w'u'}| \rangle$ ), evaluated in the (a) UCL and (b) UBL above for the difference between REF-scen and VEG50-scen for the EWcanopy (blue), NScanopy (green) and Intersect (red) topological categories.

the topological category. At the ground layer (Fig. 7.25a),  $\langle Tke \rangle$  increases and decreases with the vegetation number augmentation with almost equal probability, with a slight predominance of the  $\langle Tke \rangle$  increase in EWcanopy and decrease in NScanopy. As the height of the layer in the canopy increases, the distributions shift toward negative values, enhancing the probability of a  $\langle Tke \rangle$  increasing effect. At the roof layer, distributions are almost bimodal, with modes at 0 and  $0.04 < Tke >$  increasing factor respectively. Outside the canopy (Fig. 7.25b), distributions are almost completely negative, with modes oscillating in the range between -0.03 and -0.05. In the roughness layer, the distributions are smoothed by the large variety of obstacles that still perturb the flow, while in the inertial layer  $\langle Tke \rangle$  are almost normally distributed, each one showing a well defined mode. EWcanopy shows the smallest  $\langle Tke \rangle$  increases, with distributions that follows the in-canopy ones due to the larger coupling between the UCL and UBL above when the mean flow is parallel to the street canyon orientation. In opposition to the behavior of the canopy, the NScanopy and Intersect categories show the largest increase of  $\langle Tke \rangle$ . Once again the same behavior of the  $\langle Tke \rangle$  is retrieved also in the normalized TKMF (Fig. 7.26).

#### 7.3.2 The Effects of Morphology

Trees in the canopy layer modify the morphological parameters, by introducing a certain number of porous obstacles that interact with the mean flows by introducing a heterogeneous disposal of roughness within the domain and by modifying shapes and intensities of the turbulent structures by increasing the vortex fragmentation, inducing the energy cascade and changing the dissipation efficacy. Sect. 4.3.3 and 4.3.4 described how vegetation modifies the characteristic

## CHAPTER 7. RESULTS AND DISCUSSION: MODELING THE IMPACTS OF TREES ON THE EXCHANGE PROCESSES

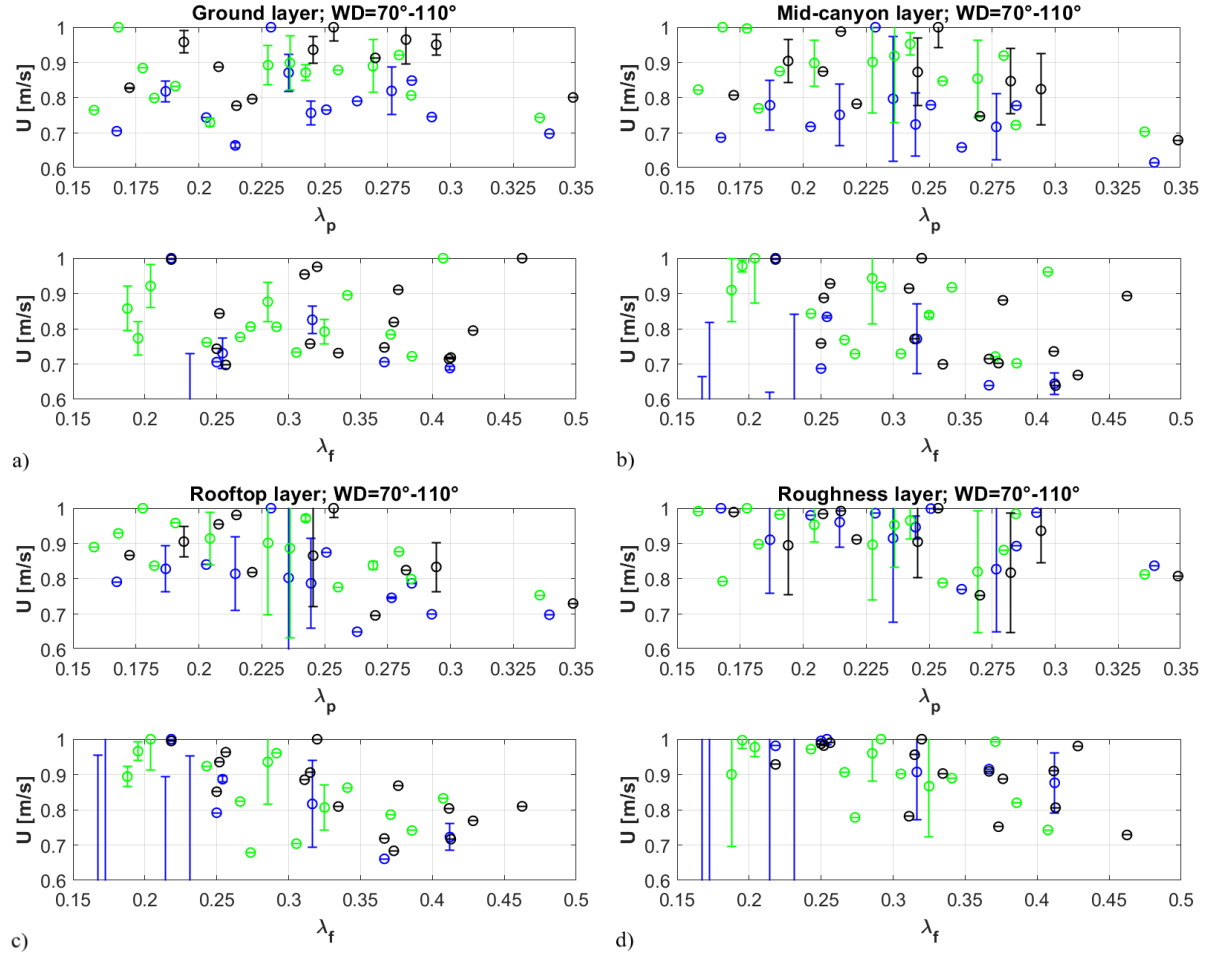


**Figure 7.27:** Wind speed as a function of the planar ( $\lambda_p$ ) and frontal ( $\lambda_f$ ) area fraction coefficients retrieved at (a) ground, (b) mid-canyon, (c) rooftop and (d) roughness layers respectively. Wind speeds are normalized over their maximum values in each layer to enhance the comparability. Blue circles identify to the REF-scen, the green ones the NOVEG-scen and the black ones the VEG50-scen. Each dot is the wind speed averaged over each  $\lambda_p$  or  $\lambda_f$  bin 0.01 large, and the error bars are the standard deviation in each bin.

morphological parameters of the analyzed domain. These modified parameters  $\lambda_p$  and  $\lambda_f$  are the geometrical tools that account for the impact of solid and vegetated (porous) obstacles on the mean flow and turbulence, changing the complexity of the urban environment. To quantify the effect of a modified morphology on the mean flow and turbulent structures as a consequence of a change of the vegetation amount, the domain has been divided in squared sub-domains of constant length  $l=250$  m and constant area  $A_t^{sd}=62500$  m<sup>2</sup>, inside which the morphological parameters  $\lambda_p$  and  $\lambda_f$  have been computed for the three scenarios REF-scen, NOVEG-scen and VEG50-scen already defined in Sect. 7.3.1. Wind speed, TKE and TKMF are respectively displayed as function of the morphological parameters  $\lambda_p$  and  $\lambda_f$  for each layer defined in Sect.

### 7.3. THE IMPACT OF TREES IN LAURA BASSI NEIGHBORHOOD UNDER THE INPUT WIND DIRECTION PERPENDICULAR FROM EAST TO THE STREET CANYON ORIENTATION

7.3.1 and with the same input conditions applied in Sect. 7.2.1. Clearly both  $\lambda_p$  and  $\lambda_f$  changes according to the investigated scenario in order to account for the respective amount of vegetation. For the NOVEG-scen,  $\lambda_p$  and  $\lambda_f$  are simply calculated from the building planar and frontal area respectively, while in REF-scen and VEG50-scen they account for the different vegetation amounts. Results for the aforementioned variables are shown in Fig. 7.27, 7.28 and 7.29 respectively. Wind speeds in each layer show similar behaviors for the three scenarios (Fig. 7.27). Frontal area fraction coefficient seems to largely affect the wind speed, which rapidly decreases as the coefficient increases. This behavior is particularly evident when the coefficient range is larger than 0.2. The tendency is quite expected since as the coefficient increases the obstacle

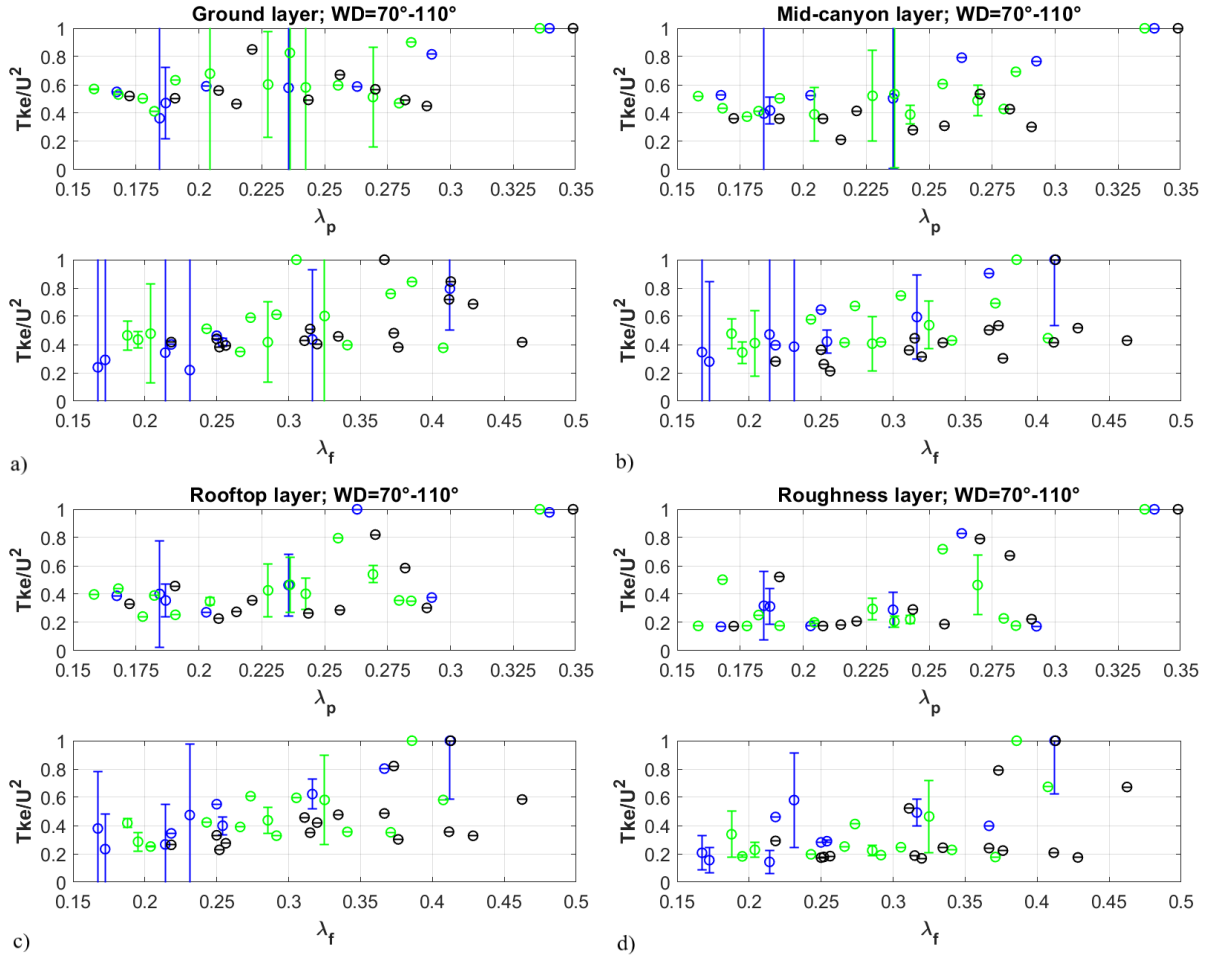


**Figure 7.28:**  $Tke$ , normalized on the squared wind speed  $U$ , as a function of the planar ( $\lambda_p$ ) and frontal ( $\lambda_f$ ) area coefficients retrieved at (a) ground, (b) mid-canyon, (c) rooftop and (d) roughness layers respectively.  $Tke/U^2$ s are normalized over their maximum values in each layer to enhance the comparability. Blue circles identify to the REF-scen, the green ones the NOVEG-scen and the black ones the VEG50-scen. Each dot is the  $Tke/U^2$  averaged over each  $\lambda_p$  or  $\lambda_f$  bin 0.01 large and the error bars are the standard deviation in each bin.

## CHAPTER 7. RESULTS AND DISCUSSION: MODELING THE IMPACTS OF TREES ON THE EXCHANGE PROCESSES

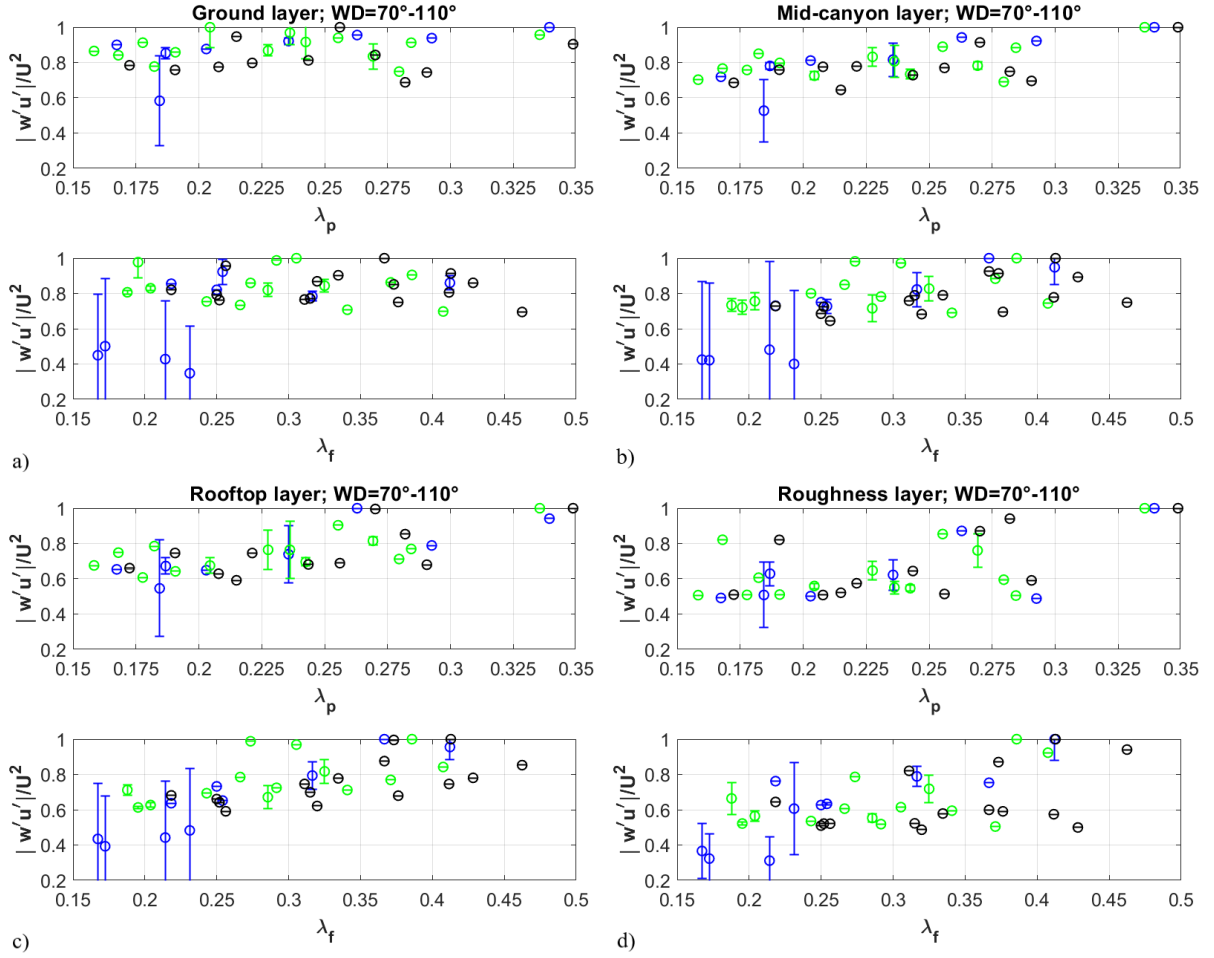


**Figure 7.29:** TKMF, normalized on the squared wind speed  $U$ , as a function of the planar ( $\lambda_p$ ) and frontal ( $\lambda_f$ ) area coefficients retrieved at (a) ground, (b) mid-canyon, (c) rooftop and (d) roughness layers respectively.  $|\overline{w'u'}|$ s are normalized over their maximum values in each layer to enhance the comparability. Blue circles identify to the REF-scen, the green ones the NOVEG-scen and the black ones the VEG50-scen. Each dot is the  $|\overline{w'u'}|$  averaged over each  $\lambda_p$  or  $\lambda_f$  bin 0.01 large and the error bars are the standard deviation in each bin.

density in the domain also increases. The flow trajectory is modified as a consequence of the interaction with the obstacles, inhibiting the flow speed. Below the 0.2 threshold the tendency of wind speed becomes more independent on the morphology since the obstacle density is too small to efficiently affect the mean flow. At the ground layer and less evidently at mid-canyon and rooftop layers (Fig. 7.27a-b), wind speed tends to increase as the coefficient increases. This behavior can be a consequence of the channeling effect on the flow caused by the enhanced pressure generated by the obstacles. The wind speed appears to be more independent on the planar area fraction coefficient especially inside the canopy. At rooftop and roughness layers (Fig. 7.27c-d), wind speed slightly decreases as the coefficient increases. As retrieved in Sect.

7.3.1, wind speed values in the NOVEG-scen are larger than the REF-scen ones, also showing larger decreasing slopes for both coefficient dependencies. Therefore, the presence of trees reduces the overall wind speed as well as the velocity gradients, leading to a more homogeneous field, both inside and above the canopy. Similar behavior is retrieved also for the VEG50-scen, despite it does not seem to have a predominance effect on the morphological dependency of the wind speeds.

$Tke/U^2$  tendencies in Fig. 7.28 show two well defined regimes, shared by both morphological coefficients in all scenarios. When  $Tke/U^2 \leq 0.225$ , it is independent on the coefficients, as it was for the wind speeds. Above this threshold,  $Tke/U^2$  rapidly increases as the coefficients increase. This second tendency is particularly evident in the REF-scen and NOVEG-scen especially at rooftop and roughness layers (Fig. 7.28c-d), while in VEG50-scen  $Tke/U^2$  often maintains a constant tendency, since the obstacles saturate the environment and  $Tke/U^2$  is dissipated rather than generated from the mean flow. Again at the ground layer (Fig. 7.28a) a tendency inversion is retrieved when  $\lambda_f$  is larger than 0.4, when the increasing number of obstacles inhibits the production of  $Tke/U^2$ .

The normalize TKMF (Fig. 7.29) somehow follows the same behavior observed for the  $Tke/U^2$ , with an increase of the flux intensities above a certain threshold and an independence on  $|w'u'|/U^2$  from morphology below it. Well defined increasing trends are found in each scenario when  $\lambda_f$  is larger than 0.25 at the roughness layers (Fig. 7.29d), while at mid-canyon and rooftop layers (Fig. 7.29b-c) the increasing trends involve the whole morphology scale.  $|w'u'|/U^2$  also increases with  $\lambda_p$  in the same layers when  $\lambda_p \geq 0.25$ , but the trends are soother. At the ground layer (Fig. 7.29a) the tendencies are even less defined. In the NOVEG-scen and VEG50-scen,  $|w'u'|/U^2$  seems independent on both morphological parameters. A discontinuity is found at  $\lambda_f=0.25$  for the REF-scen but both tendencies below and above the threshold are independent on the morphological parameter, as it is for the whole scale of  $\lambda_p$ . The overall changes that a variation of the vegetation amount cause are small if compared to the impact that buildings or solid obstacles have on the mean flow and turbulence fields modifications.

## 7.4 The Effect of Wind Direction and Surface Roughness on the Vegetation Impact

Section 7.3 investigates the impact of trees on wind speed, TKE and TKMF considering as an input condition a wind blowing from east (the EP to the reference street canyon of LB used in Sect. 7.2.1). In this section, an input wind direction change is proposed to investigate the possible variations given by a different approaching wind direction angle to the LB neighborhood. A change in the wind direction is also followed by a variation in the roughness length, since the last input parameter depends on the frontal area coefficient (see Sect. 4.3.4) which in turn varies with

## CHAPTER 7. RESULTS AND DISCUSSION: MODELING THE IMPACTS OF TREES ON THE EXCHANGE PROCESSES

the incoming wind direction. The mutual effect of the two parameters is investigated following the same analysis based on the distribution computation for the three scenarios of the whole domain and for each topological category defined in Sect. 7.3.1. The investigated input wind directions are from north and southwest, with computed roughness lengths of 1.51 m and 1.63 m respectively. The NP wind direction ensemble ( $-20^\circ < wd < 20^\circ$ ) is chosen as perpendicular to the east one and preferred to the SP due to the better agreement with measured data retrieved in Sect. 7.2.1. A new  $45^\circ$  Oblique from SouthWest (SW) wind direction ensemble ( $205^\circ < wd < 245^\circ$ ) to the canyon orientation is introduced and investigated, corresponding to the most common wind direction retrieved during the summer campaign (see Fig. 5.4 in Sect. 5.1). Apart from the wind direction and the roughness length, all the other input parameters, including the input wind speed profile, remain the same used in the Sect. 7.3 and Sect. 7.3.1 investigations, as define din Sect. 7.2.1.

### 7.4.1 Vegetation Impact Distributions and Topological Discretization

#### Input Wind Direction Parallel from North to the Street Canyon Orientation

In analogy with the previous investigations, the wind speed distributions in the whole domain of LB neighborhood is retrieved and displayed in Fig. 7.30 for the three vegetative scenarios and at the five different layers already described in Sect. 7.3.1. The behavior of the wind speed distributions in the various scenarios is completely different from the EP wind direction ensemble case. With respect to the REF-scen, a wind speed strong increase is retrieved either removing (NOVEG-scen) or adding (VEG50-scen) trees in the domain, especially above the canopy (Fig. 7.30b). These enhancements occur as shifts of the NOVEG-scen and VEG50-scen

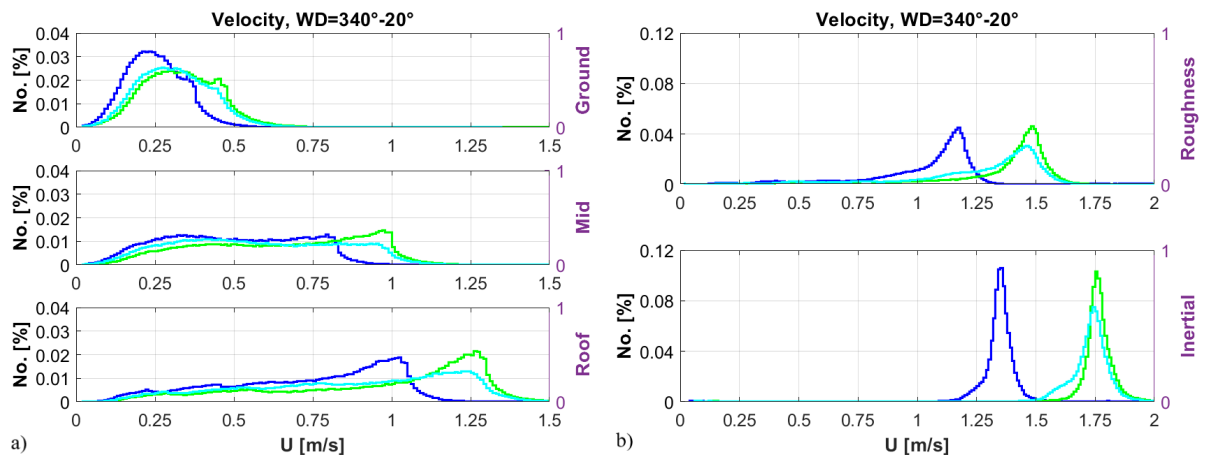


**Figure 7.30:** Wind speed  $U$  distributions evaluated in the (a) UCL and (b) UBL above for REF-scen (in blue), NOVEG-scen (in green) and VEG50-scen (in cyan). Ground layer in (a) has a different ordinate tick to make the distribution differences appreciable.

## 7.4. THE EFFECT OF WIND DIRECTION AND SURFACE ROUGHNESS ON THE VEGETATION IMPACT

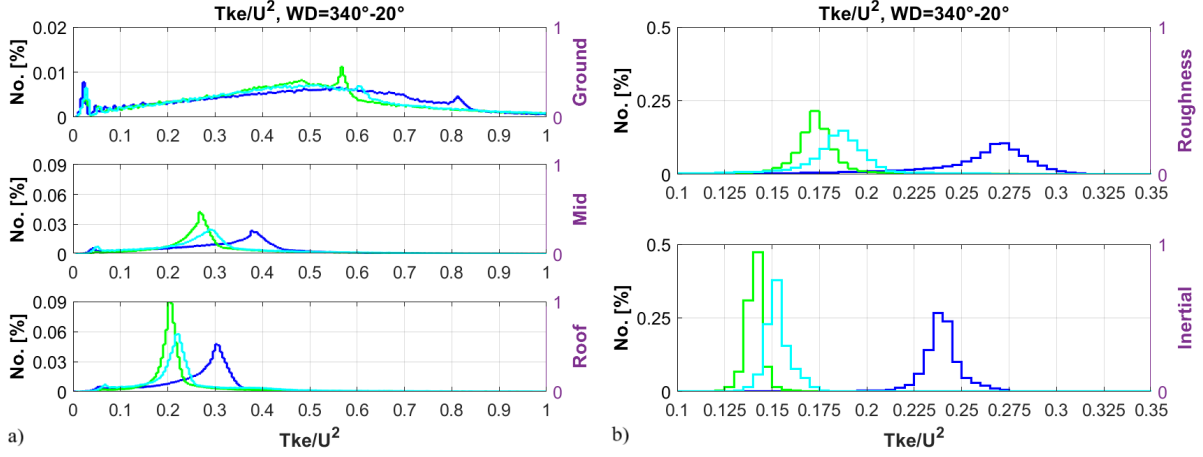


**Figure 7.31:**  $Tke$  distributions, normalized on the squared wind speed  $U$ , evaluated in the (a) UCL and (b) UBL above for REF-scen (in blue), NOVEG-scen (in green) and VEG50-scen (in cyan). Ground layer in (a) has a different ordinate tick to make the distribution differences appreciable.

related distributions toward larger wind speeds, but preserving the shapes. The shift seems to decrease as the layers approach the canopy ground (Fig. 7.30a), where the enhancement does not involve the distribution maxima. NOVEG-scen and VEG50-scen distributions are similar in shape and mode position, but the intensities are rather different. VEG50-scen is wider, with a less pronounced mode and a larger distribution spread toward small velocities. Despite this slight difference NOVEG-scen and VEG50-scen describes very similar variations with respect to the reference scenario, with two different ways to obtain a similar increase of the mean flow intensity in urban areas.

$Tke/U^2$  is strongly inhibited by either the removal and the increase of the tree number in the domain. Again the larger effects are retrieved outside the canopy (Fig. 7.31b), where the REF-scen is completely shifted from the modified scenarios. The increased vegetation in VEG50-scen saturate the domain, leading turbulent structure to be small and easily dissipated. In NOVEG-scen the  $Tke/U^2$  decrease is even stronger than VEG50-scen, because the  $Tke/U^2$  production is reduced by the decreased mean flow to porous obstacle interactions. Discrepancies between NOVEG-scen or VEG50-scen and the REF-scen decrease as the layer height decreases, until reaching the ground layer Fig. (7.31a) where the distributions are almost equal. The similar behavior of NOVEG-scen and VEG50-scen suggests that both a massive obstacle removal and an environment saturation can contribute to a drop in the turbulence energy production. These behavior of the  $Tke/U^2$  distributions opposes what was retrieved for the EP wind direction investigation (Fig. 7.19), where a  $Tke/U^2$  increase in both NOVEG-scen and VEG50-scen with respect to REF-scen. The different results among input wind directions can be associated with a possible common orientation of the main streets of the analyzed neighborhood. In fact, a pre-

## CHAPTER 7. RESULTS AND DISCUSSION: MODELING THE IMPACTS OF TREES ON THE EXCHANGE PROCESSES

dominance of channeling behavior of the mean flow or of vortex structures with axes parallel to the street canyon can impact differently on the flows and on how the flow interacts with the obstacles. This suggestion applies also to the TKMF (Fig. 7.32), where increasing or removing the trees from the domain results in an increase of the momentum transport, in partial agreement with the wind speed behavior. The agreement is partial because in the case of  $|\overline{w'u'}|/U^2$  the largest increase is retrieved for the VEG50-scen. The increase of the TKMF in VEG50-scen and NOVEG-scen with respect to REF-scen is conspicuous and well defined in each layer. Within

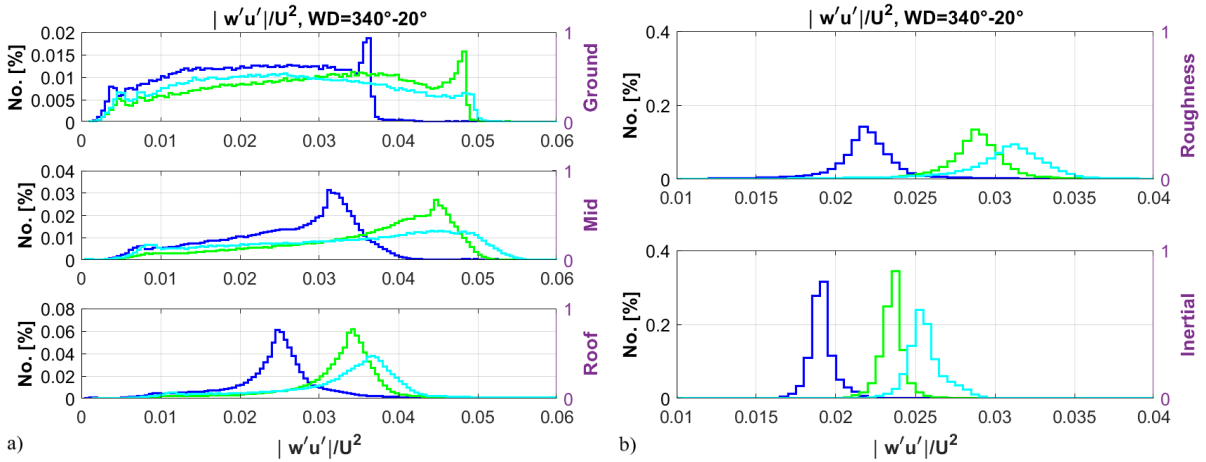


**Figure 7.32:** TKMF  $|\overline{w'u'}|$  distributions, normalized on the squared wind speed  $U$ , evaluated in the (a) UCL and (b) UBL above for REF-scen (in blue), NOVEG-scen (in green) and VEG50-scen (in cyan). Ground layer in (a) has a different ordinate tick to make the distribution differences appreciable.

the canopy (Fig. 7.32a), the increase in NOVEG-scen seems to be more effective than VEG50-scen at the ground and slightly at the mid layers. From the roof layer, but especially outside the canopy (Fig. 7.32b), VEG50-scen increase is stronger, both in terms of mode and spread of the distributions. Since the TKMF is the driver of the IC within the canopy (under weak synoptic conditions), VEG50-scen results can also describe a scenario where the IC is increased with possible favorable consequences on the street ventilation and urban air quality.

The topological analysis is represented also for the NP wind direction ensemble, starting from the  $X_{REF-scen}/X_{NOVEG-scen} - 1$  variation factor, which involves a comparison between NOVEG-scen and REF-scen. Again positive variation factor values describe an increase of  $X$  with the increasing vegetation, while a negative variation factor describes a decrease of  $X$  with the increasing vegetation. The variation factor of the wind speed (Fig. 7.33) shows a decreasing tendency, slightly dependent on the topology in each layer. The majority of this reduction is centered on the range  $-0.2 \div -0.3$ , with the strongest tail spreading toward larger reduction values. The EWcanopy are slightly more influenced by this reduction than the NScanopy, while Intersect shows peaked distributions around a mode that increases from  $-0.20$  to  $-0.23$  from the

## 7.4. THE EFFECT OF WIND DIRECTION AND SURFACE ROUGHNESS ON THE VEGETATION IMPACT

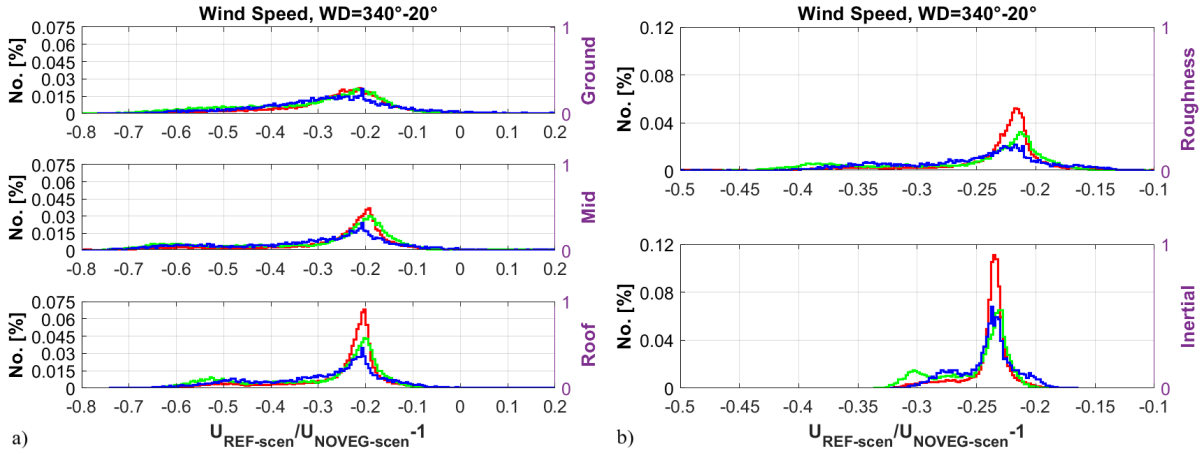


**Figure 7.33:** Wind speed  $U$  variation factor distributions evaluated in the (a) UCL and (b) UBL above for the difference between REF-scen and NOVEG-scen for the EWcanopy (blue), NScanopy (green) and Intersect (red) topological categories.

ground to the inertial layer. The inertial is the only layer where distributions are not widely spread (Fig. 7.33a), and the impact of the various topology categories is similar. Following the whole domain distributions,  $\langle Tke \rangle$  variation factor shows strong increases of the  $\langle Tke \rangle$  as the vegetation increases (Fig. 7.34). The variation factor within the canopy (Fig. 7.34a) is largely spread from strong but unlikely reductions (up to -0.5) to more than complete increases (up 1.5). Different behaviors characterize the topology categories. NScanopy, parallel to the mean flow, shows a predominance of strong  $\langle Tke \rangle$  increase, with modes always around 0.75.

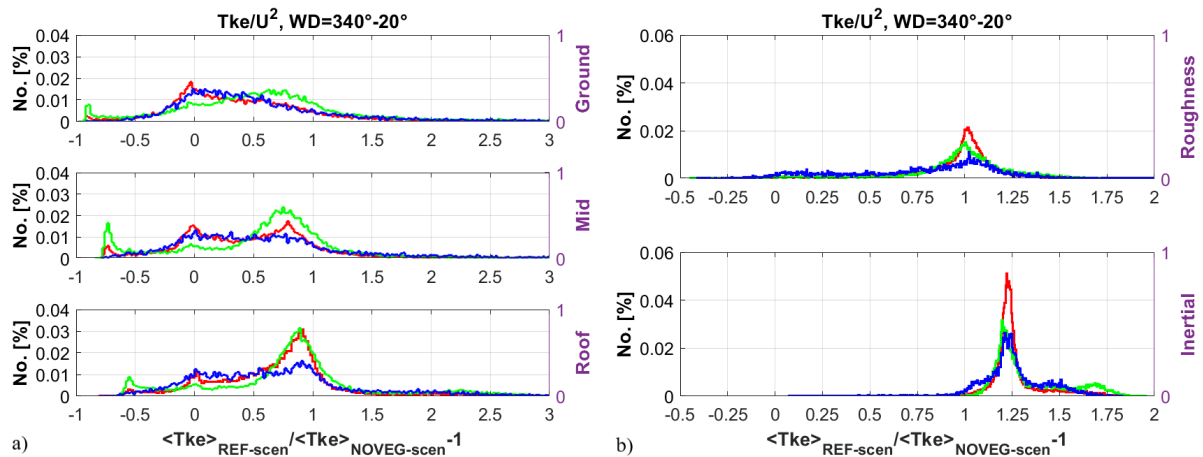


**Figure 7.34:**  $Tke$  variation factor distributions, normalized on the squared wind speed  $U$  ( $\langle Tke \rangle$ ), evaluated in the (a) UCL and (b) UBL above for the difference between REF-scen and NOVEG-scen for the EWcanopy (blue), NScanopy (green) and Intersect (red) topological categories.

## CHAPTER 7. RESULTS AND DISCUSSION: MODELING THE IMPACTS OF TREES ON THE EXCHANGE PROCESSES

A strong non-negligible mode describes a strong reduction possibility (approximately -0.75) at the mid layer. Perpendicular canopies (EWcanopy) are less prone to develop a  $\langle Tke \rangle$  enhancement situation. Distributions are wide and flat, with no clear modes and accounting for a big portion of negative values. At the roof layer, the distribution slightly follows the NScanopy category, but remains similar to the ground and mid layer ones. Intersect evolves following EWcanopy at the ground layer to the roof layer where it mimics the NScanopy category. Outside the canopy (Fig. 7.34b),  $\langle Tke \rangle$  distributions are more peaked around an increase between factors 1 and 1.25, except for the EWcanopy one in the roughness layer which follows the canopy behavior. Intersect shows the more defined mode, while NScanopy has the longest tail toward even larger  $\langle Tke \rangle$  increases, confirming the strong decrease of  $\langle Tke \rangle$  retrieved when trees are completely removed from the domain.

Differently from the behavior of the distributions retrieved for the whole domain (Fig. 7.32), TKMF topological categorized distributions (Fig. 7.35) do not follow exactly the behavior of the wind speed but show some differences. Within the canopy (Fig. 7.35a) the distributions depend on the analyzed layer and very slightly on the topological category. The ground layer shows the largest discrepancies. All the distributions are almost Gaussian and centered in zero, with a very small predominance of negative values. Randomly distributed TKMF increases and decreases are the dominant impact generated by the presence of trees. In the upper part of the canopy, TKMF reduction with the vegetation increase becomes more and more effective as the layer height increases. A certain TKMF increase is still present at mid layer where it

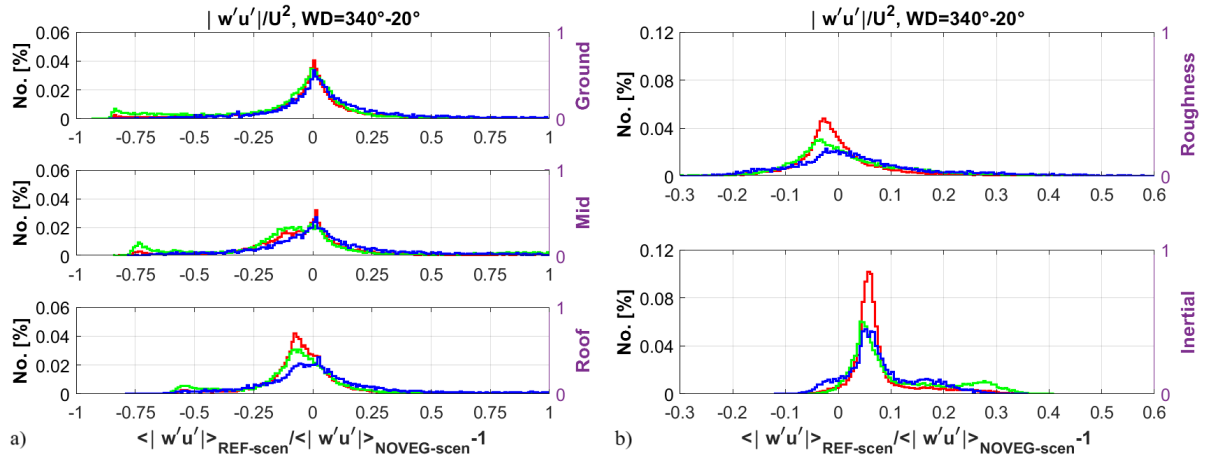


**Figure 7.35:** TKMF  $|\overline{w'u'}|$  variation factor distributions, normalized on the squared wind speed  $U$  ( $\langle |w'u'| \rangle$ ), evaluated in the (a) UCL and (b) UBL above for the difference between REF-scen and NOVEG-scen for the EWcanopy (blue), NScanopy (green) and Intersect (red) topological categories.

accounts only for the 0.1 of the increase while the reduction extends toward -0.2. As it was often retrieved, the Intersect category shows the most peaked distributions around their modes, while

#### 7.4. THE EFFECT OF WIND DIRECTION AND SURFACE ROUGHNESS ON THE VEGETATION IMPACT

the canopies are more widely spread. Nevertheless, the shapes are still very similar. Outside the canopy (Fig. 7.35b), the trend is inverted, with the decrease of  $\langle |\overline{w'u'}| \rangle$  as the vegetation is reduced directly proportional to the layer height. The inertial layer overturns this trend, as vegetation somehow increases the intensity of the TKMF (significant range between 0 and 0.1). Therefore, despite a general reduction of the turbulent fluxes, vegetation can somehow provide an input of TKMF away from the canopy.

The variation factor analysis is proposed again to evaluate the variation from REF-scen imposed by the augmented number of trees in the domain (VEG50-scen). The investigated quantity  $X_{REF-scen}/X_{VEG50-scen} - 1$  describes an increase of the variable  $X$  in the VEG50-scen with respect to REF-scen when the variation factor is negative, a reduction when positive. As always,  $X$  can be  $U$ ,  $Tke$  and  $|\overline{w'u'}|$ , and the variables are investigated for the EWcanopy, NScanopy and Intersect topological categories in the usual five layers within and above the canopy. First investigation involves again the wind speed  $U$  (Fig. 7.36). The common behavior of the distributions confirms the investigation on the whole domain (Fig. 7.30), with an increase of the wind speed in the VEG50-scen between -0.15 and -0.25. NScanopy category is the most influenced by the tree modification at all layers. Its distribution modes show the largest  $U$  and the mostly peaked increase at each layer among the other topology. Particularly outside the canopy (Fig. 7.36b), NScanopy distributions are simply shifted toward more negative factors with respect to EWcanopy and Intersect which are more superimposed one to the other, despite Intersect seems slightly more negative than EWcanopy. Toward the canopy surface (Fig. 7.36a), the distributions preserve the described discrepancies from each other, but they become wider and less peaked. Despite the spread of the distributions, only increased scenarios are described,

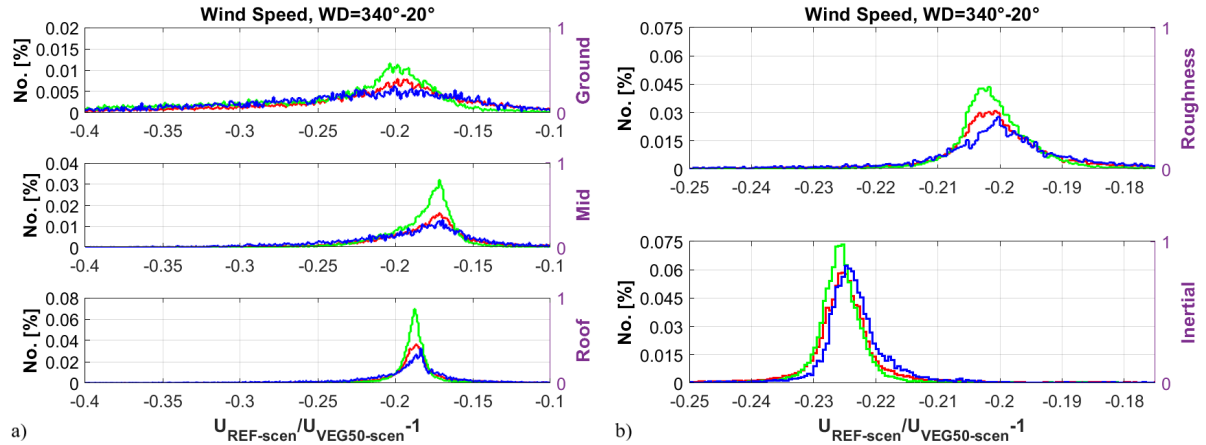


**Figure 7.36:** Wind speed  $U$  variation factor distributions evaluated in the (a) UCL and (b) UBL above for the difference between REF-scen and VEG50-scen for the EWcanopy (blue), NScanopy (green) and Intersect (red) topological categories.

fixing the positive effect of the newly planted trees in creating a favorable environment for the

## CHAPTER 7. RESULTS AND DISCUSSION: MODELING THE IMPACTS OF TREES ON THE EXCHANGE PROCESSES

wind speed increment.

Following the tendency already retrieved with the whole domain distributions (Fig. 7.31),  $\langle Tke \rangle$  shows a strong decreasing factor outside the canopy (Fig. 7.37b), when more vegetation is added to the domain. On the contrary, within the canopy (Fig. 7.37a), attenuation and increase have similar weight on  $\langle Tke \rangle$ . Outside the canopy (Fig. 7.37b), the topological categories are in good agreement with each other, showing a strong  $\langle Tke \rangle$  decrease with the increasing vegetation, whose distribution modes increase from 0.85 to 1.05 rising from the roughness to the inertial layer. Significance discrepancies between different topological category distributions are highlighted only at the roughness layer, where the mode spread increases going from the NScanopy to the EWcanopy, with Intersect in between. Inside the canopy (Fig. 7.37a), distributions at each layer are almost centered in zero, but multiple modes are retrieved, generally accounting for a  $\langle Tke \rangle$  decreasing effect. At the ground layer, distributions are single modal, with a certain skewness of the maximum value toward zero and a long positive tail for EWcanopy and Intersect categories, while NScanopy mode is centered in 0.6 with a long tail toward zero and negative values. As already observed also for the wind speed, the NScanopy, parallel oriented street canyons to the mean flow, are the most prone to develop  $\langle Tke \rangle$  changes (in this case describing a reduction with vegetation increase) with respect to the other categories. This behavior of NScanopy is still evident in the upper part of the canopy, where the distributions are bimodal, with a mode in 0 and the other at  $0.6 \div 0.7$ . The positive mode increases in intensity as the layer height increases, and becomes the only mode outside the canopy (Fig. 7.37b). NScanopy shows much clearly this bimodal behavior, with an evident predominance of the positive mode with respect to the null one, in opposition to Intersect and

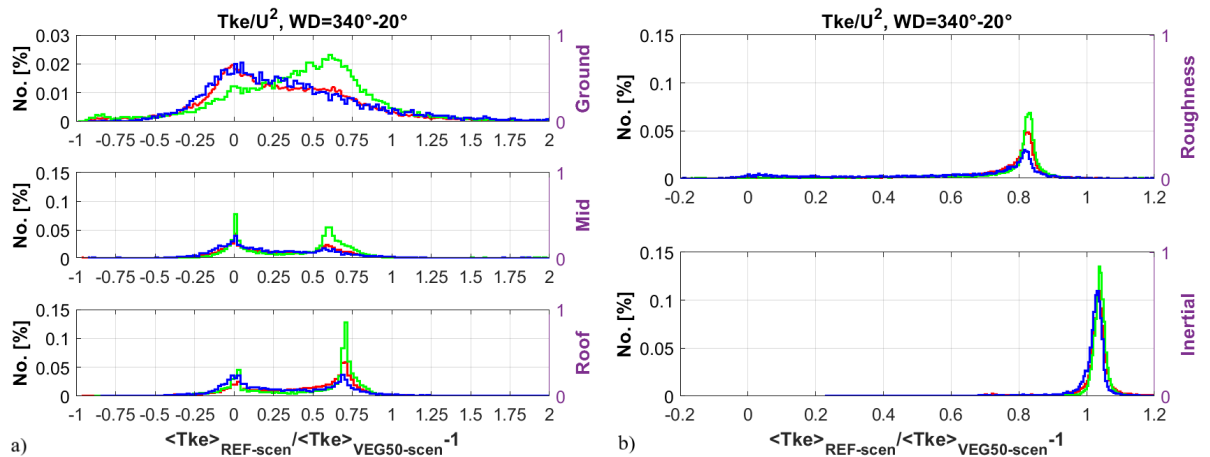


**Figure 7.37:**  $Tke$  variation factor distributions, normalized on the squared wind speed  $U$  ( $\langle Tke \rangle$ ), evaluated in the (a) UCL and (b) UBL above for the difference between REF-scen and VEG50-scen for the EWcanopy (blue), NScanopy (green) and Intersect (red) topological categories.

## 7.4. THE EFFECT OF WIND DIRECTION AND SURFACE ROUGHNESS ON THE VEGETATION IMPACT

EWcanopy where only at the roof layer this behavior is retrieved.

Normalized TKMF distributions (Fig. 7.38) show a behavior which is similar to both wind speed and TKE. The normalized TKMF distributions follow the wind speed because they are directly induced by the mean flow and, in fact, the main behavior is an increase of  $\langle |\overline{w'u'}| \rangle$  with the vegetation increase. Conversely, the shapes of the distributions are similar to the TKE ones, despite they are almost symmetrical with respect to the zero variation factor. Outside the canopy (Fig. 7.38b), the topological categories are in good agreement with each other, showing an increase of  $\langle |\overline{w'u'}| \rangle$  with the increasing vegetation, whose distribution modes (negatively) increase from -0.03 to -0.13 moving from the inertial to the roughness layer.

Significant discrepancies between different topological category distributions are highlighted only at the roughness layer, where the mode spread increases from the NScanopy to the EWcanopy, with Intersect in between. At the ground layer (Fig. 7.38a), the normalized TKMFes are

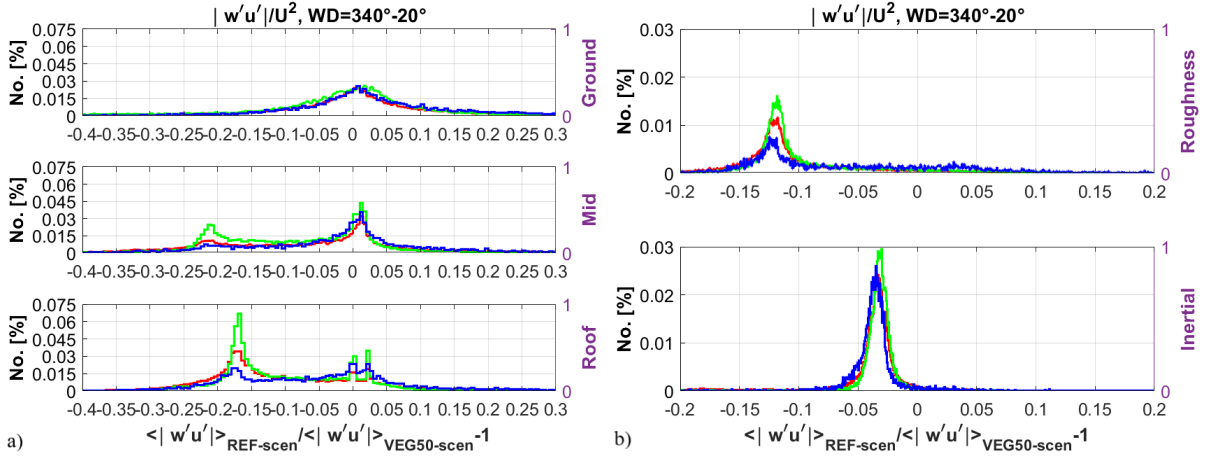


**Figure 7.38:** TKMF  $|\overline{w'u'}|$  variation factor distributions, normalized on the squared wind speed  $U$  ( $\langle |\overline{w'u'}| \rangle$ ), evaluated in the (a) UCL and (b) UBL above for the difference between REF-scen and VEG50-scen for the EWcanopy (blue), NScanopy (green) and Intersect (red) topological categories.

normally distributed with median in zero, describing a random increase and decrease efficacy caused by the vegetation amount modification. In the upper part of the canopy the distributions are bimodal, with a mode in 0 and the other at  $-0.17 \div -0.22$  depending on the layer height. The negative mode increases in intensity as the layer height increases, and become the only mode outside the canopy (Fig. 7.37b). NScanopy shows much clearly this bimodal behavior, with an evident predominance of the positive mode with respect to the null one, in opposition to Intersect and EWcanopy where only at the roof layer this behavior is retrieved.

From this analysis on the NScanopy wind direction ensemble, it is evident how incoming wind directions affect the urban flows and the vegetation perturbation impact on them. It is also evident how the investigated neighborhood has a certain prevalent major street orientation,

## CHAPTER 7. RESULTS AND DISCUSSION: MODELING THE IMPACTS OF TREES ON THE EXCHANGE PROCESSES

which modifies how the incoming flow interacts with the domain obstacles depending on its direction. To verify these last considerations, the investigation is extended to the SW wind direction ensemble, which obliquely approaches the majority of street canyons dislocated in the domain.

### Input Wind Direction from Southwest to the Street Canyon Orientation

Following the analysis in Sect. 7.3.1 and 7.4.1, the probability distribution analysis is performed also in the case of SW winds flowing over the investigated domain of LB neighborhood. The probability distributions of wind speed, TKE and TKMF are presented for the already known REF-scen, VEG50-scen and NOVEG-scen scenarios. The wind speed distributions simulated considering the three scenarios are compared in Fig. 7.39. Distributions at each layer are particularly close one to the others, especially at the ground and inertial layers, for different reasons. At the ground layer (Fig. 7.39a), the distributions are almost perfectly superimposed because the impact of the tree number variation in this input wind direction condition is overpowered by other local phenomena, such as the friction generated by the street surface roughness, as commonly observed in the previous scenarios. A similar behavior is retrieved in the inertial layer (Fig. 7.39b), where the flow has already readjusted to the unperturbed input condition and the impact of the tree becomes small. In the layers between these two extremes, some small differences between the distributions are visible, especially considering the NOVEG-scen with respect to the other two. A small increase in the number of large wind speed occurrences is found in the NOVEG-scen at mid, roof and roughness layers, but it only corresponds to an intensification of the distribution mode with respect to the REF-scen. An even smaller reduction

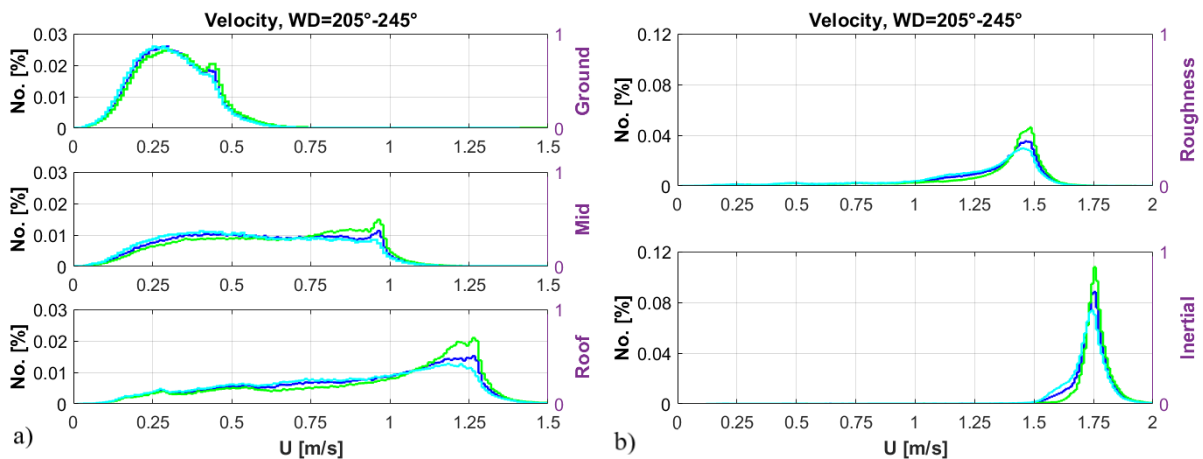


**Figure 7.39:** Wind speed  $U$  distributions evaluated in the (a) UCL and (b) UBL above for REF-scen (in blue), NOVEG-scen (in green) and VEG50-scen (in cyan). Ground layer in (a) has a different ordinate tick to make the distribution differences appreciable.

## 7.4. THE EFFECT OF WIND DIRECTION AND SURFACE ROUGHNESS ON THE VEGETATION IMPACT

of the mode intensity is found for the VEG50-scen with respect to REF-scen, but it appears to be almost negligible.

Turbulent related quantities show more appreciable differences between different scenarios, mostly concentrated at the roof layer and above.  $Tke/U^2$  distributions are very similar from mid to inertial layers (Fig. 7.40). There,  $Tke/U^2$  values are distributed almost normally, with

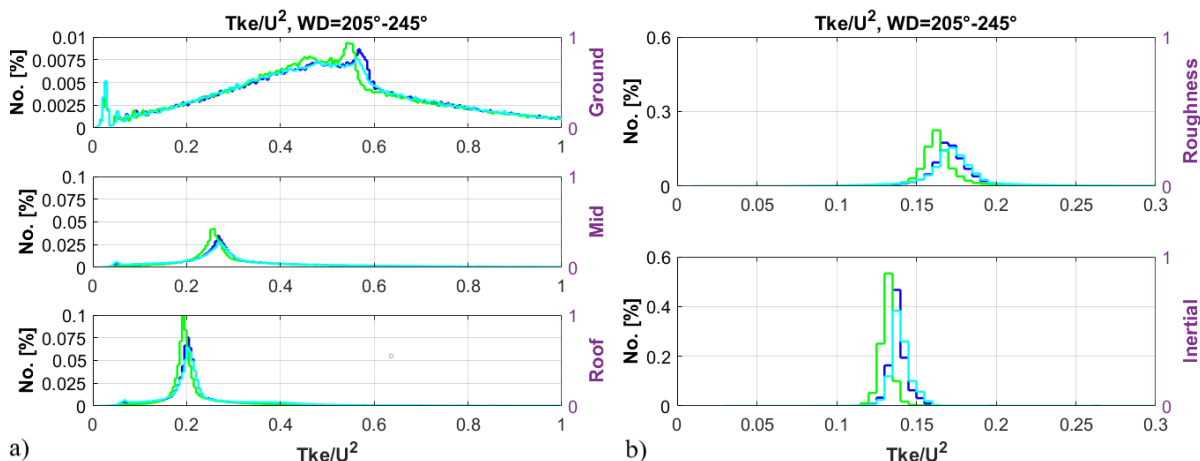


**Figure 7.40:**  $Tke$  distributions, normalized on the squared wind speed  $U$ , evaluated in the (a) UCL and (b) UBL above for REF-scen (in blue), NOVEG-scen (in green) and VEG50-scen (in cyan). Ground layer in (a) has a different ordinate tick to make the distribution differences appreciable.

the REF-scen and VEG50-scen distributions almost completely superimposed and the NOVEG-scen one slightly skewed (in the mode) and shifted toward smaller values, describing a small increase of  $Tke/U^2$  in presence of trees, but independent on the tree number. A similar  $Tke/U^2$  decreasing behavior is retrieved also at the ground layer (Fig. 7.40a) where the distributions are widely spread and skewed toward small  $Tke/U^2$  values. NOVEG-scen shows again smaller  $Tke/U^2$  values in the distribution mode with respect to either REF-scen and VEG50-scen.

The behavior of the normalized TKMF distributions is close to what already retrieved for the  $Tke/U^2$ , but with a clear distinction between the normal distributions of  $\langle |w'u'| \rangle$  outside the canopy (Fig. 7.40b) and the widely spread and skewed toward small values inside it (Fig. 7.40a). Distributions outside the canopy (Fig. 7.40b) show the exact same behavior of  $Tke/U^2$ , with a superposition of the REF-scen and VEG50-scen ones and the shift of the NOVEG-scen distribution toward smaller  $\langle |w'u'| \rangle$  values. Within the canopy (Fig. 7.40a) the NOVEG-scen distributions modes are shifted or skewed toward smaller  $\langle |w'u'| \rangle$  values, but most of the distributions remain superimposed to the REF-scen and VEG50-scen duo. Therefore, despite trees are responsible for a small mean flow attenuation, TKMFes and TKE productions are increased by the presence of trees. These attenuation of the mean flow and increase of the turbulence seem to be independent on the number of trees in the domain.

CHAPTER 7. RESULTS AND DISCUSSION: MODELING THE IMPACTS OF TREES ON THE EXCHANGE PROCESSES

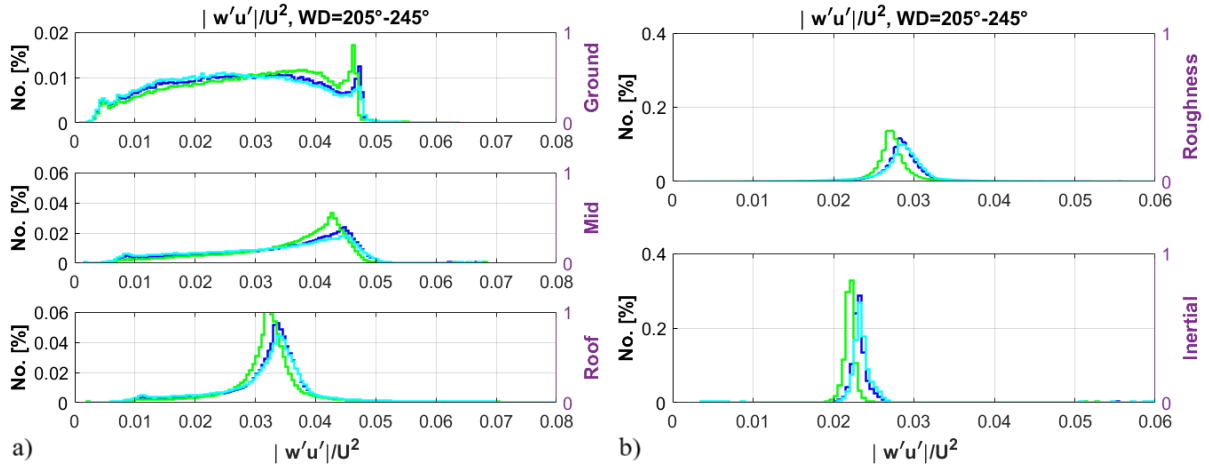


**Figure 7.41:** TKMF  $|w'u'|$  distributions, normalized on the squared wind speed  $U$ , evaluated in the (a) UCL and (b) UBL above for REF-scen (in blue), NOVEG-scen (in green) and VEG50-scen (in cyan). Ground layer in (a) has a different ordinate tick to make the distribution differences appreciable.

The variation factor analysis is proposed again to evaluate the variation from the reference scenario (REF-scen) imposed by the removal of trees in the domain (NOVEG-scen). The investigated quantity  $X_{REF-scen}/X_{NOVEG-scen} - 1$  describes an increase of the variable  $X$  in the NOVEG-scen with respect to REF-scen when the variation factor is positive, a reduction when it is negative. As always,  $X$  can be the wind speed, TKE and TKMF, and the variables are investigated for the EWcanopy, NScanopy and Intersect topological categories in the usual five layers within and above the canopy. Since the input wind direction ensemble implies winds

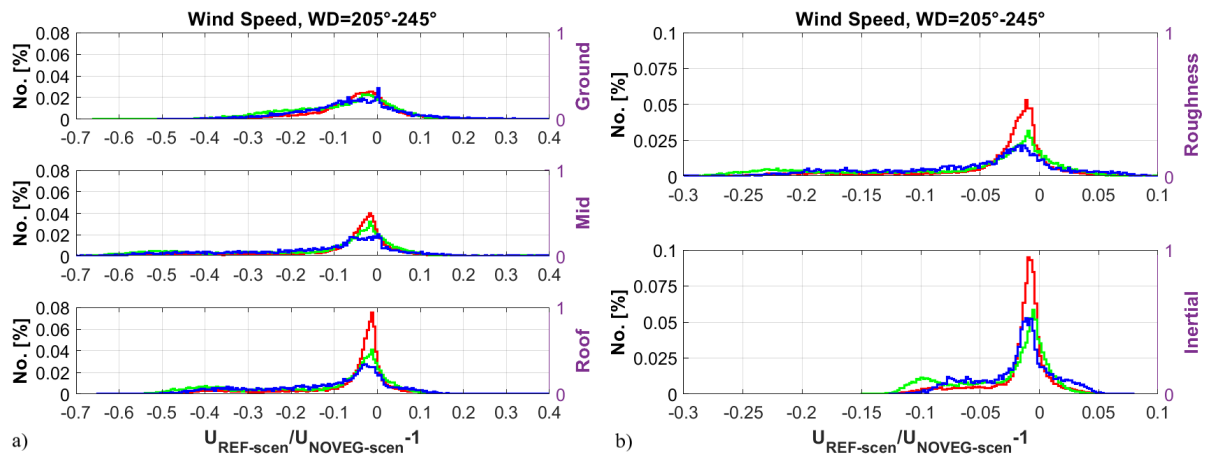


**Figure 7.42:** Wind speed  $U$  variation factor distributions evaluated in the (a) UCL and (b) UBL above for the difference between REF-scen and NOVEG-scen for the EWcanopy (blue), NScanopy (green) and Intersect (red) topological categories.

## 7.4. THE EFFECT OF WIND DIRECTION AND SURFACE ROUGHNESS ON THE VEGETATION IMPACT

coming from southwest, both EWcanopy and NScanopy are oriented at  $45^\circ \pm 20^\circ$  to them, and so they are expected to behave similarly. The wind speed distributions for the different topological categories is displayed in Fig. 7.42. Differences between topological categories are minimal, with good superposition between NScanopy and EWcanopy and a mode intensification in the Intersect with respect to the other two. Distributions are single modal, widely spread in the canopy (Fig. 7.42a), peaked outside it, especially in the inertial layer (Fig. 7.42b). Distributions account for wind speed increase with the introduction of vegetation in the domain of a variation factor in the range  $0 \div -0.1$  within the canopy,  $0 \div -0.05$  outside the canopy.

$\langle Tke \rangle$  distributions behaviors is again similar in the three categories. Within the canopy (Fig. 7.43a),  $\langle Tke \rangle$  values are normally distributed around zero or small increases of  $\langle Tke \rangle$  with the tree presence are observed. Particularly at ground layer, the distributions describe the same probability of having positive or negative contributions to  $\langle Tke \rangle$ , while as the layer increases, the distributions shift toward positive values. Outside the canopy (Fig. 7.43b), distributions show a predominance of positive factor values with modes at 0.05. Intersect shows again the most defined and peaked normal distributions, while the other two are more similar and widely spread, both inside and outside the UCL.

The behavior of the normalized TKMF distributions (Fig. 7.44) is similar to the  $\langle Tke \rangle$  ones both inside and outside the canopy. Within the canopy (Fig. 7.44a),  $\langle |\overline{w'u'}| \rangle$  values are normally distributed and widely spread around zero, with small increases of  $\langle |\overline{w'u'}| \rangle$  with the tree presence. Particularly at ground layer, the distributions describe the same probability of having positive or negative contributions to  $\langle |\overline{w'u'}| \rangle$ , while as the layer increases, the distributions shift toward positive values. The topological categories show exactly the same behavior

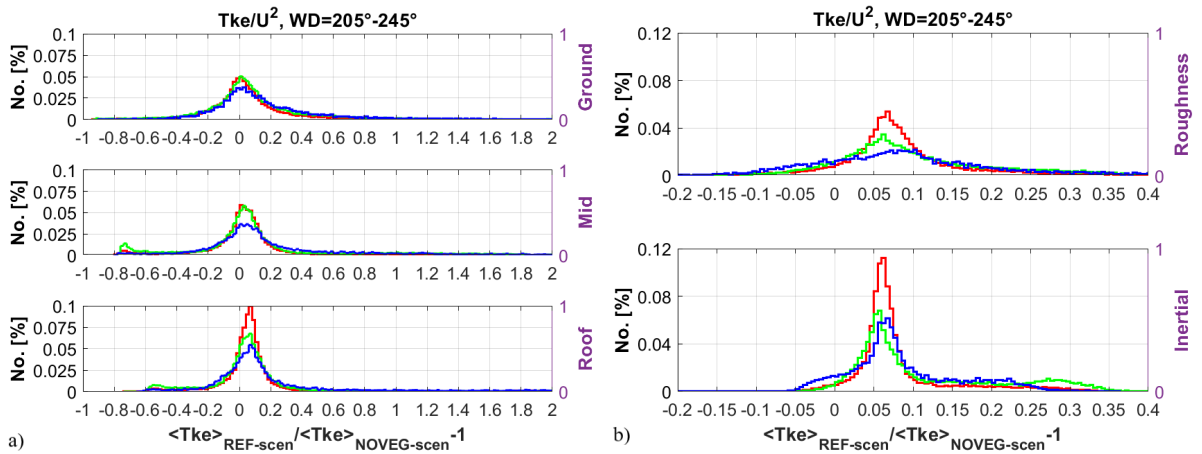


**Figure 7.43:**  $Tke$  variation factor distributions, normalized on the squared wind speed  $U$  ( $\langle Tke \rangle$ ), evaluated in the (a) UCL and (b) UBL above for the difference between REF-scen and NOVEG-scen for the EWcanopy (blue), NScanopy (green) and Intersect (red) topological categories.

## CHAPTER 7. RESULTS AND DISCUSSION: MODELING THE IMPACTS OF TREES ON THE EXCHANGE PROCESSES

with a very small intensification of the Intersect distributions modes especially at the roof layer. Outside the canopy (Fig. 7.44b), distributions show a predominance of positive factor values with modes at 0.05. The topological category analysis confirms and strengthen the results from

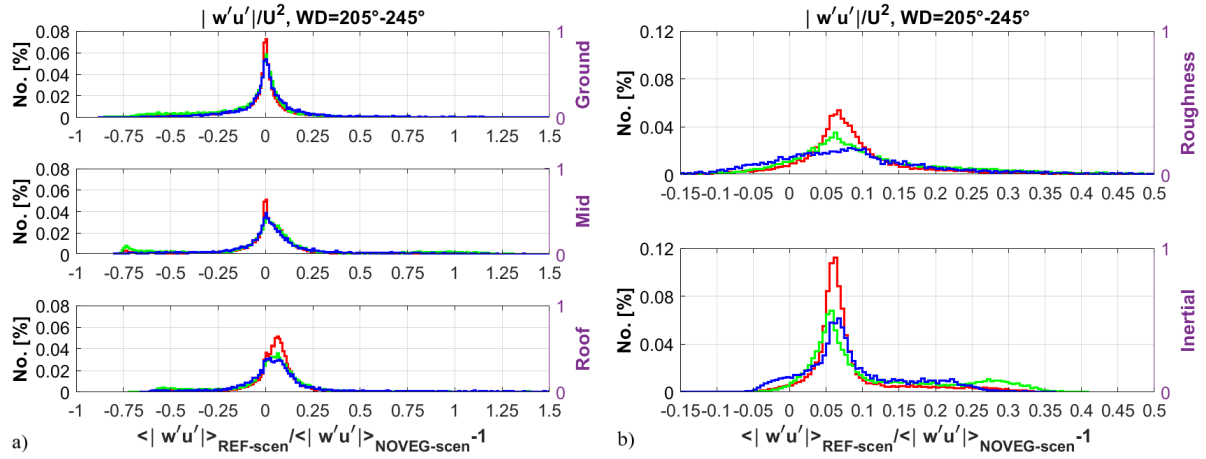


**Figure 7.44:** TKMF  $|\overline{w'u'}|$  variation factor distributions, normalized on the squared wind speed  $U$  ( $\langle |w'u'| \rangle$ ), evaluated in the (a) UCL and (b) UBL above for the difference between REF-scen and NOVEG-scen for the EWcanopy (blue), NScanopy (green) and Intersect (red) topological categories.

the whole domain investigation, retrieving a mean flow magnitude decrease as the vegetation is introduced in the canopy, enhancing the obstacle number, and an almost proportional intensification of the turbulence caused by the energy cascade from large to small spatial scales.

Finally, the variation factor analysis is used to evaluate the variation from REF-scen imposed by the increased number of trees in the domain (VEG50-scen). The investigated quantity  $X_{REF-scen}/X_{VEG50-scen} - 1$  describes an increase of the variable  $X$  in the VEG50-scen with respect to REF-scen when the variation factor is negative, a reduction when it is positive. As always,  $X$  can be the wind speed, TKE and TKMF, and the variables are investigated for the EWcanopy, NScanopy and Intersect topological categories in the usual five layers within and above the canopy. Since the SW input wind direction ensemble implies winds coming from southwest, both EWcanopy and NScanopy are oriented at  $45^\circ \pm 20^\circ$ , and so they are expected to behave similarly. Results are completely equal to the NOVEG-scen to REF-scen factor investigation, but asymmetrical with respect to the zero variation factor, since this last parameter has an opposite behavior when VEG50-scen is considered instead of NOVEG-scen. The wind speed distributions for the different topological categories is displayed in Fig. 7.45. Differences between topological categories are minimal, with an intensification in the NScanopy distributions modes with respect to the other two, leading to a small disparity between the differently oriented canopies not retrieved in for the NOVEG-scen to REF-scen variation factor investigation. Distributions are single modal, widely spread in the canopy (Fig. 7.45a), peaked outside it,

## 7.4. THE EFFECT OF WIND DIRECTION AND SURFACE ROUGHNESS ON THE VEGETATION IMPACT

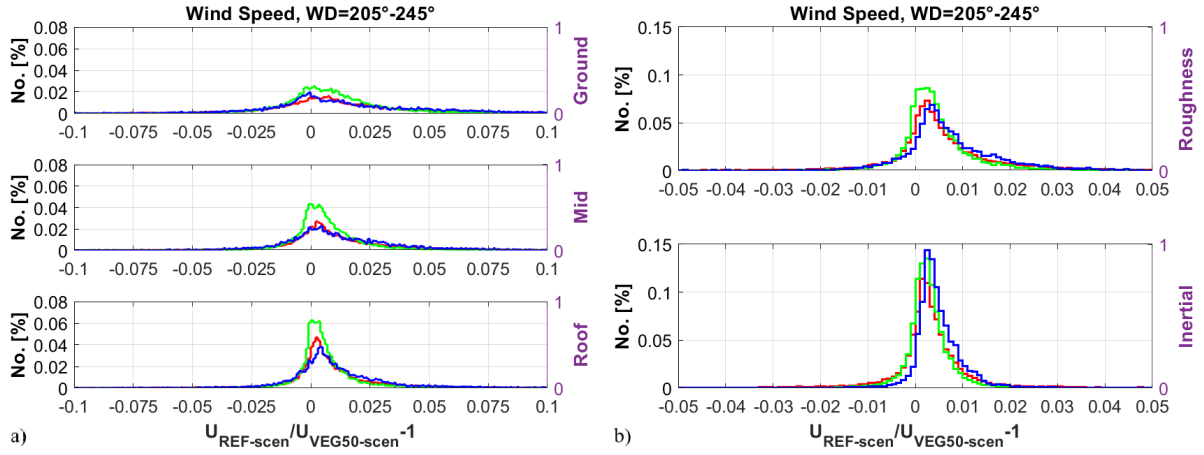


**Figure 7.45:** Wind speed  $U$  variation factor distributions evaluated in the (a) UCL and (b) UBL above for the difference between REF-scen and VEG50-scen for the EWcanopy (blue), NScanopy (green) and Intersect (red) topological categories.

especially in the inertial layer (Fig. 7.45b). Distributions account for wind speed decrease with the increase of vegetation in the domain of a significance factor in the range  $0 \div 0.025$  within the canopy,  $0 \div 0.020$  outside the canopy.

$\langle Tke \rangle$  distributions behaves similarly in the three categories, with similar discrepancies in the NScanopy one already retrieved for the in-canyon wind speed (Fig. 7.45a). Within the canopy (Fig. 7.46a),  $\langle Tke \rangle$  values are normally distributed around zero, with small increases of  $\langle Tke \rangle$  as the tree number increases. The distributions describe almost the same probability

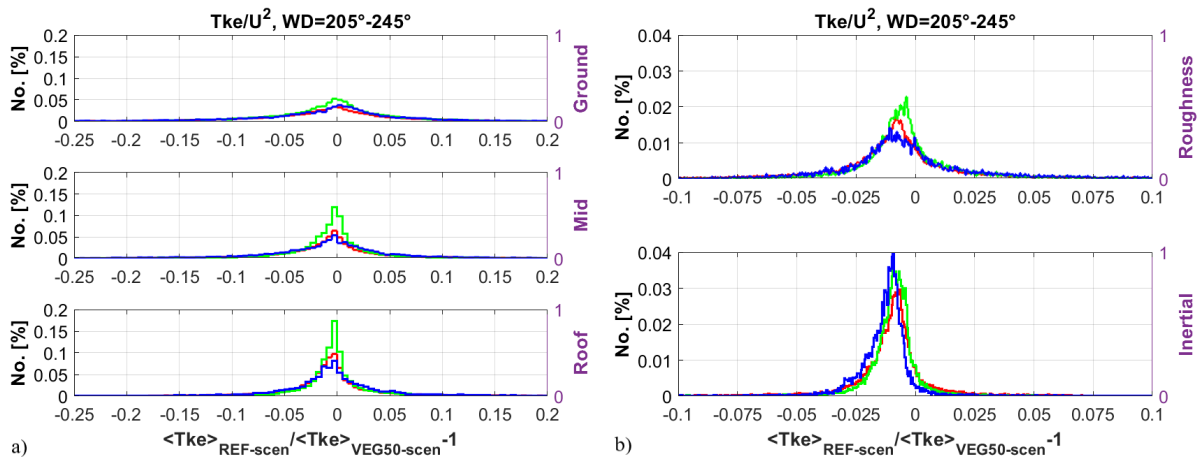


**Figure 7.46:**  $Tke$  variation factor distributions, normalized on the squared wind speed  $U$  ( $\langle Tke \rangle$ ), evaluated in the (a) UCL and (b) UBL above for the difference between REF-scen and VEG50-scen for the EWcanopy (blue), NScanopy (green) and Intersect (red) topological categories.

## CHAPTER 7. RESULTS AND DISCUSSION: MODELING THE IMPACTS OF TREES ON THE EXCHANGE PROCESSES

of having positive or negative contributions to  $\langle Tke \rangle$ . Outside the canopy (Fig. 7.46b), distributions show a predominance of negative factor values with modes at 0.01.

The behavior of the normalized TKMF distributions (Fig. 7.47) is similar to the  $\langle Tke \rangle$  ones both inside and outside the canopy. Within the canopy (Fig. 7.47a),  $\langle |\overline{w'u'}| \rangle$  values

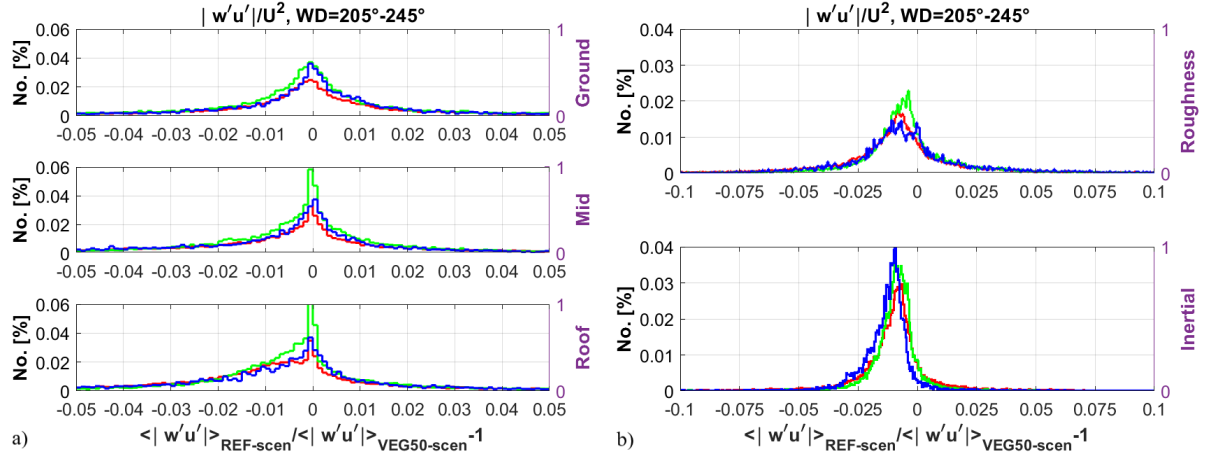


**Figure 7.47:** TKMF  $|\overline{w'u'}|$  variation factor distributions, normalized on the squared wind speed  $U$  ( $\langle |\overline{w'u'}| \rangle$ ), evaluated in the (a) UCL and (b) UBL above for the difference between REF-scen and VEG50-scen for the EWcanopy (blue), NScanopy (green) and Intersect (red) topological categories.

are normally distributed and widely spread around zero, with small increases of  $\langle |\overline{w'u'}| \rangle$  as the tree number increases. The topological categories show exactly the same behavior with a very small intensification of the NScanopy distributions modes especially at the roof layer. Outside the canopy (Fig. 7.47b), distributions show a predominance of negative factor values with modes at -0.01. Again the topological category analysis confirms and strengthens the results from the whole domain investigation, retrieving a mean flow magnitude decrease as the vegetation amount is augmented in the canopy, thus enhancing the obstacle number, and an almost proportional intensification of the turbulence caused by the energy cascade from large to small spatial scales. It is evident once again the dependency on the incoming wind direction of the urban flows, and how they react to a modification of the vegetation amounts.

### 7.4.2 The Effects of Morphology

#### Input Wind Direction Parallel from North to the Street Canyon Orientation

The morphological parameters investigation is proposed again considering the input wind direction ensemble NP as identified in Sect. 7.4.1. Wind speed, TKE and TKMF are respectively displayed as function of  $\lambda_p$  and  $\lambda_f$  for each layer defined in Sect. 7.3.1 and with the same input conditions applied in Sect. 7.4.1. Clearly both  $\lambda_p$  and  $\lambda_f$  change according to the investigated

## 7.4. THE EFFECT OF WIND DIRECTION AND SURFACE ROUGHNESS ON THE VEGETATION IMPACT

scenario in order to account for the respective amount of vegetation. Being the total area fraction coefficients, for the NOVEG-scen  $\lambda_p$  and  $\lambda_f$  are simply calculated from the building planar and frontal area respectively, while in REF-scen and VEG50-scen they account for the different vegetation amounts. Results for the aforementioned variables are shown in Fig. 7.48, 7.49 and 7.50 respectively.

Wind speeds in each layer show similar behaviors for the three scenarios (Fig. 7.48). In particular, the wind speed decreases with the increasing morphological parameter. In the planar area coefficient cases, the wind speed decrease involves the whole coefficient scale for all scenarios. The wind speed in the REF-scen shows instead a strong discontinuity when the frontal area

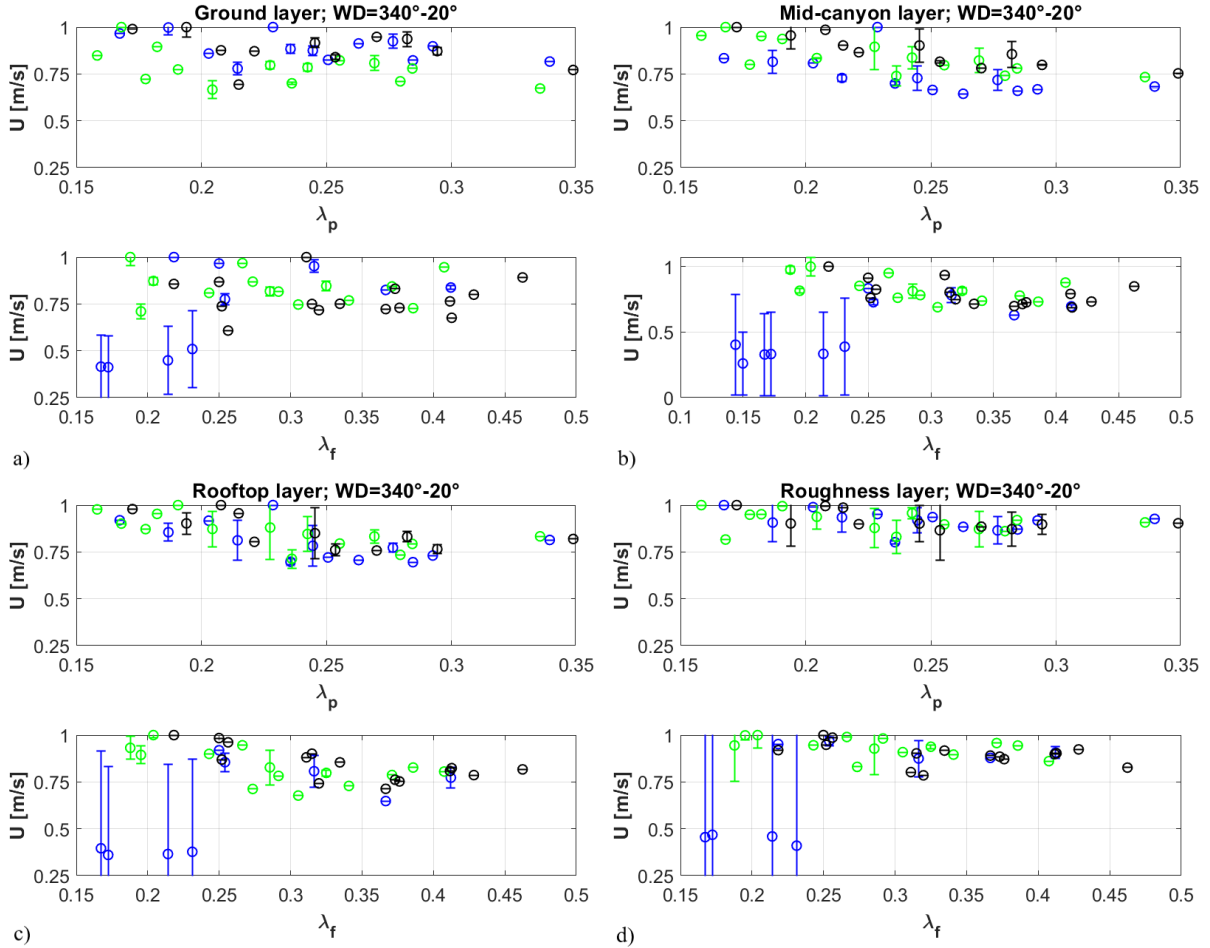


**Figure 7.48:** Wind speed as a function of the planar ( $\lambda_p$ ) and frontal ( $\lambda_f$ ) area coefficients retrieved at (a) ground, (b) mid-canyon, (c) rooftop and (d) roughness layers respectively. Wind speeds are normalized over their maximum values to enhance the comparability. Blue circles identify to the REF-scen, the green ones the NOVEG-scen and the black ones the VEG50-scen. Each dot is the wind speed averaged over each  $\lambda_p$  or  $\lambda_f$  bin 0.01 large and the error bars are the standard deviation in each bin.

## CHAPTER 7. RESULTS AND DISCUSSION: MODELING THE IMPACTS OF TREES ON THE EXCHANGE PROCESSES

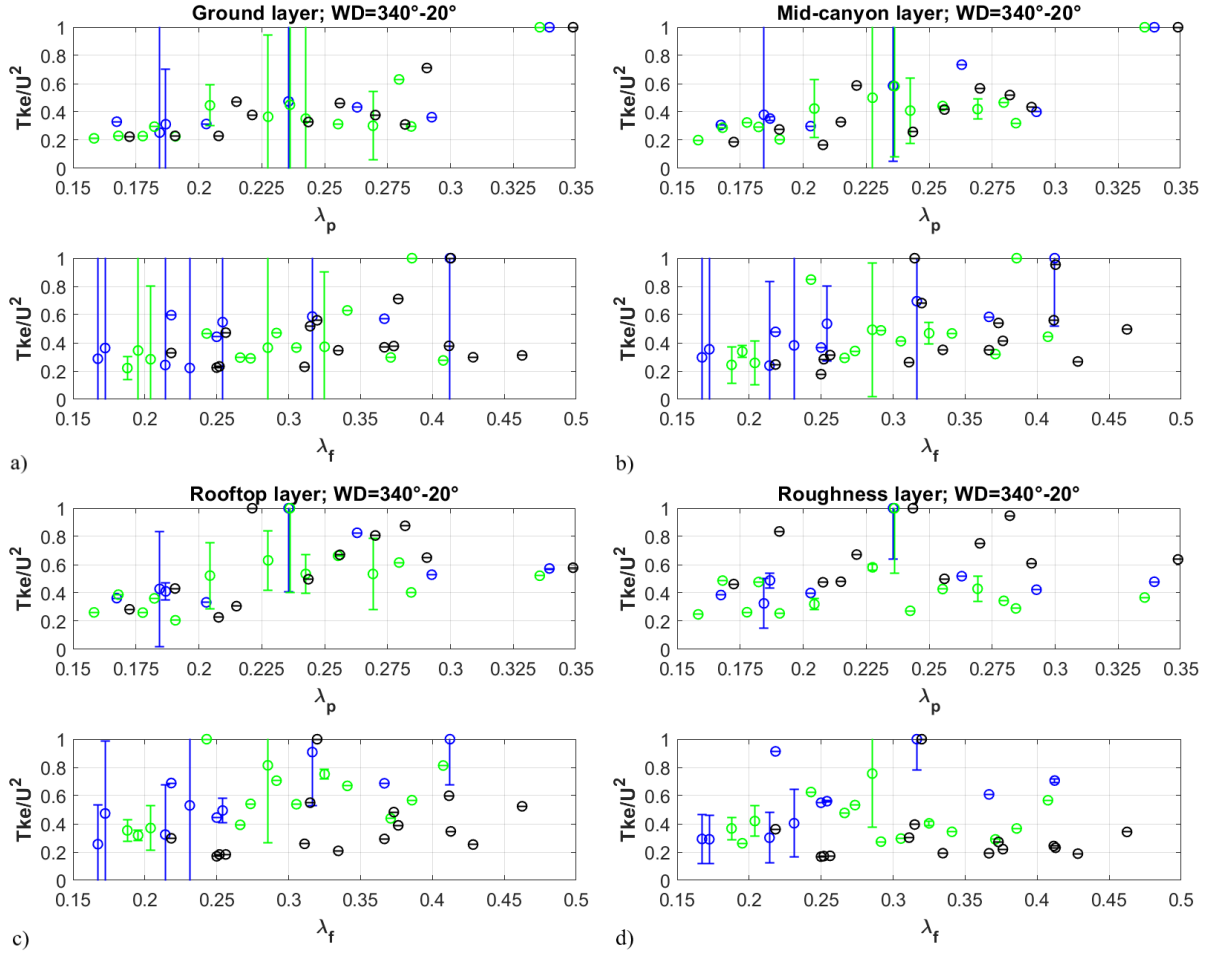


**Figure 7.49:**  $Tke$ , normalized on the squared wind speed  $U$ , as a function of the planar ( $\lambda_p$ ) and frontal ( $\lambda_f$ ) area coefficients retrieved at (a) ground, (b) mid-canyon, (c) rooftop and (d) roughness layers respectively.  $Tkes$  are normalized over their maximum values to enhance the comparability. Blue circles identify to the REF-scen, the green ones the NOVEG-scen and the black ones the VEG50-scen. Each dot is the  $Tke$  averaged over each  $\lambda_p$  or  $\lambda_f$  bin 0.01 large and the error bars are the standard deviation in each bin.

coefficient is approximately 0.25. Above this threshold, wind speed decreases with the increasing  $\lambda_f$ , following the common tendency retrieved for the other scenarios. Below the threshold, wind speed drops to very small and constant values. While the wind speed behavior above the threshold is simply a consequence of the increasing number of obstacles in the domain that weaken the wind speed, the below the threshold the behavior is much more unexpected, since it happens for the REF-scen where trees are indeed involved. The decreasing tendency of wind speed with both  $\lambda_p$  and  $\lambda_f$  is more effective where the bulk of the tree crown is present (Fig. 7.48b-c), while at the ground and roughness layers (Fig. 7.48a-d) this behavior is less defined or efficient.

## 7.4. THE EFFECT OF WIND DIRECTION AND SURFACE ROUGHNESS ON THE VEGETATION IMPACT

$Tke$  tendencies in Fig. 7.49 show two well defined regimes shared by both morphological coefficients in at least NOVEG-scen and REF-scen. When  $Tke \leq 0.225$ ,  $Tke$  is independent on the coefficients, as it was for the wind speeds. Above this threshold,  $Tke$  rapidly increases as the coefficients increase. This second tendency is sometimes present also in VEG50-scen, where  $Tke$  often maintains a constant tendency, since the obstacles saturate the environment and  $Tke$  is dissipated rather than generated from the mean flow. At the ground layer (Fig. 7.28a) a tendency inversion is retrieved when  $\lambda_f$  is larger than 0.4, when the increasing number of obstacles inhibits the production of  $Tke$ .

TKMF (Fig. 7.50) shows a very complex behavior, dependent on the considered morpholog-

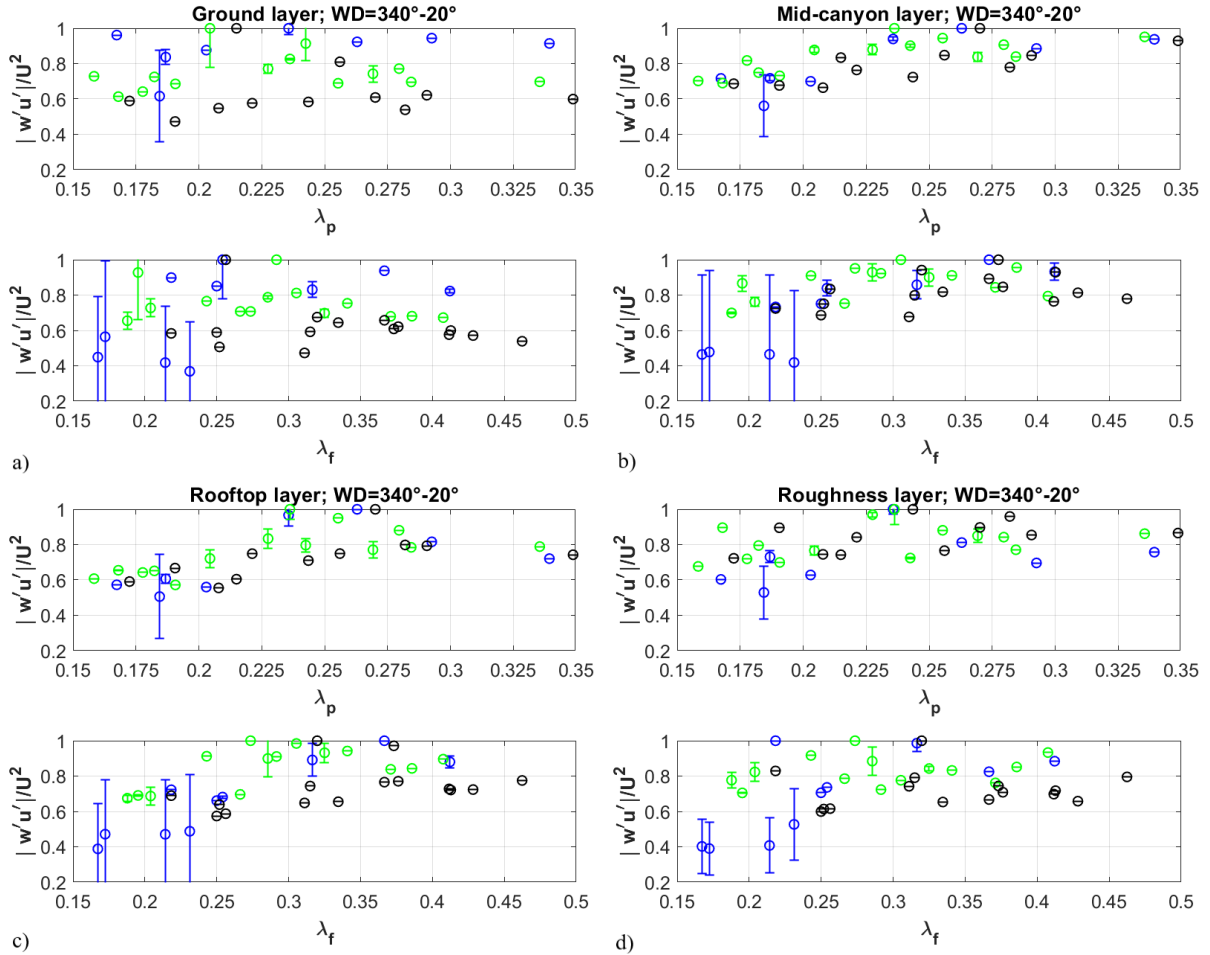


**Figure 7.50:** TKMF, normalized on the squared wind speed  $U$ , as a function of the planar ( $\lambda_p$ ) and frontal ( $\lambda_f$ ) area coefficients retrieved at (a) ground, (b) mid-canyon, (c) rooftop and (d) roughness layers respectively.  $|\overline{w'u'}|$ s are normalized over their maximum values to enhance the comparability. Blue circles identify to the REF-scen, the green ones the NOVEG-scen and the black ones the VEG50-scen. Each dot is the  $|\overline{w'u'}|$  averaged over each  $\lambda_p$  or  $\lambda_f$  bin 0.01 large and the error bars are the standard deviation in each bin.

## CHAPTER 7. RESULTS AND DISCUSSION: MODELING THE IMPACTS OF TREES ON THE EXCHANGE PROCESSES

---

ical parameters and atmospheric layers. At the mid-canyon and rooftop layers (Fig. 7.29b-c) TKMFes show the usual dual behavior, especially when investigated against  $\lambda_p$ , with an increase with increasing morphology above 0.2 and an independent tendency below it. Considering the dependency on  $\lambda_f$ , a third threshold is retrieved at 0.35 above which TKMFes are found to decrease as  $\lambda_f$  increases. This suggests that the domain is saturated of obstacles and turbulent structures are fragmented in such small vortices that carry a small amount of momentum, enhancing the dissipation efficiency. At both ground and roughness layers (Fig. 7.29a-d), TKMFes are almost independent on the morphology variation, but they show a strong decrease in the NOVEG-scen and VEG50-scen with respect to the REF-scen. Again, changes that a variation of the vegetation amount cause are small if compared to the impact that buildings or solid obstacles have on the mean flow and turbulence fields modifications.

### Input Wind Direction from Southwest to the Street Canyon Orientation

The morphological investigation is proposed once again to assess the impact of the morphology, modified by different vegetation scenarios, on the mean flow and turbulent structures when the input wind direction ensemble is SW. Wind speed, TKE and TKMF are respectively displayed as function of the morphological parameters  $\lambda_p$  and  $\lambda_f$  for each layer defined in Sect. 7.3.1 and with the same input conditions applied in Sect. 7.4.1. Clearly both  $\lambda_p$  and  $\lambda_f$  change according to the investigated scenario in order to account for the respective amount of vegetation. Being the total area fraction coefficients, for the NOVEG-scen  $\lambda_p$  and  $\lambda_f$  are simply calculated from the building planar and frontal area respectively, while in REF-scen and VEG50-scen they account for the different vegetation amounts. Results for the aforementioned variables are shown in Fig. 7.51, 7.52 and 7.53 respectively.

Wind speeds in each layer show similar behaviors for the three scenarios (Fig. 7.51). Frontal area fraction coefficient seems to largely affect the wind speed, which rapidly decreases as the coefficient increases. The tendency is similar to what already retrieved from the EP wind direction ensemble (Sect. 7.3.2), as it is caused by the obstacle density increase in the domain as the coefficient increases. The flow trajectory is modified as a consequence of the interaction with the obstacles, inhibiting the flow speed. A similar behavior is retrieved also for the planar area fraction coefficient in all layers except for the ground layer (Fig. 7.51) where a clear tendency is not evident. At rooftop and roughness layers (Fig. 7.51c-d), wind speed slightly decreases as the coefficient increases above a certain threshold (0.325). As retrieved in Sect. 7.4.1, wind speed values in the NOVEG-scen are larger than the REF-scen ones, also showing larger decreasing slopes for both coefficient dependencies. Therefore, the presence of trees reduces the overall wind speed as well as the velocity gradients, leading to more homogeneous fields, both inside and above the canopy. A similar behavior is retrieved also for the VEG50-scen, despite it does not seem to have a predominance effect on the morphological dependency of the wind speeds.

## 7.4. THE EFFECT OF WIND DIRECTION AND SURFACE ROUGHNESS ON THE VEGETATION IMPACT

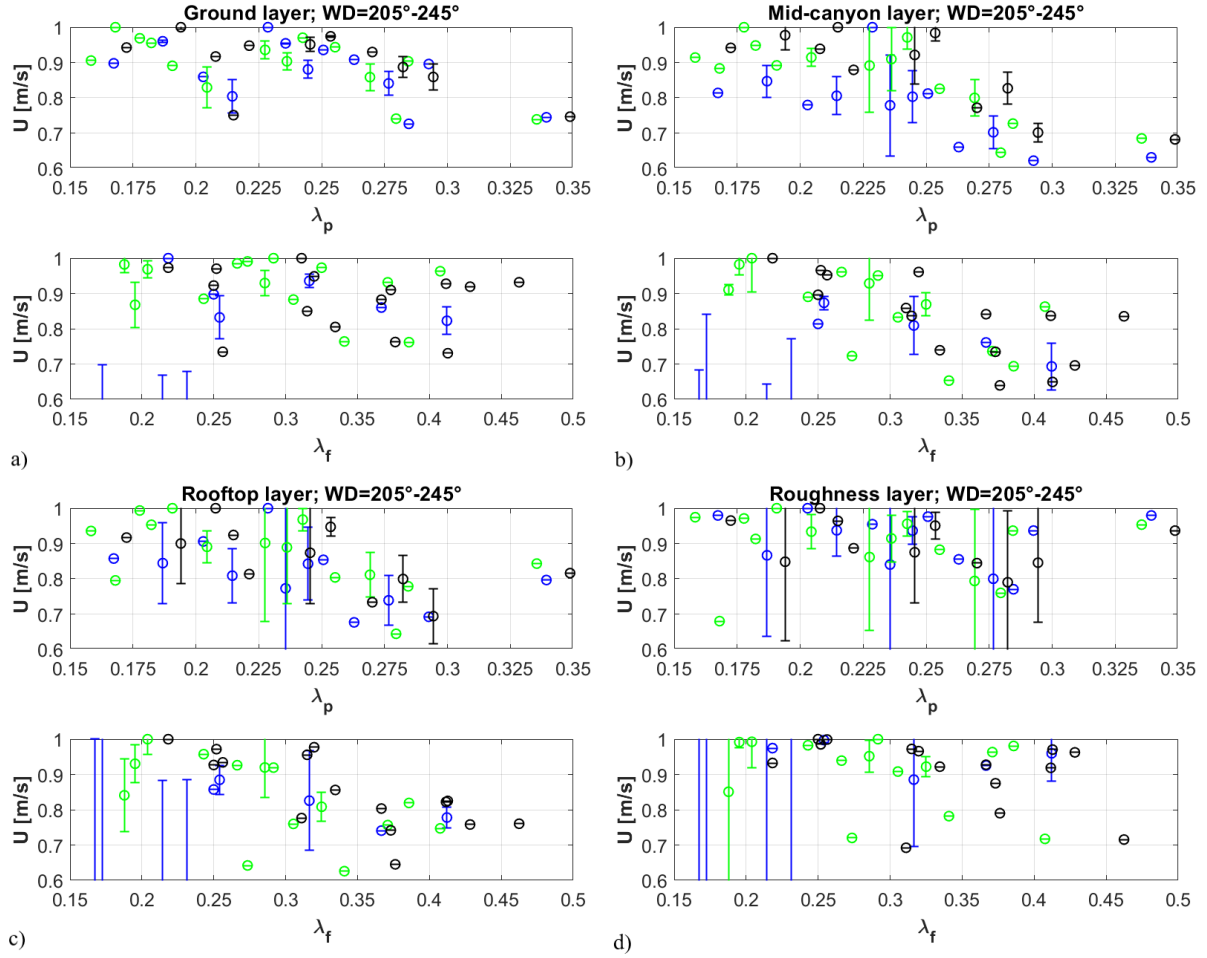


**Figure 7.51:** Wind speed as a function of the planar ( $\lambda_p$ ) and frontal ( $\lambda_f$ ) area coefficients retrieved at (a) ground, (b) mid-canyon, (c) rooftop and (d) roughness layers respectively. Wind speeds are normalized over their maximum values to enhance the comparability. Blue circles identify to the REF-scen, the green ones the NOVEG-scen and the black ones the VEG50-scen. Each dot is the wind speed averaged over each  $\lambda_p$  or  $\lambda_f$  bin 0.01 large and the error bars are the standard deviation in each bin.

*Tke* tendencies in Fig. 7.52 show two well defined regimes shared by both morphological coefficients in all scenarios. When  $Tke \leq 0.225$ , *Tke* is independent on the coefficients, as it was for the wind speeds. Above this threshold, *Tke* rapidly increases as the coefficients increase. This second tendency is particularly evident in the REF-scen and NOVEG-scen especially at rooftop and roughness layers (Fig. 7.52c-d), while in VEG50-scen *Tke* often maintains a constant tendency, since the obstacles saturate the environment and *Tke* is dissipated rather than generated from the mean flow.

TKMFes (Fig. 7.53) somehow follow the same behaviors observed for the TKE, with an increase of the flux intensities above a certain threshold and an independence of  $|w'u'|$  from

## CHAPTER 7. RESULTS AND DISCUSSION: MODELING THE IMPACTS OF TREES ON THE EXCHANGE PROCESSES

morphology below. Well defined increasing trends are found in each scenario when  $\lambda_f$  is larger than 0.25 at the roughness layers (Fig. 7.53d), while at mid-canyon and rooftop layers (Fig. 7.53b-c) the increasing trends involve the whole morphology scale.  $|w'u'|$  also increases with  $\lambda_p$  in the same layers when  $\lambda_p \geq 0.25$ . Nevertheless, the increasing tendencies appear to be generally smoother than the TKE counterparts (Fig. 7.52). At the ground layer (Fig. 7.53a) the tendencies are even less defined.  $|w'u'|$  seems independent on both morphological parameters. A discontinuity is found at  $\lambda_f=0.25$  for the REF-scen but both tendencies before and after the threshold are independent on the morphological parameter, as it is for the whole scale of  $\lambda_p$ . Confirming the EP and NP wind direction ensemble cases, the changes that a variation of the

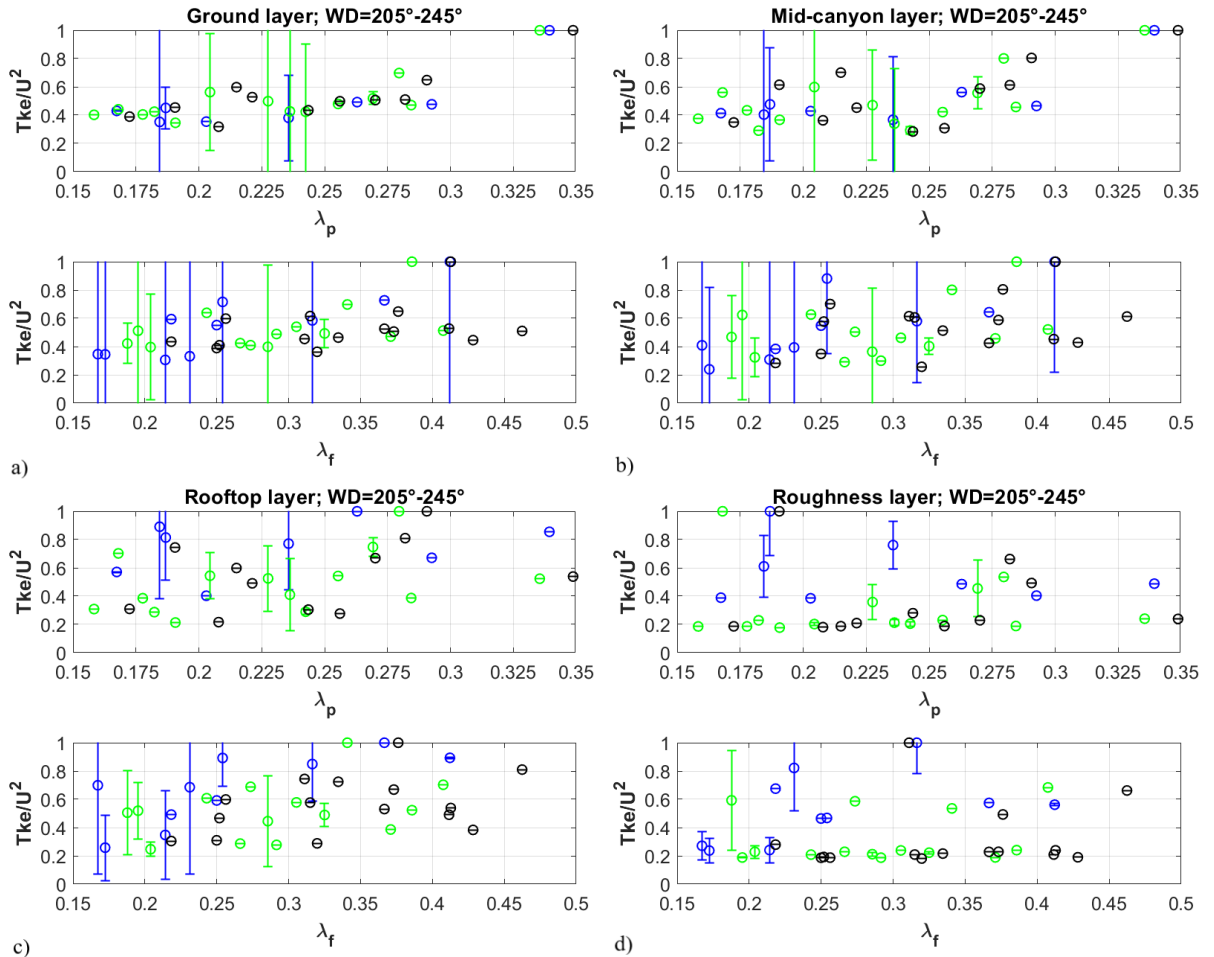


**Figure 7.52:**  $Tke$ , normalized on the squared wind speed  $U$ , as a function of the planar ( $\lambda_p$ ) and frontal ( $\lambda_f$ ) area coefficients retrieved at (a) ground, (b) mid-canyon, (c) rooftop and (d) roughness layers respectively.  $Tkes$  are normalized over their maximum values to enhance the comparability. Blue circles identify to the REF-scen, the green ones the NOVEG-scen and the black ones the VEG50-scen. Each dot is the  $Tke$  averaged over each  $\lambda_p$  or  $\lambda_f$  bin 0.01 large and the error bars are the standard deviation in each bin.

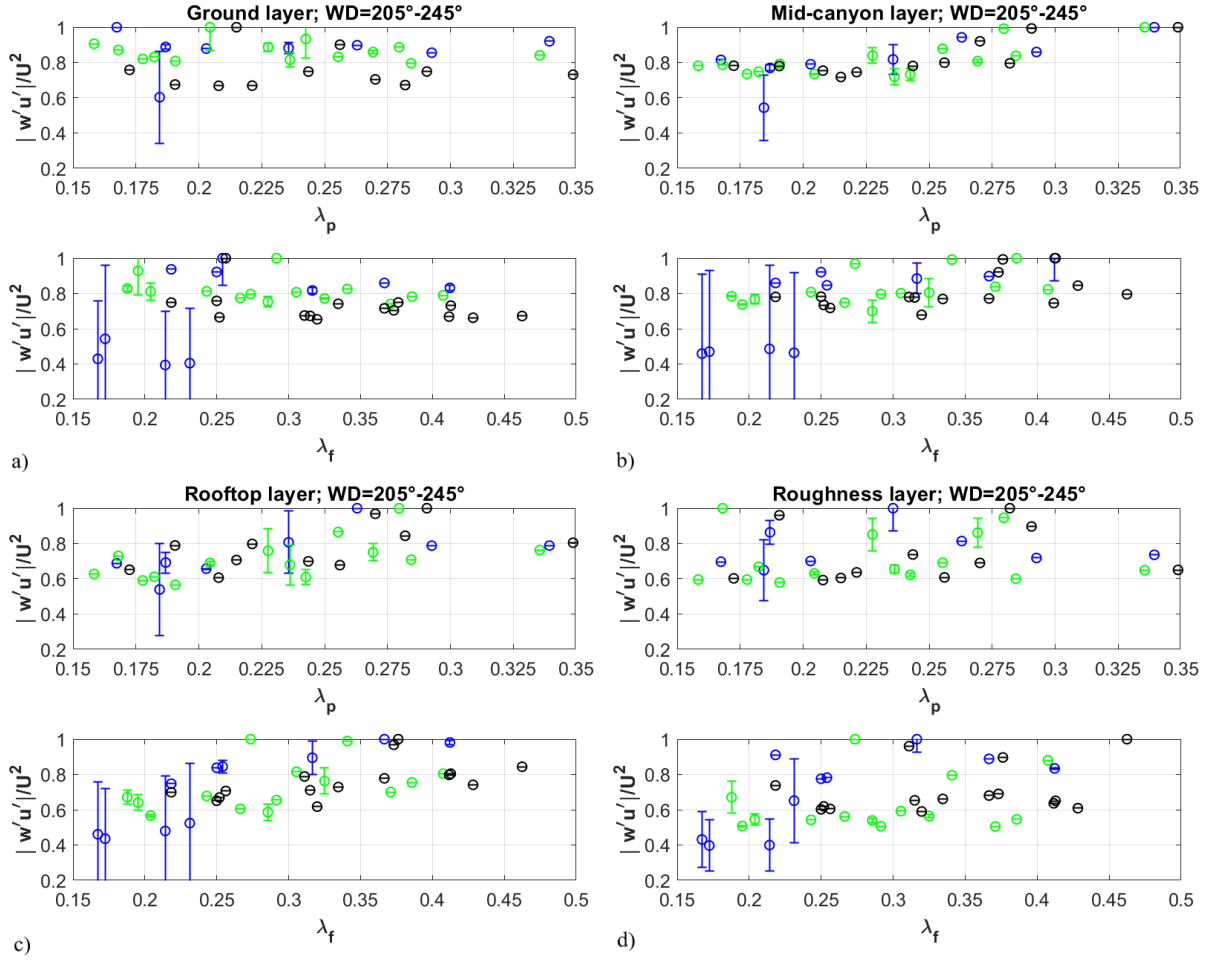


**Figure 7.53:** TKMF, normalized on the squared wind speed  $U$ , as a function of the planar ( $\lambda_p$ ) and frontal ( $\lambda_f$ ) area coefficients retrieved at (a) ground, (b) mid-canyon, (c) rooftop and (d) roughness layers respectively.  $|\overline{w'u'}|$ s are normalized over their maximum values to enhance the comparability. Blue circles identify to the REF-scen, the green ones the NOVEG-scen and the black ones the VEG50-scen. Each dot is the  $|\overline{w'u'}|$  averaged over each  $\lambda_p$  or  $\lambda_f$  bin 0.01 large and the error bars are the standard deviation in each bin.

vegetation amount cause are small if compared to the impact that buildings or solid obstacles have on the mean flow and turbulence fields modifications.

## 7.5 Summary and Conclusions

In this chapter, an investigation on the impact of trees within the real urban domain of LB is proposed using the approximated CFD model QUIC. Three different quantities have been analyzed, tackling the vegetation impact on the mean flow (wind speed) and ventilation (TKE and TKMF) characteristics.

## CHAPTER 7. RESULTS AND DISCUSSION: MODELING THE IMPACTS OF TREES ON THE EXCHANGE PROCESSES

---

Before the analysis to be made, a code modification is introduced and validated on a simple domain to better simulate the friction velocity and therefore the turbulent related quantities. The code modification theory was introduced in Sect. 7.1 to overcome some wrong values obtained for the TKE profiles from simulations. The validation of the modified code has been proven to work better than the original one for the simple and most common obstacles and morphology in urban environments, such as isolated trees and buildings, street canyons, frontal and rear wake volumes. The modified code has been successfully validated for different input wind directions and speeds, and atmospheric stability. Finally, a successful validation has been obtained also for the MA and LB domains, considering real input conditions retrieved from measurements.

After the implementation of the  $u_*$  modified computation into QUIC, simulations of wind speed, TKE and TKMF for four different wind direction ensembles have been verified on the experimental field campaign in MA and LB. The choice to have wind direction ensembles, i.e. a range of simulations taken for different wind direction under the same input conditions, was made to better account for the strong variability of the wind direction and to choose a representative interval of at least one hour that could ensure some robustness to the simulation results. The verification of the different simulations gave very good results in all the three analyzed variables, when the NP, WP and EP wind direction ensembles are considered. Conversely, the simulations for the SP wind directions ensemble gave a poor comparison with the data from measurements. This last ensemble was associated with nocturnal conditions, when a stably stratified UBL developing above a neutrally stable UCL, and a small boundary layer height provided some overestimation in the model computation. Nevertheless, QUIC is found to provide reliable and accurate estimations of the mean flow and turbulence developing within complex urban environments typical of European cities, especially when the UCL unstable or neutral stability is coupled with the rest of the UBL.

From the verification, the input conditions of the EP wind direction ensemble are chosen to investigate the vegetation impact on wind speed, TKE and TKMF in the building wake volume and the deep and narrow street canyon of LB. The overall impact of vegetation on the wind speed is found to be a blocking effect, reducing the wind speed in the UCL and propagating this reduction in the UBL above. The reduction propagation above the canopy resulted in a wavelike motion. TKE is found to increase its heterogeneous spatial distribution as the trees are introduced in the domains, both in the canopy and above it. TKE increased at the base of the trees and at their top, while decreased above them. TKE production is limited to the volumes where an intense flow interact with the tree, generating more dissipation elsewhere. TKMF is found to behave similarly to the TKE, except for the tree base and the inner-canopy region, where the vegetation was insignificant or reduced the flux.

The vegetation impact was then detailed as a function of the wind direction, by means of the characteristic quantities distributions computed for the different vertical layers LB neighbor-

hood domain has been divided into. Three different input wind directions (EP, NP and SW) were chosen for the investigation, but they all used the same input conditions of the EP wind direction ensemble, except of course the wind direction. Among these input conditions, three different topological scenarios have been investigated to detail the differences between the reference or real domain (REF-scen) and a non vegetative domain (NOVEG-scen) or a scenario where the vegetation amount is randomly increased by a 50% (VEG50-scen). Wind speed is found to increase as the vegetation is removed from the domain for all the investigated the wind direction ensembles, confirming the blocking effect of vegetation on the mean flow. As a verification, wind speed is found to decrease when the tree number is increased for the EP and SW wind directions. However, the NP wind direction revealed an increased wind speed in the VEG50-scen with respect to the REF-scen, as the vegetation may increase the channeling effect of the wind. TKE is found to show similar behaviors if vegetation is added or removed from REF-scen, but drastically change with the input wind direction. TKE is found to increase when vegetation is either removed or added, and to increase from SW to EP wind directions, in agreement with the wind speed behaviors. On the contrary, TKE is strongly reduced when the wind is NP to the canyon, for both modified scenarios, as the channeling effect on the flow tends to favor direction rather than isotropic turbulence. The similar behavior of NOVEG-scen and VEG50-scen suggested the existence of a threshold in the number of trees added in the domain, by which the TKE dissipation dominates the production. Finally, the TKMFes are generally found to follow the wind speed behaviors since these two quantities are strictly related one to the other. The strong increase of TKMF under NP wind directions supported the directional turbulence production theory suggested for the channeling flows. As the behaviors of VEG50-scen and NOVEG-scen are again coupled, the hypothesis on the turbulence dissipation-production threshold based on the number of trees in the domain is supported.

Similar results are also retrieved detailing the analysis to account for different topological categories defined within the domain. In particular, wind speed, TKE and TKMF are investigated as function of the three vegetation scenarios in an ensemble of street canyons north-south oriented (NScanopy), east-west oriented (EWcanopy) and inside the major intersections (Intersect). Results for each input wind direction ensemble confirm the overall behaviors discovered with the whole domain distribution analysis, with an increase of the channeling effect of street canyons parallel to the flow as vegetation is added in the domain, and a general flow reduction elsewhere. Turbulent quantities confirmed the whole domain distribution analysis, with the TKMF following more strictly the mean flow behaviors and TKE behaving in opposition. Moreover it appears evident how the domain has a prevalent orientation, which can also explain the different behaviors when wind directions are EP and NP.

Finally, a morphological analysis is presented, showing the dependency of the three atmospheric quantities on the morphological parameters  $\lambda_p$  and  $\lambda_f$  as the vegetation scenarios are changed.

## **CHAPTER 7. RESULTS AND DISCUSSION: MODELING THE IMPACTS OF TREES ON THE EXCHANGE PROCESSES**

---

Both mean flow and turbulent fields are found to decrease their magnitudes as the obstacle density increases in the domain, but the largest impact is given by the building disposition rather than the vegetation amounts. Below certain obstacle densities, mean flow and especially turbulence are found to be independent on the morphological parameters.

## Chapter 8

# Conclusions and Further Remarks

Local atmospheric processes, such as flow circulations, coherent and transient turbulent structures, interaction processes and local thermal budget are the key investigated aspects that drive or have an impact on the majority of the local atmospheric issues concerning the urban environment. In recent years, these fundamental aspects have been tackled to investigate city breathability and thermal comfort in the urban canopies, with the aim to find solutions for mitigating air pollution and urban heat island effects and for rising the livability of the urban environment. Of large interest is also the presence of vegetation in urban environments and how it impacts different aspects of the atmospheric processes, from the aerodynamics effects to the implication on pollutant deposition and resuspension and thermal comfort.

The present thesis was inspired by these past investigations, to focus on the analysis the ventilation processes in different real urban canopies modified by vegetative elements, and their applications to air pollutant removal. In particular, exchange processes have been investigated from measured data in real urban street canyons by means of new diagnostic quantities evaluated using the Buckingham theorem, fundamental mathematical tool of the similarity theory, with the aim to characterize mechanical and thermal aspects of the in-canyon circulation, to represent the chemically passive pollutant removal from the canopy and to evaluate the role of vegetation on the local flows and turbulent structures at the basis of the diagnostic quantities formulation. At the core of the investigation there are the two experimental field campaigns conducted in two street canyons of the city of Bologna (Italy), namely Marconi Street and Laura Bassi Street, covering part of the late summer/early fall (August-September 2017) and winter (January-February 2018) periods. Three sites located at different height in each street canyon have been fully equipped to detail the minimum variations in the flow and turbulent fields, together with a detailed measure of the principal traffic pollutant concentrations. Supporting meteorological and air quality monitoring sites have been added to establish a measurement network ensuring a good characterization of the urban boundary layer processes.

## CHAPTER 8. CONCLUSIONS AND FURTHER REMARKS

---

The diagnostic quantities are derived from processed data during a period of weak synoptic conditions and thermal circulation developing at the urban boundary layer scale. Despite the detailed analyses for the diagnostic quantities have been conducted only for the summer campaign, the similar conditions characterizing the two season's periods at the synoptic scale grant for the possible analysis extension to the winter period. As expected from two similar synoptic conditions, summer and winter periods showed some similarity, such as the time evolution of the mean flow and turbulent related quantities both within and above the canopies, where the majority of the inter seasonal differences are caused by the different amounts of available energy in the environment.

Newly developed diagnostic quantities included four time scales characterizing the time associated to mechanical and thermal exchanges between different atmospheric layers within and at the interface of the urban canopy. The time scales separately assess the momentum and heat exchange contributions, including the combined impact of mean flow and turbulent aspects related to the upward/downward transport processes. Therefore the time scales are representative of the key mechanisms regulating the exchange processes, and their values vary with the wind direction of the background flow. Detailed findings associated with the time scales analysis in the non-vegetated canyon revealed that mechanical time scales  $\tau_d$  vary within and above the canyon, with values evaluated at the rooftop level smaller than the ones evaluated at lower levels. Thermal time scales  $\tau_h$ , sustained by the heat released from the street and the building facades, are smaller and more homogeneous than the mechanical ones. In a vegetated canopy,  $\tau_d$  are homogeneous within and above the canyon, as the presence of vegetation and the lateral flow entrainment mix the mechanical exchange velocity by affecting the mechanical production of turbulence. The irregular building and street insolation, caused by the shadowing effect of the trees, affects the mixing properties of the canopy leading to heterogeneous  $\tau_h$  values.

From the time scales, another couple of new diagnostic quantities have been evaluated as the ratio between interface and in-canyon time scales, always keeping mechanical and thermal aspects separated. These new quantities have been named exchange rates  $\eta$  as they evaluate the capacity of a canopy in exchanging momentum and heat with the outer layer. When  $\eta < 1$ , the canopy circulation rapidly transports momentum or heat toward the interface, favoring the exchanges with the outer layers. When  $\eta > 1$ , the circulation is faster at the interface, which traps momentum and heat to recirculate downward and limits the exchange efficacy. Both vegetated and non-vegetated canopies are found to be favourable environment for exchange processes to develop for approximately the 50 – 75% of the rates cases, but the long tails of the distributions describe scenarios where the exchanges are totally suppressed, particularly common in the veg-

---

etated canyon. The only exception is retrieved for the thermal rates in the vegetated canyon, where the vegetation inhibits the exchanges at the surface by lowering the sensible heat fluxes.

A new total circulation dependent exchange rate  $\eta_t$  has been computed supposing the larger efficiency of mechanical processes when the in-canyon circulation is inertially driven or of the thermal processes when the circulation is thermal. Discrimination has been made using the buoyancy parameter  $B$  (the ratio between thermal and inertial circulations drivers), to find an exchange rate representative of a real environment where both circulations can be present. The total exchange rate is successfully used to reproduce the  $CO$  concentration (normalized on the canopy geometry, mean flow velocity and source emission) tendency within the canopies, revealing momentum and heat transports to be most efficient driver of mass transport within a street canyon under weak synoptic conditions.

Finally, the buoyancy parameter  $B$  enables the introduction of a new simple parametrization for in-canyon wind speed and to modify an existing one for the temperature horizontal gradient as functions of the mean canyon aspect ratio  $H/W$ . These parametrizations allow to estimate and compare flow characteristics in real street canyons with different aspect ratios, if the airflow regime within the canyon is in the skimming flow.

The bulk of the investigation on the impact of vegetation on the mean flow, turbulence kinetic energy and momentum flux is performed using the fast-responding operational computational fluid dynamics model Quick Urban & Industrial Complex (QUIC). First, a code modification was introduced to better simulate the friction velocity and therefore the turbulent related quantities. The improved code has been successfully validated among a simple idealized domain, and then proved more accurate for the investigated vegetated and non-vegetated neighborhoods domains.

The model was then verified on both domains, testing real conditions characterized by four different wind direction ensembles to the reference canyons orientations as input for the simulations. The choice of simulating ensembles of wind directions minimized the uncertainties of the model and associated with the transient nature of the wind direction. The model verification gave very good results in all the three analyzed variables when the northerly, westerly and easterly wind direction ensembles are considered, while the southerly comparison with measured data is poor, as a stably stratified UBL developing above a neutrally stable UCL, and a small boundary layer height provided some overestimation in the model computation. Definitively, QUIC is proved to perform reliable and accurate estimations of the mean flow and turbulence developing within complex urban environments typical of European cities, especially when the urban canopy unstable or neutral stability is coupled with the rest of the boundary layer.

## CHAPTER 8. CONCLUSIONS AND FURTHER REMARKS

---

A qualitative impact of vegetation is addressed by simulating representative volumes of the vegetated street canyon in presence and absence of trees. The overall impact of vegetation on the wind speed is found to be a blocking effect, reducing the wind speed in the whole boundary layer. The reduction propagation above the canopy resulted in a wavelike motion. Turbulence is found to increase its heterogeneous spatial distribution as the trees are introduced in the domains, both in the canopy and above it. A turbulence production is found to be limited to the volumes where an intense flow interact with the tree, generating more dissipation elsewhere.

A quantitative investigation is then proposed to assess the vegetation impact in the whole domain on the mean flow and turbulence under different input wind directions, comparing the real environment to scenarios with no vegetation and more vegetation. Wind speed is found to increase as the vegetation is removed from the domain for all the investigated the wind directions, confirming the blocking effect of vegetation on the mean flow. As a verification, wind speed is found to decrease when the tree number is increased for perpendicular and oblique wind directions. However, the parallel wind direction revealed an increased wind speed as the number of trees increase in the domain, as the vegetation may increase the channeling effect of the wind. TKE is found to increase when vegetation is either removed or added, and to increase from oblique to perpendicular wind directions, in agreement with the wind speed behaviors. On the contrary, TKE is strongly reduced when the wind is parallel to the canyon, for both modified scenarios, as the channeling effect on the flow tends to favor direction rather than isotropic turbulence. The existence of a threshold in the number of trees added in the domain is speculated, by which the TKE dissipation dominates the production. Finally, the TKMFes are generally found to follow the wind speed behaviors since these two quantities are strictly related one to the other. The strong increase of TKMF under parallel wind directions supported the directional turbulence production theory suggested for the channeling flows. Since the turbulent quantities showed similar behaviors for the non-vegetated and more vegetated scenarios, the existence of a threshold in the number of trees added in the domain is speculated, by which the turbulence dissipation dominates on the production.

Similar results are also retrieved detailing the analysis to account for different topological categories defined within the domain. Results for each input wind direction confirm the overall behaviors discovered with the whole domain distribution analysis, with an increase of the channeling effect of street canyons parallel to the flow as vegetation is added in the domain, and a general flow reduction elsewhere. Also turbulent quantities confirmed the whole domain distribution analysis, with the TKMF following more strictly the mean flow behaviors and TKE behaving in opposition.

Finally, a morphological analysis is presented, showing the dependency of the three atmospheric quantities on the morphological parameters  $\lambda_p$  and  $\lambda_f$  as the vegetation scenarios are changed. Both mean flow and turbulent fields are found to decrease their magnitudes as the obstacle density increases in the domain, but the largest impact is given by the building disposition rather than the vegetation amounts. Below certain obstacle densities, mean flow and especially turbulence are found to be independent on the morphological parameters.

## 8.1 Future Perspectives

Several aspects of the urban canopy flows and ventilation processes have been tackled in this thesis and more generally during the last two decades. Through the challenges of the world population growth and rising urbanization, the investigations concerning the urban environment are expected to further increase and embrace a wider range of aspects from the fundamental process investigation to the citizen adaptation strategies. In this context, our investigation tackles fundamental aspects of the canopy flow and turbulence in real urban environments and extend them to the more practical topic of air pollution mitigation. Further application of the current method must be done for the winter campaign where the local atmospheric stability is expected to play a key role on the exchanges, while the absence of the vegetation leaves can offer another clue to establish the impact of tree crowns. Further studies are expected and suggested in the recent future following this approach.

The capitalization of experimental field campaigns is fundamental to extend as much as possible all numerical and laboratory studies of idealized scenarios in real environment, to study the implication of transient behaviors of the atmospheric flows on local aspects, given the complexity of a real city morphology. In the context of the exchange processes, further studies are needed to test the implication of an irregular skyline, also in terms of rooftop shape, and dense real street networks on the city breathability. Moreover, the majority of the recent studies, as the current one, has focused on synoptically stable conditions, leaving a large spectrum of background conditions to be investigated. In these scenarios, must be included the effects of vegetations, whose roles needs further and more detailed investigations especially in real environments. Last suggestion involves the complex interaction between chemically or photochemically active pollutants, the transport and exchange atmospheric processes and the vegetation deposition and transpiration processes which still provide a contemporary challenging research topic.



# Appendices



## Appendix A

# Technical Specifications for the Instrumentation

The following tables contain the main technical specifications for instrumentation used during the experimental field campaigns.

Sonic anemometer Gill Windmaster 3D	
Wind speed specifications	
Range	0-50 m s <sup>-1</sup>
Accuracy	≤1.0% RMS @ 12 m s <sup>-1</sup>
Resolution	0.01 m s <sup>-1</sup>
Wind direction specifications	
Range	0-359°
Accuracy	0.5° RMS @ 12 m s <sup>-1</sup>
Resolution	0.1°
Sonic temperature specifications	
Range	-40°C to +70°C
Accuracy	-20°C to +30°C within ±2°C of ambient temperature
Resolution	0.01°C
Operating environmental specifications and sampling rate	
Protection class	IP65
Operating humidity	≤5% to 100%
Operating temperature	-40°C to +70°C
Operating precipitation	300 mm hr <sup>-1</sup>
Sampling rate	20 Hz

**Table A.1:** Technical specifications of sonic anemometers.

**APPENDIX A. TECHNICAL SPECIFICATIONS FOR THE INSTRUMENTATION**

Sonic anemometer Metek uSonic-3	
Wind speed specifications	
Range	0-60 m s <sup>-1</sup>
Accuracy	0.1 m s <sup>-1</sup>
Resolution	0.01 m s <sup>-1</sup>
Wind direction specifications	
Range	0-359°
Accuracy	2° @ 5 m s <sup>-1</sup>
Resolution	0.1°
Sonic temperature specifications	
Range	-40°C to +60°C
Accuracy	2°C @ 5 m s <sup>-1</sup>
Resolution	0.01°C
Operating environmental specifications and sampling rate	
Operating humidity	5% to 100%
Operating temperature	-40°C to +60°C
Sampling rate	20 Hz
Sonic anemometer Young 81000	
Wind speed specifications	
Range	0-40 m s <sup>-1</sup>
Accuracy	±0.1%
Resolution	0.01 m s <sup>-1</sup>
Wind direction specifications	
Range	0-360°
Accuracy	2° @ 30 m s <sup>-1</sup>
Resolution	0.1°
Sonic temperature specifications	
Range	-50°C to +50°C
Accuracy	2°C @ 30 m s <sup>-1</sup>
Resolution	0.01°C
Operating environmental specifications and sampling rate	
Operating humidity	0% to 100%
Operating temperature	-50°C to +50°C
Sampling rate	10 Hz

**Table A.2:** Technical specifications of sonic anemometers.

Sonic anemometers deployed within the canyons are listed in Tab. A.1. The technical specifications include the basic information about operational functioning, measurement ranging and resolutions. Particularly, for the Windmaster 3D sonic anemometer measurement ranges are reported for wind speed, wind direction and sonic temperature, together with accuracy and resolutions. Operating environmental specifications, as the range of humidity, temperature and precipitation under which a correct functioning of the instrumentation is expected. As last, protection class of the instrumentation and sampling rate used during the campaigns are also reported. Tab. A.2 summarizes the specifications of the sonic anemometers deployed at the rooftop levels of each canyon. As a reminder, sonic anemometer uSonic-3 from Metek was installed on Marconi Street rooftop while the Young 81000 was placed on Laura Bassi Street one. Specifications follow the same scheme adopted to describe the Windmaster 3D in Tab. A.1. Coupled to the uSonic-3 Metek sonic anemometer in Marconi Street, the open path gas analyzer LI-COR LI-7500A specifications are reported in Tab. A.3.

Open path gas analyzer LI-COR LI7500A	
<i>CO</i> <sub>2</sub> specifications	
Range	0-3000 ppm
Accuracy	1%
Zero drift	±0.1-0.3 ppm
RMS noise at 5 Hz	0.08 ppm
RMS noise at 10 Hz	0.11 ppm
RMS noise at 20 Hz	0.16 ppm
Gain drift	±0.02-0.1%
Direct sensitivity to <i>H</i> <sub>2</sub> <i>O</i>	±4×10 <sup>-4</sup>
<i>H</i> <sub>2</sub> <i>O</i> specifications	
Range	0-60 ppt
Accuracy	2%
Zero drift	±0.03-0.05 ppt
RMS noise at 5 Hz	0.0034 ppt
RMS noise at 10 Hz	0.0047 ppt
RMS noise at 20 Hz	0.0067 ppt
Gain drift	±0.15-0.3%
Direct sensitivity to <i>CO</i> <sub>2</sub>	±0.05
Operating environmental specifications and sampling rate	
Operating temperature	-25°C to 50°C
Path length	12.5 cm
Sampling rate	10 Hz

**Table A.3:** Technical specifications of the open path gas analyzer.

**APPENDIX A. TECHNICAL SPECIFICATIONS FOR THE INSTRUMENTATION**

Thermohygrometer Campbell Scientific HCS2S3	
	Thermometer specifications
Range	-40°C to +60°C
Accuracy	±0.1°C at 23°C
Long-term stability	≤0.1°C year <sup>-1</sup>
	Hygrometer specifications
Range	0 to 100%
Accuracy	±0.8% at 23°C
Long-term stability	≤1% year <sup>-1</sup>
	Operating specifications and sampling rate
Electronic operating limits	-40°C to +100°C
Storage operating range	-50°C to +100°C
Sampling rate	1 Hz
Net radiometer CNR4 Kipp & Zonen	
	Specifications
Pyranometer spectral response	305 to 2800 nm
Pyrgeometer spectral response	4.5 to 42 $\mu m$
Temperature dependence of sensitivity	≤ 18% (-10°C to +40°C)
Sensitivity range	5 to 20 $\mu VW^{-1}m^2$
Pyranometer uncertainty in daily total	≤ 5% (95% of confidential level)
Pyrgeometer uncertainty in daily total	≤ 10% (95% of confidential level)
Directional error	≤ 20 $Wm^{-2}$ (pyranometer)
Operating temperature range	-40°C to +80°C
Averaging rate	1 minute
Barometer Vaisala PTB110	
	Specifications
Range	500 to 1100 hPa
Linearity	±0.25 hPa
Calibration uncertainty	±0.15 hPa
Accuracy at +20°C	±0.3 hPa
Accuracy at -40°C ... +60°C	±1.5 hPa
Long-term stability	±0.1 hPa year <sup>-1</sup>
Operating temperature	-40°C to +60°C
Sampling rate	1 Hz

**Table A.4:** Technical specifications of HCS2S3 thermohygrometer, CNR4 net radiometer and PTB110 barometer.

Supplementary meteorological measurements are gathered within and above the canyons by slow sampling instrumentation in Tab. A.4. Specifications of the thermohygrometers, the barometers and the net radiometers are listed.

Gas analyzers placed inside the ARPAE mobile laboratories at the ground level, as well as inside the ARPAE stations of the air quality monitoring network, are reported on Tab. A.5 and A.6.

Gas analyzer T300 <i>CO</i> specifications	
Range	0-1000 ppm full scale
Precision	0.5% if reading above 5 ppm
Linearity	1% of full scale
Operating environmental specifications and sampling rate	
Operating temperature	+5°C to +40°C
Sampling rate	0.2 Hz (van)
Averaging rate	1 minute (van), 60 minute (network)
Gas analyzer T200 <i>NO<sub>x</sub>/NO/NO<sub>2</sub></i> specifications	
Range	0-20000 ppm full scale
Precision	0.5% if reading above 50 ppm
Linearity	1% of full scale
Operating environmental specifications and sampling rate	
Operating temperature	+5°C to +40°C
Sampling rate	0.2 Hz (van)
Averaging rate	1 minute (van), 60 minute (network)
Gas analyzer T100 <i>SO<sub>2</sub></i> specifications	
Range	0-20000 ppm full scale
Precision	0.5% if reading above 50 ppm
Linearity	1% of full scale
Operating environmental specifications and sampling rate	
Operating temperature	+5°C to +40°C
Sampling rate	0.2 Hz (van)
Averaging rate	1 minute (van)

**Table A.5:** Technical specifications of *CO*, *NO<sub>x</sub>* and *SO<sub>2</sub>* gas analyzers.

## APPENDIX A. TECHNICAL SPECIFICATIONS FOR THE INSTRUMENTATION

Gas analyzer Thermo Scientific 49i specifications	
Range	0-200 ppm full scale
Precision	1 ppm
Linearity	1% of full scale
Operating environmental specifications and sampling rate	
Operating temperature	0°C to +45°C
Sampling rate	0.2 Hz (van)
Averaging rate	1 minute (van), 60 minutes (network)
Gas analyzer Thermo Scientific 49i specifications	
Range	0-200 ppm full scale
Precision	1 ppm
Linearity	1% of full scale
Operating environmental specifications and sampling rate	
Operating temperature	0°C to +45°C
Sampling rate	0.2 Hz (van)
Averaging rate	1 minute (van), 60 minutes (network)
Gas analyzer airTOXIC Chromatotech specifications	
Range	0-1000 ppm full scale
Precision	2%
Linearity	1% of full scale
Operating environmental specifications and sampling rate	
Operating temperature	+10°C to +35°C
Sampling rate	0.2 Hz (van)
Averaging rate	1 minute (van), 60 minutes (network)

**Table A.6:** Technical specifications of  $O_3$  and  $BTX$  gas analyzers.

As for the gas analyzers, particulate matter samplers placed inside the ARPAE mobile laboratories at the ground level, as well as inside the ARPAE stations of the air quality monitoring network, are reported on Tab. A.7. Both gas analyzers and particulate matter samplers perform automatic calibration tests each night to ensure the correct functioning and performance of the sampling procedure. The larger sampling rate in the gas analyzers occurring in the fixed stations of the air quality monitoring network are caused by the necessity to undergo the European

legislation for air quality monitoring. The equipment placed inside the mobile laboratories is

Particulate sampler	
FAI Swam 5a specifications	
Mass thickness reproducibility	$\pm 2 \mu\text{g}/\text{cm}^2$
Mass measure reproducibility	$\pm 23 \mu\text{g}, 11.95 \text{ cm}^2$
Operating flow rate	0.8-2.5 $\text{m}^3/\text{h}$
Flow rate reproducibility	1%
Flow rate relative uncertainty	2%
Operating environmental specifications and sampling rate	
Operating temperature	-10°C to +55°C
Operating humidity	<85%
Averaging rate	1 day

**Table A.7:** Technical specifications of  $PM_{10}$  and  $PM_{2.5}$  particulate samplers.

completed by the thermohygrometers (Tab. A.8) and the cup and vane anemometers (Tab. A.9). Both mobile laboratories share the same instrumentation, therefore single tables are reported.

Thermohygrometer LSI Lastem EXP815	
Thermometer specifications	
Range	-50 to 70°C
Accuracy	$\pm 0.1^\circ\text{C}$ at 0°C
Resolution	$\pm 0.01^\circ\text{C}$
Long-term stability	$<0.1^\circ\text{C years}^{-1}$
Respond time	4 s (if wind speed 1 $\text{ms}^{-1}$ )
Hygrometer specifications	
Range	0-100%
Accuracy	$\pm 1\%$ if 5-95% RH
Resolution	$\pm 0.1\%$
Long-term stability	$\pm 1\% \text{ years}^{-1}$
Respond time	10 s (if wind speed 1 $\text{ms}^{-1}$ )
Operating environmental specifications and averaging rate	
Operating temperature	-40 to 80°C
Averaging rate	1 minute

**Table A.8:** Technical specifications of thermohygrometers inside the mobile laboratories.

## APPENDIX A. TECHNICAL SPECIFICATIONS FOR THE INSTRUMENTATION

Cup and vane anemometer DNA301.1 and DNA310.1	
Wind speed specifications	
Range	0-75 ms <sup>-1</sup>
Resolution	< 0.06 ms <sup>-1</sup>
Accuracy	± 0.25 ms <sup>-1</sup> if ≤ 25ms <sup>-1</sup> 2% if > 25ms <sup>-1</sup>
Starting threshold	0.26 ms <sup>-1</sup>
Wind direction specifications	
Range	0-360°
Damping coefficient	0.21 m (10 ms <sup>-1</sup> )
Overshoot path	1.2 m (10 ms <sup>-1</sup> )
Accuracy	3%
Starting threshold	0.15 ms <sup>-1</sup>
Operating environmental specifications and averaging rate	
Operating temperature	-40°C to +80°C
Storage temperature	-60°C to +65°C
Averaging rate	1 minute

**Table A.9:** Technical specifications of the cup and vane anemometers inside the mobile laboratories.

The ceilometer specifications are reported in Tab. A.10. Basic functioning of the instrumentation is the shot of a collimate laser pulse plumbing the atmospheric boundary layer depth. From

Ceilometer CL31	
Specifications	
Range	0-7700 m
Resolution	10 m
Laser	InGaAs diode
Wavelength	910 nm
Operating environmental specifications and sampling rate	
Operating temperature	-40°C to +60°C
Operating humidity	0-100%
Operating wind speed	≤ 55 ms <sup>-1</sup>
Operating vibration	5-13.2 Hz, ±1.0 mm 13.2-100 Hz, ±0.79 g
Storing rate	16 s

**Table A.10:** Technical specifications of the ceilometer CL31.

the backscatter signal of the pulse the ceilometer is able to retrieve several information of atmospheric characteristics, first of which the boundary layer height. Being focus on the operating specifications of the instrumentation, the recommendations on the use of the laser generator and the warning concerning the exposure risks are not reported in Tab. A.10.

Meteorological instrument specifications for assessing background air temperature and humidity at Silvani Street and Asinelli Tower are listed in Tab. A.11. Note the different automatic averaging time to fulfill the respective scope. Silvani Street is indeed a urban station, so it needs a greater time resolution to catch the mean flow dynamics and thermodynamics. Being use to assess the synoptic conditions over the city, Asinelli Tower can rely on a coarser time resolution.

Theromhygrometer Vaisala HMP230	
Thermometer specifications	
Range	-40 to 60°C
Accuracy	± 0.1°C at 20°C
Hygrometer specifications	
Range	0-100%
Accuracy	± 1% if 0-90% RH ± 2% if 90-100% RH
Operating environmental specifications and averaging rate	
Operating temperature	-40 to 60°C
Storage temperature	-40 to 70°C
Averaging rate	30 minutes
Thermohygrometer CAE THS	
Thermometer specifications	
Range	-50 to 100°C
Precision	± 0.2°C at 23°C
Hygrometer specifications	
Range	0-100%
Precision	± 1.5%
Operating environmental specifications and averaging rate	
Operating temperature (hygrometer)	-20 to 50°C
Averaging rate	1 Hour

**Table A.11:** Technical specifications of thermohygrometers in Silvani Street and Asinelli Tower.

## APPENDIX A. TECHNICAL SPECIFICATIONS FOR THE INSTRUMENTATION

In the end, Tab. A.12 lists the specifications of the cup and vane anemometers deployed at Silvani Street and Asinelli Tower. The different averaging times used in the two sites can be explained as previously done for the thermohygrometers in Tab. A.11.

Cup and vane anemometer Vaisala WMS301	
Wind speed specifications	
Range	0.5-60 ms <sup>-1</sup>
Sensibility	< 0.02 ms <sup>-1</sup>
Accuracy	± 0.3 ms <sup>-1</sup> if ≤ 10ms <sup>-1</sup> < 2% if > 10ms <sup>-1</sup>
Starting threshold	0.4 ms <sup>-1</sup>
Wind direction specifications	
Range	0-355°
Damping ratio	0.3
Overshoot ratio	0.4
Accuracy	± 3°
Starting threshold	< 1.0 ms <sup>-1</sup>
Operating environmental specifications and averaging rate	
Operating temperature	-40°C to +55°C
Storage temperature	-60°C to +65°C
Averaging rate	30 minutes
Cup and vane anemometer CAE Vv20 and Dv20	
Wind speed specifications	
Range	0-61 ms <sup>-1</sup>
Sensibility	< 0.02 ms <sup>-1</sup>
Resolution	0.06 ms <sup>-1</sup>
Precision	± 0.07 ms <sup>-1</sup> or < 1%
Starting threshold	0.5 ms <sup>-1</sup>
Wind direction specifications	
Range	0-360°
Precision	± 2.8°
Resolution	0.35°
Operating environmental specifications and averaging rate	
Operating temperature	-30°C to +60°C (heated)
Averaging rate	1 Hour

**Table A.12:** Technical specifications of the cup and vane anemometers in Silvani Street and Asinelli Tower.

## Appendix B

# Application of Buckingham Theorem

In this appendix, the Buckingham Theorem is applied to evaluate the time scale  $\tau_d^H$ . The same computation is then used for the other  $\tau$  extrapolated in Sect. 4.2.2. The equation in Eq. (4.1a) states that  $\tau_d^H$  is a function of  $\overline{w'u'}|_H$ ,  $H$ ,  $W$ ,  $L$  and  $\frac{\Delta U_b}{\Delta z}$ :

$$\tau_d^H = f(\overline{w'u'}|_H, H, L, W, \frac{\Delta U_b}{\Delta z}). \quad (\text{B.1})$$

The dimensional analysis is performed for each term, so that

$$[\tau_d^H] = s, \quad (\text{B.2a})$$

$$[\overline{w'u'}|_H] = m^2 s^{-2}, \quad (\text{B.2b})$$

$$[H] = m, \quad (\text{B.2c})$$

$$[L] = m, \quad (\text{B.2d})$$

$$[W] = m, \quad (\text{B.2e})$$

$$[\frac{\Delta U_b}{\Delta z}] = s^{-1}. \quad (\text{B.2f})$$

The theorem states that the product of the variable dimensions on the right hand side of Eq. (B.1) powered to real coefficients must be equal to the actual dimension of the term on the left of the same equation. Therefore,

$$s^1 = (m^2 s^{-2})^a (m)^b (m)^c (m)^d (s^{-1})^e, \quad (\text{B.3a})$$

$$[\tau_d^H]^1 = [\overline{w'u'}|_H]^a [H]^b [L]^c [W]^d [\frac{\Delta U_b}{\Delta z}]^e. \quad (\text{B.3b})$$

The number of possible combinations of the variables whose  $\tau_d^H$  is function is given by the number of independent variables (5) minus the number of dimensions (2). To find this combination, the coefficients have to be extrapolated considering separately the contribution of each variable

## APPENDIX B. APPLICATION OF BUCKINGHAM THEOREM

---

dimension on the desired result. In particular:

$$[m] \quad 0 = 2a + b + c + d \quad (\text{B.4a})$$

$$[s] \quad 1 = -2a - e, \quad (\text{B.4b})$$

that gives the following result

$$e = -2a - 1 \quad (\text{B.5a})$$

$$c = -2a - d - b. \quad (\text{B.5b})$$

Since  $a$ ,  $b$  and  $d$  are arbitrary coefficients,  $a$  and  $d$  are set equal to -1 while  $b$  equals 3. Therefore,

$$a = -1, d = -1 \text{ and } b = 3 \rightarrow c = 0 \text{ and } e = 1. \quad (\text{B.6})$$

Substituting the coefficient in Eq. (B.3b)

$$(\tau_d^H)^1 = (\overline{w'u'}|_H)^{-1} W^{-1} L^0 H^3 \left( \frac{\Delta U_b}{\Delta z} \right)^1, \quad (\text{B.7})$$

and eventually

$$\tau_d^H = \frac{H^3 \Delta U_b}{\overline{w'u'}|_H W \Delta z}. \quad (\text{B.8})$$

## Appendix C

# Generalized Extreme Value Distribution Theory

In the probability theory and statistics, the Generalized Extreme Value (GEV) is a generalized distribution which gathers the three possible distributions suitable for extreme events description: Gumbel, Fréchet and Weibull distributions. The GEV depends on three parameters: the location ( $\mu \in \mathbb{R}$ ), the scale ( $\sigma \in \mathbb{R}_+$ ) and the shape ( $\xi \in \mathbb{R}$ ).  $\mu$  and  $\sigma$  account for the mean properties while  $\xi$  is responsible for the tail's shape of the distribution. GEV density function can be written as:

$$f(x | \mu, \sigma, \xi) = \frac{1}{\sigma} t(x)^{\xi+1} e^{-t(x)}, \quad (\text{C.1})$$

where

$$t(x) = \begin{cases} \left(1 + \xi \left(\frac{x-\mu}{\sigma}\right)\right)^{-\frac{1}{\xi}} & \text{if } \xi \neq 0 \\ e^{-\left(\frac{x-\mu}{\sigma}\right)} & \text{if } \xi = 0. \end{cases} \quad (\text{C.2})$$

$\xi$  is the discerning parameter to determine which distribution member of the family the GEV falls into:

- Gumbel distribution ( $\xi = 0$ ): it is the only distribution which does not depend on the shape parameter and it is formally a result of GEV taken for  $\xi \rightarrow 0$  (considering  $\xi = 0$  the GEV distribution is undefined). It is defined on an infinite domain ( $x \ni [-\infty, +\infty]$ ) and it is written as

$$f(x | \mu, \sigma) = \frac{1}{\sigma} e^{-\left(\frac{x-\mu}{\sigma} + e^{-\left(\frac{x-\mu}{\sigma}\right)}\right)}. \quad (\text{C.3})$$

- Fréchet distribution ( $\xi > 0$ ): it depends on all three parameters, it is bounded on the lower side ( $x > 0$ ) and it is characterized by a long and heavy upper tail. It is defined on

## APPENDIX C. GENERALIZED EXTREME VALUE DISTRIBUTION THEORY

---

the domain  $x \ni [\mu - \sigma/\xi, +\infty]$  and it is written as

$$f(x | \mu, \sigma, \xi) = \frac{1}{\xi\sigma} \left( \frac{x - \mu}{\sigma} \right)^{-\frac{1}{\xi}-1} e^{-\left(\frac{x-\mu}{\sigma}\right)^{-\frac{1}{\xi}}}. \quad (\text{C.4})$$

- Weibull distribution ( $\xi < 0$ ): it depends on the positive part of the parameters, it is bounded on the upper side ( $x < 0$ ) and it is widely used in different areas due to its flexibility. Moreover, when  $\xi = 1$ , this distribution reduces to the exponential model, and when  $\xi = 2$ , it mimics the Rayleigh distribution. In addition, it resembles the Normal distribution when  $\xi = 3.5$ . It is defined on the domain  $x \ni [-\infty, \mu - \sigma/\xi]$  and it is written as

$$f(x | \mu, \sigma, \xi) = \frac{\xi}{\sigma} \left( \frac{x - \mu}{\sigma} \right)^{-\xi-1} e^{-\left(\frac{x-\mu}{\sigma}\right)^{\xi}}. \quad (\text{C.5})$$

Additional information can be found in the original or more representative studies of these distributions, namely [Gumbel \(1958\)](#), [Fisher and Tippett \(1928\)](#) and [Weihull \(1951\)](#).

# Bibliography

- Arnfield AJ (2003) Two decades of urban climate research: A review of turbulence, exchanges of energy and water, and the urban heat island. *Intern J Clim* 23(1):1–26, DOI 10.1002/joc.859
- Bady M, Kato S, Huang H (2008) Towards the application of indoor ventilation efficiency indices to evaluate the air quality of urban areas. *Build Environ* 43(12):1991–2004
- Barlow JF (2014) Progress in observing and modelling the urban boundary layer. *Urban Clim* 10(P2):216–240, DOI 10.1016/j.uclim.2014.03.011
- Barlow JF, Belcher SE (2002) A wind tunnel model for quantifying fluxes in the urban boundary layer. *Boundary-Layer Meteorol* 104:131–150
- Barlow JF, Harman IN, Belcher SE (2004) Scalar fluxes from urban street canyons. Part I: laboratory simulation. *Boundary-Layer Meteorol* 113:369–385
- Bentham T, Britter R (2003) Spatially averaged flow within obstacle arrays. *Atmos Environ* 37(15):2037–2043
- Britter RE, Hanna SR (2003) Flow and Dispersion in Urban Areas. *Annual Review of Fluid Mechanics* 35(1):469
- Buccolieri R, Gromke C, Di Sabatino S, Ruck B (2009) Aerodynamic effects of trees on pollutant concentration in street canyons. *Scien Tot Environ* 407(19):5247–5256, DOI 10.1016/j.scitotenv.2009.06.016
- Buccolieri R, Sandberg M, Di Sabatino S (2010) City breathability and its link to pollutant concentration distribution within urban-like geometries. *Atmos Environ* 44(15):1894–1903
- Buccolieri R, Salim SM, Leo LS, Di Sabatino S, Chan A, Ielpo P, de Gennaro G, Gromke C (2011) Analysis of local scale tree-atmosphere interaction on pollutant concentration in idealized street canyons and application to a real urban junction. *Atmos Environ* 45(9):1702–1713, DOI 10.1016/j.atmosenv.2010.12.058

## BIBLIOGRAPHY

---

- Buccolieri R, Salizzoni P, Soulhac L, Garbero V, Di Sabatino S (2015) The breathability of compact cities. *Urban Clim* 13:73–93
- Buccolieri R, Jeanjean AP, Gatto E, Leigh RJ (2018) The impact of trees on street ventilation, NO<sub>x</sub> and PM<sub>2.5</sub> concentrations across heights in Marylebone Rd street canyon, central London. *Sust Cities Soc* 41:227–241, DOI 10.1016/j.scs.2018.05.030
- Buccolieri R, Santiago JL, Rivas E, Sánchez B (2019) Reprint of: Review on urban tree modelling in CFD simulations: Aerodynamic, deposition and thermal effects. *Urb Fore Urb Green* 37:56–64, DOI 10.1016/j.ufug.2018.07.004
- Chan AT, Au WT, So ES (2003) Strategic guidelines for street canyon geometry to achieve sustainable street air quality—part II: multiple canopies and canyons. *Atmos Environ* 37(20):2761–2772, DOI 10.1016/S1352-2310(03)00252-8
- Chen L, Hang J, Sandberg M, Claesson L, Di Sabatino S, Wigo H (2017) The impacts of building height variations and building packing densities on flow adjustment and city breathability in idealized urban models. *Build Environ* 118:344–361, DOI 10.1016/j.buildenv.2017.03.042
- Cheng H, Hayden P, Robins A, Castro I (2007) Flow over cube arrays of different packing densities. *J Wind Eng Ind Aerodyn* 95(8):715–740, DOI 10.1016/j.jweia.2007.01.004
- Cheng WC, Liu CH, Leung DYC (2009a) On the comparison of the ventilation performance of street canyons of different aspect ratios and Richardson number. *Build Simul* 2(1):53–61
- Cheng WC, Liu CH, Leung DYC (2009b) On the correlation of air and pollutant exchange for street canyons in combined wind-buoyancy-driven flow. *Atmos Environ* 43(24):3682–3690
- Chester S, Meneveau C, Parlange MB (2007) Modeling turbulent flow over fractal trees with renormalized numerical simulation. *J Comput Phys* 225(1):427–448, DOI 10.1016/j.jcp.2006.12.009
- Cionco MR (1965) A mathematical model for air flow in vegetative canopy. *J Appl Meteorol* 4:517–522
- Dallman A, Di Sabatino S, Fernando HJ (2013) Flow and turbulence in an industrial/suburban roughness canopy. *Environ Fluid Mech* 13(3):279–307
- Dallman A, Magnusson S, Britter R, Norford L, Entekhabi D, Fernando HJS (2014) Conditions for thermal circulation in urban street canyons. *Build Environ* 80:184–191
- Di Bernardino A, Monti P, Leuzzi G, Querzoli G (2018) Pollutant fluxes in two-dimensional street canyons. *Urban Clim* 24:80–93

- Di Sabatino S, Buccolieri R, Pulvirenti B, Britter RE (2007) Simulations of pollutant dispersion within idealised urban-type geometries with CFD and integral models. *Atmos Environ* 41(37):8316–8329
- Di Sabatino S, Leo LS, Cataldo R, Britter RE (2010) Construction of Digital Elevation Models for a Southern European City and a Comparative Morphological Analysis with Respect to Northern European and North American Cities. *J Appl Meteorol Clim* 49:1377–1396
- Di Sabatino S, Buccolieri R, Pappaccogli G, Leo LS (2015) The effects of trees on micrometeorology in a real street canyon: consequences for local air quality. *Intern J Environ Poll* 58(1/2):100, DOI 10.1504/ijep.2015.076587
- Durst F (2008) Similarity Theory. In: *Fluid Mechanics*, Springer Berlin Heidelberg, chap 7, pp 193–219
- Eliasson I, Offerle B, Grimmond CSB, Lindqvist S (2006) Wind fields and turbulence statistics in an urban street canyon. *Atmos Environ* 40:1–16
- Fernando H, Zajic D, Di Sabatino S, Dimitrova R, Hedquist B, Dallman A (2010) Flow, turbulence, and pollutant dispersion in urban atmospheres. *Phys Fluids* 22:1–20
- Finardi S, Silibello C, D Allura A, Radice P (2014) Analysis of pollutants exchange between the Po Valley and the surrounding European region. *Urb Clim* 10:682–702, DOI 10.1016/j.uclim.2014.02.002
- Fisher RA, Tippett LHC (1928) Limiting forms of the frequency distribution of the largest or smallest member of a sample. *Math Proc Cambridge Philosophical Society* 24(2):180–190
- Garratt JR (1980) Surface influence upon vertical profiles in the atmospheric near-surface layer. *Quart J Royal Meteorol Soc* 106(450):803–819, DOI 10.1002/qj.49710645011
- Gowardhan AA, Brown MJ, Pardyjak ER (2010) Evaluation of a fast response pressure solver for flow around an isolated cube. *Environ Fluid Mech* 10:311–328, DOI 10.1007/s10652-009-9152-5
- Grimmond CS, Oke TR (2002) Turbulent heat fluxes in urban areas: Observations and a local-scale urban meteorological parameterization scheme (LUMPS). *J Appl Meteorol* 41(7):792–810, DOI 10.1175/1520-0450(2002)041<0792:THFIUA>2.0.CO;2
- Grimmond CS, Salmond JA, Oke TR, Offerle B, Lemonsu A (2004) Flux and turbulence measurements at a densely built-up site in Marseille: Heat, mass (water and carbon dioxide), and momentum. *J Geophys Res* 109(24):1–19, DOI 10.1029/2004JD004936

## BIBLIOGRAPHY

---

- Gromke C, Blocken B (2015) Influence of avenue-trees on air quality at the urban neighborhood scale. Part I: Quality assurance studies and turbulent Schmidt number analysis for RANS CFD simulations. *Environ Poll* 196:214–223, DOI 10.1016/j.envpol.2014.10.016
- Gromke C, Ruck B (2008) Aerodynamic modelling of trees for small-scale wind tunnel studies. *Forestry* 81(3):243–258, DOI 10.1093/forestry/cpn027
- Gromke C, Ruck B (2009) On the impact of trees on dispersion processes of traffic emissions in street canyons. *Boundary-Layer Meteorol* 131(1):19–34, DOI 10.1007/s10546-008-9301-2
- Gromke C, Buccolieri R, Di Sabatino S, Ruck B (2008) Dispersion study in a street canyon with tree planting by means of wind tunnel and numerical investigations - Evaluation of CFD data with experimental data. *Atmos Environ* 42(37):8640–8650, DOI 10.1016/j.atmosenv.2008.08.019
- Gromke C, Blocken B, Janssen W, Merema B, van Hooff T, Timmermans H (2015) CFD analysis of transpirational cooling by vegetation: Case study for specific meteorological conditions during a heat wave in Arnhem, Netherlands. *Build Environ* 83:11–26, DOI 10.1016/j.buildenv.2014.04.022
- Guan D, Zhang Y, Zhu T (2003) A wind-tunnel study of windbreak drag. *Agric Fore Meteorol* 118(1-2):75–84, DOI 10.1016/S0168-1923(03)00069-8
- Gumbel E (1958) *Statistics of extremes*. Columbia University press, New York, USA
- Hang J, Sandberg M, Li Y (2009) Age of air and air exchange efficiency in idealized city models. *Build Environ* 44(8):1714–1723
- Hang J, Li Y, Buccolieri R, Sandberg M, Di Sabatino S (2012) On the contribution of mean flow and turbulence to city breathability: The case of long streets with tall buildings. *Sci Tot Environ* 416:362–373
- Hang J, Luo Z, Sandberg M, Gong J (2013) Natural ventilation assessment in typical open and semi-open urban environments under various wind directions. *Build Environ* 70:318–333
- Harman IN, Barlow JF, Belcher SE (2004) Scalar Fluxes from Urban Street Canyons Part II: Model. *Boundary-Layer Meteorol* 113(3):387–410
- Hayati AN, Stoll R, Kim JJ, Harman T, Nelson MA, Brown MJ, Pardyjak ER, Brown MJ (2017) Comprehensive Evaluation of Fast-Response, Reynolds-Averaged Navier-Stokes, and Large-Eddy Simulation Methods Against High-Spatial-Resolution Wind-Tunnel Data in Step-Down Street Canyons. *Boundary-Layer Meteorol* 164:217–247, DOI 10.1007/s10546-017-0245-2

- Hayati AN, Stoll R, Pardyjak ER, Harman T, Kim J (2019) Comparative metrics for computational approaches in non-uniform street-canyon flows. *Build Environ* 158:16–27, DOI 10.1016/j.buildenv.2019.04.028
- Højstrup J (1993) Statistical data screening procedure. *Meas Sci Technol* 4(2):153–157
- Hong B, Qin H, Lin B (2018) Prediction of wind environment and indoor/outdoor relationships for PM<sub>2.5</sub> in different building-tree grouping patterns. *Atmosphere* 9(2), DOI 10.3390/atmos9020039
- Hosker R (1987) Effects of buildings on local dispersion. Modeling the urban boundary layer. *Amer Meteorol Soc* pp 95–159
- Jeanjean A, Buccolieri R, Eddy J, Monks P, Leigh R (2017) Air quality affected by trees in real street canyons: The case of Marylebone neighbourhood in central London. *Urb Fore Urb Green* 22:41–53, DOI 10.1016/j.ufug.2017.01.009
- Kaimal J, Finnigan J (1994) Atmospheric boundary layer flows, their structure and measurement, vol 41. Oxford University Press, DOI 10.1016/0169-8095(95)00045-3
- Kanda M, Moriwaki R (2006) Spatial variability of both turbulent fluxes and temperature profiles in an urban roughness layer. *Boundary-Layer Meteorol* 121(2):339–350
- Kaplan H, Dinar N (1996) A lagrangian dispersion model for calculating concentration distribution within a built-up domain. *Atmos Environ* 30(24):4197–4207, DOI 10.1016/1352-2310(96)00144-6
- Kastner-Klein P, Rotach MW (2004) Mean flow and turbulence characteristics in a urban roughness sublayer. *Boundary-Layer Meteorol* 111:55–84
- Kastner-Klein P, Berkowicz R, Britter R (2004) The influence of street architecture on flow and dispersion in street canyons. *Meteorol Atmos Phys* 87:121–131
- Kato S, Huang H (2009) Ventilation efficiency of void space surrounded by buildings with wind blowing over built-up urban area. *J Wind Eng Ind Aerodyn* 97(7-8):358–367
- Katul GG, Mahrt L, Poggi D, Sanz C (2004) One- and two-equation models for canopy turbulence. *Boundary-Layer Meteorol* 113:81–109
- Kent WC, Grimmond S, Gatey D (2017) Aerodynamic roughness parameters in cities: inclusion of vegetation. *J Wind Engin Ind Aerodyn* 169:168–176
- Kim J, Baik J (1999) A numerical study of thermal effects on flow and pollutant dispersion in urban street canyons. *J Appl Meteorol* 38:1249–1261

## BIBLIOGRAPHY

---

- Kim JJ, Baik JJ (2001) Urban street-canyon flows with bottom heating. *Atmos Environ* 35(20):3395–3404, DOI 10.1016/S1352-2310(01)00135-2
- Kim JJ, Baik JJ (2003) Effects of inflow turbulence intensity on flow and pollutant dispersion in an urban street canyon. *J Wind Eng Ind Aerodyn* 91(3):309–329
- Klein PM, Galvez JM (2015) Flow and turbulence characteristics in a suburban street canyon. *Environ Fluid Mech* 15:419–438
- Kotz S, Nadarajah S (2000) Extreme value distributions: theory and applications. World Scientific
- Kubilay A, Neophytou MK, Matsentides S, Loizou M, Carmeliet J (2017) The Pollutant Removal Capacity of an Urban Street Canyon and its Link to the Breathability and Exchange Velocity. *Proc Eng* 180:443–451
- Li Q, Wang ZH (2018) Large-eddy simulation of the impact of urban trees on momentum and heat fluxes. *Agricult Forest Meteorol* 255:44–56, DOI 10.1016/j.agrformet.2017.07.011
- Li XX, Britter RE, Norford LK, Koh TY, Entekhabi D (2012) Flow and Pollutant Transport in Urban Street Canyons of Different Aspect Ratios with Ground Heating: Large-Eddy Simulation. *Boundary-Layer Meteorol* 142(2):289–304
- Li XX, Britter RE, Norford LK (2015) Transport processes in and above two-dimensional urban street canyons under different stratification conditions: results from numerical simulation. *Environ Fluid Mech* 15(2):399–417
- Li XX, Britter R, Norford LK (2016) Effect of stable stratification on dispersion within urban street canyons: A large-eddy simulation. *Atmos Environ* 144:47–59
- Li Y, Zhang J, Sailor DJ, Ban-Weiss GA (2019) Effects of urbanization on regional meteorology and air quality in Southern California. *Atmos Chem Phys* 19(7):4439–4457, DOI 10.5194/acp-19-4439-2019
- Liu CH, Wong CC (2014) On the pollutant removal, dispersion, and entrainment over two-dimensional idealized street canyons. *Atmos Res* 135:128–142
- Liu CH, Leung DY, Barth MC (2005) On the prediction of air and pollutant exchange rates in street canyons of different aspect ratios using large-eddy simulation. *Atmos Environ* 39(9):1567–1574
- Lo KW, Ngan K (2017) Characterizing ventilation and exposure in street canyons using Lagrangian particles. *J Appl Meteorol Clim* 56(5):1177–1194

- Louka P, Belcher S, Harrison R (1998) Modified street canyon flow. *J Wind Eng Ind Aerodyn* 74:485–493
- Louka P, Belcher SE, Harrison RG (2000) Coupling between air flow in streets and the well-developed boundary layer aloft. *Atmos Environ* 34(16):2613–2621
- Macdonald RW, Griffiths RF, Hall DJ (1998) An improved method for the estimation of surface roughness of obstacle arrays. *Atmos Environ* 32(11):1857–1864
- Mazzola M, Lanconelli C, Lupi A, Busetto M, Vitale V, Tomasi C (2010) Columnar aerosol optical properties in the Po Valley, Italy, from MFRSR data. *J of Geophys Res Atmos* DOI 10.1029/2009JD013310
- McMillen R (1988) An eddy correlation technique with extended applicability to non-simple terrain. *Boundary-Layer Meteorol* 43(3):231–245
- Moradpour M, Afshin H, Farhanieh B (2017) A numerical investigation of reactive air pollutant dispersion in urban street canyons with tree planting. *Atmos Poll Res* 8:253–266
- Nazarian N, Martilli A, Kleissl J (2017) Impacts of Realistic Urban Heating, Part I: Spatial Variability of Mean Flow, Turbulent Exchange and Pollutant Dispersion. *Boundary-Layer Meteorol* 166:367–393
- Nazarian N, Martilli A, Norford L, Kleissl J (2018) Impacts of Realistic Urban Heating. Part II: Air Quality and City Breathability. *Boundary-Layer Meteorol* 168:321–341
- Nelson MA, Pardyjak ER, Klein P (2011) Momentum and Turbulent Kinetic Energy Budgets Within the Park Avenue Street Canyon During the Joint Urban 2003 Field Campaign. *Boundary-Layer Meteorol* 140:143–162
- Nowak DJ, Hirabayashi S, Bodine A, Hoehn R (2013) Modeled PM<sub>2.5</sub> removal by trees in ten U.S. cities and associated health effects. *Environ Poll* 178:395–402
- Ntziachristos, Leonidas, Boulter P (2009) EMEP/EEA air pollutant emissions inventory guide-book 2009: road vehicle tyre and brake wear; road surface wear
- Oke T (1987) *Boundary-layer climates*, 2nd edn. Routledge, London
- Oke TR (1976) The distinction between canopy and boundary-layer urban heat Islands. *Atmosphere* 14(4):268–277, DOI 10.1080/00046973.1976.9648422
- Oke TR (1988) Street Design and Urban Canopy Layer Climate. *Energy Build* 11(1-3):103–113
- Oke TR, Mills G, Christen A, Voogt JA (2017) *Urban Climates*. Cambridge University Press, Cambridge, DOI 10.1017/9781139016476

## BIBLIOGRAPHY

---

- Panagiotou I, Neophytou MKA, Hamlyn D, Britter RE (2013) City breathability as quantified by the exchange velocity and its spatial variation in real inhomogeneous urban geometries: An example from central London urban area. *Sci Tot Environ* 442:466–477
- Piringer M, Grimmond CSB, Joffre SM, Mestayer P, Middleton DR, Rotach MW, Baklanov A, De Ridder K, Ferreira J, Guilloteau E, Karppinen A, Martilli A, Masson V, Tombrou M (2002) Investigating the Surface Energy Budget in Urban Areas-Recent Advances and Future Needs. *Water, Air Soil Poll (2)*:1–16, DOI 10.1023/A:1021302824331
- Pope S (2000) *Turbulent flows*. Cambridge University Press, Cambridge
- Rafael S, Vicente B, Rodrigues V, Miranda AI, Borrego C, Lopes M (2018) Impacts of green infrastructures on aerodynamic flow and air quality in Porto’s urban area. *Atmos Environ* 190:317–330, DOI 10.1016/j.atmosenv.2018.07.044
- Ratti C, Di Sabatino S, Britter R, Brown M, Caton F, Burian S (2002) Analysis of 3-D urban databases with respect to pollutant dispersion for a number of European and American cities. *Water Air Soil Pollut* 2:459–469
- Raupach M, Antonia R, Rajagopalan S (1991a) Rough-wall turbulent boundary layer. *Appl Mech Rev* 44(1):1–25
- Raupach MR, Antonia RA, Rajagopalan S (1991b) Rough-Wall Turbulent Boundary Layers. *Appl Mech Rev* 44(1):1–25, DOI 10.1115/1.3119492
- Rockle R (1990) Bestimmung der Stromungsverhältnisse im Bereich komplexer Bebauungsstrukturen. PhD thesis, der Technischen Hochschule Darmstadt, Germany
- Rotach M (1995) Profiles of turbulence statistics in and above an urban street canyon. *Atmos Environ* 29(13):1473–1486, DOI 10.1016/1352-2310(95)00084-C
- Rotach MW (1999) On the influence of the urban roughness sublayer on turbulence and dispersion. *Atmos Environ* 33(24-25):4001–4008, DOI 10.1016/S1352-2310(99)00141-7
- Rotach MW, Vogt R, Bernhofer C, Batchvarova E, Christen A, Clappier A, Feddersen B, Gryning SE, Martucci G, Mayer H, Mitev V, Oke TR, Parlow E, Richner H, Roth M, Roulet YA, Ruffieux D, Salmond JA, Schatzmann M, Voogt JA (2005) BUBBLE-an Urban Boundary Layer Meteorology Project. *Theor Appl Climatol* 81:231–261
- Roth M (2000) Review of atmospheric turbulence over cities. *Q J R Meteorol Soc* 126:941–990
- Roth M, Oke T (1995) Relative efficiencies of turbulent transfer of heat, mass and momentum over a patchy urban surface. *American Meteorol Soc* 52(11):1863–1874

- Salizzoni P, Soulhac L, Mejean P (2009) Street canyon ventilation and atmospheric turbulence. *Atmos Environ* 43(32):5056–5067
- Salizzoni P, Marro M, Soulhac L, Grosjean N, Perkins RJ (2011) Turbulent Transfer Between Street Canyons and the Overlying Atmospheric Boundary Layer. *Boundary-Layer Meteorol* 141(3):393–414
- Sasaki Y (1958) An Objective Analysis Based on the Variational Method. *J Meteorol Soc Japan* 36(3):77–88
- Sasaki Y (1970) Numerical variational analysis formulated under the constraints as determined by longwave equations and a low-pass filter. *Monthly Weather Rev* 98(12):884–898
- Schmid H, Cleugh H, Grimmond C, Oke T (1991) Spatial variability of energy fluxes in suburban terrain. *Boundary-Layer Meteorol* 54:249–276
- Schmid HP, Grimmond CB, Cropley F, Offerle B, Su HB (2000) Measurements of CO<sub>2</sub> and energy fluxes over a mixed hardwood forest in the mid-western United States. *Agric For Meteorol* 103(4):357–374
- Sherman CA (1978) A mass-consistent model for wind fields over complex terrain. *J Appl Meteorol* 17:312–319
- Singh B, Hansen BS, Brown MJ, Pardyjak ER (2008) Evaluation of the QUIC-URB fast response urban wind model for a cubical building array and wide building street canyon. *Environ Fluid Mech* 8:281–312, DOI 10.1007/s10652-008-9084-5
- Solazzo E, Britter RE (2007) Transfer processes in a simulated urban street canyon. *Boundary-Layer Meteorol* 124:43–60, DOI 10.1007/s10546-007-9176-7
- Soulhac L, Salizzoni P (2010) Dispersion in a street canyon for a wind direction parallel to the street axis. *J Wind Eng Ind Aerodyn* 98(12):903–910
- Soulhac L, Perkins RJ, Salizzoni P (2008) Flow in a Street Canyon for any External Wind Direction. *Boundary-Layer Meteorol* 126:365–388
- UN DESA (2018) Revision of the World Urbanization Prospects
- Van Renterghem T, Botteldooren D (2008) Numerical evaluation of tree canopy shape near noise barriers to improve downwind shielding. *J Acoust Soc Amer* 123(2):648–657, DOI 10.1121/1.2828052
- Vickers D, Mahrt L (1997) Quality Control and Flux Sampling Problems for Tower and Aircraft Data. *J Atmos Ocean Technol* 14(3):512–526

## BIBLIOGRAPHY

---

- Vos PE, Maiheu B, Vankerkom J, Janssen S (2013) Improving local air quality in cities: To tree or not to tree? *Environ Poll* 183:113–122, DOI 10.1016/j.envpol.2012.10.021
- Weihull W (1951) A statistical distribution function of wide applicability. *J Appl Mech* 18:290–293
- Williams MD, Brown MJ, Boswell D, Singh B, Pardyjak ER (2004) Testing of the QUIC-PLUME model with wind-tunnel measurements for a high-rise building. In: *Ame Meteor Soc (ed) Testing of the QUIC-PLUME model with wind-tunnel measurements for a high-rise building*, Vancouver, BC, Canada, p 10
- Wilson JD (1985) Numerical studies of flow through a windbreak. *J Wind Eng Ind Aerodyn* 21(2):119–154, DOI 10.1016/0167-6105(85)90001-7
- Winkler SL, Anderson JE, Garza L, Ruona WC, Vogt R, Wallington TJ (2018) Vehicle criteria pollutant (PM, NO<sub>x</sub>, CO, HCs) emissions: how low should we go? *Clim Atmos Science* 1:26, DOI 10.1038/s41612-018-0037-5
- Xiaomin X, Zhen H, Jiasong W (2006) The impact of urban street layout on local atmospheric environment. *Build Environ* 41(10):1352–1363, DOI 10.1016/j.buildenv.2005.05.028
- Zajic D, Fernando HJ, Calhoun R, Princevac M, Brown MJ, Pardyjak ER (2011) Flow and turbulence in an urban canyon. *J Appl Meteorol Clim* 50(1):203–223

# Acknowledgements

I wish to acknowledge everyone who helped me, contributed to my growth through this adventure, supported me and sustained me all the time.

I wish to acknowledge my supervisor, Professor Silvana Di Sabatino, for the trust she gave me (together with some very good help) since the beginning of this PhD. The role of a supervisor is to guide the a student through is growth as a researcher and she embraces this role as always in her own personal way. She has been fleeing more than ones, but I could always count on her when I needed most. No matter how difficult was the task, she was always able to offer me all the tools I needed to find the best solution but following my own thoughts and knowledge.

I wish also to acknowledge Professor Eric Pardyjak who hosted me for few months in his research group, giving me the opportunity to enjoy a similar but totally different research experience in the US. To him goes all my gratitude as it goes to the people (professors and researchers) who helped me embracing the atmospheric modeling world.

I acknowledge the iSCAPE project for having granted me the economical support for the PhD and all the participant I was given the pleasure to work and interact with.

I acknowledge all the people who have somehow contributed to the experimental campaigns. Carla Barbieri and Luca Torreggiani from ARPAE for the deployment and maintenance of the instrumentation for air quality measurements and their constant support to the best development of the research. Marianna Nardino from CNR for the deployment and installation of part of the instrumentation for the measurement of turbulence. Beatrice Pulvirenti from the Department of Industrial Engineering of the University of Bologna and Enrico Minguzzi from ARPAE for all the support given during the realization of the campaign and the fruitful discussions to finalize the research. The CGIL (Confederazione Generale Italiana del Lavoro) and private citizens for having host part of the instrumentation on private balcony or rooftop.

I want to thanks the guys of the laboratory (Francesca, Erika, Laura, Leonardo, Marco, Carlo, Davide and William), and the students who have passed by having the bad idea to ask any help from us. Thanks for your help, for the good moments, for the lunches, but also the yelling and outbursts. I know most of the time I'm stubborn and tricky but i really like all of

you and I'm proud to be part of the group.

I really want to thanks Massimo, he allows me to survive in the field and taught me there is always a solution for everything. My PhD would have been much different without you.

I want also to thanks Thomas, James, Andrea and Federico because I could have and still can always count on them. More than once they have saved my day, adding colors when my eyes had only see shades of black.

I want to thanks my families, my kinsman for the support and the faith in me and my choices. Thanks to my adoptive family, my roommates, for everything. I will miss you.

Last but not least I want to thanks Silvia for convincing me that giving a possibility to who deserves it is the best you can do.